A Thesis Submitted for the Degree of Doctor of Philosophy

Rethinking Ducted Turbines: The Fundamentals of Aerodynamic Performance and Theory

Scott McLaren-Gow

Wind Energy Systems Centre for Doctoral Training
Electronic and Electrical Engineering
University of Strathclyde

2020

This thesis is the result of the author's original research. It has been composed by the author and has not been previously submitted for examination which has led to the award of a degree.

Scott McLaren-Gow
23/1/2020

Abstract

Ducted turbines are designed to augment the flow through a rotor and consequently increase power extraction, with the aim of reducing the cost of wind energy. Despite many years of research, however, much uncertainty remains on a fundamental level: uncertainty that is not conducive to maximising performance or to commercial success.

This work reduces the problem's complexity and improves understanding of the fundamentals by examining the underlying inviscid behaviour of ducted turbines, which are also known as diffuser augmented turbines. Numerical results show that the Betz limit does not apply, even using duct exit area, confirm the applicability of inviscid simulations to attached viscous flow, and clarify the influence of duct geometry.

A comparison demonstrates that the diffuser conceptual model, which has dominated research thus far, is outperformed by an aerofoil conceptual model. The latter gives a closer match between intuition and actual performance, is easier to work with, and allows the influence of the rotor to be thought of as a change in the flow seen by the duct. It is therefore recommended as the standard for future studies.

Theoretical examinations establish that invalid simplifying assumptions in existing theories leave the requirement for empirical parameters intact, and that velocity at the rotor may better fill the empirical parameter role than exit pressure or duct drag. A detailed derivation for the relationship between inviscid duct drag and augmentation is also described for the first time.

An analysis suggests that ducts inherently reduce the optimum rotor loading in inviscid flow, with increases in rotor loading decreasing duct performance by reducing the effective duct wall angle and effective free stream velocity magnitude. Viscous effects may then increase the optimum, play a larger role than otherwise appears, and have greater potential for performance improvements than previously thought.

Acknowledgements

Many people have contributed to my completion of this work, starting of course with my supervisors Peter Jamieson and Professor Mike Graham. Their knowledge and advice have been invaluable throughout. Helpful comments from my examiners Professor Gerard van Bussel and Doctor Julian Feuchtwang were likewise gratefully received.

I'd also like to thank the staff of the Wind Energy Systems CDT for all the effort they put into my education, and I particularly appreciate the patience of Professor Bill Leithead and the way Drew Smith always looks out for everyone. Funding from the EPSRC under project reference number EP/G037728/1 must also be acknowledged.

It would not have been possible to reach this point without the continuous support of my family, to whom I am extremely grateful. Thanks also to Eilidh for making the interminable weeks seem a little shorter, and to my friends and fellow students for all of the good times we had.

Contents

Nomenclature

Latin Symbols

A	Area
$\mathcal{A}_j$	Ratio of area at j to rotor area
a	Axial induction
a_0	Axial induction without energy extraction for Jamieson's ideal diffuser
C	Circumference
C_D	Duct drag coefficient
C_F	Coefficient of total duct force per radian
C_P	Power coefficient
C_{Pmax}	Maximum power coefficient
C_p	Pressure coefficient
C_R	Coefficient of radial duct force per radian
C_S	Duct axial force coefficient as defined by Werle and Presz
C_T	Thrust coefficient
C_{Topt}	Optimum thrust coefficient for maximum power
C_v	Specific heat at constant volume
C_Γ	Duct circulation coefficient
D	Rotor diameter
$\mathbf{d}\boldsymbol{l}$	Directed segment of vorticity
$\mathbf{d}\boldsymbol{s}$	Directed line segment
e	Internal energy per unit mass
F_D	Drag force on duct walls
F_{ds}	Axial force on portion of streamtube downstream of duct
$F_{d,in}$	Axial reaction force on flow from duct inside surface
$F_{d,out}$	Axial reaction force on flow from duct outside surface
F_r	Reaction force on flow from rotor
F_T	Thrust force on actuator disc
F_{TD}	Total axial force on ducted turbine
F_{us}	Axial force on portion of streamtube upstream of duct
$F_{viscous}$	Force on control volume from viscous stresses
$\boldsymbol{f}$	Body force per unit mass
I_{jk}	Influence coefficient for vortex ring k on point j
k	Constant
L	Length
$\dot{m}$	Mass flow rate
$\hat{\boldsymbol{n}}$	Unit normal vector
P	Power extracted by actuator disc
p	Static pressure
p_{loss}	Viscous losses inside duct
Q	Volume flow rate
$\hat{\boldsymbol{q}}$	Unit direction vector
R	Outer radius
R^2	Coefficient of determination
$\mathcal{R}_{aug}$	Power and velocity augmentation ratio relative to a bare rotor at equal C_T
R_s	Specific gas constant
r	Radius, radial position
S	Surface

S_{jc}	Circumferential surface j
$\boldsymbol{U}$	Velocity
$\mathcal{U}_j$	Ratio of axial velocity at j to free stream velocity
u	Axial velocity
u_{dsr}	Axial velocity induced by the duct's vorticity lumped into a single vortex ring
V	Volume
v	Radial velocity
x	Axial position

Greek Symbols

α	Duct wall angle from direction of free stream velocity
β	Velocity correction factor for the momentum equation
Γ	Circulation, vortex element strength
γ	Velocity correction factor for Bernoulli's equation
γ_x	Velocity correction factor for Bernoulli's equation using axial velocity only
ΔM	Change in axial momentum flow rate from far upstream to far downstream
Δp	Pressure drop across actuator disc
Δs	Vortex panel length
$\boldsymbol{\zeta}$	Vorticity vector
Λ_Γ	Circulation dispersion ratio
η_{diff}	Diffuser efficiency
η_Γ	Circulation effectiveness ratio
θ	Angle
μ	Dynamic viscosity
ρ	Density
Φ	Velocity potential

Subscript Symbols

$bare$	Bare rotor result
c	Chord line
cam	Camber line
d	Duct
$diff$	Diffuser
d, in	Portion of streamtube passing through duct
ds	Downstream portion of streamtube
e	Duct exit
eff	Effective quantity
i	Duct inlet
in	Inside surface
opt	Corresponding to maximum power coefficient
out	Outside surface
r	Rotor
rad	Radial surface of control volume
rd	Downstream side of rotor
ru	Upstream side of rotor
us	Upstream portion of streamtube
w	Far downstream
$wake$	Rotor's wake vorticity
x	Axial component, axial direction
∞	Far upstream, free stream conditions

Chapter 1

Introduction

We don't think about ducted turbines in the right way. Despite the allure of cheaper wind energy inspiring considerable research since the 1970s, not to mention a century long history, common beliefs and points of view still conspire with uncertainty to hinder development. Difficulties in this regard stem from the complex aerodynamics involved. Adding a structure to draw more air through a wind turbine's rotor may be simple in concept, but interrelationships and the nature of the flow through the duct serve only to confuse.

Figure 1.1: Photographs of a 100kW Wind Lens ducted turbine at Kyushu University in Japan. View from upwind side (left) and downwind side with person for scale (right).

Experiments have nevertheless demonstrated the main effect of a duct: comparing ducted and unducted rotors of the same size shows an augmentation of the flow rate through the rotor and a consequently larger power extraction. Such an analysis cannot test the economic argument, but it does prove that the ducted rotor can exceed the theoretical limit on the bare rotor. This conclusion has been the driver for much of the interest in ducted turbines, thus far culminating in construction of the 100kW prototype [1] in Figure 1.1 at Kyushu University in Japan.

Investigations have been lacking, however, on more fundamental levels. Two main schools of thought exist for the mechanism behind augmentation, for example, but one

dominates investigations of duct geometry without having been proven superior. Many theoretical relationships have been derived, but without sufficient validation and comparison. A ducted rotor can exceed the theoretical power extraction limit for a bare rotor of equal area, but existing research leaves it unclear if the limit applies when using the duct exit area instead.

Commercial success has not been forthcoming for ducted turbines, and it may be that the concept is simply unviable. An incomplete understanding of the fundamentals is not conducive to maximising performance, however, and uncertainty over limits on power extraction makes a best case economic analysis impossible. There is insufficient information to come to a conclusion, and a reduced cost of wind energy may yet arise from the ability of the duct to more than double power extraction for a given rotor size [2], to allow operation in lower wind speeds [3], and to reduce drivetrain costs [4].

Aerodynamics has been the main focus of previous research. However, the majority of investigations were limited either to simplified theory or to viscous simulations and experiments. An intermediate approach of simplified inviscid simulations instead proves useful here when examining the fundamentals and building up a base of understanding for future design activities. Existing theories are tested and the underlying inviscid behaviour of ducted turbines assessed, while the conventional approach to duct geometry studies is challenged and a theoretical limit on power extraction shown not to exist.

This chapter begins with an overview of standard wind turbine theory, followed by an introduction to ducted turbines and the different points of view on the mechanism behind augmentation. After an examination of the approaches used in previous research, the choice to use simplified inviscid simulations is justified. Open questions in the existing literature are then identified, leading to a set of objectives for this work and an outline of the remaining chapters.

1.1 Conventional Wind Turbines and the Betz Limit

Ducted turbines are often described by comparison to the conventional wind turbine, sometimes called a bare rotor because it lacks a duct, and extract energy from the flow using the same basic principle. Aerodynamic forces act on each of the blades making up the rotor, causing the rotor to turn with a conversion to electrical energy in the generator. If the influence of these blades is averaged in time, the rotor can be viewed as a permeable surface – the actuator disc – that extracts energy from the air flowing through it.

A theoretical momentum analysis [5] of an actuator disc is shown in Figure 1.2, which models the fluid as having zero viscosity. The undisturbed free stream flow appears on

the left with a purely axial velocity u_∞, pressure p_∞, and cross sectional area A_∞, then progressively expands to the rotor area A_r as the axial velocity drops to u_r and the pressure increases to p_{ru}. Energy extraction by the actuator disc manifests as a drop in pressure Δp, before a gradual return from p_{rd} to p_∞ as the flow continues to expand to A_w and slow to u_w in the far wake. The power extracted P can be calculated from Equation 1.1.

$$P = \Delta p A_r u_r \qquad \textbf{Equation 1.1}$$

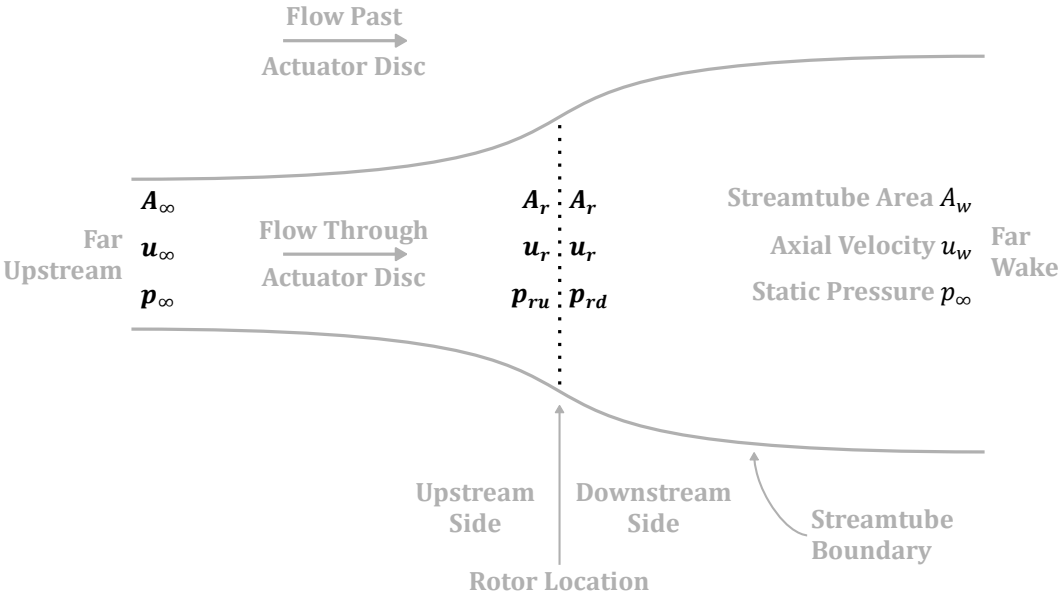

Figure 1.2: Cross section of the flow through a standard wind turbine, where the rotor is represented by an actuator disc.

Although the momentum analysis makes substantial simplifications, it leads to an important theoretical result: the Betz limit. More correctly called the Betz-Joukowsky limit [6], it describes the maximum power extraction possible by a wind turbine in terms of the power coefficient. For air density ρ, the power coefficient C_P is defined by Equation 1.2.

$$C_P = \frac{P}{\frac{1}{2}\rho A_r u_\infty^3} \qquad \textbf{Equation 1.2}$$

The Betz limit also identifies the optimum pressure drop for maximum power extraction in terms of the thrust, or rotor loading, coefficient C_T defined in Equation 1.3.

$$C_T = \frac{\Delta p}{\frac{1}{2}\rho u_\infty^2} \qquad \textbf{Equation 1.3}$$

And finally, the Betz limit specifies the optimum axial velocity at the rotor using the axial induction factor a_r defined in Equation 1.4.

$$a_r = 1 - \frac{u_r}{u_\infty} \qquad \textbf{Equation 1.4}$$

In idealised theory, then, the Betz limit states that the maximum power extraction C_{Pmax} is 16/27, or roughly 0.593, found at the optimum rotor loading C_{Topt} = 8/9 and axial induction $a_{r,opt}$ = 1/3. Equation 1.2 compares the actual power extracted from the wind to what is often described as the power in the wind; wind turbines have therefore been viewed as extracting less than 60% of what is available. It is the attraction of exceeding this value – of beating the Betz limit – that drives much of the interest in ducted turbines.

1.2 Ducted Wind Turbines

1.2.1 A Device for Increasing Flow Rate

The most significant change introduced in a ducted wind turbine is the structure around the circumference of the rotor, as illustrated in Figure 1.3. Names for this structure include duct wall, duct, diffuser, and shroud, although diffuser may also refer to the expanding section only. Corresponding names for the entire device are ducted turbine, diffuser augmented wind turbine, often shortened to DAWT, and shrouded turbine. Inlet, meanwhile, can denote both a contracting section upstream of the rotor and the plane where flow enters the duct. The centrebody houses the generator and other drivetrain components, and is often held in place by a support structure connecting to the duct, supported in turn by the tower.

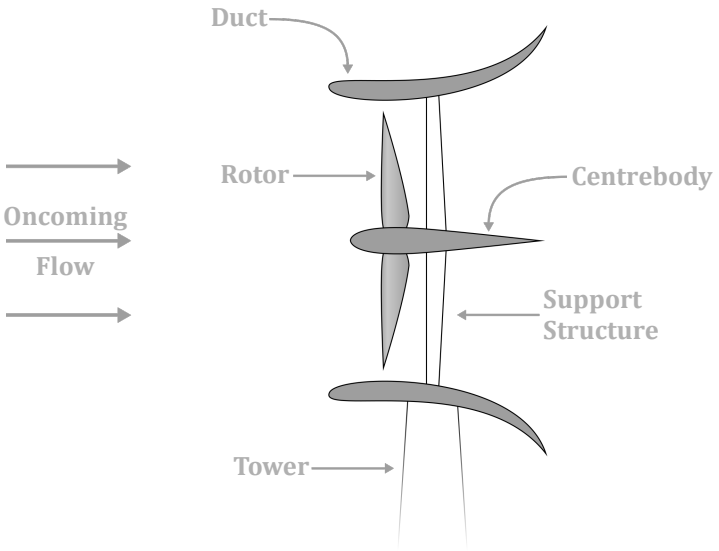

Figure 1.3: Illustration of a ducted turbine cross section, identifying the main components.

Attempts at commercialising this concept have had limited success, beginning in the 1990s with the failure of the Vortec 7 to meet expectations [7]. Numerous small scale designs [8–13] have since been unsuccessful, and Ogin, formerly FloDesign, collapsed after $150,000,000 of investment while developing a 100kW turbine [14, 15]. Tidal projects have fared no better, with Lunar Energy [16] unable to progress their design to the construction stage [17], and with the 500kW Solon turbine apparently abandoned in favour of bare rotor designs by Atlantis Resources after testing in 2009 [18, 19].

These setbacks, however, have not ended commercial interest. Development of the Wind Lens turbine continues, including a multi-rotor configuration [20], and Halo Energy has been formed by ex-Ogin employees to focus on sub-10kW designs using technology purchased from their former employer [21]. Academic interest may even be increasing, evidenced by the introduction of a mini-symposium on the topic at the Wind Energy Science Conference in 2017 and its repeat in 2019.

Commercial designs have generally resembled Figure 1.3, but significant variations are possible. Rotors may be of the vertical rather than horizontal axis type [22, 23], while the entire structure can be made lighter than air for an airborne device [24, 25], be mounted vertically or horizontally on a rooftop [26–29], or have side inlets for the flow [30]. It has even been suggested that two high-rise buildings could form a duct with a rotor between them [31], that the duct could be in the form of an underground tunnel [32], or that the turbine could be mounted on a moving vehicle [33–35]. Tidal stream designs sometimes accept flow from either end alternately [36], perhaps with an adaptable duct shape to increase power extraction [37].

With a focus on the fundamentals of ducted turbine performance, this work is restricted to the typical case of a free standing and horizontally mounted duct. Substantial diversity of design still exists, however, as demonstrated in Figure 1.4. Ducts need not be the wing-like shape shown in Figure 1.3, but they do share the common feature of expanding radially downstream of the rotor. Some also incorporate slots in the duct wall to re-energise the internal flow, delaying duct wall separation, and radial flanges at the exit aimed at increasing augmentation.

Further reductions in scope were chosen in line with the project objectives. The influence of nearby obstructions and of the tower, support structure, and centrebody were selected as factors to be considered separately from the fundamentals. While there is perhaps some limited evidence of benefit from a contracting duct upstream of the rotor without a downstream expansion [38], such devices are also not considered here.

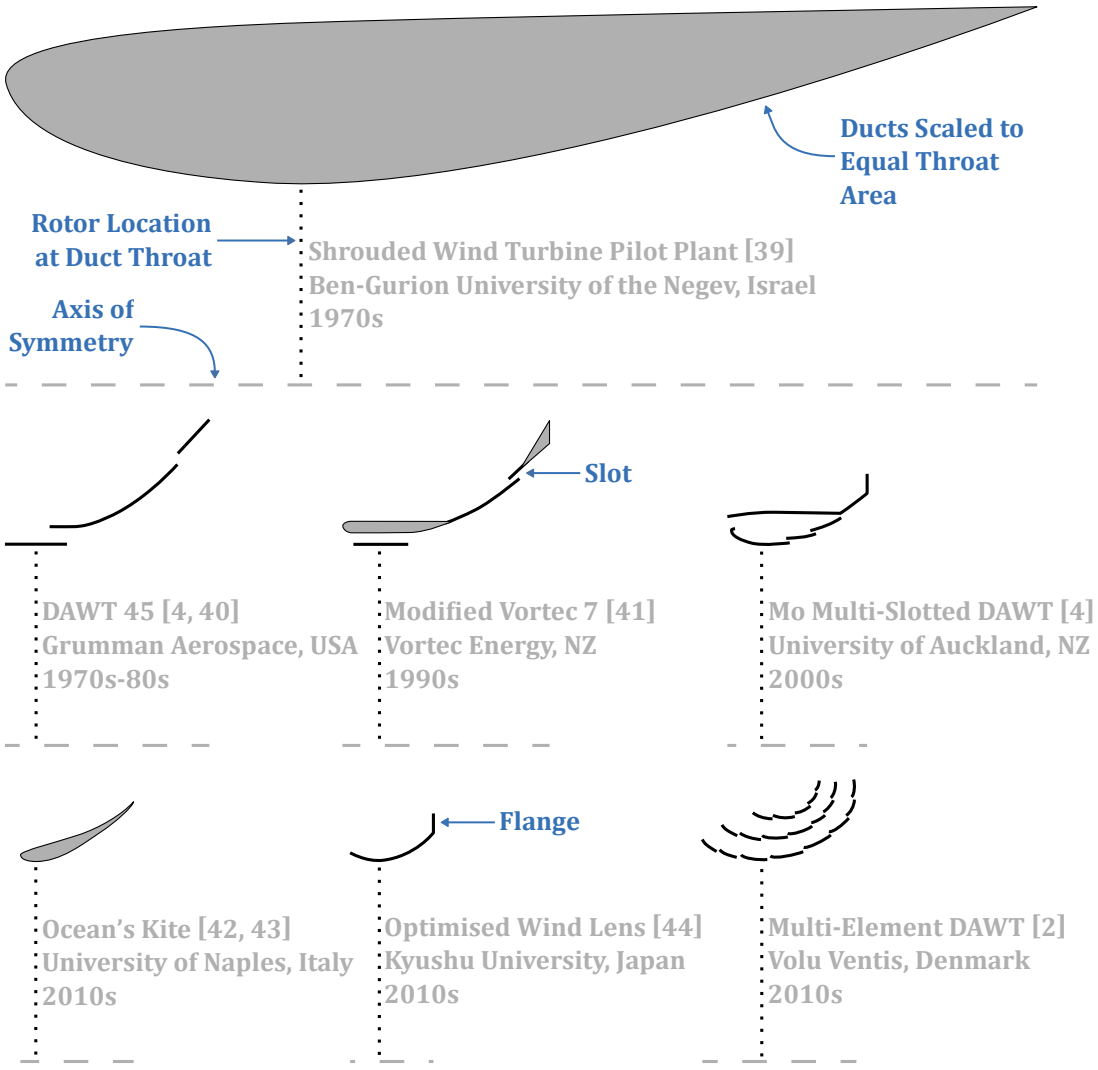

Figure 1.4: Illustration of various duct designs, scaled to equal duct throat areas. Shapes and dimensions are approximations only, while support structures and centrebodies are excluded.

Rather than slowing upstream of the rotor, as was seen in Figure 1.2 for a standard turbine, the flow can be accelerated by the duct [45] to reach u_i at the duct inlet and a value of u_r greater than u_∞ at the rotor. A resulting contraction of the streamtube [46] is visible in Figure 1.5. As in the bare turbine case, the rotor causes a pressure drop Δp that recovers to p_e at the duct exit and p_∞ in the far wake as the flow slows to u_e and u_w respectively. As there can be substantial radial variations in pressure and velocity, p and u are defined as averages over the cross sectional area at the station specified.

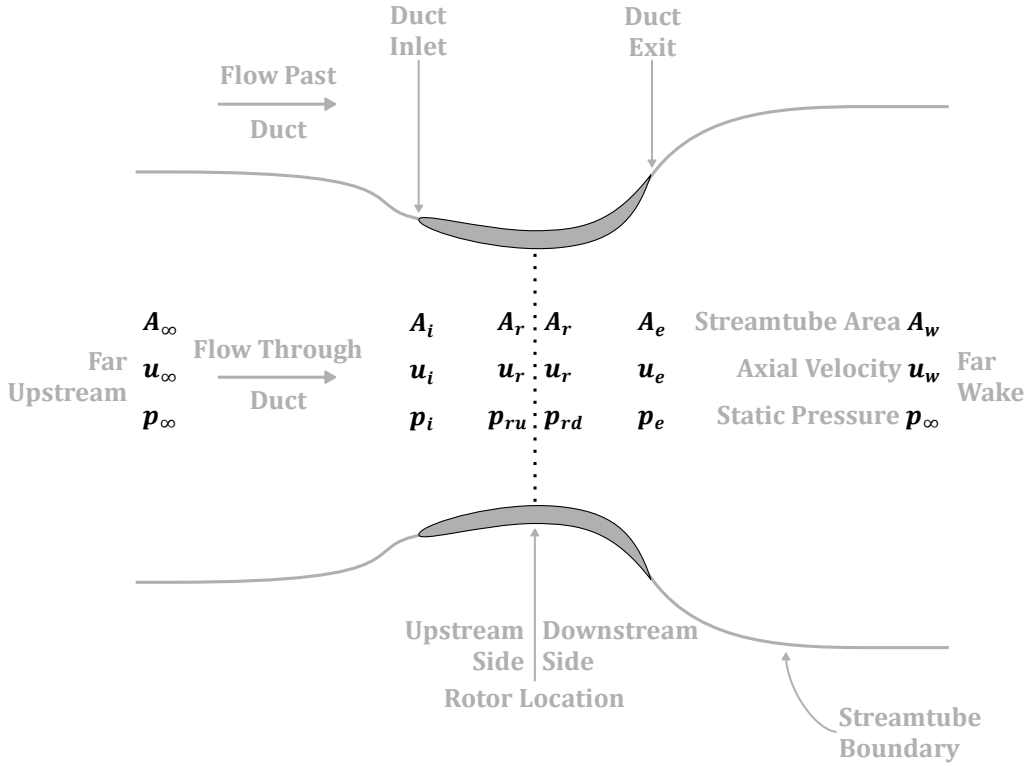

Figure 1.5: Cross section of the flow through a ducted wind turbine, where the rotor is represented by an actuator disc.

1.2.2 Mechanisms of Augmentation

Accelerated flow through the rotor leading to increased power extraction is central to the concept of a ducted turbine. Explanations for this augmentation differ, however, and an investigation of the published literature found two main kinds: one relating to the changes in pressure induced by the duct and one treating the duct section as similar to a wing. Both are examined here, along with more niche explanations and a possible secondary mechanism of increased power extraction per unit mass flow.

Reduced Pressure Explanation for Mass Flow Augmentation

A recurring explanation for augmentation was that the duct creates a region of reduced static pressure that draws more flow through the rotor. Some authors focused on the pressure at the duct exit in this explanation [30, 47–54]; empirical observation has

confirmed that this pressure can be substantially sub-atmospheric [39, 55], and more negative than the pressure immediately downstream of a bare rotor [4]. Viewpoints differed on the cause of this reduction, with some attributing it to blockage of the flow by the duct [41, 56, 57] and some stating that it is caused by the duct forcing a radial expansion of the flow [4, 58, 59].

In other studies, the suction effect on the flow was ascribed to the low pressure region inside the duct rather than at the exit [2, 57, 60–65]: the diffusion of the flow as the duct expands was viewed as causing a reduction in pressure at the duct throat. Some authors explicitly considered the reduced pressure at the exit as a contribution to augmentation, but one that is enhanced by a further reduction in pressure at the throat [41, 56, 57, 66]. An alternative to the diffusion point of view is to consider the duct wall as an annular wing that has its low pressure surface on the inside of the duct [39, 67, 68].

Aerofoil Explanation for Mass Flow Augmentation

A purely aerofoil-based approach characterised the second main explanation for mass flow augmentation. Figure 1.6 shows the general form of an aerofoil, which is usually the cross sectional shape of a wing but here is flipped to be the upper wall of a duct. The chord line connects the leading and trailing edges, and forms a positive angle of attack α to horizontal when the aerofoil is rotated anticlockwise. Another important parameter is the aerofoil's camber line, defined as the mid-point between the upper and lower surfaces, and measured by the maximum distance between the chord and camber lines.

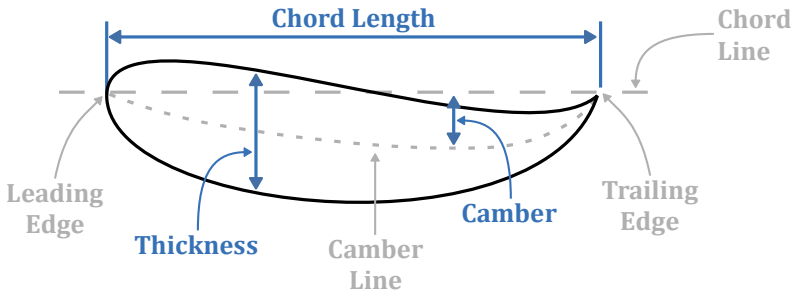

Figure 1.6: Aerofoil terminology, applied to the upper wall of a duct.

It has been empirically observed that the flow over an aerofoil leaves smoothly at the sharp trailing edge [69]. By introducing camber or by rotating to a non-zero angle of attack, the flow near to the aerofoil must therefore adapt within certain limits imposed by viscosity. This change can be measured by the circulation Γ around the aerofoil, defined in Equation 1.5 for a closed curve C around the upper duct wall with segments $\mathbf{d}\boldsymbol{s}$ and velocity vector $\boldsymbol{U}$.

$$\Gamma = \oint_C \boldsymbol{U} \cdot \mathbf{d}\boldsymbol{s} \qquad \textbf{Equation 1.5}$$

A positive value of circulation around the upper duct wall by definition means a greater axial velocity passing through the inside of the duct than passing by the outside. Through the Kutta-Joukowski theorem [69], the change in the flow can also be related to the lift force acting on the aerofoil. These two facts serve as the basis of differing points of view on the aerofoil explanation of augmentation.

The first perspective concerns the lift force produced by an aerofoil shape, which becomes a radially inward force when the aerofoil is rotated about an axis to form an axisymmetric duct. It has been suggested that the consequent reaction force on the flow causes it to expand radially downstream of the duct, with mass continuity then leading to an increase in the size of the streamtube upstream of the duct and a larger mass flow [4, 70–73]. While Aranake, Lakshminarayan, and Duraisamy [74] encountered different mass flows through ducts with the same radial force, they suggested that this could be accounted for by differences in the position of the leading edge stagnation point.

The second type of aerofoil-based explanation is related to the circulation developed around the aerofoil that causes an acceleration of the flow inside the duct. Some authors used circulation to connect radial force to augmentation, stating that the force causes circulation rather than describing it as forcing flow expansion [55, 75–77]. Phillips [4] considered these explanations equivalent. Other authors took the view that the circulation is induced directly by the duct wall shape, and made no reference to the radial force [2, 25, 82, 46, 60, 71, 74, 78–81].

Other Explanations for Mass Flow Augmentation

Ducts with an outlet flange typically have been viewed as having a somewhat distinct mechanism of augmentation. Separated flow, which will be discussed further in Section 1.2.3, exists on a flange's downstream side; some authors described augmentation directly in terms of this region having low pressure and drawing more flow through [59, 83–85], while others specified that the low pressure results from vortex formation [33, 37, 86–90]. One study attributed the augmentation to obstruction by the flange causing the flow to have an 'easier path' through the duct [91], while explanations by analogy to trailing edge flaps on aerofoils were not found.

More unusual explanations for the mechanism of augmentation for all ducts included a lower pressure on the suction side of the rotor blades leading to an increased blade lift force and power extraction [51], and vortex formation or separation as the cause of augmentation even in the absence of a flange [92, 93]. One group of authors considered augmentation to result from the combination of circulation, reduced pressure at the duct exit due to separation, and the area change between throat and exit [60, 78].

Wake Mixing: A Secondary Mechanism?

Viscous wake mixing downstream of the turbine has been proposed as a secondary cause of augmentation [4, 35], an effect not shown in Figure 1.5 where the fluid has no viscosity. Additional energy would be transferred from the external flow into the wake by this mixing, potentially increasing the optimum rotor loading coefficient compared to a bare rotor. As an increase in C_T is equivalent to an increase in the power extracted per unit mass flow [4], this augmentation would be additional to any increases in flow rate. However, Section 1.5.6 will show that it is not yet clear how the inclusion of a duct affects the optimum value of C_T.

Questions Raised

While both the reduced pressure and aerofoil explanations have frequently been put forth to explain the mass flow augmentation, no detailed comparison of the two was found in the literature surveyed. It is therefore unclear whether there are advantages to one over the other, or if they are truly equivalent. Furthermore, little consideration seems to have been given to an aerofoil-based explanation for flanged diffusers. The magnitude of any augmentation per unit mass flow through wake mixing is also uncertain.

To ease comparisons between the two main augmentation theories later in this work, one viewpoint was selected from each. Reduced exit pressure was chosen over inside pressure, as it was commonly included in theoretical models and investigations here confirmed an exact theoretical relationship with augmentation. In any case, the viewpoints may be equivalent: Phillips suggested that a change in pressure at the exit can be translated throughout the entire duct [4].

There are also reasons to believe that both aerofoil-based viewpoints are equivalent: the Kutta-Joukowski theorem states that there is a linear relationship between circulation and force for a 2D aerofoil, and some authors have linked the two phenomena for ducted turbines. Circulation was chosen as the primary representative for the aerofoil-based mechanisms in this work, a decision borne out by the results in Section 7.2.

1.2.3 The Influence of Viscosity

All real fluids have some non-zero level of viscosity, but models that assume inviscid flow can still have value: the basic theory for flow through a wind turbine discussed in Section 1.1, for example, makes exactly that assumption. Care must be taken to consider the impact of neglecting viscosity, however. For a ducted turbine, using an inviscid flow means that the fluid always leaves the duct trailing edge smoothly, but in reality a sufficiently large duct wall angle results in flow separation. The main fluid flow then leaves the surface early and a region of recirculation results, as illustrated in Figure 1.7.

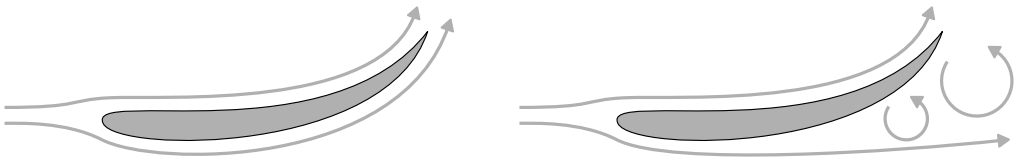

Figure 1.7: Illustration of attached and separated flow on the inside surface of a duct upper wall.

Broadly speaking, separated flow was viewed by other authors as reducing or limiting the performance of a ducted turbine [e.g. 50, 55, 66, 94]. Both the lift force and the circulation decrease when separation is present on an aerofoil, while inside a diffuser it can be viewed as limiting the expansion of the flow [57, 95]. Hjort and Larsen [2] introduced a second limitation for highly performing ducts that avoid separation on their surface: what they termed diffuser wake stall. In this case, flow reversal can occur downstream of the duct exit when pressure recovery in the wake leads to sufficiently low velocities.

The impact of viscous effects on ducted turbines has been measured using the diffuser efficiency parameter [39, 55], defined as the ratio between the actual pressure rise in the duct's expanding section to the rise without any viscous effects. Similar parameters exist for inlet section efficiency [56, 57] and overall duct efficiency [32]. With the inviscid rise calculated from Bernoulli's equation, the diffuser efficiency η_{diff} is shown in Equation 1.6.

$$\eta_{diff} = \frac{(p_e - p_{rd})_{actual}}{(p_e - p_{rd})_{inviscid}} = \frac{p_e - p_{rd}}{\frac{1}{2}\rho(u_r^2 - u_e^2)} = \frac{p_e - p_{rd}}{\frac{1}{2}\rho u_r^2\left(1 - \frac{A_r^2}{A_e^2}\right)} \quad \textbf{Equation 1.6}$$

This parameter is reduced by viscous losses such as flow separation [55, 57, 96] and friction between the duct and flow [55], and there was general agreement that power extraction is consequently reduced [4, 32, 39, 49, 50, 56, 96]. Highly efficient diffusion has therefore been sought after [55, 79], even before structural requirements from increased drag and buffeting forces were considered.

Viscous effects were not always viewed negatively, however, as was discussed in Section 1.2.2: a region of separated flow was sometimes considered the cause of augmentation for a flanged diffuser. The same argument has been applied to a design with a large expansion angle that does not reach the extent of being a radial flange [60]. An inviscid flow would also prevent wake mixing and any subsequent augmentation of power extracted per unit mass flow.

1.2.4 Measures of Performance

Power and Thrust Coefficients

As with bare rotors, the power coefficient is a commonly used measure of performance for ducted turbines. A certain level of controversy exists, however, over the correct choice of reference area. Many studies followed the conventional definition and used rotor area [4, 55, 76, 77, 97], and it has been suggested that this may be the most common approach [98]. Other studies used the duct exit area [36, 43, 53, 81, 99, 100], some presented results using both [44, 66, 74, 101], and one suggested using rotor area when interested in energy capture and exit area when interested in economics [32].

Arguments for exit area included the claim that it was the fairest approach by comparing using the area of free stream flow intercepted by the ducted turbine [36, 99], and that it allowed direct comparison with a bare rotor equal in size to the duct's largest diameter [43, 81, 100, 102, 103]. Foreman, Gilbert, and Oman [50], however, argued that any reference area can be chosen so long as it is used consistently: questions of economics will always be resolved with cost of energy calculations rather than by comparing power coefficient values.

It is the latter point of view that is accepted here. Vast differences in design can exist even when comparing with a fixed reference area, as illustrated in Figure 1.4, so the power coefficient cannot be used to determine which design is superior. An assessment in Section 4.2.1 suggests that the standard definition involving rotor area, given in Equation 1.2, is the most convenient; that definition is therefore used throughout this work unless otherwise stated. The rotor loading coefficient is also used in its standard form as defined in Equation 1.3.

Augmentation Ratio

Another way of measuring the performance of a ducted turbine is the augmentation over the performance of a bare rotor. This comparison can be made in a number of ways: using power extracted or flow rate through the rotor, using equal bare and ducted rotor areas or with the bare rotor equal in area to the duct exit, and using both rotors at the same C_T or with the bare rotor always at the Betz limit value of $C_T = 8/9$. Whatever choices are made, a fair comparison requires both rotor designs to be optimised for the presence or absence of a duct as appropriate [56], although comparisons may still be complicated by factors such as differing tip losses.

The default definition used here is the ratio of the power extracted by the ducted turbine to that from a bare rotor of equal rotor area and at the same rotor loading. An actuator disc is always used so that rotor efficiency is at the theoretical maximum, so the power and velocity augmentations are equal, giving the augmentation ratio $\mathcal{R}_{aug}$ in Equation 1.7.

$$\mathcal{R}_{aug} = \frac{C_P}{C_{P,bare}} = \frac{u_r}{u_{r,bare}} \qquad \textbf{Equation 1.7}$$

An exit augmentation ratio $\mathcal{R}_{aug,e}$ can be defined using the power coefficient calculated at the duct exit $C_{P,e}$ as in Equation 1.8.

$$\mathcal{R}_{aug,e} = \frac{C_{P,e}}{C_{P,bare}} = \frac{u_e}{u_{r,bare}} \qquad \textbf{Equation 1.8}$$

$\mathcal{R}_{aug} > 1$ therefore indicates augmentation of the flow, and $\mathcal{R}_{aug} < 1$ curtailment of the flow. Although $C_P/C_{P,bare}$ is undefined at $C_T = 0$, the equation still holds for the power term in the limit as C_T approaches 0 and can be calculated using the velocity term. It must also be noted that augmentation is employed only as an aid to understanding, and a value above 1 does not imply that the ducted turbine should be preferred to a bare rotor.

Drag Coefficient

It has been suggested that increased power extraction can exist only in the presence of increased duct drag [66], although there can be mass flow augmentation without drag if the rotor is not extracting energy [76] and no studies were found viewing drag as a cause of augmentation. Phillips [4] proposed the conceptual explanation that the axial force is somehow related to the radial force on the duct wall, but did not discuss in detail. Investigations of the duct drag F_D are included in this work, usually made dimensionless with the drag coefficient C_D defined in Equation 1.9.

$$C_D = \frac{F_D}{\frac{1}{2}\rho u_\infty^2 A_r} \qquad \textbf{Equation 1.9}$$

Velocity Ratio and Exit Pressure Coefficient

While axial induction is typically used as a dimensionless measure of velocity for a bare rotor, ducted investigations have often used the velocity ratio $\mathcal{U}$ defined in Equation 1.10.

$$\mathcal{U} = \frac{u}{u_\infty} \qquad \textbf{Equation 1.10}$$

The exit pressure coefficient $C_{p,e}$ was also frequently encountered due to the reduced pressure explanation of augmentation, with a lower case p distinguishing it from the power coefficient C_P. The definition is given in Equation 1.11.

$$C_{p,e} = \frac{p_e - p_\infty}{\frac{1}{2}\rho u_\infty^2} \qquad \textbf{Equation 1.11}$$

1.3 Previous Investigative Approaches

Most of the research reviewed focused on the aerodynamics of ducted turbines, with three main approaches used: theory, experiment, and numerical simulation. Theoretical investigations endeavoured to build a set of equations that relate various parameters of interest, while experiments and simulations were frequently used to test the performance of a particular turbine. Each approach is summarised here, with further details that are particularly relevant for this work to come in Section 1.5.

1.3.1 Theory

The development of simple theoretical descriptions of ducted turbine behaviour was relatively common in the literature, with an equation for the power extracted usually derived from momentum and energy considerations [e.g. 4, 49, 58, 104]. While some theories focused on rotor design [e.g. 49, 96, 105, 106] and so took radial variations of the flow into account, the majority [e.g. 4, 63, 96, 107] took a quasi-1D approach: no radial variations except a step change between the flow inside the rotor's wake streamtube and the flow outside it radially. A radially constant pressure drop was applied to the flow in this approach to model the rotor.

In itself, developing a set of equations can be a useful way to find the influences on performance. Some studies attempted to go further, however, by assessing the relative importance of each of the various parameters included in the equations [e.g. 4, 39, 50, 56]. By holding the other parameters constant, the influence of one could be determined by varying it and noting the change in power coefficient. However, interrelationships between parameters may limit the accuracy of such an approach.

Although the starting points for the theories examined were generally similar, the end points could be disparate. Almost all required at least one empirical parameter to calculate the performance of a particular duct, but no consensus has been reached on the most appropriate parameter. Exit pressure coefficient [66], diffuser efficiency [41], duct drag [104], velocity at the rotor [55], exit [32], or far wake [76], and rotor loading coefficient [108] have all been used, where the references are given as examples. The ratio of duct exit to throat area was the only geometrical parameter commonly included [e.g. 58, 63, 66, 96].

1.3.2 Experiment

Experiments have commonly been used in the study of ducted turbines, with the most frequent type found in the literature being those carried out in a wind tunnel [e.g. 100, 109–111]. Generally such investigations were part of the design process for a duct [e.g. 67, 83, 89, 112] or rotor [e.g. 109, 113–115], and involved measurements of the power extracted or velocity at the rotor plane.

A range of rotor representations were used in these studies, including rotors designed for use inside a duct [39, 116] or without a duct [67, 117], mesh screens designed to induce a pressure drop [39, 56, 62, 104, 118], and physical rotor models of unclear or unspecified design [35, 59, 89, 115, 119]. Some compared the performance of the same rotor in and out of a duct [e.g. 65, 100, 111, 120], despite recognition that such a comparison is unfair: a rotor optimised for one use will be sub-optimal in the other [67, 79].

Validation of simulation results was another common use for experiments [e.g. 30, 59, 62, 114]. More unusual investigations included studies of the flow structure [52, 59, 90], validation of rotor design processes [61, 68], and assessment of real world factors such as the performance of two turbines placed in proximity [116], yaw [4, 121], and flow turbulence [4, 100]. There have also been occasional field tests of prototype ducted turbines, including of the Vortec 7 with a 7.3m rotor diameter [41, 62] and of Wind Lens turbines up to a 13m rotor diameter model rated at 100kW [1].

1.3.3 Simulation

The vast majority of numerical studies encountered were carried out using viscous Computational Fluid Dynamics (CFD) simulations [e.g. 64, 122–124]. While some authors used a full 3D model for the duct and rotor [e.g. 36, 51, 74, 91], most took advantage of the geometrical symmetry and simplified the problem with an axisymmetric model of a radial slice of duct [e.g. 4, 43, 87, 125]. It was also common to treat the flow as steady in time [e.g. 57, 59, 84, 91], with some authors finding little difference to the time-averaged power result from unsteady simulations [36, 99, 100].

Simplifications were also common for the rotor model, with only the most comprehensive studies directly including the rotor blade geometry in simulations [e.g. 51, 81, 117, 126]. Rather more authors chose to reduce the computational complexity by representing the blades indirectly with an actuator disc, imposing a pressure drop across the rotor plane [e.g. 85, 127–129]. In some cases no mention of a rotor was made at all [e.g. 86, 89, 112, 130], suggesting the study of an empty duct.

Most investigations focused on one of three topics: inspecting the performance of a particular ducted turbine [e.g. 59, 62, 89, 122], testing the influence of various geometrical parameters on performance [e.g. 52, 89, 119, 131], and optimising the duct shape for maximum power extraction [e.g. 43, 121, 128, 132]. Other studies carried out an optimisation of rotor design for ducted turbines [110, 113, 129, 133], highlighting the need to avoid simply using a standard bare rotor. Numerical results were also occasionally used in testing theoretical descriptions of ducted turbines [41, 55, 134].

Another much rarer class of investigation employed inviscid simulations, either using CFD packages with zero viscosity or inviscid panel method codes. This approach has been used as a first step in the selection of duct shape [73], to improve understanding of the fundamental behaviour of ducted turbines [2, 46, 80], and to quantify the influence of wind tunnel wall proximity [135]. There have also been investigations into the applicability of ducted turbine theories on an inviscid level [2, 136], and an assessment of 3D effects and cavitation risk for a ducted marine current turbine rotor [81].

1.4 The Need for an Inviscid Approach

A large body of research already exists for ducted turbines, but the previous section shows that the majority was split between only two main categories: the development of simplified theory, and design-focused studies using experiments or simulations with the full complexity of viscous flow. Research in the space between these groups was scarce, mostly comprising some simplified inviscid simulations, examinations of flow phenomena, and attempts at validating theoretical equations.

Significant scope remains for research bridging the gap between theory and design, and that is where this work is focused. Inviscid simulations were chosen as the basis of this investigation, and have proven to be a useful tool throughout. At first, that may seem a surprising choice: a viscous phenomenon sets limits on augmentation through separation, and viscous losses generally may be a pervasive cause of reduced performance. How can simulations excluding such an important factor be of value?

Ideally, it would be possible to examine the aerodynamic problem in all its detail and come to a complete understanding of the system. Ducted turbines are complex, however, suffering from many influencing parameters and an interaction between the duct and rotor [4]. Aspects of uncertainty and disagreement therefore still exist in the literature, as will become clear in Section 1.5; removing viscosity strips back some of the complexity, and allows a clearer picture to emerge of the underlying inviscid behaviour.

Valuable understanding of the overall system can still result from such an analysis. The momentum theory underlying the Betz limit, for example, is inviscid [5], but it forms a cornerstone in the field of wind energy. An inviscid relationship between lift and circulation underlies aerofoil theory, even though the behaviour changes with separation and viscosity generally [69]. Likewise an inviscid understanding can inform prediction and interpretation of ducted turbine performance, and provide future studies with a base from which to isolate and quantify viscous effects.

Other authors have also recognised the value of this simplification for theory development in particular [e.g. 55, 58, 76, 137], but also for the numerical studies discussed in Section 1.3.3. An inviscid analysis may approximate real flows for designs where viscous effects are minimised [46], with the potentially related field of annular wings serving as an example that has had a large number of inviscid investigations [80]. Qualitative agreement has been found between inviscid simulations and experiment for ducted turbines [46, 80], along with approximate quantitative agreement with viscous simulations [73, 97]. An inviscid approach also leads to faster simulations [2] and allows the remaining assumptions in inviscid theories to be tested [136].

1.5 Questions Raised from Previous Research

An examination of the previous research revealed a number of areas predisposed to an inviscid investigation. Focused on the fundamentals, topics still covered a wide range including theory, the Betz limit, and the influence of geometrical parameters. A review of the relevant literature is presented here with the aim of providing a justification of, and background information to, the investigations conducted in this work. The questions raised feed into the research objectives discussed in Section 1.6.

1.5.1 Are Ducted Turbine Theories Valid?

Previous Research

Only a few authors investigated the validity of their quasi-1D theories. In general, two types of tests were carried out: assessments of theoretical conclusions, such as equations for power coefficient, and assessments of particular assumptions made in the development of the theory. Comparisons were generally made between theories and results from experiments or viscous simulations, even for theories that neglected viscous effects.

Of the assumptions tested, the majority were found to be inaccurate. A linear relationship was not found between duct drag and rotor loading [2, 104], exit pressure was not independent of local rotor loading coefficient [39], and the quasi-1D assumption applied only for ducts with small area ratios [39]. Results for the Vortec 7 revealed inaccurate assumptions, but did not identify the problem areas [62]. Some evidence, however, has been found to support the assumption that a radially constant rotor pressure drop maximises power extraction [2], a vortex ring-based theory provided accurate centreline velocities [138], and one theory made reasonable predictions for power when using experimental results for the other parameters [133].

Viscous results have shown some theories to over-predict power coefficients by between 15% and 100% [2, 62, 105]. Jamieson [137], however, found good agreement

after corrections to allow his ideal diffuser theory to apply to a real duct, although the exact meaning of ideal diffuser has not yet been identified. Van Bussel [66] also found good agreement with experiment after correcting for mass flow through slots, but he, Werle and Presz [108], and Khamlaj [133] all blamed viscous effects for disagreements with simulation results at higher rotor loadings.

Inviscid studies were rare. Hjort and Larsen [2] used an inviscid panel method alongside viscous CFD simulations, but suggested that differences between the two were due to inferior precision of the panel method rather than the presence of viscous effects. Aranake, Lakshminarayan, and Duraisamy [136] used inviscid CFD simulations, but validation checks against bare rotor theory revealed errors that reached more than 10% by C_T = 0.6 and increased further with rotor loading.

Rather than assessing power coefficient, Lawn [56] compared duct centreline velocities and found that the best performing experimental results matched theoretical expectations. This approach, however, neglects any radial variations in the flow. Hansen, Sørensen, and Flay [55], meanwhile, confirmed one of their key theoretical conclusions: that the ratio of power coefficients between ducted turbine and bare rotor is equal to the ratio of the mass flows through each rotor.

Questions Raised

The prevalence of inaccurate theories and assumptions highlights the importance of validation. That does not necessarily mean showing a perfect match between theory and reality, but rather showing that a theory is accurate on a chosen level of simplification. Bare rotor theory is valid, for example, even though it neglects viscous effects. Rather less certainty exists for ducted turbine theories, where validation work has not been comprehensive.

Further study is needed to confirm whether errors in inviscid theories are solely due to viscous effects: previous checks using inviscid simulations suffered from accuracy problems. Studies have also not always ascertained the source of inaccuracies generally. Underlying these theories is the quasi-1D assumption, but experiments have shown significant radial variations and it is unclear whether accuracy is consequently affected. Finally, Jamieson introduced the ideal diffuser concept, but has left open the question of its exact definition.

1.5.2 Which Parameters for Duct Geometry?

In principle, any of the sets of parameters found in the literature can be used to describe duct geometry so long as they completely specify the shape. Parameters that have a clear link to an aspect of performance are more valuable, however; for example, angle of attack, camber, and length all have distinct effects on lift for aerofoils [69]. Two

main types of parameter were used in studies investigating the influence of duct shape, and both are surveyed here. Discussion of their impact on performance follows in Section 1.5.3.

Previous Research: Diffuser Parameters

The main approach used to describe duct shape relates to the expanding diffuser section. Diffuser expansion angle, length, and area ratio make up the basic parameter set, where the area ratio is defined as the duct exit cross sectional area divided by the duct throat cross sectional area. Any two of these parameters are sufficient to define the shape of a straight walled diffuser, and the previous studies are split between those that used length and angle [e.g. 37, 47, 89, 131], area ratio and angle [122], and area ratio and length [51, 98, 128].

Diffuser parameters are defined here as all three of those mentioned above, plus the parameters that are used alongside them. The inlet area ratio is included, for example, which was more rarely encountered than exit area ratio and was usually controlled by fixing the inlet length and angle [37, 48, 112, 131]. Where the duct design included an outlet flange, the height of the flange was typically also specified [37, 88, 89, 119, 131].

Studies using a straight walled duct [e.g. 48, 51, 88, 122] were able to generate the duct geometry directly from the basic parameters. The approach with more complex shapes is less clear, however, with examples of curvature being introduced without noting how to generate the shape from the parameters [98, 131]. Shives and Crawford [57] avoided this problem by modifying a NACA0015 aerofoil and then calculating the diffuser parameters from the result, while Foote and Agarwal [128] did the same with the output of their shape optimisation process.

Deviations from the basic set of parameters were also found. Shives and Crawford [57] used exit and inlet area ratios, along with the inside and outside surface exit angles. These were defined relative to the axial direction at the duct trailing edge. Phillips [4] also selected the outside surface exit angle and exit area ratio, along with the rather less precise recommendations of an inlet design that maximises flow uniformity and an inside surface that maximises diffuser efficiency.

Previous Research: Aerofoil Parameters

Many of the authors that ascribed augmentation to radial force or circulation did so with reference to aerofoils or wings [e.g. 46, 55, 76, 139]. However, unlike with diffuser parameters, there have been few investigations of duct shape using aerofoil parameters. Those investigations that have been conducted [e.g. 25, 73, 81, 101] have assessed one or more of duct wall angle of attack, camber, and thickness.

Questions Raised

Diffuser parameters have proven the more popular for specifying duct shape, but no comparison with aerofoil parameters was found that determined their relative utility. It remains to be seen whether a clearer link exists between performance and parameter for either approach. It is also unclear if the more complex diffuser approaches can be used to specify duct shapes, rather than simply measuring geometries generated in a different way.

1.5.3 How Does Duct Geometry Affect Performance?

A number of experiments and simulations have been used to test how the various duct shape parameters affect performance, but the answers have not always been clear. The performance impacts found are reviewed in this section, which is again split between the diffuser and aerofoil approaches discussed previously.

Previous Research: Diffuser Parameters

Diffuser parameters identified as having an influence on performance include diffuser section length and angle, exit area ratio, and measures of duct wall shape and inlet design. Unique amongst these is the area ratio: the only geometrical parameter found in Section 1.3.1 to be included in ducted turbine theories, and one that has been considered as having the most significant impact [39, 55, 63, 113, 128]. Differences in power extraction have still been found, however, for designs with the same area ratio [66, 122].

Accurately assessing the importance of area ratio is difficult due to interrelationships: even for the simplest case of a straight and thin walled diffuser, a change in area ratio also changes diffuser angle or length. Shives and Crawford [57] fitted a regression model to CFD simulations to try and isolate the influence of increased area ratio, finding decreases in diffuser efficiency and exit pressure. Phillips [4] instead argued that diffuser length alone was immaterial, concluding that velocity increased up to an area ratio around 3 at a fixed expansion angle.

A number of other studies attempted to measure the influence of the basic parameters, despite the interrelationships. In very general terms, increases in area ratio [51, 98, 122], diffuser angle [48, 51, 112, 122], and diffuser length [48, 88, 112, 119] led to increased velocity at the rotor up to a point, but the increases could have been caused indirectly through changes in the other parameters. Indeed, increases in velocity with length have been attributed to reduced flow separation due to reduced diffuser angle [51, 98, 113, 128].

More complex designs introduce curved duct walls, but the importance of this change is unclear. Area ratio has been considered paramount to the point of excluding curvature

from performance investigations [47, 48, 51, 98, 122], but curvature may influence the duct radial force [55, 77], exit pressure [4, 56, 57], and viscous losses [4, 55, 124]. Phillips [4] argued that viscous losses depend on the internal surface shape, and that increased external surface exit angles lead to increased radial projection of the flow and lower exit pressure. Shives and Crawford [57] concurred, and proposed the internal exit angle as representative of that whole surface.

Another factor introduced when moving away from the simplest designs is duct wall thickness, which Shives and Crawford [57] used as a parameter to generate duct shapes. They did not, however, investigate its influence on performance. Nor did any diffuser-based study encountered. It may be that authors who treat the internal and external surfaces as independent consider thickness to be a consequence of the choice of wall shapes rather than a parameter in its own right.

Inlet design was generally viewed in terms of the potential for negative effects on power extraction rather than as contributing to augmentation in itself. Careful design may avoid or mitigate inlet flow separation [4, 66, 88, 89, 140], and reduce yaw sensitivity and flow asymmetry [4], while Khamlaj [133] found no direct influence on performance from a theoretical analysis on an inviscid level. Both increases [112] and decreases [48] in flow velocity have been reported when increasing inlet length and angle, while Shives and Crawford [57] found little impact on power extraction from inlet efficiency for inlet area ratios between 1.07 and 1.73.

Previous Research: Aerofoil Parameters

Rather fewer studies have explored how performance is affected by changes in the aerofoil parameters. One study [81] used inviscid simulations and found increasing power extraction with wall angle at fixed camber until a peak at 13°; the peak occurred because the rotor area was reduced as the angle increased. Likewise increasing power extraction was found with increasing camber, but details of these results were not presented. Another inviscid investigation assessed 12 two-dimensional ducts and found increased velocity with camber and little change with thickness, although each duct shape was from a different aerofoil family [73].

Viscous simulations have also been used, with an investigation of 3 duct shapes suggesting that increased camber and thickness increase the power coefficient [25], and tests with a single shape at a number of wall angles showing increases in power coefficient until separation was reached [101]. Wind tunnel tests of a planar aerofoil have also shown that the lift coefficient increases with wall angle in the presence of a screen representing a rotor, but decreases with rotor loading [141] and tip clearance [142].

Some studies have alternatively applied standard aerofoil data to ducted turbines, and it has been suggested that the chord angles for separation are equal [81]. Others, however, argued that the rotor influences the flow to change the effective angle of the duct wall, with increased separation attributed to that effect on the external surface in one case [36] and decreased separation internally in others [43, 72]. Designs more generally have been based on high lift aerofoils [2, 43], flap [4, 39] and slot [4] data has proven useful, and annular aerofoil data was used to explain yaw performance [139].

Questions Raised

Almost all of the studies examined in this section were understandably viscous in nature, but it would be valuable to fully establish the underling inviscid contribution to performance and later the importance of viscous effects. A number of more specific questions exist for the diffuser parameters, not least concerning the importance of area ratio. Does its influence reflect its status as the only geometrical parameter used in theoretical work, or would changes in other parameters have a large impact on performance even at a fixed area ratio?

Although they are interrelated, it may be possible to isolate each of the diffuser parameters with careful selection of duct shape. Would these then have the expected influence on performance? Would changes in length really have no impact in inviscid flow? It must also be questioned whether inlet design is important to viscous effects only, as inlet design affects aerofoil parameters that have an influence on circulation.

Further study of the aerofoil parameters would be less about resolving confusion and more about simply building up basic understanding due to the limited existing research. The effect of wall angle on performance seems to match expectations, but it is not known how changes in the other parameters affect its influence. Two investigations were found that presented camber and thickness results, but one only compared two values of each parameter and the other did not hold all other parameters constant. No studies were found that examined length or aerofoil family. There is therefore a need for wider ranging and more systematic examinations.

1.5.4 How Do Flow Rate and Rotor Loading Affect Power Extraction?

Previous Research

Two points of view dominated the debate on how the power extracted by a ducted turbine varies with the flow velocity at the rotor: a linear variation or a variation with velocity cubed. A linear relationship was found in the early theoretical work at Grumman Aerospace [45], studies near the turn of the millennium by van Bussel [58] and Hansen, Sørensen, and Flay [143], and in the equations [65, 66, 77, 105, 115] and results [2, 4, 136] of several authors since.

Despite van Bussel [58] calling it a common mistake, however, many published studies have continued to assert that power extraction varies with velocity cubed [e.g. 84, 85, 132, 144]. Some authors have used equations based on this point of view to calculate results from simulations or experiments [e.g. 28, 86, 112, 119], while some experimental results appear to support a velocity cubed relationship [88]. Three cases were also encountered where authors argued that power varied with velocity cubed but only linearly with the mass flow through the rotor [34, 51, 145], despite velocity being proportional to mass flow.

Also relevant to power extraction is uncertainty over the relationship between flow rate and rotor loading. A decrease in mass flow augmentation with rotor loading has been found numerically [55], and some authors agree that there is an interaction [27, 122]. Other simulations have shown no connection [136], however, which is a belief apparently shared by authors who assessed the augmentation provided by their designs without including a rotor [e.g. 48, 78, 123, 146]. Some later concluded that there is in fact a relationship when their design underperformed with a rotor in place [112, 119].

Questions Raised

Although a number of studies already provide evidence of a linear relationship between power and velocity at the rotor, some authors remain unconvinced or unaware. Additional proof may be of value. Of more interest is the relationship between flow augmentation and rotor loading, as it remains an open question whether increased C_T reduces the augmentation or leaves it unaffected. Given the importance of flow augmentation to power extraction, it would be beneficial to determine the true relationship.

1.5.5 Does the Betz Limit Apply?

Previous Research

It is relatively well accepted that the Betz limit does not apply to ducted turbines when calculating the power coefficient using the rotor area, as supported by a number of experimental results [4, 34, 96, 103], numerical results [55, 91, 128], and assertions [77, 137]. A common response [2], however, is that the exit area of the duct should be used when comparing to the Betz limit rather than the rotor area.

Some researchers agreed that the Betz limit does apply when using the exit area power coefficient [42, 48, 53, 102], but there is also some evidence to the contrary. A momentum analysis by van Bussel [66] did not reveal a theoretical limit, while simulations have found exit area power coefficients of 0.61 [124], 0.67 [101], 0.73 [43], and 0.74 [127]. Of particular note is the value of 0.88 found by Hjort and Larsen [2] for

their multi-walled design using CFD, and a value of 0.62 from wind tunnel experiments with an optimised Wind Lens turbine [44].

The evidence presented here may not convince critics, who could point out that absence of proof of a theoretical limit is not proof of absence, and that most of the numerical studies did not include an assessment of discretisation error. Both Bagheri-Sadeghi et al and Hjort and Larsen did state that their discretisation achieved mesh independence, but did not quantify the error or describe their testing process. The latter's results were, however, 2% to 17% lower than studies they compared to. Critics may also consider experimental error a likely explanation for the modest increases seen with the Wind Lens turbine.

Questions Raised

In some ways, the assertion that the Betz limit on power extraction does not apply at all to ducted turbines would be contrary to conventional wisdom in the wider field of wind energy. Strong evidence would be required to persuade critics that the exit area power coefficient can actually exceed 0.593, and it is questionable whether the existing data would convince. There is a need for highly accurate results that test the applicability of the Betz limit on the inviscid level of the theory itself.

1.5.6 How Is the Optimum Rotor Loading Affected?

Previous Research

A range of optimum rotor loadings have been suggested for ducted turbines: below [36, 55, 97, 99, 128, 129], equal to [58, 66, 105], and above [4, 22, 72, 79, 147] the bare rotor value of 8/9. Hjort and Larsen [2] additionally found both higher and lower values for different designs. A need to reduce the impedance of the flow caused by the rotor has been cited as an explanation for reduced values of C_{Topt} [62], while higher values have been attributed to viscous wake mixing with the flow bypassing the duct [76, 137]. One study, however, found increased C_{Topt} using simulations that excluded viscous effects [46].

Questions Raised

It is unclear why such a range of optimum rotor loadings exists in the literature. It may simply be that duct shape has a significant influence, but no study was found examining the nature of any such relationship. Explanations for deviations from C_{Topt} = 8/9 are also unsatisfactory, with no justification for why lower rotor impedance may be needed with a duct and no reason for an increased C_{Topt} without viscous effects. Removing any potential viscous mechanisms that would obscure the inviscid behaviour seems a prudent first step in addressing these questions.

1.6 Research Objectives

A wide range of questions have been left unanswered in the current literature, as has been seen throughout this chapter. These questions are not focused directly on designing a particular ducted turbine, but are relevant to producing a solid base of knowledge for future design activities. Answers could help maximise performance and lead to a reduced cost of wind energy. Objectives were chosen to bring clarity to some of these areas, and in combination they form the overall aim of this work: building a better understanding of fundamental aspects of ducted turbine performance.

An exploration of the inviscid behaviour of ducted turbines was the first objective, in order to enhance prediction and interpretation of performance. Several different analyses were conducted, leading to arguments that the Betz limit does not apply, that area ratio is no more important than other parameters, and that inviscid simulations can sometimes approximate viscous results. Other studies included simulations suggested as upper performance limits, and assessments of the importance of wall thickness and inlet design.

An important part of the overall aim concerns the differing points of view on the mechanism of augmentation and on the choice of parameters used to define duct shapes. These separate strands led to a single question: what is the better conceptual model for ducted turbines? If one must predict how a change in duct shape will affect performance through engineering intuition alone, for example, should one think of an aerofoil inducing circulation or a diffuser reducing exit pressure? It is argued that the aerofoil-based conceptual model is superior.

The initial objectives concerning theory were validation of existing equations on the same level as bare rotor theory, an assessment of radial variations in the flow, and clarification of the ideal diffuser concept. However, further objectives arose: finding evidence of a link between drag and power extraction missing from current derivations, and comparing equations for power coefficient. It is suggested as a result that drag and exit pressure be treated as consequences of augmentation rather than as empirical parameters from which to calculate power, and that simplifications removing the need for empirical parameters entirely are not valid.

A deeper understanding of optimum rotor loading was the final objective, starting with an initial numerical study to confirm that it can differ from the bare rotor value. Further investigations tested the influence of duct geometry in inviscid flow, and examined theoretical equations for further information. It required more extensive simulations combined with an explanation from the aerofoil conceptual model, however, to reach the main contention: that there is an inherent reduction in C_{Topt} for a ducted turbine in inviscid flow.

1.7 Outline

Meeting the objectives set out for this work necessitated the development of an inviscid simulation code. Background theory and a detailed description are given in Chapter 2, along with a demonstration that it is capable of producing highly accurate results on an inviscid level. An approach to viscous CFD modelling using a commercial software package is also set out.

Several small investigations are described in Chapter 3, for example examining area ratio, power extraction, and limits on performance. The accuracy of inviscid simulations to real flows where separation is avoided is also tested. Results from across these investigations are used in an initial assessment of the diffuser and aerofoil conceptual models.

Diffuser and aerofoil parameters are then compared directly in Chapter 4, where both approaches are used to generate duct shapes and the difficulty involved assessed. The influences of the various parameters on performance are compared to expectations from the respective conceptual models.

Changing focus, Chapter 5 selects three theories from the literature and tests their accuracy in inviscid flow. Jamieson's theory [137] is also examined to improve understanding of the ideal diffuser concept, and equations across all four theories are compared in an assessment of the parameters included.

Chapter 6 then presents further derivations, including a numerical study that provides the missing link in developing drag-based equations. Theoretical relationships provide further context to results from Chapter 2, and alternative equations for power coefficient are compared.

Finally, a numerical study in Chapter 7 suggests that ducts intrinsically reduce the optimum rotor loading in inviscid flow. Circulation effectiveness and dispersion ratios are then introduced to resolve imperfections in the circulation explanation of augmentation, leading to a plausible cause for the negative influence on optimum rotor loading.

1.8 Summary

Ducted turbines are designed to augment the flow rate through a rotor and consequently increase the power extracted. While the ensuing potential to reduce the cost of wind energy has driven research over many decades, there remains an incomplete understanding in a number of fundamental areas of the aerodynamic problem. The resulting uncertainty is not conducive to maximising performance, and may have contributed to a lack of commercial success.

A review of the existing research found most to be split between only two main categories: the development of simplified theory, and design-focused studies using experiments or simulations with the full complexity of viscous flow. An intermediate approach of inviscid simulations was chosen here to strip back some of the complexity of ducted turbines. By building a clearer picture of the underlying inviscid behaviour, uncertainty can be reduced and the prediction and interpretation of real ducted turbine performance improved.

Objectives for this work were chosen based on questions raised when reviewing the literature. An exploration of the inviscid behaviour of ducted turbines was the first, leading to strong evidence that the Betz limit does not apply to ducted turbines amongst other results. A comparison was then sought between the diffuser conceptual model that has dominated ducted turbine investigations and the aerofoil conceptual model that is argued to be superior here.

Theory was chosen for further examination, to test whether assumptions can truly eliminate dependence on empirical parameters, to find a missing link in current derivations, and to assess the suitability of the various equations for power extraction. Finally, the influence of the duct on the optimum rotor loading was selected for study, leading to the conclusion that there is an inherent reduction in inviscid flow. Together, these objectives form the overall aim of this work: building a better understanding of ducted turbine fundamentals that will be useful in future design activities.

2 Chapter

Modelling a Ducted Turbine

The main focus of this chapter is the development of an inviscid panel method for modelling ducted turbines. A majority of the results presented in this work are derived from this method, and so the theoretical background and assumptions, the modelling approach, and validation cases are all described in detail. Viscous modelling is the basis of the remainder of the results, and the approach to these simulations is also discussed.

2.1 Inviscid Panel Methods

The modelling of fluid flows is not often straightforward, with various simplifications applied and assumptions made depending on the situation concerned. These can reduce the difficulty of the problem, but they can also place limitations on the applicability of the solutions; it is important to be aware of the assumptions in order to properly evaluate the results. With reference to Anderson [69], this section will therefore provide a brief overview of inviscid panel methods with an emphasis on the assumptions which underlie them.

2.1.1 Governing Equations

Fundamental physical laws can be applied to derive three important governing equations for the solution of continuous fluid flows. The continuity equation states that mass cannot be created or destroyed, the momentum equation relates the force acting to the fluid's time rate of change of momentum, and the energy equation states that energy can only change form. By assuming incompressible flow, however, the fluid's density is made constant leaving only velocity and pressure as the primary unknown variables. These can be found through the solution of the continuity and momentum equations alone.

Momentum Equation

The Navier-Stokes equation is a statement of the momentum equation, given here for an incompressible, constant viscosity, Newtonian fluid in Equation 2.1 [148, Sec. 1.6].

$$\frac{\partial \boldsymbol{U}}{\partial t} + \boldsymbol{U} \cdot \nabla \boldsymbol{U} = \boldsymbol{f} - \frac{\nabla p}{\rho} + \frac{\mu}{\rho} \nabla^2 \boldsymbol{U} \qquad \textbf{Equation 2.1}$$

$\boldsymbol{U}$ is velocity, t is time, $\boldsymbol{f}$ is body force per unit mass, p is pressure, ρ is density, and μ is dynamic viscosity.

Adding the assumption of inviscid flow then leads to Euler's equation in Equation 2.2 [148, Sec. 1.6].

$$\frac{\partial \boldsymbol{U}}{\partial t} + \boldsymbol{U} \cdot \nabla \boldsymbol{U} = \boldsymbol{f} - \frac{\nabla p}{\rho} \qquad \textbf{Equation 2.2}$$

With the additional assumption of a steady flow negligibly influenced by gravity or other body forces, Euler's equation can then lead to the form of Bernoulli's equation in Equation 2.3 [148, Sec. 2.6].

$$\frac{p}{\rho} + \frac{|\boldsymbol{U}|^2}{2} = \text{constant} \qquad \textbf{Equation 2.3}$$

The left hand side of this equation is constant everywhere in irrotational flows, or along a streamline in rotational flows, allowing pressure values that satisfy the momentum equation to be calculated from velocity results.

Potential Flow

Before moving to the continuity equation, a valuable simplification can be made. First, the vorticity vector $\boldsymbol{\zeta}$, which is equal to twice the angular velocity of an infinitesimal fluid element, is defined by Equation 2.4.

$$\boldsymbol{\zeta} = \nabla \times \boldsymbol{U} \qquad \textbf{Equation 2.4}$$

The vorticity transport equation can be derived by taking the curl of the Navier-Stokes equation and assuming that any body forces are conservative, leading to Equation 2.5 [148, Sec. 2.2].

$$\frac{\mathrm{D}\boldsymbol{\zeta}}{\mathrm{D}t} = \boldsymbol{\zeta} \cdot \nabla \boldsymbol{U} + \frac{\mu}{\rho} \nabla^2 \boldsymbol{\zeta} \qquad \textbf{Equation 2.5}$$

This equation describes the transport of vorticity through the flow, and it can be shown that the rate of diffusion is much lower than the rate of convection at high Reynolds numbers [148, Sec. 2.2]. Vorticity that is created at a boundary with a solid surface therefore remains in the boundary layer and in a thin trailing wake, leaving the remaining flow free from vorticity when the upstream flow is uniform. Further assuming inviscid flow leads to Equation 2.6 [148, Sec. 2.2].

$$\frac{\mathrm{D}\boldsymbol{\zeta}}{\mathrm{D}t} = \boldsymbol{\zeta} \cdot \nabla \boldsymbol{U} \qquad \textbf{Equation 2.6}$$

When the upstream flow is uniform and so has zero vorticity, the downstream flow is irrotational as no vorticity can be generated. It is then possible to replace the velocity vector components with a single scalar value known as the velocity potential Φ at each point. Velocity vectors can be calculated with Equation 2.7 [148, Sec. 2.4].

$$\boldsymbol{U} = \nabla\Phi \qquad \textbf{Equation 2.7}$$

Instead of solving for multiple unknown velocity components, a solution need only be found for the velocity potential.

Continuity Equation

With only the assumption of a continuum fluid, the continuity equation in Equation 2.8 [148, Sec. 1.6] can be derived.

$$\frac{\mathrm{D}\rho}{\mathrm{D}t} + \rho\nabla \cdot \boldsymbol{U} = 0 \qquad \textbf{Equation 2.8}$$

Adding the assumption of incompressible flow then leads to Equation 2.9 [148, Sec. 1.6].

$$\nabla \cdot \boldsymbol{U} = 0 \qquad \textbf{Equation 2.9}$$

Finally, substituting Equation 2.7 into Equation 2.9 gives Equation 2.10 [148, Sec. 2.4].

$$\nabla^2\Phi = 0 \qquad \textbf{Equation 2.10}$$

This is Laplace's equation, the form of the continuity equation for an incompressible and irrotational flow.

2.1.2 Solution Methodology

Finding a velocity potential that satisfies Laplace's equation is at the core of a panel method, and it is a boundary value problem: either the velocity potential must be defined on all surfaces bounding the flow, or its derivative normal to the surfaces. For example, an aerofoil can be represented by a solid boundary with a zero normal velocity condition and a return to free stream conditions infinitely far from the aerofoil. The momentum equation is then satisfied in a second stage, where the pressure distribution is calculated from the velocity result.

The linear nature of Laplace's equation and the boundary conditions makes it easier to satisfy, as multiple solutions can be summed into one still valid solution. Complex flow fields can therefore be built up from much simpler elementary flows, such as uniform flow and the source, dipole, and vortex field singularity solutions. A straight and infinitely long vortex filament and a point vortex in 2D flow, for example, induce a velocity potential that varies with the azimuthal angle θ, given for a vortex of strength Γ in Equation 2.11.

$$\Phi = \frac{\Gamma}{2\pi}\theta \qquad \textbf{Equation 2.11}$$

Uniform flow can be used to represent free stream conditions, as the velocity is a constant value throughout the flow field whose potential satisfies Laplace's equation. Vortex flow is illustrated in Figure 2.1 for both a single vortex filament and a vortex sheet, where the induced velocity reduces to zero at infinite distance r from the vortex. While vortex flow is rotational in its infinitesimal core, it is irrotational at all other points so satisfies Laplace's equation. Both also enforce the infinity boundary condition.

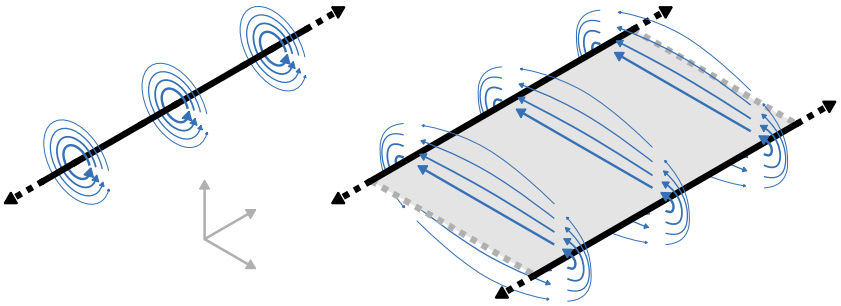

Figure 2.1: Illustration of velocity induced by a vortex filament and a flat vortex sheet.

Wall boundary conditions are not inherently satisfied by the elementary flows themselves, but rather through selecting an appropriate combination of elementary flows. A vortex sheet forming an aerofoil's surface, for example, would have a strength distribution chosen to prevent flow through the surface in the presence of a uniform flow free stream. While there is no unique solution to Laplace's equation for a closed body in two dimensional flow, the empirically observed Kutta condition states that attached flow over an aerofoil leaves smoothly at the trailing edge and thereby specifies a single strength distribution.

The purpose of a panel method is to find this strength distribution. However, an approximation must first be introduced: the vortex sheet of continuously varying strength is split into a series of panels. Into each is inserted a vortex element, such as a point vortex or a straight segment of constant strength vortex sheet, and a control point where the boundary condition is imposed for that panel. A linear system of equations can then be formed relating the strength of each panel to the velocity induced at the control points, with the Kutta condition enforced either by the final control point's position or by an explicit statement.

Solving the system of equations satisfies Euler's equation, the boundary conditions, and the Kutta condition. A complete description of the flow field then results, as the velocity induced by the vortex elements and the free stream velocity can be combined to give the velocity at any point in the flow field. The static pressure can be determined using Bernoulli's equation, and the lift generated by the aerofoil can be calculated.

2.1.3 Justification of Assumptions

Vortex panel methods are a standard approach to aerodynamic modelling that have been widely used since the early 1970's, and the philosophy behind them has physical significance: the viscous boundary layer over a surface is a region of rotational flow, which becomes a thin vortex sheet in the limit of infinite Reynolds number. Despite this, many assumptions are required that must be justified in terms of the flow being modelled and the aim of this work.

The most significant assumption made is that of inviscid flow, which was found a necessary one for achieving the objectives chosen for this work in Sections 1.4 to 1.6. Application of the Kutta condition commonly follows from the inviscid assumption [69, 148], although many ducts in the literature had attached flow [e.g. 39, 55] and therefore satisfied it anyway. Irrotational flow also follows: vorticity cannot diffuse through the flow, as discussed in Section 2.1.1, and is limited only to the surface of bodies and to thin layers if any wakes exist. It is therefore reasonable to represent boundary layers with thin vortex panels.

Below a Mach number of 0.3, the density of a gas varies by less than 5% and incompressible flow can be assumed [69, Sec. 1.10.3]. A ducted turbine would require a velocity augmentation of 3.6 to reach this threshold at a wind speed of 30m/s, an augmentation far larger than those reported in the literature [e.g. 4, 66]. It is likely that this assumption is valid for at least a subset of the possible duct designs when combined with the actuator disc rotor model used in this work, although compressibility effects may become significant in more advanced models due to the increased local flow velocity seen over discrete blades.

Time averaged values for power extraction were little different from those found in steady flow by some authors, as discussed in Section 1.3.3, and the reduced complexity can be further justified as necessary for examining the fundamentals. Neglecting gravity should also have little impact, as it can induce no velocity for incompressible flow where density is constant and the variation in pressure with elevation is generally negligible compared to the forces caused by the moving fluid [69, Sec. 1.9].

The final approximation was discretising continuous variations of vorticity into a series of discrete panels, introducing a discretisation error that tends to zero as the number of panels approaches infinity. The value of this error is dependent on the details of each simulation, and was minimised by choosing an appropriate number of panels as described in Section 2.2.4. An additional source of error came from the use of a digital computer: numbers can only be represented to a finite number of decimal places. While a significant loss of accuracy can sometimes result [149], this rounding error was minimised here by using double precision numbers throughout.

2.2 A Panel Method for Ducted Turbines

Where the last section described the general approach and assumptions for a vortex panel method, this section presents the details of the method that was implemented in Matlab [150] for this work. An outline of the method is given first, followed by details of the discretisation, solution and post-processing approaches. The remainder of the section covers simulation setup and validation of the model.

2.2.1 Method Outline

An axisymmetric approach was chosen to take advantage of the geometrical symmetry of a duct, in common with many of the previous investigations discussed in Section 1.3.3, with vortex rings around the duct's circumference selected as the vortex element. A zero thickness approach was taken to the duct wall, where the vortex rings were placed along the duct's camber line. This approach can be interpreted as modelling a theoretical duct that is infinitely thin walled, suitable for examining the fundamentals, but Section 3.3.2 will also show it to be a reasonable approximation even for ducts of moderate thickness in inviscid flow.

Modelling the turbine rotor required an additional set of vortex rings that represented the surface of the rotor's wake. Figure 2.2 illustrates this concept with a set of green vortex rings taking the shape of the grey duct including an exit flange, a set of blue vortex rings expanding to the final wake radius then a blue cylinder showing the far wake continuing with constant radius to downstream infinity.

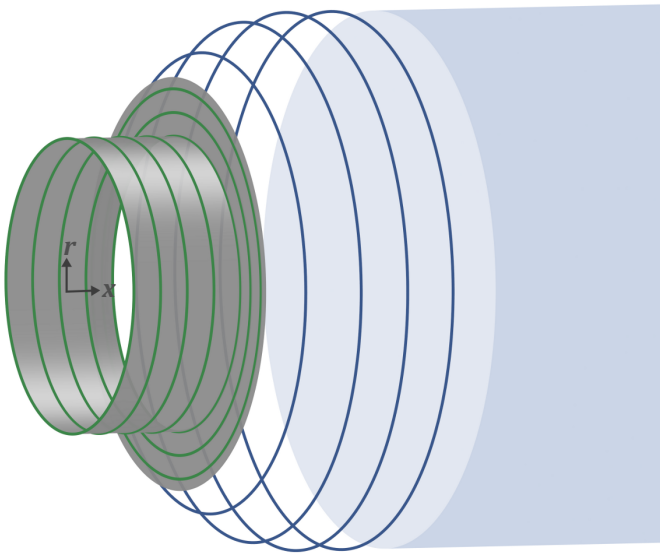

Figure 2.2: Qualitative illustration of model constituent parts. Shown from left to right are the duct rings, wake rings, and semi-infinite vortex cylinder. The duct shape represented by the rings is shaded.

Wake ring strengths were calculated with an iterative approach, but further iterations were needed to account for the influence of the duct and wake vortex ring sets on each other. Calculations for each alternated until convergence was reached. The wake rings were then relaxed to remain on the surface of the rotor's wake by modifying the position and radius of each ring, necessitating a further layer of iterations. A summary of this solution process is shown in Figure 2.3.

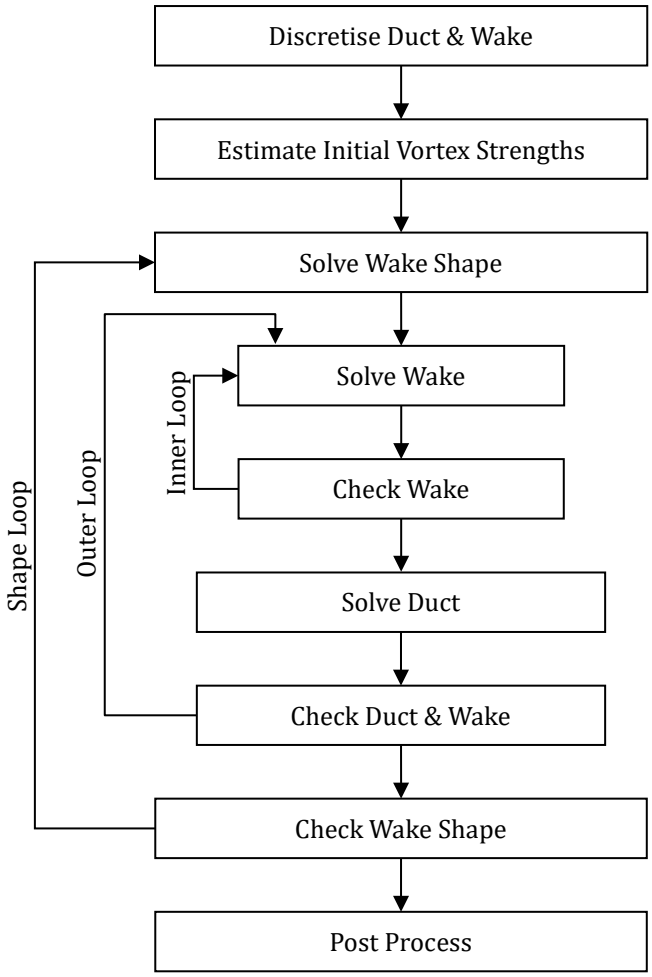

Figure 2.3: Flowchart describing model solution process.

2.2.2 Method Details

The Vortex Ring

The vortex ring was the elementary flow upon which this panel method was built, which induces a velocity illustrated by Figure 2.4. While lumping all the vorticity associated with a panel into a ring may require smaller panels for the same discretisation error, solutions for the velocity induced by a vortex ring were more readily available than a conical distributed vorticity element and could be rapidly calculated using both a numerical and an analytical technique.

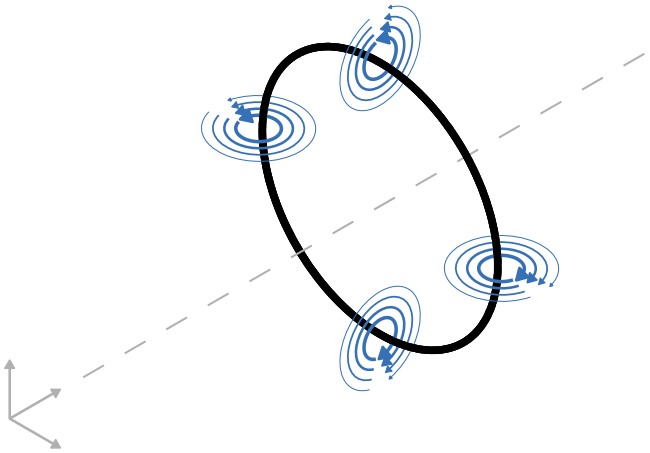

Figure 2.4: Isometric illustration of a vortex ring and the velocity it induces.

Both approaches were used in this work, as the analytical method was faster to compute but inappropriate in some circumstances. In the numerical approach the velocity induced by a segment of vortex ring was sampled around the ring using the Biot-Savart law [69, Sec. 5.2], with the total velocity induced found by integrating around the ring. A directed segment of vorticity $\mathbf{d}\boldsymbol{l}$ of strength Γ induces a velocity $\mathbf{d}\boldsymbol{U}$ at a distance from $\mathbf{d}\boldsymbol{l}$ described by the radius vector $\boldsymbol{r}$ as calculated by Equation 2.12.

$$\mathbf{d}\boldsymbol{U} = \frac{\Gamma}{4\pi}\frac{\mathbf{d}\boldsymbol{l} \times \boldsymbol{r}}{|\boldsymbol{r}|^3} \qquad \textbf{Equation 2.12}$$

The analytical solution [151] to the velocity induced by a vortex ring is shown in Equation 2.13 and Equation 2.14.

$$u = \frac{\Gamma}{4\pi} r_v \left[\left(r_v + r\frac{G}{H}\right)J_2 - \frac{r}{H}J_1\right] \qquad \textbf{Equation 2.13}$$

$$v = \frac{\Gamma}{4\pi} r_v \left(\frac{x - x_v}{H}\right)(J_1 - GJ_2) \qquad \textbf{Equation 2.14}$$

These equations are shown in a cylindrical coordinate system, where a velocity (u, v) is induced at a location (x, r) by a vortex ring of strength Γ, radius r_v, and axial position x_v. Definitions are given in Equation 2.15, where $\mathcal{K}(m)$ and $\mathcal{E}(m)$ refer to the complete elliptic integrals of the first and section kind respectively.

$$J_1 = \frac{4}{b}\mathcal{K}(m) \qquad J_2 = \frac{4}{b}\frac{\mathcal{E}(m)}{(1-m)}$$

$$G = (x - x_v)^2 + r^2 + r_v^2 \qquad H = -2r_v r \qquad \textbf{Equation 2.15}$$

$$m = \frac{4r_v r}{b^2} \qquad b^2 = (r + r_v)^2 + (x - x_v)^2$$

One situation requiring the numerical technique was calculation of the velocity induced on the surface of a ring itself, needed when determining the wake ring strengths, to account for a singularity causing the velocity to increase to infinity as the ring is approached. This singularity is illustrated on the left of Figure 2.5. Velocities could still be calculated with the analytical method for locations at least one panel length distant from the nearest point on a vortex ring, as discussed in Section 2.2.4, and at the duct control points between the vortex rings where the singularities balance.

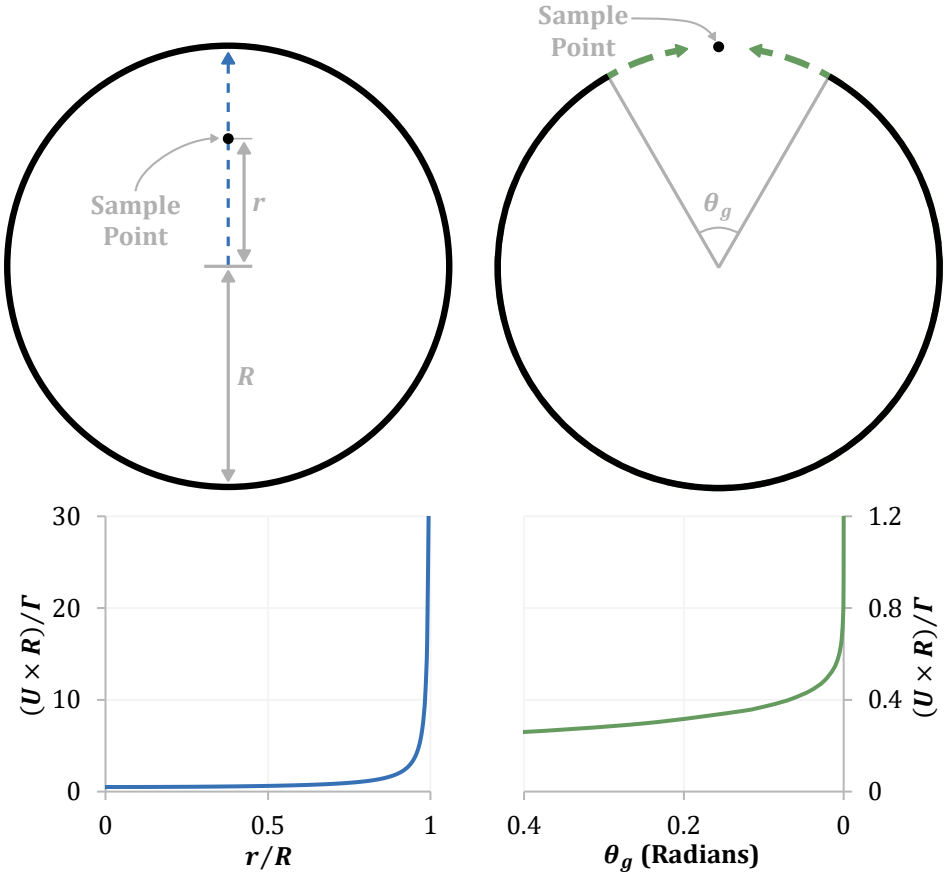

Figure 2.5: Illustration of singularities in dimensionless velocity $(U \times R)/\Gamma$ caused by proximity to a whole vortex ring (left) and by gap size θ_g in an incomplete vortex ring (right), for rings of strength Γ. The plotted velocity values are truncated as they tend towards infinity.

In order to remove the singularity as the ring is approached, the segment of the ring at the point of interest was removed. A correction had then to be made to account for a second singularity which occurs as the size of the gap is reduced for the axial velocity only, as illustrated on the right of Figure 2.5. This correction for the axial velocity induced in a gap of size θ_g was calculated numerically by measuring the variation in non-dimensional velocity with non-dimensional gap size, and had the value $u_{correction}$ for a ring of radius R and strength Γ defined in Equation 2.16.

$$u_{correction} \approx 0.08 \frac{\Gamma}{R} \ln\left(\frac{\theta_g}{R}\right) \qquad \textbf{Equation 2.16}$$

With the singularities removed, the ring's local contribution to the induced velocity was replaced by the contribution from a two-dimensional vortex sheet element. Based on a series expansion of the velocity terms carried out by de Bernardinis [152], this contribution can be split into two components. First, a contribution to the axial velocity at the point of interest in the gap $u_{replacement}$ that is given for a panel of strength Γ and length Δs by Equation 2.17.

$$u_{replacement} = -\frac{\Gamma}{4\pi R}\left[\ln\left(\frac{\Delta s}{R}\right) - 1 - \ln(2)\right] \qquad \textbf{Equation 2.17}$$

Second, a step change $\boldsymbol{U_{step}}$ between the two sides of the point as the panel surface is crossed. Where $\hat{\boldsymbol{q}}$ is a unit vector describing the direction of the panel, $\boldsymbol{U_{step}}$ is given by Equation 2.18.

$$\boldsymbol{U_{step}} = \pm\hat{\boldsymbol{q}}\frac{\Gamma}{2\Delta s} \qquad \textbf{Equation 2.18}$$

Duct Model

Each duct was represented by a set of vortex rings distributed along its camber surface, generally with half cosine spacing to concentrate rings near where rapid changes in the flow were expected. Figure 2.6 illustrates how the spacing was calculated based on distance along the surface of the duct, with a small number of rings for clarity, and that the control points for enforcing the boundary conditions were placed half way between each ring at the local duct radius.

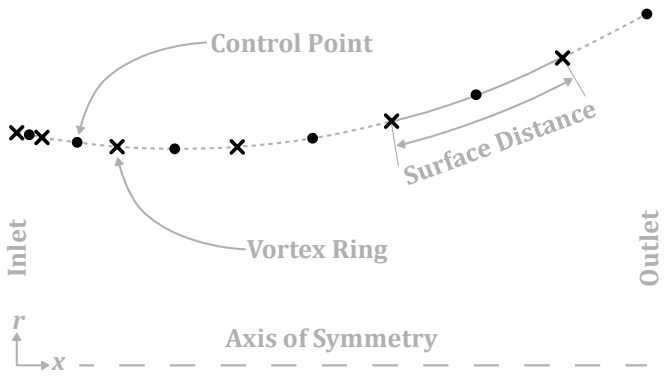

Figure 2.6: Illustration showing the axial positions and radii for a set of duct rings and control points that have been spaced using the half-cosine method. Marked points show where rings pass through the page.

A final control point one half panel length downstream of the last ring marked the end of the duct, ensuring the flow left the trailing edge of the duct smoothly thereby satisfying the Kutta condition. A wall boundary condition of zero normal velocity was applied to each control point, using a unit surface normal vector $\hat{\boldsymbol{n}}$ calculated over a

short length of duct with central differencing and the surface velocity $\boldsymbol{U}$ as stated in Equation 2.19.

$$\boldsymbol{U} \cdot \hat{\boldsymbol{n}} = 0 \qquad \textbf{Equation 2.19}$$

Duct shapes were specified either with an equation relating duct radius to axial location or by interpolating between a set of points with a piecewise cubic Hermite spline that prevented overshoot [153]. While this interpolation causes a discontinuous second derivative, no impact was expected on inviscid duct performance. Sharp changes in curvature could be modelled with the interpolation approach, up to a right angled flanged duct. Full cosine spacing was then used in the cylindrical section, as illustrated in Figure 2.7, followed by half cosine spacing where the panel lengths at the corner were closely matched.

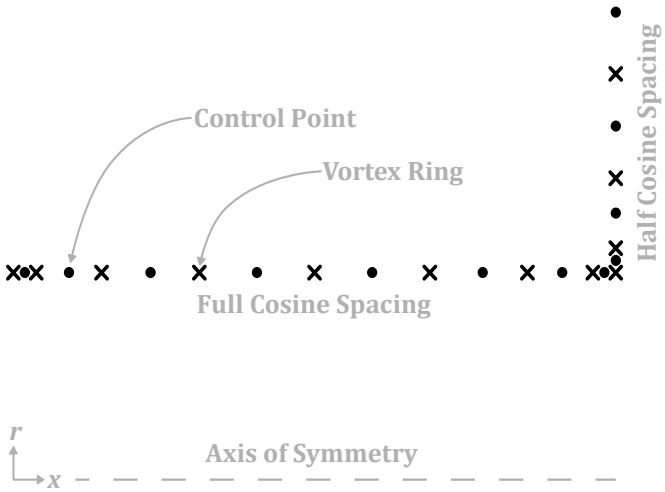

Figure 2.7: Illustration showing the axial positions and radii for a set of duct rings and control points that have been spaced using the right angle method.

Shapes such as these would experience separation at the sharp corner in real flows, which is avoided here due to the inviscid flow assumption. The Kutta condition can therefore still applied at the trailing edge. There is, however, a certain contradiction in this choice: while panel methods applying the Kutta condition are referred to as inviscid [69, 148], it is the viscous mechanism of friction that causes the flow to leave smoothly at the trailing edge in a real flow. It may be more precise to think of the inviscid assumption as neglecting all viscous phenomena other than the Kutta condition. The complexities of separation and viscous losses are still removed, which was the original purpose of assuming inviscid flow.

Once the duct was discretised, ring strengths were found by application of the wall boundary condition. Rewriting Equation 2.19 for a particular control point j and

separating out the velocity contributions from the free stream $\boldsymbol{U}_\infty$, the entire wake vorticity $\boldsymbol{U}_{\boldsymbol{wake},j}$, and the N duct rings gives Equation 2.20.

$$\sum_{k=1}^{k=N} \boldsymbol{U}_{jk}\, \Gamma_k \cdot \hat{\boldsymbol{n}}_j + \boldsymbol{U}_\infty \cdot \hat{\boldsymbol{n}}_j + \boldsymbol{U}_{\boldsymbol{wake},j} \cdot \hat{\boldsymbol{n}}_j = 0 \qquad \textbf{Equation 2.20}$$

With $\boldsymbol{U}_{jk}$ as the velocity induced by duct ring k at unit strength, an influence coefficient I_{jk} can be defined for its influence on point j with Equation 2.21.

$$I_{jk} = \boldsymbol{U}_{jk} \cdot \hat{\boldsymbol{n}}_j \qquad \textbf{Equation 2.21}$$

Substituting Equation 2.21 into Equation 2.20 and applying the result to each duct control point led to a linear system of equations expressed using matrix notation in Equation 2.22.

$$\begin{bmatrix} I_{11} & \cdots & I_{1k} \\ \vdots & \ddots & \vdots \\ I_{j1} & \cdots & I_{jk} \end{bmatrix} \begin{bmatrix} \Gamma_1 \\ \vdots \\ \Gamma_k \end{bmatrix} = \begin{bmatrix} -\boldsymbol{U}_\infty \cdot \hat{\boldsymbol{n}}_1 - \boldsymbol{U}_{\mathbf{wake},1} \cdot \hat{\boldsymbol{n}}_1 \\ \vdots \\ -\boldsymbol{U}_\infty \cdot \hat{\boldsymbol{n}}_j - \boldsymbol{U}_{\boldsymbol{wake},j} \cdot \hat{\boldsymbol{n}}_j \end{bmatrix} \qquad \textbf{Equation 2.22}$$

A two-step process was used to find the duct ring strengths [148, Sec. 11.1.1], beginning with calculation of the duct ring influence coefficients and the velocity contributions from the free stream and wake. Equation 2.22 was then solved for Γ using an appropriate solver that was automatically selected [154].

Rotor and Wake Model

An actuator disc was chosen to represent the rotor in this method, filling the duct cross section and causing a radially uniform drop in static and total pressure. The radial uniformity is optimum for a bare rotor excluding losses [5, Sec. 3.7.2], while the actuator disc itself can be considered as the limit when a rotor tends towards an infinite number of blades that are infinitely slender and turning at infinite rotational speed with the power and pressure drop held constant [155, Sec. 4.3]. Theoretical and numerical investigations of ducted turbines have commonly used actuator discs, as discussed in Section 1.3, and the approach is suitable for this work's aim of examining the fundamentals.

When the number of blades is approaching infinity, with the solidity of the overall rotor held finite, the vorticity shed from the blade tips forms a vortex sheet that convects downstream with the flow [5, Sec. 3.4]. While the static pressure recovers to atmospheric, this boundary of vorticity maintains the total pressure deficit to downstream infinity for inviscid flow where the vorticity cannot spread to allow velocity recovery. Along with the imposition of a step change in pressure, then, a vortex sheet was included in the model on the surface of the wake.

Simulations started with a cylindrical sheet of wake vorticity, equal in radius to the duct exit, discretised so that the vortex rings were coincident with the control points in the centre of each wake panel. The first wake panel length was set equal to the final duct panel, with the remainder either of equal panel length or increasing linearly to 4 times the initial length over the first 5 rotor diameters of wake length. Discretisation error was reduced in most results with variable length panels, compared to the same number of fixed length panels, at the cost of increased error for results computed at the wake end.

A semi-infinite vortex cylinder extending to downstream infinity terminated the wake vortex rings at their downstream end, of radius and strength per unit length equal to the final panel. The vortex cylinder had a velocity contribution that could be calculated analytically [156], avoided an unrealistic end shape from a finite length wake, and provided a closer match between theory and simulation setup. Five vortex rings between the cylinder and the wake rings proper, set equal to the strength and radius of the cylinder, prevented numerical problems caused by the junction.

Wake vortex ring strengths were calculated to prevent a pressure discontinuity across the wake surface, as the wake surface is not a physical object and cannot support a jump in static pressure. An equation describing this boundary condition was derived by considering the pressure at a control point in the wake. To begin, the Bernoulli equation was applied twice at this control point: once each for the sides inside and outside the wake. The latter is given in Equation 2.23.

$$\frac{1}{2}\rho|\boldsymbol{U}_\infty|^2 + p_\infty = \frac{1}{2}\rho|\boldsymbol{U_{out}}|^2 + p_{out} \qquad \textbf{Equation 2.23}$$

ρ is the air density, ∞ signifies free stream conditions, p is static pressure, Δp is the pressure drop across the rotor, and out and in signify the sides outwith and inside the wake. The application inside the wake yields Equation 2.24.

$$\frac{1}{2}\rho|\boldsymbol{U}_\infty|^2 + p_\infty - \Delta p = \frac{1}{2}\rho|\boldsymbol{U_{in}}|^2 + p_{in} \qquad \textbf{Equation 2.24}$$

To enforce the no pressure jump condition, p_{out} and p_{in} are set equal. These two equations then lead to Equation 2.25.

$$\Delta p = \frac{1}{2}\rho(|\boldsymbol{U_{out}}| + |\boldsymbol{U_{in}}|)\,(|\boldsymbol{U_{out}}| - |\boldsymbol{U_{in}}|) \qquad \textbf{Equation 2.25}$$

The right hand side can be considered in terms of the difference in velocity between the two sides $\boldsymbol{\Delta U}$ and the average of the two velocities $\overline{\boldsymbol{U}}$. $\boldsymbol{\Delta U}$ is given by Equation 2.26.

$$|\boldsymbol{U_{out}}| - |\boldsymbol{U_{in}}| = |\boldsymbol{\Delta U}| \qquad \textbf{Equation 2.26}$$

$\bar{\boldsymbol{U}}$ is shown in Equation 2.27.

$$\frac{1}{2}\left(|\boldsymbol{U}_{\boldsymbol{out}}| + |\boldsymbol{U}_{\boldsymbol{in}}|\right) = |\bar{\boldsymbol{U}}| \qquad \textbf{Equation 2.27}$$

Both of these equations are only valid when the average and difference velocity vectors align. The rest of the solution method makes this assumption, and the equations derived from this point are incorrect otherwise. When a converged solution for a simulation was reached, however, the assumption held as the wake shape solver that is described later in this section aligned these velocities while it kept the panels on the wake surface.

Derivations then continued by replacing the vortex ring local to the control point with the gap vortex ring discussed earlier in Section 2.2.2. It is the constant strength element contained in a gap vortex ring panel that is responsible for inducing the velocity difference, shown for a panel of strength Γ and length Δs in Equation 2.28.

$$|\boldsymbol{\Delta U}| = \frac{\Gamma}{\Delta s} \qquad \textbf{Equation 2.28}$$

Splitting the contributions to the average velocity between those influenced by the strength of the current panel and those not gives Equation 2.29.

$$|\bar{\boldsymbol{U}}| = \left|\boldsymbol{U}_{\boldsymbol{g}}\Gamma + \boldsymbol{U}_{\boldsymbol{other}}\right| \qquad \textbf{Equation 2.29}$$

Here, $\boldsymbol{U}_{\boldsymbol{g}}$ is the velocity induced by the rest of the gap vortex ring at unit strength and $\boldsymbol{U}_{\boldsymbol{other}}$ is the velocity induced by all the other sources of velocity in the model.

Substituting Equation 2.28 and Equation 2.29 into Equation 2.25 using the definitions in Equation 2.27 and Equation 2.26 then leads to the boundary condition for the wake panels in Equation 2.30.

$$\Delta p = \rho\left|\boldsymbol{U}_{\boldsymbol{g}}\Gamma + \boldsymbol{U}_{\boldsymbol{other}}\right|\frac{\Gamma}{\Delta s} \qquad \textbf{Equation 2.30}$$

Solving this equation for the unknown Γ to enforce the boundary condition led to a quartic equation for which no analytical solution could be found. A numerical method was used instead to find the roots of the polynomial by calculating the eigenvalues of the companion matrix [157], with the appropriate root selected as the strength for the panel.

A solution for the complete wake was found by applying Equation 2.30 to each panel in turn, with the process then repeated iteratively until convergence to account for changes in the wake panel strengths affecting $\boldsymbol{U}_{\boldsymbol{other}}$. To begin the very first iteration in a simulation, an initial estimate of the wake strength was found by attributing $\bar{\boldsymbol{U}}$ only to

the free stream velocity. For a constant strength cylindrical wake and an axial free stream velocity, Equation 2.25 then leads to Equation 2.31.

$$\Gamma_{estimate} = \frac{\Delta p \Delta s}{\rho u_\infty} \qquad \textbf{Equation 2.31}$$

Separately from the calculation of wake panel strengths, the wake panels were displaced so that the wake took up a more realistic shape. In the desired state each panel was aligned with the velocity local to it. To begin, the velocity at each control point was calculated to find the desired angle of each panel. Then, starting at the duct exit, each panel in turn was rotated around its upstream end to match the calculated angle. Again an iterative approach was required, with the shape recalculated each time a converged set of duct and wake ring strengths was found until a converged wake shape was reached.

2.2.3 Results Processing

Flow Rate

A number of results could be found from a converged solution, including calculation of the mass flow rate through the duct by splitting the cross section into a set of annuli. The velocity was sampled once in each annulus, with the outermost velocity sample point placed one local panel length distant from the duct surface to avoid the vortex ring singularity and the remaining points spaced equally to the centreline. Where u_j is the axial velocity in annulus j of area A_j, the volume flow rate though a set of N annuli is given by Equation 2.32.

$$Q = \sum_{j=1}^{j=N} u_j A_j \qquad \textbf{Equation 2.32}$$

Multiplying by the air density then gave mass flow rate $\dot{m}$ in Equation 2.33.

$$\dot{m} = \rho A u = \rho Q \qquad \textbf{Equation 2.33}$$

A similar approach was used to find the radius of a streamtube with a known mass flow rate, with radius varied using an optimisation algorithm [158] until the required flow rate was found. When results were required far downstream, an axial location was chosen sufficiently far from the rotor that only negligible changes occurred with increased distance.

Power and Rotor Thrust

Dimensionless coefficients for power and rotor thrust are discussed in Section 1.2.4, with power extraction P itself calculated from simulation results using Equation 2.34.

$$P = \Delta p A_r u_r = \Delta p Q_r \qquad \textbf{Equation 2.34}$$

Conditions at the actuator disc model of the rotor are indicated with r, and u_r is the mean axial velocity over the disc cross section. Thrust force F_T was defined only by inputs to the simulation through Equation 2.35.

$$F_T = \Delta p A_r \qquad \textbf{Equation 2.35}$$

Duct Circulation

Circulation is by definition the line integral of velocity around a chosen closed curve, and is equivalently the area integral of all vorticity normal to the surface bounded by the curve. For a surface S bounded by a curve C that has the directed line segment $\mathbf{ds}$, the circulation can therefore be calculated using Equation 2.36.

$$\Gamma = \oint_C \boldsymbol{U} \cdot \mathbf{d}\boldsymbol{s} = \iint_S \boldsymbol{\zeta} \cdot \mathbf{d}\boldsymbol{S} \qquad \textbf{Equation 2.36}$$

The curve defining the duct circulation Γ_d was chosen to encompass one half of a cross section through the duct, as illustrated in Figure 2.8: the circulation around each half would cancel to give zero circulation for a curve encompassing the entire cross section.

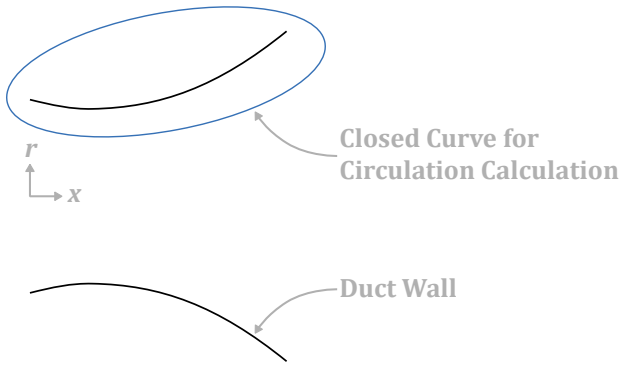

Figure 2.8: Illustration of the closed curve used in the definition of duct circulation Γ_d.

It was not necessary to carry out either of the integrations shown above, as the circulation is equal to the sum of the vortex element strengths enclosed by the curve [159]. The duct circulation was therefore found by summing the strengths of the duct vortex rings. Based on the results in Section 4.2.3, the duct circulation coefficient C_Γ was defined using the rotor diameter D and Equation 2.37.

$$C_\Gamma = \frac{\Gamma_d}{u_\infty D} \qquad \textbf{Equation 2.37}$$

Duct Force

Calculation of the total force on the duct began by examining an infinitesimal section of a single panel's circumference, which has a contribution $\mathbf{d}\boldsymbol{F}$ to the total force given by Equation 2.38.

$$\mathbf{d}\boldsymbol{F} = -\rho\Gamma(\boldsymbol{U} \times \mathbf{d}\boldsymbol{l}) + \Delta p \Delta s \hat{\boldsymbol{n}} |\mathbf{d}\boldsymbol{l}| \qquad \textbf{Equation 2.38}$$

The first term on the right hand side is the force on an infinitesimal segment of vorticity $\mathbf{d}\boldsymbol{l}$ at strength Γ [160], negative due to the positive anticlockwise definition of Γ used here, where the velocity $\boldsymbol{U}$ is that induced by the remainder of the panel's vortex ring, all other sources of vorticity, and the free stream. Added to that is the influence of the rotor's pressure drop in the second term, where the panel length Δs is modified to be the length of the panel in the reduced total pressure region and $\hat{\boldsymbol{n}}$ is the unit normal vector describing the panel surface's orientation.

Integration of $\mathbf{d}\boldsymbol{F}$ around the circumference to find the force on the entire panel leaves only a drag force, as the radial component cancels out due to the axisymmetry. The overall drag force of all the panels combined F_D can then be non-dimensionalised into a drag coefficient C_D by Equation 2.39.

$$C_D = \frac{F_D}{\frac{1}{2}\rho u_\infty^2 A_r} \qquad \textbf{Equation 2.39}$$

Examination of the radial and total forces took place by converting $\mathbf{d}\boldsymbol{F}$ into a per unit radian value and summing across all the panels, as represented by Equation 2.40.

$$\boldsymbol{F}_{\boldsymbol{radian}} = \sum_{j=1}^{j=N} 2\pi \frac{|\mathbf{d}\boldsymbol{l}_j|}{C_j} \mathbf{d}\boldsymbol{F}_j \qquad \textbf{Equation 2.40}$$

$\boldsymbol{F}_{\boldsymbol{radian}}$ is then the total force vector acting on the duct per unit radian, where C_j is the circumference of each of the N duct panels. The associated coefficient of total force per radian C_F is given by Equation 2.41.

$$C_F = \frac{|\boldsymbol{F}_{\boldsymbol{radian}}|}{\frac{1}{2}\rho u_\infty^2 A_r} \qquad \textbf{Equation 2.41}$$

Defining the radial component of $\boldsymbol{F}_{\boldsymbol{radian}}$ as F_R, positive inwards, the coefficient of radial force per radian is defined by Equation 2.42.

$$C_R = \frac{F_R}{\frac{1}{2}\rho u_\infty^2 A_r} \qquad \textbf{Equation 2.42}$$

Duct forces calculated using this approach were validated against results from the integral momentum equation for steady inviscid flow applied to a cylindrical control volume encompassing the duct.

Duct Performance Characterisation

To completely characterise a duct, a batch of simulations was run to measure the performance at a pre-determined set of rotor pressure drops. An optimisation algorithm then found the optimum rotor loading for maximum power to within a specified tolerance using additional simulations, based on a golden section search and parabolic interpolation [161]. Results from previous simulations in a batch were used to speed computations by providing a set of initial conditions for the wake vortex strength and shape iterations.

Ring strength initial conditions were found by scaling previous results from the simulation with the closest pressure drop by the fractional difference in pressure drop. Wake end radius predictions were made by fitting a spline to the variation of previous results with rotor loading, with the wake shape from the closest previous simulation then scaled appropriately. Simulations during the search for maximum power were not used as prediction sources due to a consequent increase in the iterative convergence of individual simulations. Although not problematic in itself, resulting tiny changes in power coefficient caused significant changes in the computed optimum rotor loading.

2.2.4 Simulation Settings

Various decisions were required to run simulations, not least the level of iterative convergence required for the inner loop checking wake ring strengths, the outer loop checking duct and wake ring strengths, and the wake shape loop. Inner and outer loops measured the percentage change in ring strengths between iterations, while shape convergence was measured by the change in axial position and radius of each ring and also by any misalignment between each panel and the local velocity. A threshold of 0.03% was selected in all cases, as smaller values made a negligible difference to the results.

Other settings were also chosen using test simulations that examined their influence on results, including the choice of optimisation tolerance in the search for maximum power, the number of segments the gap vortex ring was split into, and the number of annuli used in measuring volume flow rate. One panel length was also found to be sufficient distance to avoid singularity effects. Velocity components differed by less than 2.5% when a single ring panel was replaced by 32 rings of the same total strength, reducing to 1.5% for velocity magnitude and 1% for velocity components at 1.5 panel lengths distant.

Finally, discretisation error was held to an acceptable level using a discretisation dependence study for each set of simulations. Two parameters controlled the discretisation: the length of the final duct panel, from which all panel lengths could be calculated, and the length of wake modelled by vortex rings. Although the wake model included a semi-infinite vortex cylinder, a sufficient length of expanding wake section was needed to achieve convergence of the far wake diameter.

While the required computational time also had to be considered, it was generally expected that the main parameters of interest should change by less than 1% with a halving of panel lengths or a doubling of the wake length. A 2% difference in results was usually accepted at the highest loading of C_T = 0.95, however, as achieving discretisation independency was found to be more difficult as the rotor loading increased.

2.2.5 Validation against Actuator Disc Theory

Highly accurate inviscid simulations were sought, necessitating rigorous validation of the simulation code. Although a number of ducted turbine theories exist, as discussed in Section 1.5.1, they were unsuitable for this task as they themselves were to be tested by simulations in this work. A partial validation was possible against actuator disc theory for a bare rotor [5], however, with further validation against other simulation results to follow in Section 2.2.6.

Simulations of a bare rotor, excluding the duct model, were compared to actuator disc theory using seven parameters. The first of these were optimum rotor loading C_{Topt} and power coefficient C_{Pmax}, with a range of rotor loadings being used for the remaining five: power coefficient C_P, axial induction computed at the rotor a_r, axial induction computed in the far wake a_w, far upstream streamtube radius R_∞, and far wake streamtube radius R_w.

Discretisation Dependence Study

Three rotor loading coefficients were used in testing discretisation dependence with the methodology laid out in Section 2.2.4: 8/9, 0.95, and the optimum as determined by the maximisation algorithm. Although C_{Topt} should be 8/9 to match theory, the value was subject to numerical inaccuracies and therefore had to be validated. As discretisation error was expected to increase with rotor loading, results at low loadings were not examined.

Table 2.1 shows how the results varied as the panel lengths were halved, for various wake lengths and at the discussed rotor loadings. Examining the rows for a panel length of 0.0025 rotor diameters (D) shows that the change from a panel length of $0.005D$ met the criteria of less than 2% change with halved panel length at C_T = 0.95 and less than

1% at lower rotor loadings. The results in Table 2.2 for changing wake length show that a length of $16D$ was sufficient: the largest change from $16D$ to $32D$ was 0.88%.

Aside from the choice of resolution for this study, Table 2.1 and Table 2.2 allow two more general inferences: first, that the convergence rate of C_{Topt} does not place a limitation on other variables at that loading, as shown particularly in Table 2.1 where several variables show smaller changes than C_{Topt}. Reaching a converged value for C_{Topt} appears unimportant if it is not the parameter of interest.

It also appears unnecessary to examine all combinations of panel and wake lengths. The results show that while there is some interdependence in the choice of these parameters, it caused a difference of more than 0.15 percentage points in only 6 cases across both Table 2.1 and Table 2.2. All 6 occurred at C_{Topt} = 0.95 and for parameters computed at the wake end, reaching 0.52 points at most. As a result the influence of panel length and wake length were treated as independent in subsequent studies, except when a high accuracy was needed for wake end parameters.

Table 2.1: Change in bare rotor results as the panel length is halved, for various dimensionless wake lengths and rotor loadings.

Panel Length (L/D)	Wake Length (L/D)	% Difference from Doubled Panel Length					
		C_P	a_r	a_w	R_∞	R_w	C_{Topt}
At C_{Topt}							
0.0025	8	-0.42	-0.09	-0.16	0.02	-0.03	-0.46
0.00125	8	-0.23	-0.08	-0.10	0.04	-0.02	-0.27
0.0025	16	-0.42	-0.09	-0.15	0.02	-0.03	-0.46
0.00125	16	-0.23	-0.09	-0.11	0.02	-0.03	-0.28
0.0025	32	-0.42	-0.20	-0.27	0.05	-0.12	-0.52
0.00125	32	-0.23	-0.09	-0.11	0.02	-0.03	-0.28
At $C_T = 8/9$							
0.0025	8	-0.39	0.81	0.69	-0.18	0.55	
0.00125	8	-0.22	0.45	0.41	-0.11	0.33	
0.0025	16	-0.39	0.81	0.73	-0.18	0.60	
0.00125	16	-0.22	0.45	0.43	-0.11	0.36	
0.0025	32	-0.39	0.81	0.74	-0.18	0.61	
0.00125	32	-0.22	0.45	0.44	-0.11	0.37	
At $C_T = 0.95$							
0.0025	8	-0.70	1.15	0.89	-0.37	1.08	
0.00125	8	-0.40	0.65	0.52	-0.20	0.65	
0.0025	16	-0.71	1.17	1.03	-0.38	1.40	
0.00125	16	-0.41	0.67	0.60	-0.20	0.85	
0.0025	32	-0.71	1.17	1.08	-0.38	1.51	
0.00125	32	-0.41	0.66	0.63	-0.20	0.92	

Table 2.2: Change in bare rotor results as wake length is doubled, for various dimensionless panel lengths and rotor loadings.

Panel Length (L/D)	Wake Length (L/D)	% Difference from Halved Wake Length					
		C_P	a_r	a_w	R_∞	R_w	C_{Topt}
At C_{Topt}							
0.005	16	-0.01	-0.08	0.81	0.02	0.83	-0.05
0.005	32	0.00	0.12	0.30	-0.03	0.27	0.06
0.0025	16	-0.01	-0.08	0.82	0.02	0.83	-0.05
0.0025	32	0.00	0.00	0.18	0.00	0.18	0.00
0.00125	16	-0.01	-0.09	0.81	0.00	0.82	-0.05
0.00125	32	0.00	0.00	0.18	0.00	0.18	0.00
At $C_T = 8/9$							
0.005	16	-0.01	0.02	0.81	0.00	0.76	
0.005	32	0.00	0.00	0.16	0.00	0.15	
0.0025	16	-0.01	0.02	0.85	0.00	0.81	
0.0025	32	0.00	0.00	0.17	0.00	0.16	
0.00125	16	-0.01	0.02	0.88	0.00	0.84	
0.00125	32	0.00	0.00	0.17	0.00	0.17	
At $C_T = 0.95$							
0.005	16	-0.07	0.11	1.82	-0.03	2.67	
0.005	32	0.00	0.01	0.45	0.00	0.69	
0.0025	16	-0.08	0.13	1.96	-0.04	2.99	
0.0025	32	0.00	0.01	0.50	0.00	0.80	
0.00125	16	-0.09	0.14	2.05	-0.04	3.19	
0.00125	32	0.00	0.01	0.53	0.00	0.88	

Results at Selected Discretisation

Figure 2.9 shows reasonable agreement between simulation and theory at the chosen discretisation, although differences increased substantially at C_T > 0.8 and reached a peak of 4.2%. At C_T = 8/9, however, the difference was still less than 2% in all cases, and was 1.1% for C_{Topt}. General predictions could be made based on this level of agreement, but there was not sufficient evidence to consider the model validated. An error of up to 4% would introduce too much uncertainty into the validation of ducted theories: it would be too easy to dismiss somewhat small differences as numerical inaccuracy.

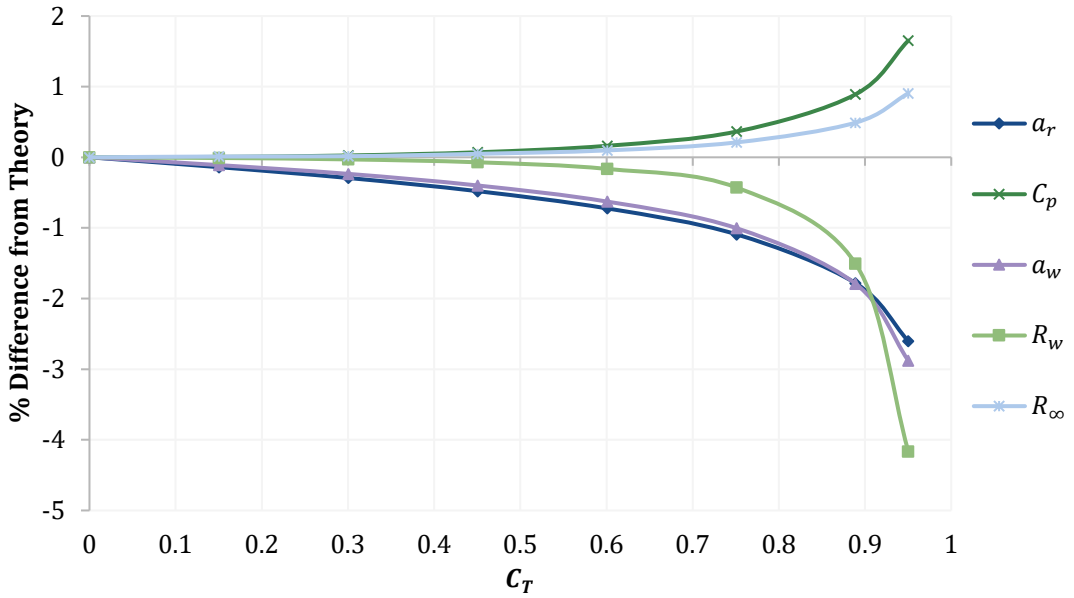

Figure 2.9: Difference between theory and simulation results for selected parameters, with panel length = 0.005D and wake length = 16D.

Results at Varied Discretisation

The largest differences in Figure 2.9 were for results with the lowest discretisation convergence. Figure 2.10 and Figure 2.11 show how the difference from theory varied with increased resolution, in terms of wake length and panel length individually, confirming that agreement improved with increased resolution. Looking first at C_T = 0.95 in Figure 2.10, improvement with increased wake length was substantial for wake end parameters and slight for the others. Shorter panel lengths improved all results, and they could plausibly be tending towards no difference from theory at small or zero length. The same trends were seen at C_T = 8/9.

A change in the pattern is seen when examining C_{Topt} in Figure 2.11. There now appears to be a worsening of the wake end parameters above a wake length of around 16D on the right of the figure, but comparison with the left suggests it would likely reduce or disappear with increased panel length and so is not indicative of any

problems with wake length. C_{Topt} itself showed a slight improvement with wake length and a larger improvement with panel length.

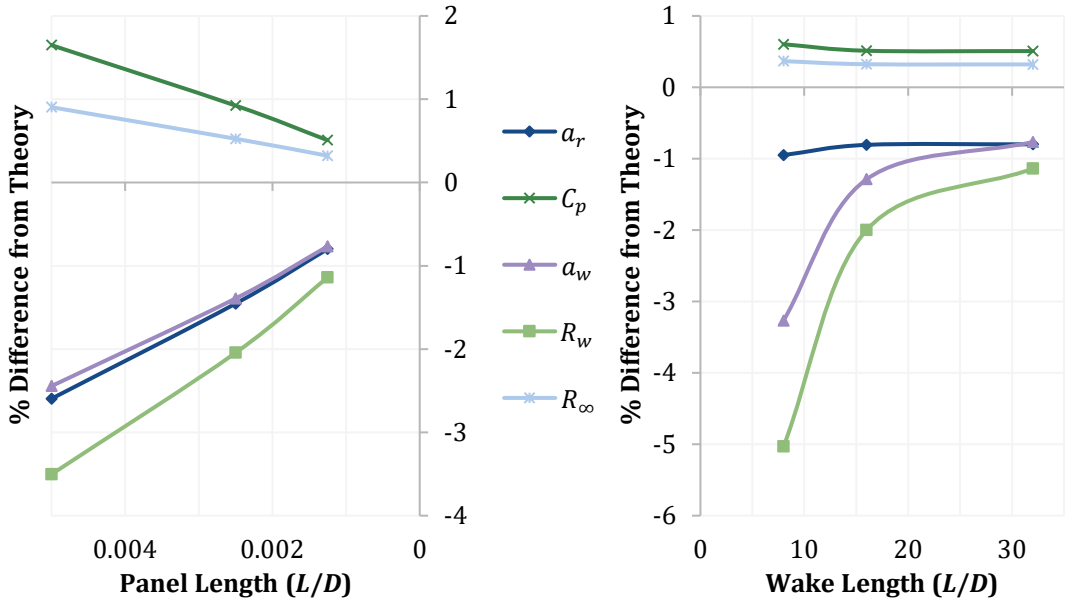

Figure 2.10: Difference between theory and simulation results at C_T = 0.95, for a range of panel lengths with wake length = 32D (left), and a range of wake lengths with panel length = 0.00125D (right).

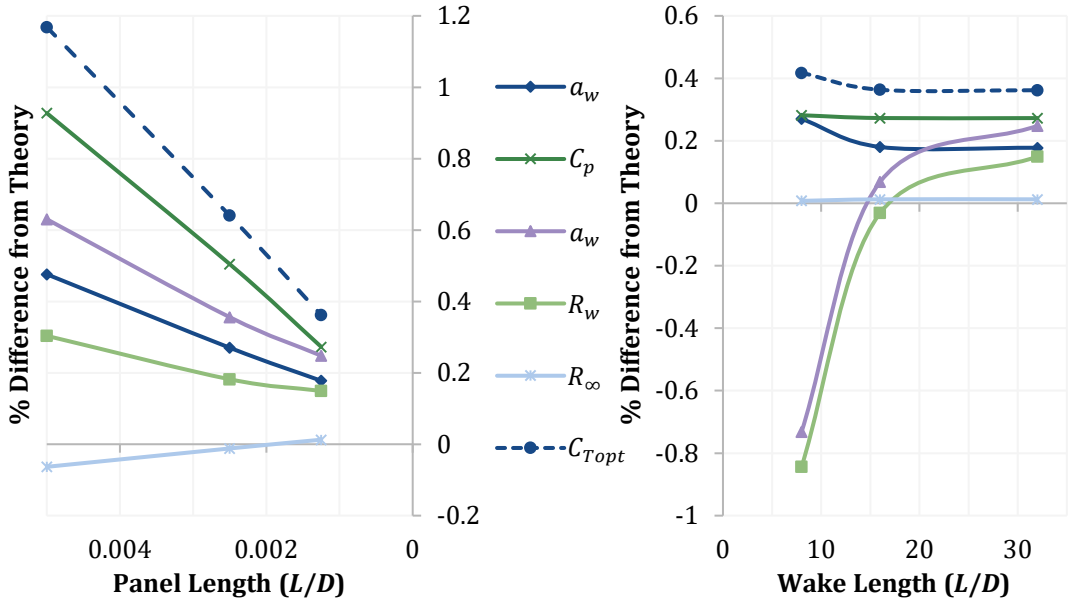

Figure 2.11: Difference between theory and simulation results at C_{Topt}, for a range of panel lengths with wake length = 32D (left), and a range of wake lengths with panel length = 0.00125D (right).

Increased resolution led to closer agreement with theory at all three loadings, and further increases would probably have delivered even closer agreement. After 16D, however, only the wake end parameters benefitted from increased wake length. That the errors reduce towards very small values increases confidence in the model, as it

implies that other sources of error or uncertainty are very small and a careful choice of discretisation gives results with a high degree of accuracy.

Results at Highest Resolution Discretisation

Returning to a single discretisation across a range of rotor loadings, Figure 2.12 shows the difference to theory with a panel length of $0.00125D$ and a wake length of $32D$. The magnitude of the differences was much reduced compared to the earlier selected discretisation: the largest was 1.1% for far wake radius and 0.8% excluding that, and at C_T = 8/9 the largest difference was 0.54%. The difference for C_{Topt} was 0.36%, and comparing C_{Pmax} at this loading gave a difference of 0.27% from the theoretical value of 16/27.

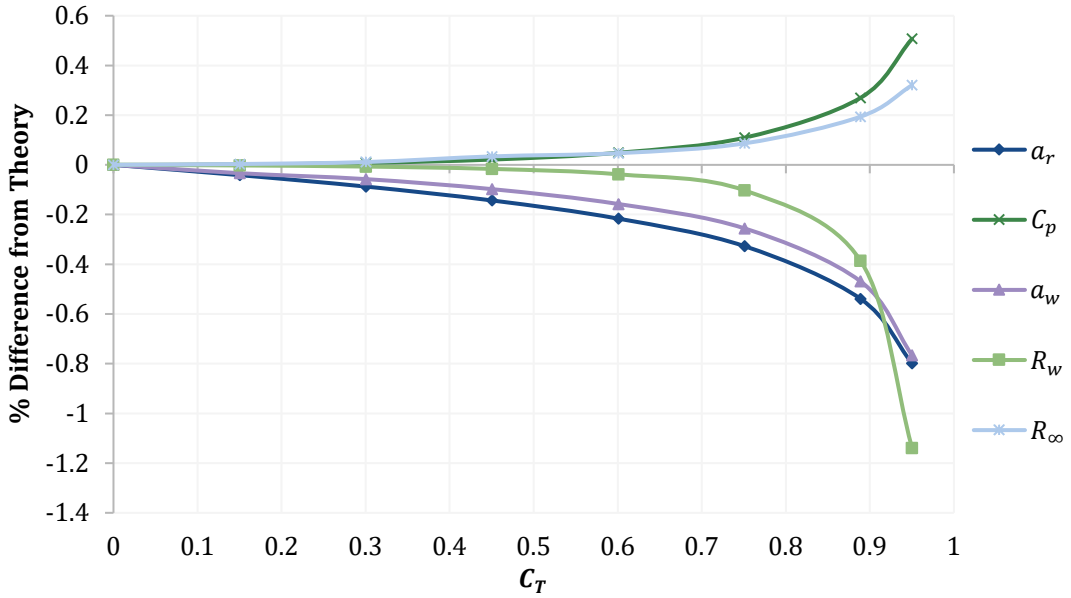

Figure 2.12: Difference between theory and simulation results for selected parameters, with panel length = $0.00125D$ and wake length = $32D$.

Validity of Model

Validation at the discretisation dependence study resolution demonstrated that both the model and the methodology for selecting a discretisation are valid for general use, with an error in C_P of less than 2%. Increasing the resolution then confirmed that the difference from theory was primarily due to discretisation error, controllable through the choice of discretisation. Very close agreement with theory was found at the highest resolution: just 0.36% and 0.27% for C_{Topt} and C_{Pmax} respectively. The model has therefore been validated against actuator disc theory to a high degree of accuracy.

2.2.6 Validation against Inviscid Simulation

Validation tests of the duct model compared results from the panel method code to results from ANSYS Fluent 15.0 running in an inviscid mode with an actuator disc model for the rotor. Five parameters were compared in this study: power coefficient C_P, velocity at the rotor u_r, duct drag F_D, duct circulation Γ_d, and exit pressure p_e. The required level of agreement was lower here than in the comparison to actuator disc theory, as both sets of results were subject to error and uncertainty.

Model Details and Discretisation Dependence

Figure 2.13 shows the duct shape chosen for this study. 2% thickness was added for the Fluent simulations, as initial tests without thickness found a region of separated flow even without viscosity. Not only did this thickness cause a difference in the results, it caused an additional difference for dimensionless parameters defined using rotor area. Even if the power results for both simulations were the same, for example, the power coefficients would be different. Thin duct dimensions were therefore used for dimensionless parameters so that the relative change in coefficient and raw result were equal.

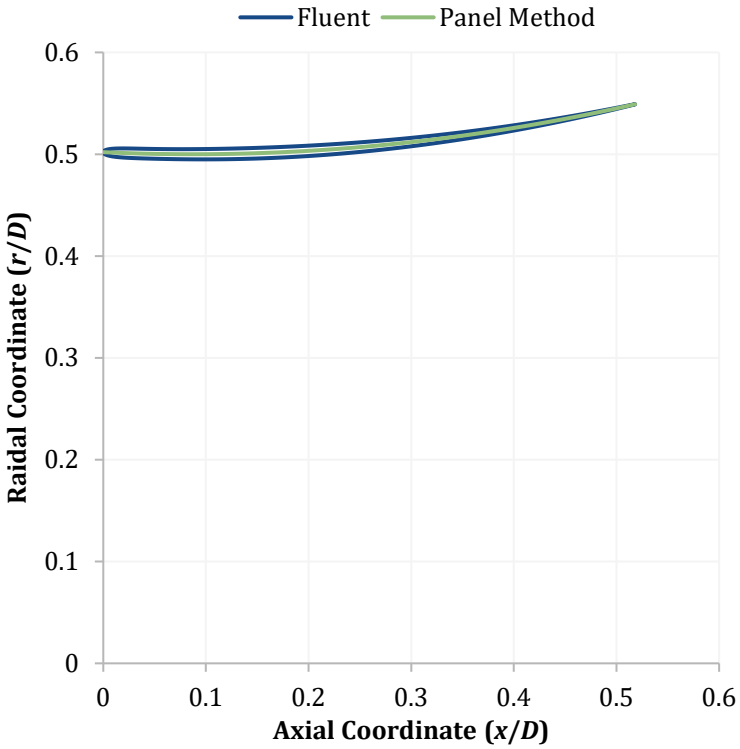

Figure 2.13: Validation duct shape, as used in panel method and with thickness for use in Fluent.

Discretisation dependence study results are shown in Table 2.3 for the panel method simulations. An expanding wake length of $8.29D$ was chosen, as doubling it changed the results by less than 0.12%. Despite drag and exit pressure difficulties at C_T = 0.95, a

duct end panel length of $0.0013D$ was selected. Those results must be treated with some caution. Note that at C_T = 0 the wake vortex rings had zero strength and made exactly zero difference to the results, and drag was excluded to avoid misleading percentages due to tiny numerical variations from its true value of 0.

Table 2.3: Change in panel method results for validation shape as discretisation is changed from duct end panel length = $0.0013D$ and expanding wake length = $8.29D$, at three rotor loadings.

	% Difference with					
	Halved Panel Length			Doubled Wake Length		
	$C_T = 0$	C_{Topt}	$C_T = 0.95$	$C_T = 0$	C_{Topt}	$C_T = 0.95$
$\dot{m}$ & C_P	-0.10	-0.08	-0.69	0	0.00	-0.03
C_D	-	-0.79	3.71	0	-0.01	0.12
Γ_d	-0.12	0.29	1.06	0	0.01	0.03
p_e	-0.16	-0.50	-2.44	0	0.00	-0.08

A grid convergence study for the Fluent results is shown in Table 2.4. The approximate relative error is the difference between the 2nd finest and the finest grid results as a percentage of the latter, and the grid convergence index is an error estimate at the finest grid that is defined later in Section 2.3.3. Poor convergence was found for drag and exit pressure at the top two loadings, for circulation at C_T = 0.3 and 0.6, and additional error for drag at high loadings was found when testing domain size convergence in Table 2.5. While these difficulties must be kept in mind, overall convergence was good.

Table 2.4: Error estimates for chosen Fluent simulation discretisation, calculated from simulations with 152,000, 241,000 and 470,000 cells.

C_T	0	0.15	0.3	0.45	0.6	0.75	8/9	0.95
Approximate Relative Error (%)								
$\dot{m}$ & C_P	0.1	0.1	0.0	0.1	0.1	0.1	0.3	0.6
C_D	-	2.3	0.6	0.3	0.3	0.9	9.8	6.7
Γ_d	0.1	0.3	0.7	2.0	13.8	1.1	0.6	0.6
p_e	0.2	0.0	0.2	0.5	0.5	0.5	1.0	1.6
Grid Convergence Index (%)								
$\dot{m}$ & C_P	0.0	0.0	0.0	0.1	0.0	0.0	1.1	1.5
C_D	-	0.7	0.2	0.1	0.0	0.1	4.2	167.2
Γ_d	0.0	0.1	8.9	1.8	1.9	1.2	0.9	0.5
p_e	0.0	0.0	0.1	0.4	0.2	0.1	4.2	3.2

Table 2.5: Change in Fluent results for validation shape with domain length and radius doubled from 41.8D and 20.9D respectively.

	% Difference with Doubled Domain Dimensions	
	$C_T = 0$	$C_T = 0.95$
$\dot{m}$ & C_P	-0.01	-0.42
C_D	-	1.56
Γ_d	-0.09	-0.37
p_e	0.10	0.62

Comparison of Fluent and Panel Method Results

Visually comparing the Fluent and panel method results in Figure 2.14 to Figure 2.16 shows very good agreement for power and velocity, diverging only slightly at higher rotor loadings. Less good but still reasonable matches were found for the other parameters. Special consideration is needed for circulation, which was calculated for the Fluent results using Equation 2.43 [69, Sec. 2.13].

$$\Gamma = \oint \boldsymbol{U} \cdot \mathbf{d}\boldsymbol{S} \qquad \textbf{Equation 2.43}$$

This equation was applied to a circular curve surrounding the upper duct wall, but the curve extended downstream of the duct exit thereby including some of the wake vorticity and reducing the accuracy. It was unclear how small the curve could be before excluding duct bound circulation, so the Fluent circulation results at $C_T > 0$ include an additional error that increases with loading.

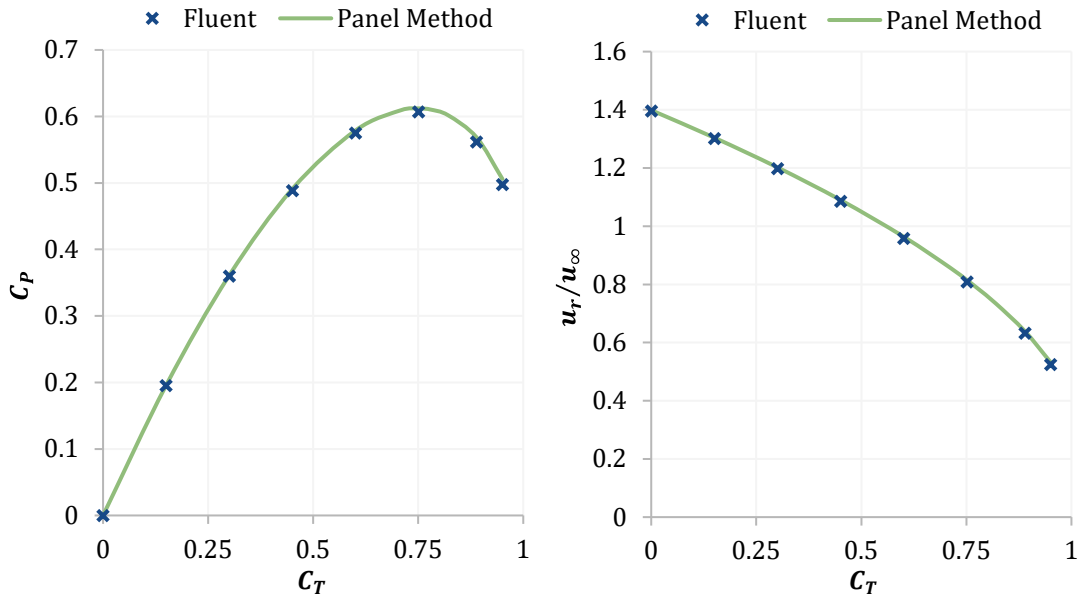

Figure 2.14: Power coefficient C_P (left) and velocity in the rotor plane u_r (right) results from Fluent and the panel method code.

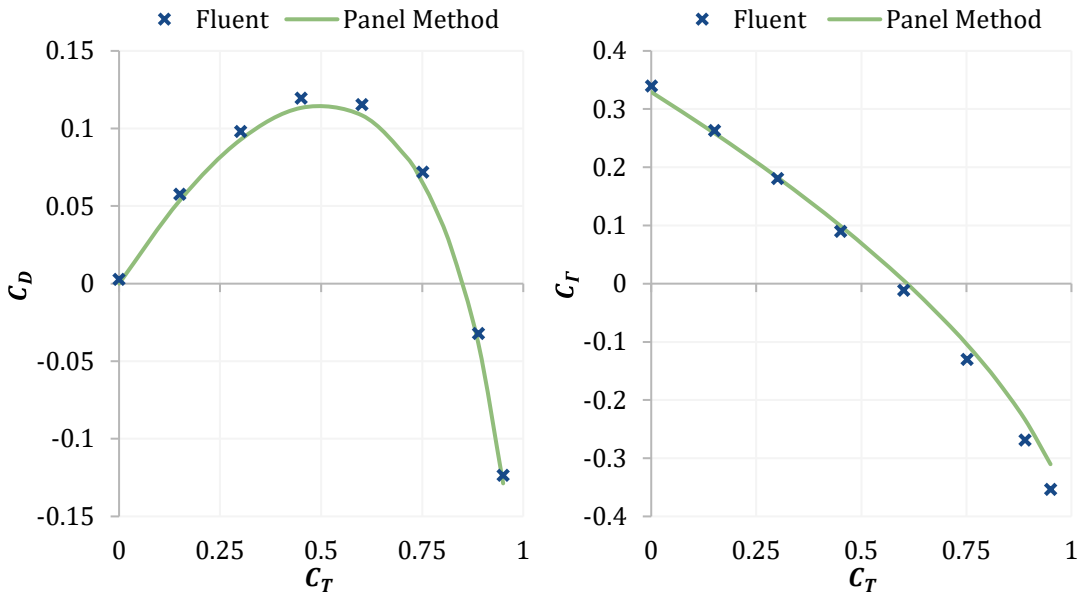

Figure 2.15: Duct drag C_D (left) and circulation C_Γ (right) results from Fluent and the panel method code.

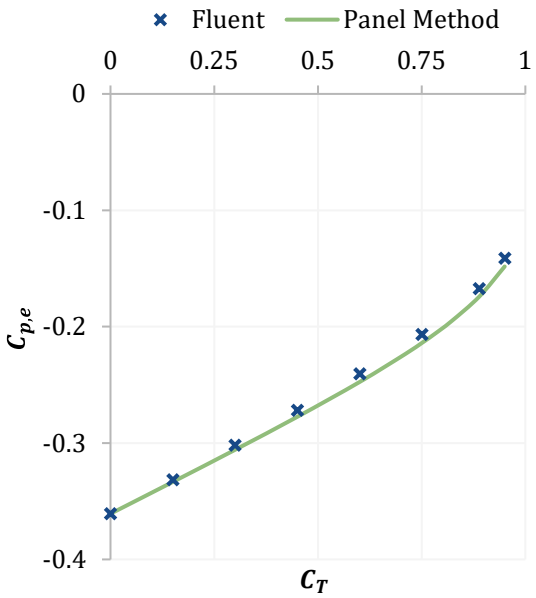

Figure 2.16: Exit pressure $C_{p,e}$ results from Fluent and the panel method code.

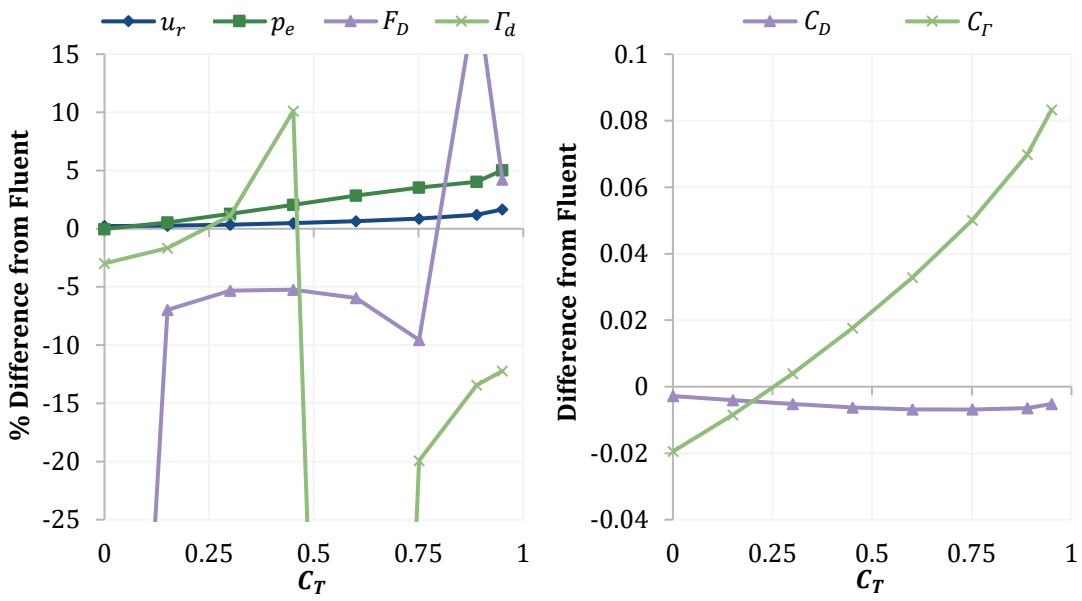

Figure 2.17: Percentage (left) and absolute (right) difference between panel method and Fluent. Large differences due to results passing through zero are excluded from the plot area.

Figure 2.17 presents the results as a percentage difference from the Fluent results, where power coefficient and velocity percentages are identical. Agreement for power and velocity was very good, reaching a maximum of 1.7%, while exit pressure reached a maximum of 5% as the coefficient tended towards zero. Interpreting the other parameters was more difficult, as the results passed through zero near C_T = 0 and C_T = 0.85 for duct drag and C_T = 0.6 for circulation. This led to spikes in the percentage differences that are not representative of the actual accuracy

A difference of around 5% is realistic for duct drag at the loadings unaffected by the error spike, but the discretisation convergence difficulties at C_T = 0.95 may mean the actual error was higher there. For circulation, the only reliable value was a 3% difference at C_T = 0 due to the wake vorticity included in the Fluent results. Looking at the right of Figure 2.13, it is quite plausible that increased wake vorticity with rotor loading caused an increasing difference. Nevertheless, there was still moderate agreement of 12% or less ignoring spikes.

Validity of Model

It is fair to conclude that the panel method code produces accurate results for power extracted, velocity at the rotor, and exit pressure, based on maximum differences of 1.7%, 1.7%, and 5% respectively. Assessment of duct drag was more difficult due to two zero-drag loadings; those excluded, 5% is a realistic value. Circulation could not be directly assessed above C_T = 0, but if circulation is a cause of augmentation then circulation values should be accurate based on the other results. In combination with the actuator disc validation, then, these results show the panel method code to be suitable for use in this work.

2.3 Viscous Modelling of Ducted Turbines

Alongside the inviscid modelling which made up the bulk of this investigation, the commercial package ANSYS [162] was used to set up and solve the Navier-Stokes equations [163] for the viscous flow around ducted turbines. Duct geometry was created in DesignModeler 15.0, before the discretisation was carried out in Meshing 15.0.1. Any repairs needed to the generated mesh were completed in ICEM CFD 15.0. Fluent 15.0 was then used to set up and carry out the numerical solution process. This section describes the choices made in modelling the flow and the approach to discretisation and estimating discretisation error.

2.3.1 Modelling Approach

ANSYS Fluent gives several choices in the approach taken to solving the Navier-Stokes equations, and the appropriate option was selected with reference to the Fluent documentation [164, 165]. The pressure based solver and coupled algorithm were chosen as appropriate for the incompressible flow being modelled and for speed of convergence. The least-squares method was used for the calculation of gradients, the second order upwind scheme was used for discretisation of the momentum, turbulent kinetic energy and specific dissipation rate convective terms, the second order central difference scheme was used for diffusion terms, and the second order scheme was used for interpolating pressure values.

Various turbulence models have been used for ducted turbines, including k-ε [115, 122, 125], k-ω [115], SST k-ω [55, 57, 99, 129, 131, 166], and direct numerical simulation [89, 114]. A comparison of the k-ε and standard k-ω models for a bare rotor found the k-ε model to provide a better match to theory [115], but validation work on the SST k-ω model for separating flow strongly supports its use for ducted turbines [57]. The SST k-ω model was selected here together with the Enhanced Wall Treatment, which reduces sensitivity to the near wall mesh size by blending between wall function and fully resolved approaches depending on the mesh size.

All simulations were run as steady problems, but pseudo-transient relaxation was used when convergence difficulties were encountered. This option adds an implicit under-relaxation based on a pseudo time step Δt that is automatically calculated from details of the domain size and flow field, demonstrated for the discretised general transport equation in Equation 2.44.

$$\rho_p \Delta V \frac{\phi_p - \phi_p^{old}}{\Delta t} + a_p \phi_p = \sum_{nb} a_{nb} \phi_{nb} + b \qquad \textbf{Equation 2.44}$$

For this equation only ΔV is the volume of cell p, nb signifies the neighbouring cells, ϕ represents a property that is being transported through the flow field and old indicates

the value of this property in the previous solver iteration, a is the linearised coefficient for ϕ, and b is the constant part of the source term.

The rotor was modelled as an actuator disc causing a uniform pressure drop using Fluent's built in fan model. This pressure drop was applied across an infinitely thin plane leading to a discontinuous change in the pressure, matching the panel method code. Many previous ducted turbine studies took an actuator disc approach, as discussed in Section 1.3.3, it is considered a valid approach for bare rotors [129], and shows good agreement with actuator disc theory [55, 57].

2.3.2 Discretising the Flow Field

An axisymmetric approach was taken to match the panel method code, but it was not possible to use identical duct shapes: the infinitely thin ducts in the panel method led to leading edge separation in results from Fluent, and so some thickness was added. The design of the mesh for this geometry was focused on increased resolution near the duct and wake surface with a coarser mesh away from the areas of interest to allow a larger domain size.

Figure 2.18 illustrates the general meshing approach: areas A and B consisted of an unstructured triangular cell mesh, coarser in area A, and with an automatically generated [167] smooth transition in cell size. Edge sizing increased resolution around D, representing the duct, E, representing the rotor, and F, placed near the expected position of the wake surface. An inflation layer of quadrilateral cells on the duct surface ensured cells sufficiently small for modelling the boundary layer. Finally, the small area C at the root of the rotor had a quadrilateral mesh to overcome a solution problem when using triangular cells.

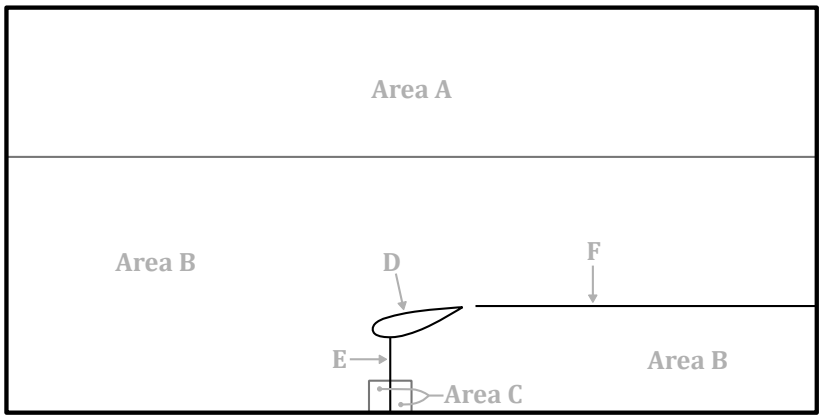

Figure 2.18: Illustration of mesh specification approach. Not to scale.

Fan and no-slip wall boundary conditions were applied to edges E and D respectively, while edge F was treated as part of the flow domain. The exit of the domain on the right side of Figure 2.18 was set as a pressure outlet at atmospheric pressure, while the

bottom boundary was the rotational axis of symmetry. A velocity inlet was applied to the left and top edges of the domain, with constant axial velocity and turbulence parameters specified. Inlet turbulence was required to ensure turbulent boundary layers on the duct surface, and reasonable atmospheric values were arbitrarily chosen. For a height above ground level z of 40m and a surface roughness length z_0 of 0.05m [168], a turbulence intensity I_u of 15% was calculated from Equation 2.45 [169].

$$I_u \approx \frac{1}{\ln\left(z/z_0\right)} \qquad \textbf{Equation 2.45}$$

A turbulence length scale ${}^{x}L_u$ of 110m was then found from Equation 2.46 [170].

$${}^{x}L_u \approx 25\frac{z^{0.35}}{z_0^{0.063}} \qquad \textbf{Equation 2.46}$$

2.3.3 Sources of Error

Despite their differences, there is a similarity in the sources of error in Fluent and the panel method code. Both make an approximation in discretising the problem that had to be assessed for its influence on the solution, although the method used for Fluent differs and will be described in this section. Rounding error was again minimised by using a double precision representation of numerical values. Finally, a choice had to be made as to when iterations should be stopped that balanced computational time against errors from stopping too early.

The decision to stop iterations was made partly on the basis of global residuals, which compare the two sides of each equation being solved. A drop to 10^{-3} is recommended by ANSYS for globally scaled residuals. As the residuals can be misleading, for example when a good initial guess is made for the solution [164], the key performance measure of mass flow rate through the duct was also examined. Only when mass flow did not change significantly with further iterations was the solution judged converged.

Both domain size and mesh cell size affect discretisation error, with the former evaluated by doubling the domain's linear dimensions and checking for inconsequential changes in the results of interest. Mesh size was assessed using the recommended [171, 172] Grid Convergence Index approach, developed by Roache [173] and based on Richardson Extrapolation. Three mesh sizes are required, where mesh 1 is the finest. The Grid Convergence Index GCI estimates the error of a result ϕ as the difference between the value from mesh 1 and the extrapolated value, and is reported as a percentage of the mesh 1 value with a safety factor of 1.25.

In the calculation of the grid convergence index, $\mathcal{O}$ is the order of the numerical scheme, e_a^{21} is the approximate relative error which quantifies the difference between the result

from mesh 1 and 2, and $\mathcal{R}_{21}$ is the refinement ratio between meshes 2 and 1. GCI, then, is calculated using Equation 2.47.

$$GCI = \frac{1.25e_a^{21}}{\mathcal{R}_{21}^{\mathcal{O}} - 1} \qquad \textbf{Equation 2.47}$$

The approximate relative error is given by Equation 2.48.

$$e_a^{21} = \frac{\phi_1 - \phi_2}{\phi_1} \qquad \textbf{Equation 2.48}$$

In refining the mesh, the number of cells was controlled by adjusting all mesh sizing parameters other than the duct boundary layer by a constant factor. Where here $\mathcal{D}$ is the dimensionality of the mesh and so was set as 2, the total number of cells N can be used to calculate the refinement ratio $\mathcal{R}_{jk}$ between mesh j and k using Equation 2.49.

$$\mathcal{R}_{jk} = \left(\frac{N_k}{N_j}\right)^{1/\mathcal{D}} \qquad \textbf{Equation 2.49}$$

While GCI can be calculated from two meshes if $\mathcal{O}$ is set as the formal order of the scheme, the error may not reduce exactly as that order suggests and so a safety factor of 3 would be required [172]. Instead, an apparent order $\mathcal{O}$ was calculated from the change in results over three meshes using Equation 2.50 [171].

$$\mathcal{O} = \frac{1}{\ln(\mathcal{R}_{21})}\left|\ln\left|\frac{\varepsilon_{32}}{\varepsilon_{21}}\right| + \ln\left(\frac{\mathcal{R}_{21}^{\mathcal{O}} - \sigma}{\mathcal{R}_{32}^{\mathcal{O}} - \sigma}\right)\right| \qquad \textbf{Equation 2.50}$$

This equation was solved for $\mathcal{O}$ using a fixed point iteration algorithm [174] and the definitions in Equation 2.51.

$$\sigma = 1 \cdot \text{sign}\left(\frac{\varepsilon_{32}}{\varepsilon_{21}}\right)$$
$$\varepsilon_{jk} = \phi_j - \phi_k \qquad \textbf{Equation 2.51}$$

2.4 Summary

The majority of simulation results presented in this work are from an axisymmetric vortex ring panel method, in which the flow was modelled as inviscid. While the results must therefore be treated with caution, as there may be large differences between predictions and real flows, an inviscid approach has advantages useful for achieving the research objectives set out in the Introduction chapter. Both irrotational and attached flow assumptions follow from the choice of inviscid flow, an assessment of flow rates found that incompressible flow can reasonably be assumed, and the literature suggests little loss of accuracy by assuming steady flow.

The basis of the method was finding a set of vortex ring strengths that enforced boundary conditions of no flow through the duct surface and no static pressure jump across the wake surface. Each simulation started with the specification of the thin walled duct shape and the pressure drop at the actuator disc, then an iterative solution process found the ring strengths and wake shape. To ensure discretisation error was kept to an acceptable level, discretisation dependence studies assessed the variation in important results with increased resolution for each investigation.

Validation against actuator disc theory for the case of a bare rotor found very good agreement, with a difference from theory of 0.36% and 0.27% for C_{Topt} and C_{Pmax} respectively. Comparison with inviscid ANSYS Fluent simulations for a ducted turbine showed a maximum difference of 1.7% for power, 5% for exit pressure, and 5% for duct drag. This agreement was still good given the additional errors incurred by comparing to simulation results rather than a validated theory. Together, both tests show that the model was capable of predicting the inviscid performance of ducted turbines to a high degree of accuracy.

A second modelling approach using ANSYS Fluent 15.0 was used for viscous simulations. The SST k-ω turbulence model was selected with the Enhanced Wall Treatment, and a second order approach was used for spatial discretisation of the governing equations. As with the panel method, the simulations were steady and axisymmetric in nature and represented the rotor with an actuator disc. However, the thin ducts from the inviscid simulations had thickness added to avoid leading edge separation. Discretisation error was estimated for each simulation using the Grid Convergence Index, which is based on Richardson Extrapolation.

3 Chapter

The Behaviour of Ducted Turbines

The primary aim of this chapter is to answer a number of the more straightforward questions raised in the introduction in an unambiguous way, using the inviscid panel method code to avoid any confusion from varying levels of viscous losses or separation. These idealised results are also shown to be reasonable approximations to real ducted turbines in some circumstances, and the maximum power extractable by a ducted turbine of given dimensions is estimated after an optimisation procedure. Finally, the results are drawn together to compare the conceptual models for a ducted turbine: is intuition based on a diffuser or an aerofoil closer to the actual behaviour?

3.1 Initial Investigations

3.1.1 A Set of Ducted Turbines

Ducts with fixed length and exit diameter ratios, measured against the throat diameter, form the basis of this section. Shown in Figure 3.1, they allowed an assessment of the significance of duct shape and produced important results relating to power, rotor loading and exit pressure. These ducts were chosen to give a wide range of shapes within the limitations of the panel method code, and in all cases the rotor was placed at $x/D = 0$.

Discretisation convergence was good, as shown in Table 3.1 and Table 3.2, excepting a few cases at $C_T = 0.95$ with relatively small absolute values and ignoring the far wake results at $C_T = 0.95$ which were unused. The worst cases of convergence were always for the most extreme shapes, justifying the approach taken in later modelling when testing every shape became impractical.

Table 3.1: Largest magnitude change of result for ducts A to G when discretisation was changed from last duct panel length = $0.00125D$ and wake length = $8D$.

	Worst % Difference with					
	Halved Panel Length			Doubled Wake Length		
	$C_T = 0$	C_{Topt}	$C_T = 0.95$	$C_T = 0$	C_{Topt}	$C_T = 0.95$
$\dot{m}$ & C_P	0.33	0.31	0.71	0.00	0.02	0.65
C_{Topt}	-	0.09	-	-	0.09	-
C_D	-	0.12	14.42	-	0.04	1.69
p_e	0.17	0.71	2.29	0.00	0.11	1.11
R_w	0.02	0.04	0.27	0.04	0.96	6.07

Table 3.2: Median change of result magnitude for ducts A to G when discretisation was changed from last duct panel length = $0.00125D$ and wake length = $8D$.

	Median % Difference with					
	Halved Panel Length			Doubled Wake Length		
	$C_T = 0$	C_{Topt}	$C_T = 0.95$	$C_T = 0$	C_{Topt}	$C_T = 0.95$
$\dot{m}$ & C_P	0.24	0.25	0.42	0.00	0.01	0.31
C_{Topt}	-	0.06	-	-	0.02	-
C_D	-	0.10	0.37	-	0.01	0.28
p_e	0.13	0.21	0.97	0.00	0.01	0.65
R_w	0.01	0.03	0.24	0.01	0.47	4.07

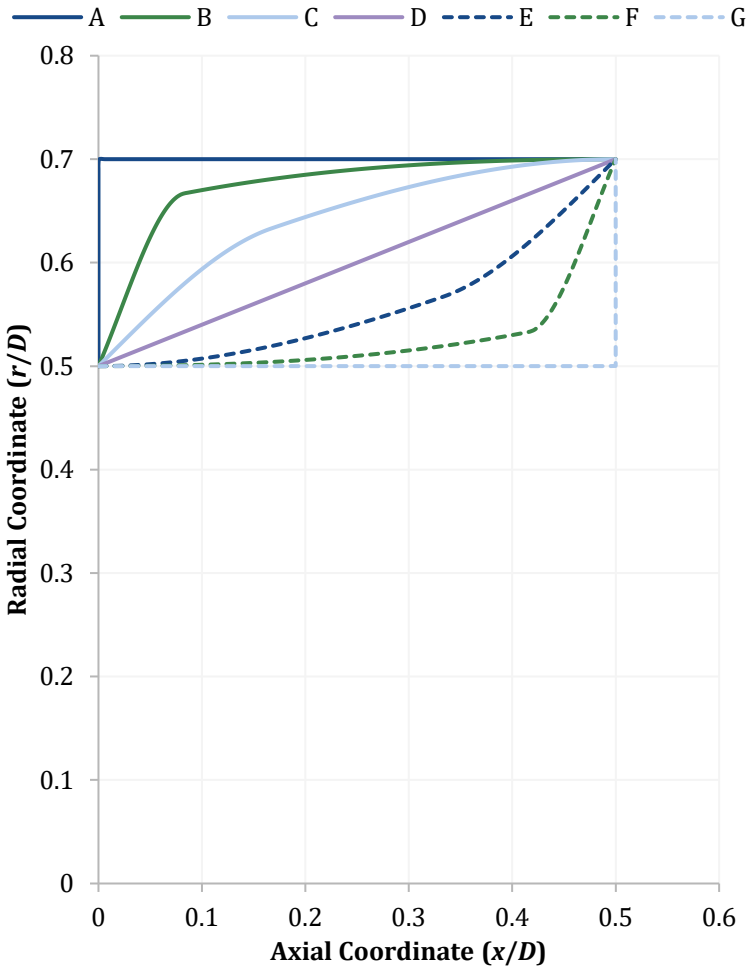

Figure 3.1: Duct shapes A to G, shown in terms of the rotor diameter D.

3.1.2 Area Ratio Does Not Define Performance

Area ratio is often treated as the most important geometrical parameter for performance, as discussed in Section 1.5.3. It is immediately apparent from Figure 3.2, however, that the duct shape has a significant impact at fixed area ratio: power coefficient more than doubles going from duct A to G. Similar increases with shape were found for dimensionless velocity at the rotor u_r/u_∞ in Figure 3.3, while the influence on the duct drag coefficient C_D was even larger.

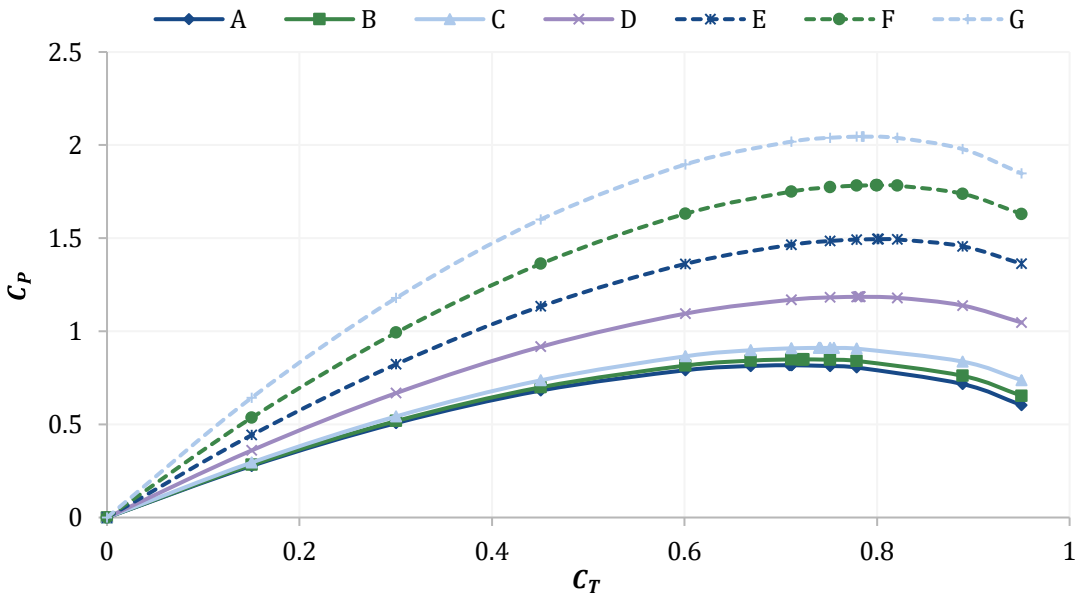

Figure 3.2: Variation of power coefficient C_P with thrust coefficient C_T for ducts A to G.

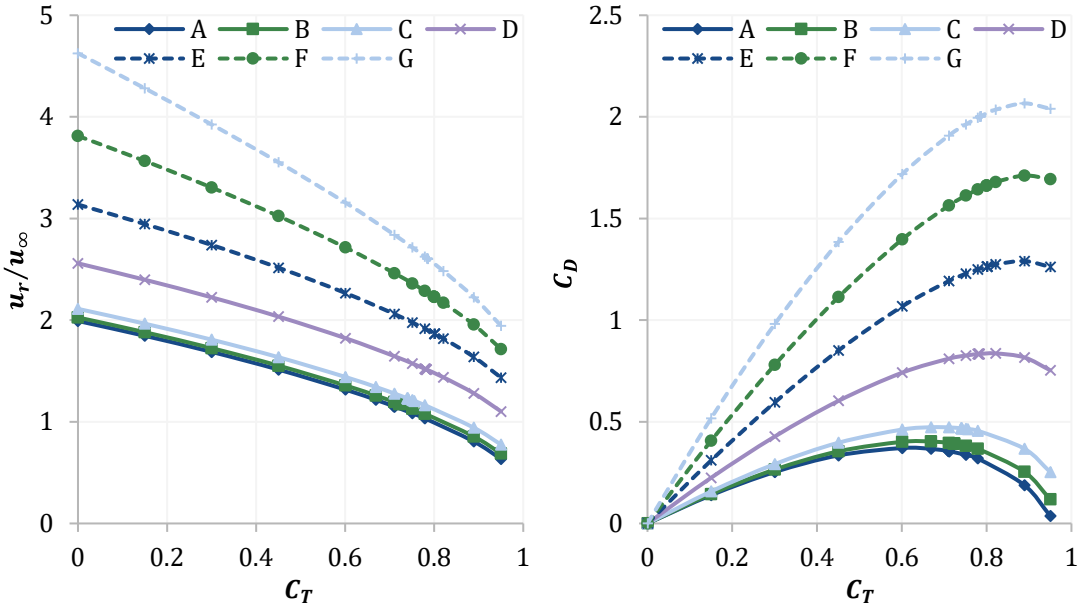

Figure 3.3: Variation of velocity at the rotor u_r (left) and duct drag coefficient C_D (right) with thrust coefficient C_T for ducts A to G.

When the duct is considered from an aerofoil point of view, the increase in velocity and power is quite logical. As the camber of the shape increases from duct A to duct G so does the circulation, which induces greater velocity at the rotor. However, these results are also consistent with an explanation based solely on the angle of the duct trailing edge. Phillips [4] noted that a change in this angle away from the axial direction should force a greater expansion in the wake causing an increase in the flow rate through the duct. These explanations will be compared further in Section 3.4.

3.1.3 Power Is Proportional to Flow Rate at Fixed Loading

Comparison of Figure 3.2 and Figure 3.3 shows that the power extracted P increases with velocity u_r at a fixed pressure drop Δp, a relationship shown to be linear for rotor area A_r and volume flow rate Q_r in Equation 3.1 [5].

$$P = \Delta p A_r u_r = \Delta p Q_r \qquad \textbf{Equation 3.1}$$

However, Section 1.5.4 notes that a misconception of power proportional to u_r^3 has not yet been completely eliminated. Figure 3.4 provides additional evidence of a linear variation at fixed loading using the rate of kinetic energy in the streamtubes through ducts A to G, as computed far upstream and downstream at C_T = 0.75.

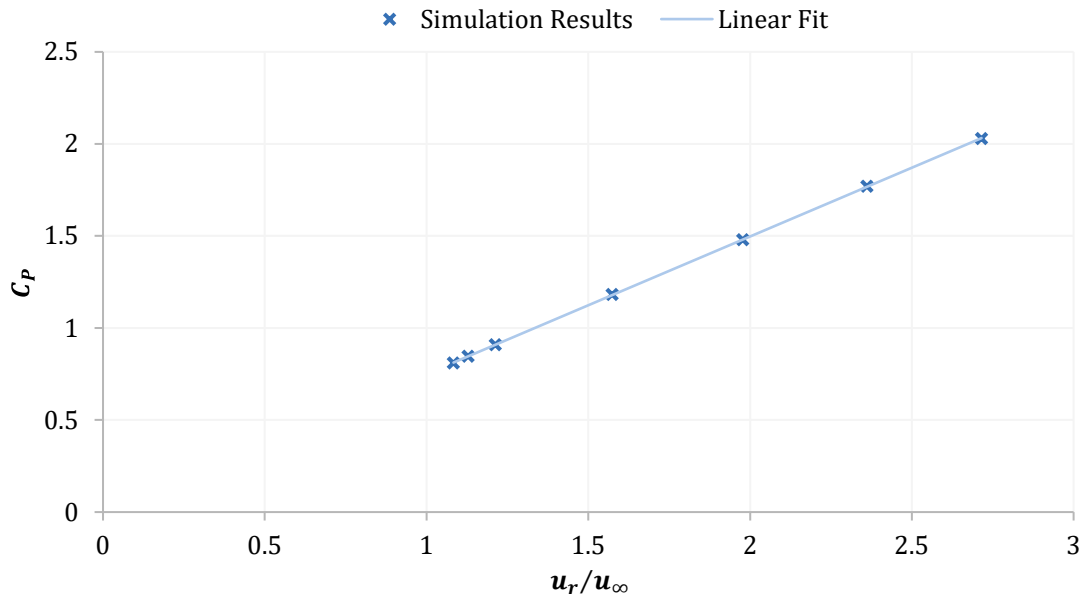

Figure 3.4: Variation of power coefficient C_P with velocity at the rotor u_r, for ducts A to G operating at C_T = 0.75.

3.1.4 Optimum Rotor Loading Is Not 8/9

While power is proportional to flow rate at a fixed loading, Figure 3.5 shows the optimum loading varied with duct shape and was between 10% and 20% less than the bare actuator disc value of C_{Topt} = 8/9. While this evidence cannot show that C_{Topt} is always reduced, it is clear that care must be taken in discussing augmentation: dividing C_{Pmax} by 16/27 is not equivalent to a comparison at the same loading. The former was 3% to 8% less than the latter at each duct's C_{Topt} here, less than half the drop in C_{Topt}, implying through Equation 3.1 a variation in augmentation with C_T that partially compensated for the reduced optimum loading.

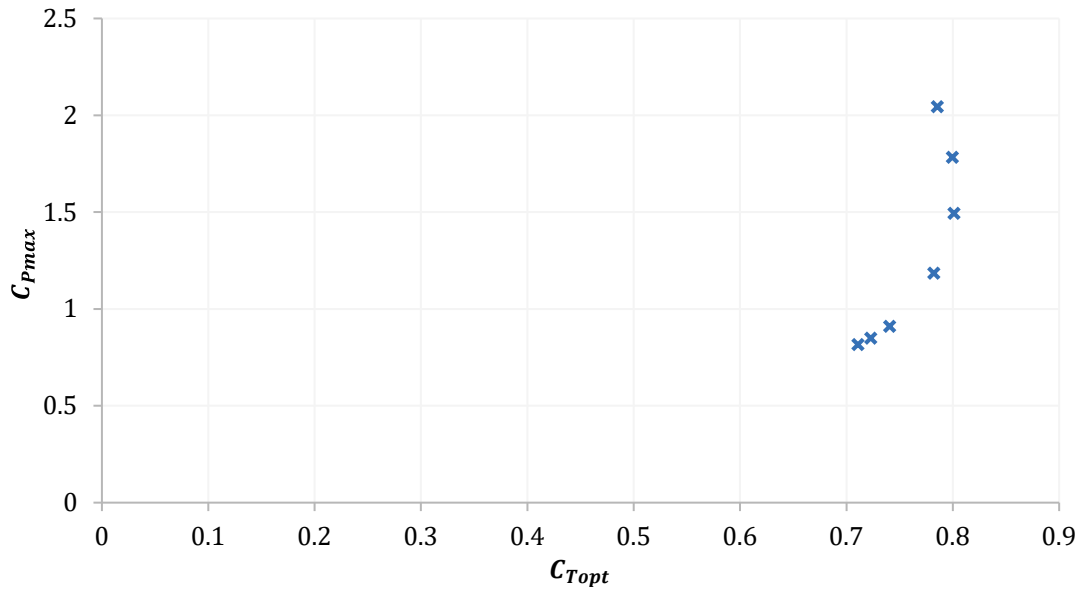

Figure 3.5: Variation of C_{Pmax} with C_{Topt} for ducts A to G. The ducts appear in order from A with the smallest C_{Pmax} to G with the largest.

3.1.5 Variation of Augmentation with Rotor Loading

A direct test of augmentation over a bare rotor at the same loading is given in Figure 3.6, confirming a reduction with C_T. The error in assuming otherwise is shown to be substantial in Figure 3.7, and further assuming C_{Topt} = 8/9 increases the largest C_{Pmax} error to 44%. Both assumptions have previously been made, as discussed in Sections 1.5.4 and 1.5.6. These two assumptions are connected: decreasing augmentation implies a drop in velocity more rapid than a bare rotor experiences, reducing C_{Topt} by changing the balance between flow rate and power extraction per unit mass flow.

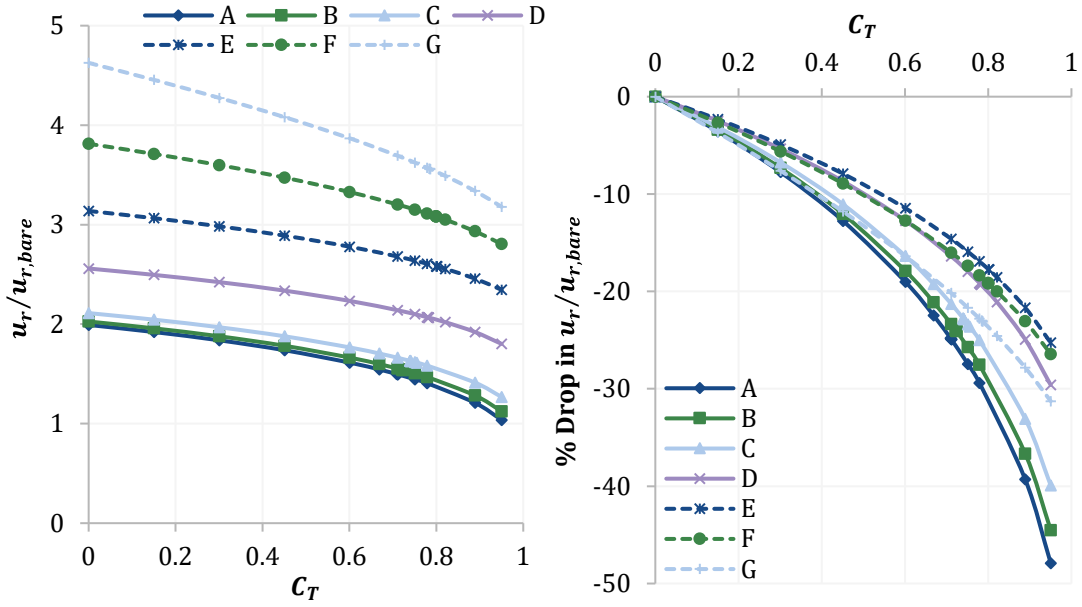

Figure 3.6: Variation of augmentation $u_r/u_{r,bare}$ compared to a bare actuator disc operating at the same C_T (left), and percentage reduction in $u_r/u_{r,bare}$ from value at C_T = 0 (right), both for ducts A to G.

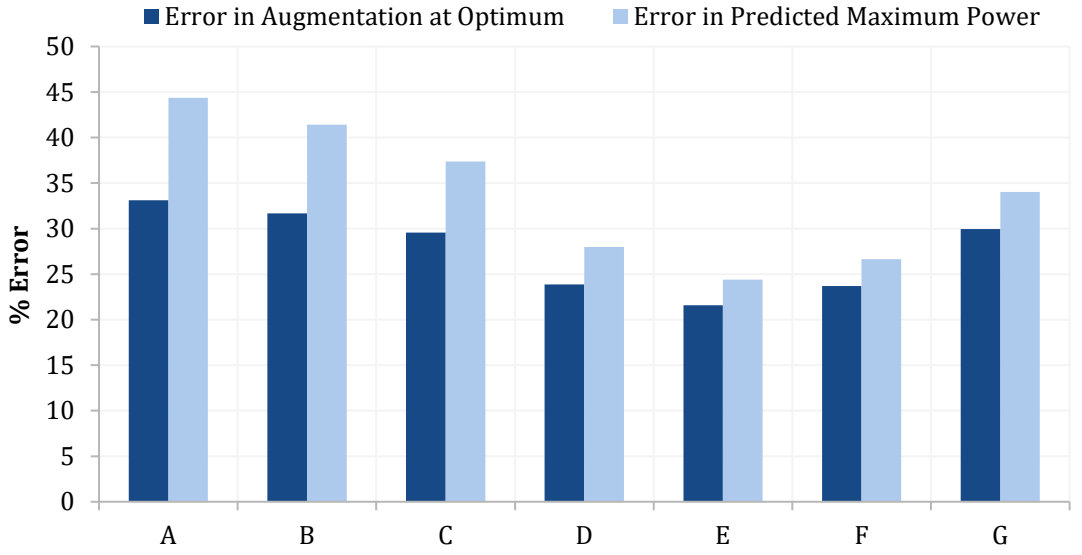

Figure 3.7: Percentage error in assuming that the augmentation $u_r/u_{r,bare}$ does not vary from its value at C_T = 0 for ducts A to G, where the error is calculated for the actual augmentation at C_{Topt} and for the predicted maximum power if C_{Topt} = 8/9 is also assumed.

3.1.6 Influences on Augmentation

Three parameters have been linked to the augmentation performance of ducted turbines, as discussed in Sections 1.2.2 and 1.2.4: inviscid duct drag, exit pressure coefficient, and duct circulation. Each is tested here, beginning with the ratio of duct drag to thrust on the rotor C_D/C_T in Figure 3.8 for all loadings modelled except zero. A clear linear relationship existed, with a best fit of all the data suggesting a gradient of 1 and an intercept of 1 to within 0.5%. Section 6.1 will present a derivation that leads to this relationship.

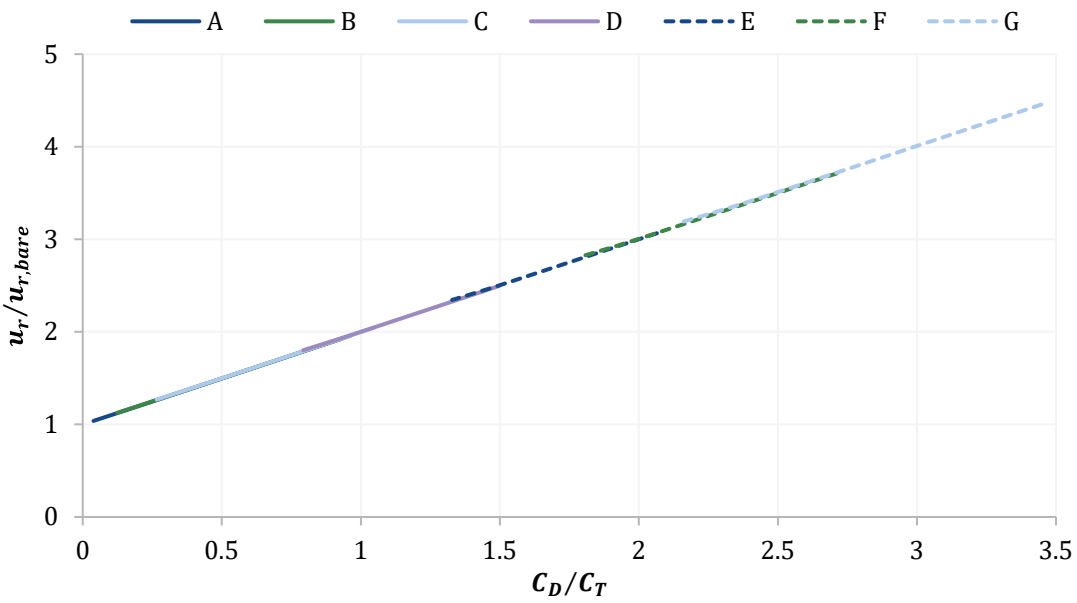

Figure 3.8: Variation of augmentation over a bare actuator disc $u_r/u_{r,bare}$ with the ratio of inviscid duct drag C_D to thrust on the rotor C_T, for ducts A to G.

Excluding ducts A and G for numerical reasons, the augmentation ratio was compared to the exit pressure coefficient in three ways: directly, with the value of the rotor pressure drop subtracted, and with the pressure on the downstream side of a bare actuator disc subtracted. None of these approaches gave a unique value of exit pressure coefficient for each value of augmentation ratio, as exemplified by Figure 3.9. Plotting against the exit augmentation ratio highlights the fact that that these ducts experienced exit augmentation when the exit pressure coefficient was more negative than the downstream side of a bare rotor.

Augmentation was also multi-valued for circulation, as Figure 3.10 shows, although the parameters were again relatively close to collapsing onto a single curve. Positive circulation did not coincide perfectly with exit augmentation; rotor augmentation, meanwhile, existed even for the negative values of circulation. Neither exit pressure nor circulation achieved anywhere near as perfect an association as drag ratio, even though the former two are considered mechanisms of augmentation, but note that rotor loading was allowed to vary in this examination and may be a confounding factor. These associations will be examined further later in this work.

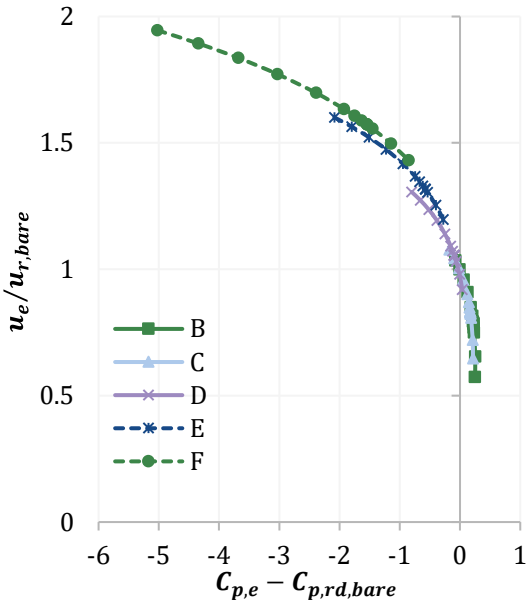

Figure 3.9: Variation of velocity augmentation at the duct exit $u_e/u_{r,bare}$ with the difference between the exit pressure coefficient $C_{p,e}$ and the pressure coefficient on the downstream side of a bare actuator disc at the same loading $C_{p,rd,bare}$, for ducts B to F. A negative difference indicates that the duct exit pressure was more negative that the disc downstream side.

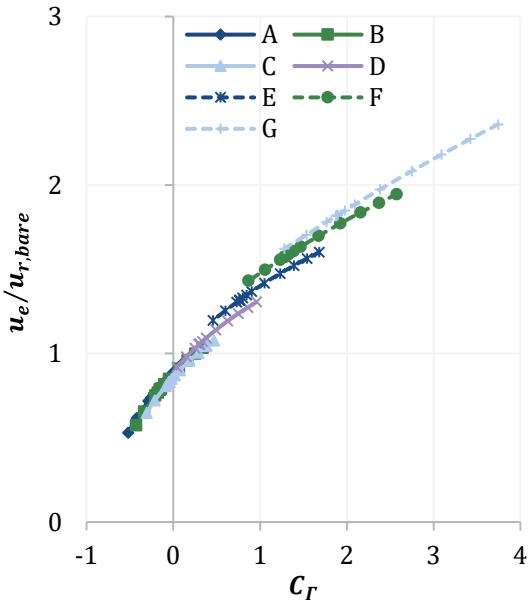

Figure 3.10: Variation in velocity augmentation at the duct exit $u_e/u_{r,bare}$ with dimensionless circulation C_Γ for ducts A to G.

3.1.7 Variation of Exit Pressure

The results in the previous section suggest that substantially subatmospheric exit pressures are possible in inviscid flow, with both duct shape and rotor loading having a large influence. Figure 3.11 confirms these findings by plotting $C_{p,e}$ against C_T. Adding the value of C_T to $C_{p,e}$ on the right of the figure removed the direct contribution of the rotor pressure drop from $C_{p,e}$, illustrating a change in $C_{p,e}$ associated with changes in flow velocity.

Although the relationships between $C_{p,e}$ and C_T appear almost linear, the scale of the plot masks a non-linear variation for ducts B and C at least. Adding C_T to $C_{p,e}$ did reveal close fits to linear relationships where both the gradient and intercept depended on duct shape, although it is questionable whether this result is meaningful given that both parameters are a function of C_T. However, the association may be stronger than seen between the pressure coefficient on the downstream side of bare rotor and C_T, with $R^2 > 0.999$ in the ducted cases and $R^2 = 0.986$ over the same C_T range in the bare case.

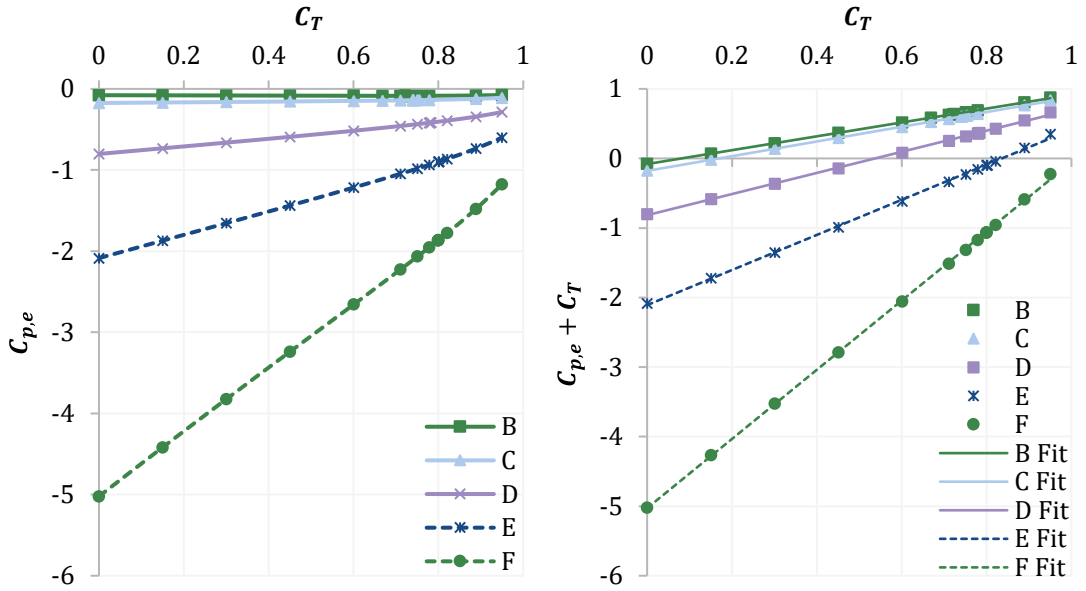

Figure 3.11: Variation of the exit pressure coefficient $C_{p,e}$ (left), and the sum of $C_{p,e}$ and C_T (right), both with rotor loading and for ducts B to F.

Rotor loading also affected the radial distribution of pressure at the exit, as shown on the left of Figure 3.12. C_T was added here simply for clarity, as it prevented overlap at the outer radii. Based on the exit pressure coefficient, without removing C_T, the pressure at the outermost radius was 5.4% of the root value at C_T = 0 and 28.8% at C_T = 0.95. Both the magnitude and form of this radial variation then also changed with duct shape. As will be discussed in Section 5.3, these radial variations add complexity when looking for relationships between exit pressure and velocity.

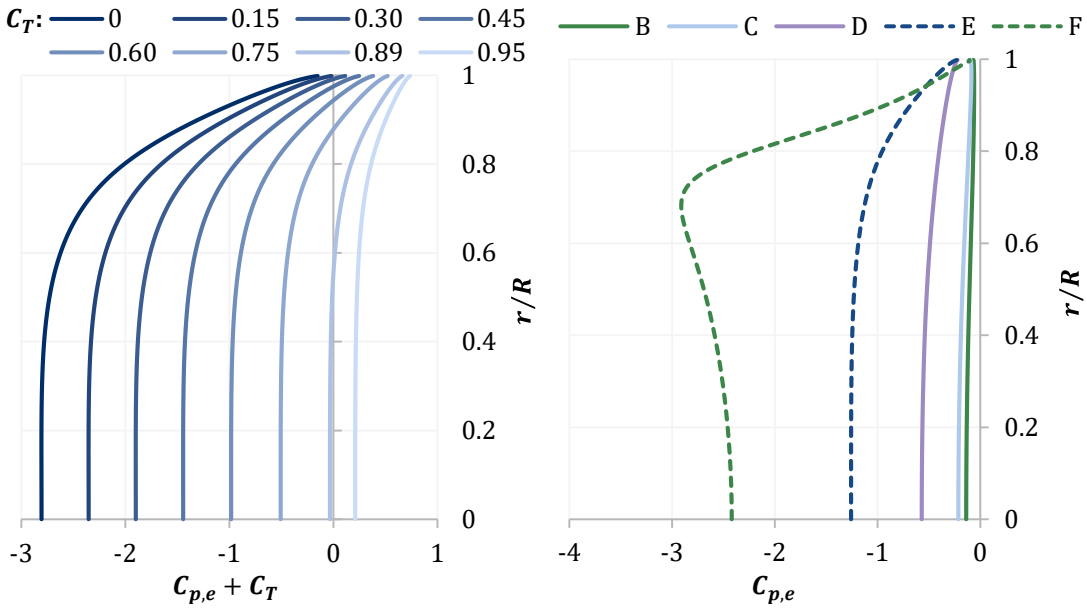

Figure 3.12: Radial variation of pressure in the exit plane $C_{p,e}$: for duct E at C_T = 0 to C_T = 0.95 (left), and for ducts B to F at C_T = 0.75 (right).

3.1.8 The Betz Limit Does Not Apply

Results in this chapter have shown the ease with which the Betz limit of C_{Pmax} = 0.593 can be exceeded in inviscid flow when defining C_P with rotor area. Figure 3.13 provides strong evidence that the limit can also be exceeded when C_P is based on duct exit area; a ducted turbine can extract more power than a bare actuator disc, even when the disc is as large as the duct exit. Practical limits from viscosity will remain, but more trust can now be placed in the previous viscous results discussed in Section 1.5.5 that may otherwise have been doubted by critics.

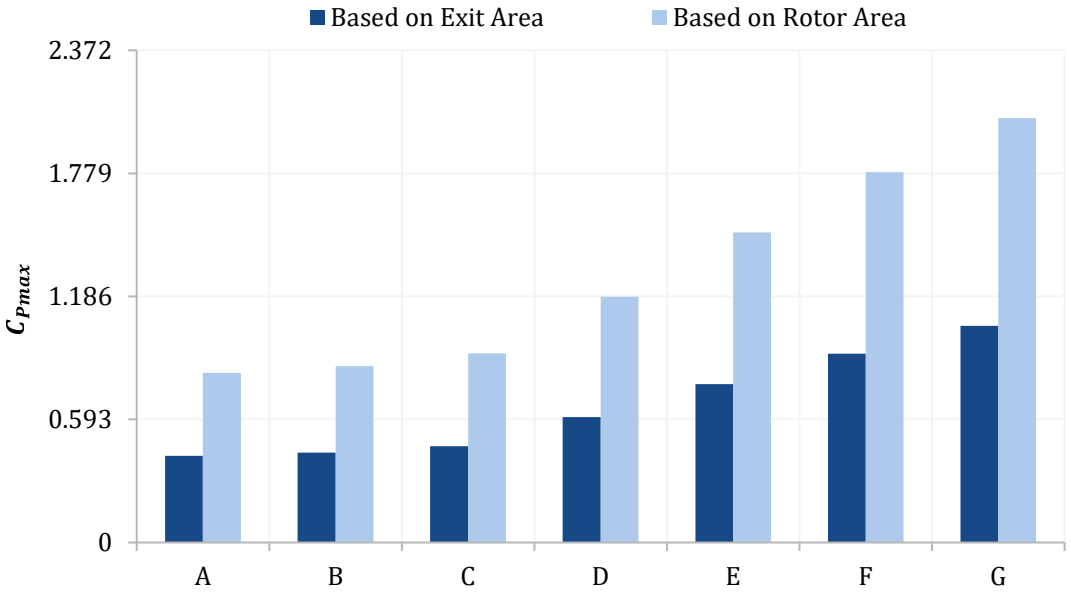

Figure 3.13: Maximum power coefficients achieved by ducts A to G, where a coefficient calculated from the rotor area and another calculated from the duct exit area is shown.

An interesting result that is not obvious from Figure 3.13 is that C_{Pmax} = 1.04 for duct G, based on exit area. While exceeding a value of 1 for C_P may be initially surprising, it is really only an artefact of the definition of power coefficient in Equation 3.2.

$$C_P = \frac{P}{{}^1/_2 \rho A_r u_\infty^3} \qquad \textbf{Equation 3.2}$$

Note that the denominator is the rate of kinetic energy passing through an area equal to the rotor A_r when the flow is at the free stream velocity u_∞. In other words, it is the power available to a bare rotor when the rotor is not operating rather than a quantity that exists with a duct. A ducted turbine that achieves C_P > 1 is only extracting more power than is available to a bare rotor; it is not creating power from nowhere and 1 is not a theoretical limitation. The increase in available power comes from a larger far upstream streamtube area A_∞, or source area, as shown by Sections 3.1.2 and 3.1.3 where the ducts are augmenting power through an increased flow rate.

Despite the much greater C_{Pmax} for the ducted turbines, Section 3.1.5 implies that the source area reduced at a faster rate with C_T when compared to a bare rotor. Figure 3.14 also shows that they captured a smaller fraction of the available power, with the fraction of the actual source area having a value equal to the rotor loading [175]. $C_P > 1$ is therefore not concerning, as there was simply an abundance of available power combined with a power coefficient definition that loses its expected physical meaning – the ratio of actual to available power – when applied to a ducted turbine.

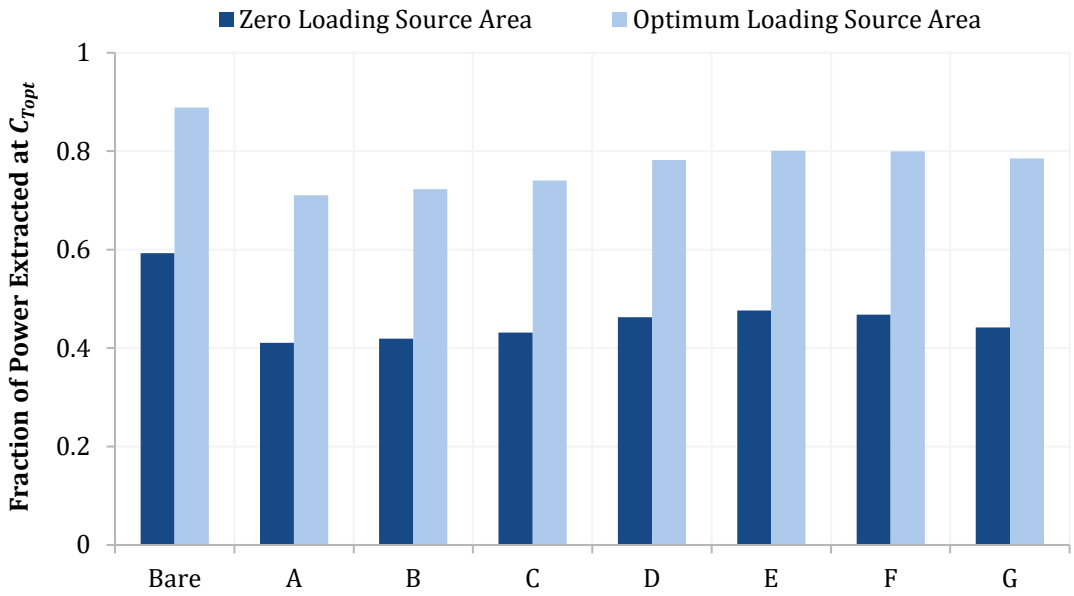

Figure 3.14: The maximum power extracted for ducts A to G given as a fraction of the power available in each duct's streamtube source area at zero rotor loading and at the optimum loading. Results for a bare actuator disc are also shown.

3.2 Right Angled Exit Ducts

3.2.1 The Optimum Shape in Inviscid Flow

Of the duct shapes modelled in Section 3.1, the best performing in terms of C_{Pmax} was the right angled duct G. Although consistent with the camber and exit angle explanations in Section 3.1.2, too few ducts were modelled to show generality. A more thorough test is presented here using an optimisation procedure that found the duct shape for maximum mass flow at two rotor loadings. Three stages of discretisation were used throughout, shown in Table 3.3, to ensure convergence.

Fixed nodes at the duct inlet and outlet set an inlet radius of $0.5D$, outlet radius of $0.7D$, and length of $0.5D$, and formed the axial and radial bounds for the movable nodes. Interpolation between nodes used a piecewise cubic Hermite spline. A single moveable node was used first, starting at an axial position of $0.25D$ and radius $0.6D$, before repeating with two moveable nodes beginning at $x = 0.3D$ and $0.4D$, and at $r = 0.51D$ and $0.53D$. An interior point algorithm [176] was used, with the stopping criteria selected by tightening them until they no longer affected the result.

Table 3.3: Discretisation settings used for each stage of the duct shape optimisation process.

	Stage 1	Stage 2	Stage 3
Duct Last Panel Length	$0.02D$	$0.01D$	$0.005D$
Expanding Wake Length	$4D$	$8D$	$8D$

Table 3.4: Change in results with a finer discretisation for the two node optimum shapes found at $C_T = 0$ and $C_T = 8/9$ and a right angle shape, where the change was calculated from a last duct panel length of $0.00125D$ and expanding wake section of $8D$.

	% Difference with					
	Halved Panel Length			Doubled Wake Length		
	$C_T = 0$ Shape	$C_T = 8/9$ Shape	Right Angle	$C_T = 0$ Shape	$C_T = 8/9$ Shape	Right Angle
$\dot{m}$ at $C_T = 0$	0.01	-	0.16	0.00	-	0.00
$\dot{m}$ at $C_T = 8/9$	-	0.07	0.11	-	-0.02	-0.02

The optimum shapes are shown in Figure 3.15 and Figure 3.16 for one and two moveable nodes respectively. All had a fully radial exit angle, while the addition of a second movable node brought the only significant deviation closer to a right angle. Comparisons to an exact right angled shape, for which the discretisation convergence is in Table 3.4, showed that the algorithm didn't quite reach the true optimum of a right angle: the right angle achieved a 0.61% greater mass flow than the Stage 3 shape for $C_T = 0$, and 0.25% greater than the $C_T = 8/9$ shape at its loading.

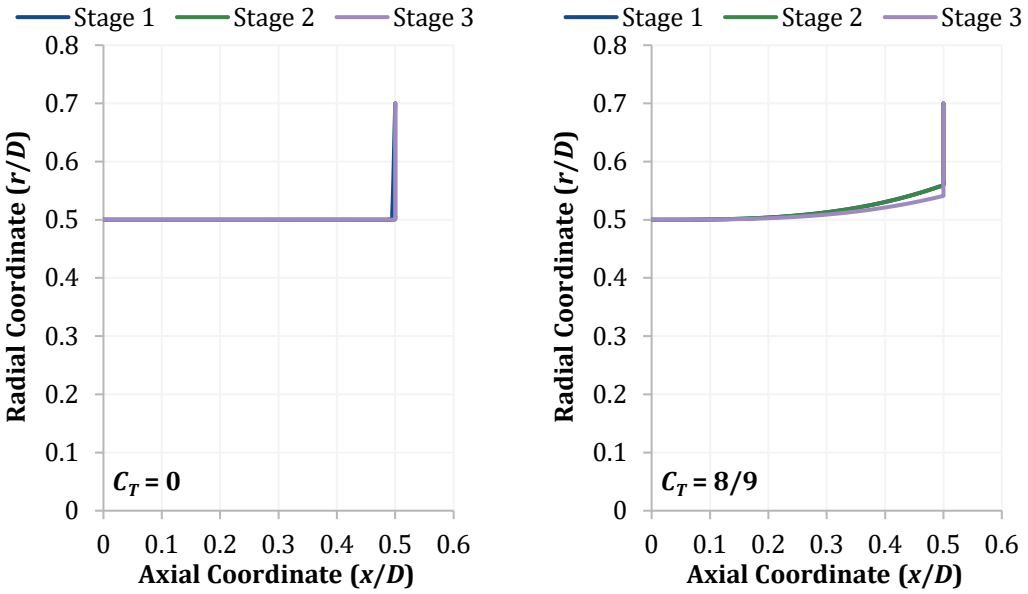

Figure 3.15: Duct shapes that maximised mass flow rate at C_T = 0 and C_T = 8/9 from one node optimisation. The resolution of discretisation increased from stage 1 to stage 3.

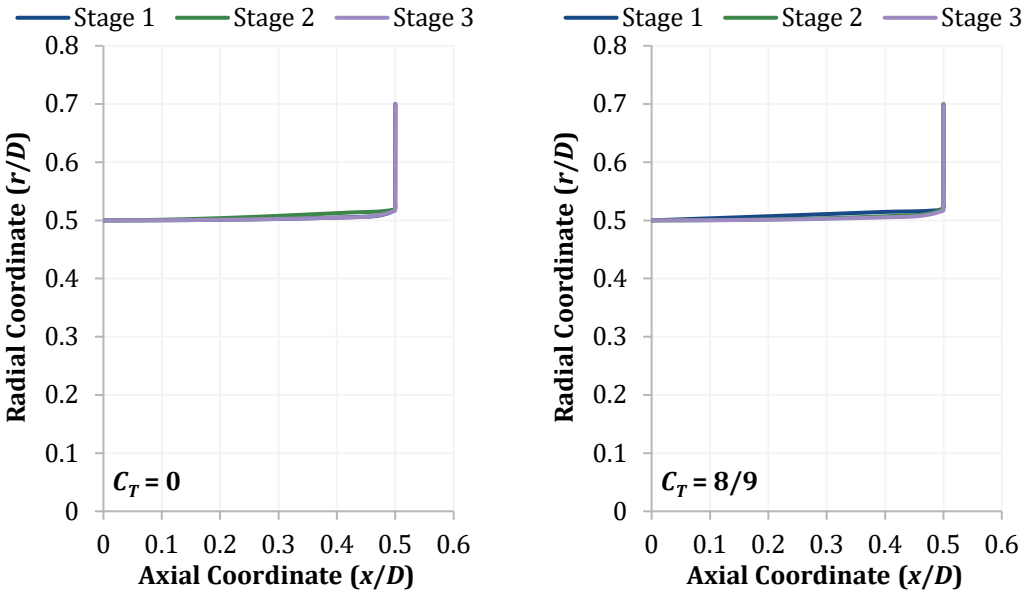

Figure 3.16: Duct shapes that maximised mass flow rate at C_T = 0 and C_T = 8/9 from two node optimisation. The resolution of discretisation increased from stage 1 to stage 3.

It must be stressed that these findings are for inviscid flow, and it is not suggested that a right angled shape will maximise power for a real ducted turbine. While it is interesting to note the similarities between these ducts and those developed for viscous flow at Kyushu University [177], the main conclusions to be drawn here are theoretical: within the constraints specified, the shape for best performance did not vary with rotor loading, was the one with most camber, and had the largest exit angle possible.

3.2.2 Limits on Ducted Turbine Performance

Substantial separation is expected for these right angled ducts when placed into viscous flow. It seems reasonable to expect a considerable drop in C_{Pmax} to ensue, despite both viscous wake mixing [4] and vortex formation [88] having been reported as mechanisms of augmentation. Therefore, the set of inviscid predictions for right angled ducts presented in this section have practical significance as limiting values for a given size of duct. A wide range of sizes were used, specified by the length of the cylindrical section and height of the exit rim, and the discretisation convergence in Table 3.5 was adequate for this purpose.

Table 3.5: Change in C_{Pmax} with a finer discretisation for a range of right angled ducts. Discretisation was changed from a last duct panel length of $0.005D$ and an expanding wake section of $64D$ or shorter: the assessment of wake length was stopped once convergence was reached.

Duct Cylinder Length (L/D)	0	0	0.125	0.125	0.125	8	8	8
Duct Rim Height (L/D)	0.125	4	0	0.125	4	0	0.125	4
% Difference in C_{Pmax} with Halved Panel Length	-1.48	-0.57	0.32	-1.06	-0.39	-0.04	-0.58	-0.33
% Difference in C_{Pmax} with Doubled Wake Length	-0.01	-0.13	0.00	0.00	-0.13	0.00	0.00	-0.02

Figure 3.17 presents results for a subset of the ducts examined that avoided the truly outrageous values of C_{Pmax} possible in inviscid flow. Basing C_{Pmax} instead on exit area shows an optimum rim height rather than ever increasing performance in Figure 3.18, and emphasises in Figure 3.19 the asymptotic change with increasing cylinder length that was suggested in Figure 3.17. A purely cylindrical duct with zero rim height, meanwhile, reduced power compared to a bare rotor.

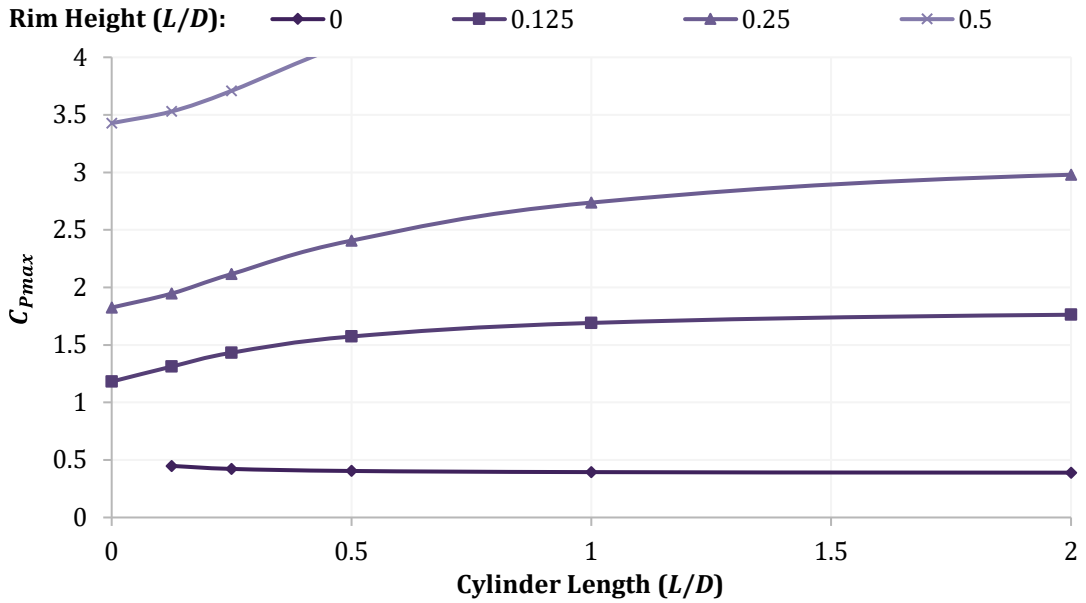

Figure 3.17: Variation of C_{Pmax} with cylinder length, for a range of rim heights.

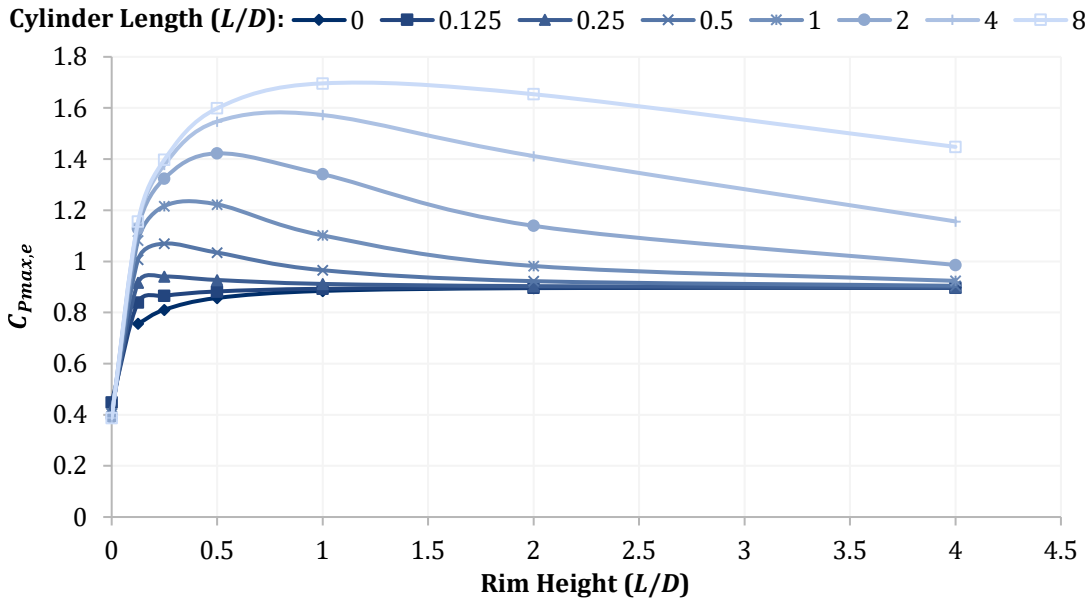

Figure 3.18: Variation of exit area C_{Pmax} with rim height, for a range of cylinder lengths.

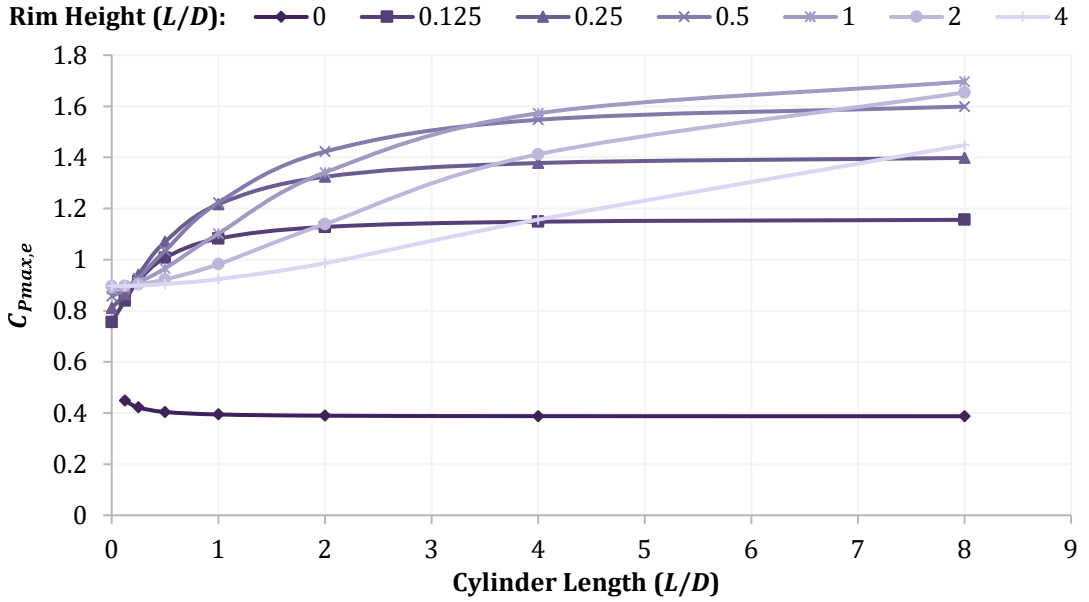

Figure 3.19: Variation of exit area C_{Pmax} with cylinder length, for a range of rim heights.

Comparison with an optimised flanged turbine in viscous flow is consistent with the inviscid results as limiting values: Oka et al. [44] found C_{Pmax} = 1.05 for a duct with length ratio L_d/D = 0.25 and radius increase $(R_e - R_r)/D$ = 0.15. None of the ducts modelled here matched both dimensions exactly, but a somewhat smaller turbine with L_d/D = 0.25 and $(R_e - R_r)/D$ = 0.125 still achieved the larger C_{Pmax} value of 1.43.

3.2.3 Small Duct Limits

Substantial augmentation was found in the previous study even at the smallest sizes, albeit only as limiting values; nevertheless, small ducts with modest augmentations may be a path to economic feasibility. Three such ducts were tested here, of equal

cylinder length and rim height and with sizes given as a percentage of the rotor diameter. Discretisation convergence was good, as shown in Table 3.6, while the results in Table 3.7 show that appreciable augmentation remained despite the reduction in size. While these are again only limiting values, there may be sufficient margin that a real ducted turbine of this size could achieve augmentation.

Table 3.6: Change in results with finer discretisation for right angled shapes with a size of 0.5% and 5% of rotor diameter. Base last duct panel length = $0.0003125D$ and base expanding wake length = $8D$.

	% Difference with			
	Halved Panel Length		Doubled Wake Length	
	0.5% Shape	5% Shape	0.5% Shape	5% Shape
C_{Pmax}	-0.24	-0.23	-0.01	-0.01
C_{Topt}	-0.21	-0.18	-0.03	-0.04

Table 3.7: Percentage change in maximum power and optimum rotor loading coefficients from their bare rotor values with a right angled duct of varied size.

% Change from Bare Rotor of	0.5% Shape	2.5% Shape	5% Shape
C_{Pmax}	4.7	23.0	45.6
C_{Topt}	-1.9	-4.4	-5.9

3.2.4 Small Flanges

A small section of duct at a right angle to the free stream need not form part of a right angled duct: it can be applied as a flange to a duct of any shape. Three flanges, with heights ranging from 0.5% of rotor diameter to 5%, were applied to the duct in Figure 3.20 in order to assess this approach. Table 3.8 indicates that good discretisation convergence was achieved, while Table 3.9 shows that the flange increased performance more than right angled ducts of the same size and that flange height was an important parameter.

Table 3.8: Change in results with finer discretisation for flange test duct shapes, where discretisation was changed from last duct panel length = $0.000625D$ and expanding wake = $8D$.

	% Difference with					
	Halved Panel Length			Doubled Wake Length		
Flange Size (% of D):	None	0.5%	5%	None	0.5%	5%
C_{Pmax}	-0.28	-0.39	-0.30	-0.01	-0.02	-0.03
C_{Topt}	-0.31	-0.22	-0.27	-0.05	-0.07	-0.12

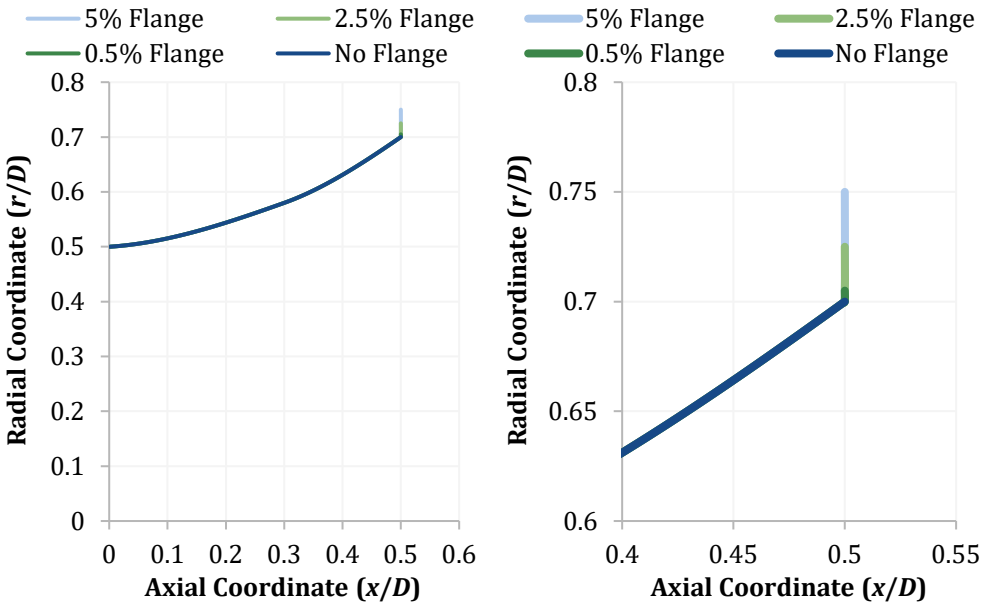

Figure 3.20: Duct shapes used in the flange study, with a detail view of the duct trailing edge on the right.

Table 3.9: Percentage change in C_{Pmax} and C_{Topt} from the duct without a flange as the flange size is varied.

% Change from No Flange of	0.5% Shape	2.5% Shape	5% Shape
C_{Pmax}	14.2	34.1	51.7
C_{Topt}	0.2	0.4	0.5

3.3 Applicability to Real Ducted Turbines

3.3.1 Camber Line Best Matches a Thick Duct

A zero thickness duct wall is a significant assumption in this work; while designs with little thickness do exist [41, 177], the applicability of the thin walled results to rather thicker designs [113, 139] must be tested. As a first step, this section identifies the thin shape that best estimates mass flow for the 8% thick aerofoil shown on the left of Figure 3.21. The candidate thin shapes are shown on the right of the figure, and included the camber line translated radially to maintain the thick duct's rotor area.

Thick ducts were modelled using ANSYS Fluent in an inviscid mode, and thin ducts using the panel method code. While using two different models is not ideal, Section 2.2.6 found they agreed to within 1.7% for power and 5% for drag. Discretisation convergence tests in Table 3.10 show a largest change in mass flow of 0.87% at C_T = 0.95 and 0.14% otherwise for the thin shapes, while discretisation convergence for all thick shapes used in this section and the next is given by Table 3.11 and Table 3.12 for thicknesses of 2% and 10%.

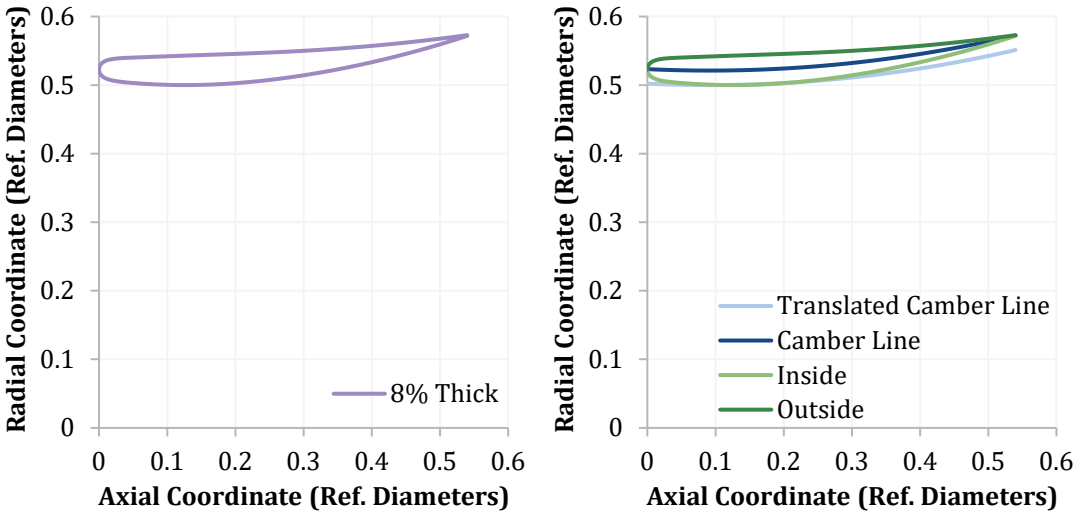

Figure 3.21: Coordinates for the 8% thick duct and the thin ducts based on it, where the reference diameter is the thick duct's rotor diameter.

Table 3.10: Change in results with finer discretisation for the thin duct shapes. Discretisation was changed from last duct panel length = 0.0014D and expanding wake length = 8.6D for the Translated Camber Line and Inside Surface ducts, 0.0013D and 8.3D for the Actual Camber Line duct, and 0.0013D and 8.4D for the outside surface duct.

	% Difference in $\dot{m}$ with					
	Halved Panel Length			Doubled Wake Length		
	$C_T = 0$	C_{Topt}	$C_T = 0.95$	$C_T = 0$	C_{Topt}	$C_T = 0.95$
Translated Camber Line	-0.11	-0.08	-0.72	0.00	0.00	-0.03
Actual Camber Line	-0.10	-0.08	-0.69	0.00	0.00	-0.03
Inside Surface	-0.06	-0.14	-0.80	0.00	0.00	-0.04
Outside Surface	-0.14	-0.12	-0.87	0.00	0.00	-0.02

Table 3.11: Discretisation error estimates for 2% thick duct Fluent simulations, calculated from simulations with 152,000, 241,000, and 470,000 cells.

C_T	0	0.15	0.3	0.45	0.6	0.75	8/9	0.95
Approximate Relative Error (%)								
$\dot{m}$	0.1	0.1	0.0	0.1	0.1	0.1	0.3	0.6
F_D	-	2.3	0.6	0.3	0.3	0.9	9.8	6.7
Γ_d	0.1	-	-	-	-	-	-	-
Grid Convergence Index (%)								
$\dot{m}$	0.0	0.0	0.0	0.1	0.0	0.0	1.1	1.5
F_D	-	0.7	0.2	0.1	0.0	0.1	4.2	167.2
Γ_d	0.0	-	-	-	-	-	-	-

Table 3.12: Discretisation error estimates for 10% thick duct Fluent simulations, calculated from simulations with 84,000, 157,000, and 354,000 cells.

C_T	0	0.15	0.3	0.45	0.6	0.75	8/9	0.95
Approximate Relative Error (%)								
$\dot{m}$	0.4	0.3	0.2	0.0	0.1	0.3	0.7	1.3
F_D	-	3.8	1.4	1.0	1.3	3.7	46.2	10.6
Γ_d	0.0	-	-	-	-	-	-	-
Grid Convergence Index (%)								
$\dot{m}$	0.1	0.1	0.0	0.0	0.1	8.8	0.8	0.4
F_D	-	1.2	0.9	10.3	1.6	50.9	576.3	41.4
Γ_d	0.0	-	-	-	-	-	-	-

Error estimates for mass flow and circulation results from Fluent were below 1.5% for the thick ducts, excepting minor oscillatory discretisation convergence at C_T = 0.75 for the 10% duct. Caution must be applied to drag at high loadings, however, although note that drag passed through zero near C_T = 8/9 for the 10% duct. The change with doubled domain size was ≤ 1% for mass flow and circulation, as Table 3.13 indicates, with some further concern for drag.

Table 3.13: Change in Fluent results for 2% and 10% thick ducts with doubled domain length and radius.

	% Difference with Doubled Domain Dimensions			
	2% Duct		**10% Duct**	
	C_T **= 0**	C_T **= 0.95**	C_T **= 0**	C_T **= 0.95**
$\dot{m}$	0.0	-0.4	-0.5	1.0
F_D	-	1.6	-	4.8
Γ_d	-0.1	-	-0.6	-

Care is needed when assessing the results because of the effect thickness had on rotor area. For example, consider the dimensionless mass flow in Equation 3.3.

$$\text{Dimensioness Mass Flow} = \frac{\dot{m}}{\rho A_r u_\infty} = \frac{u_r}{u_\infty} \qquad \textbf{Equation 3.3}$$

Even where the mass flows through two ducts are equal, the dimensionless mass flows will differ if the rotor areas are different. Figure 3.22 compares the thin and thick ducts on a dimensionless basis, while Figure 3.23 gives dimensionless and dimensional results as a percentage difference from the thick duct. There was no single thin shape that provided the closest match in all cases, and only the outside surface was never the best option. However, one of the camber line options was almost always closest, including around the approximate value of 0.75 for C_{Topt}, and actual camber line has the substantial advantage of not changing shape with thickness.

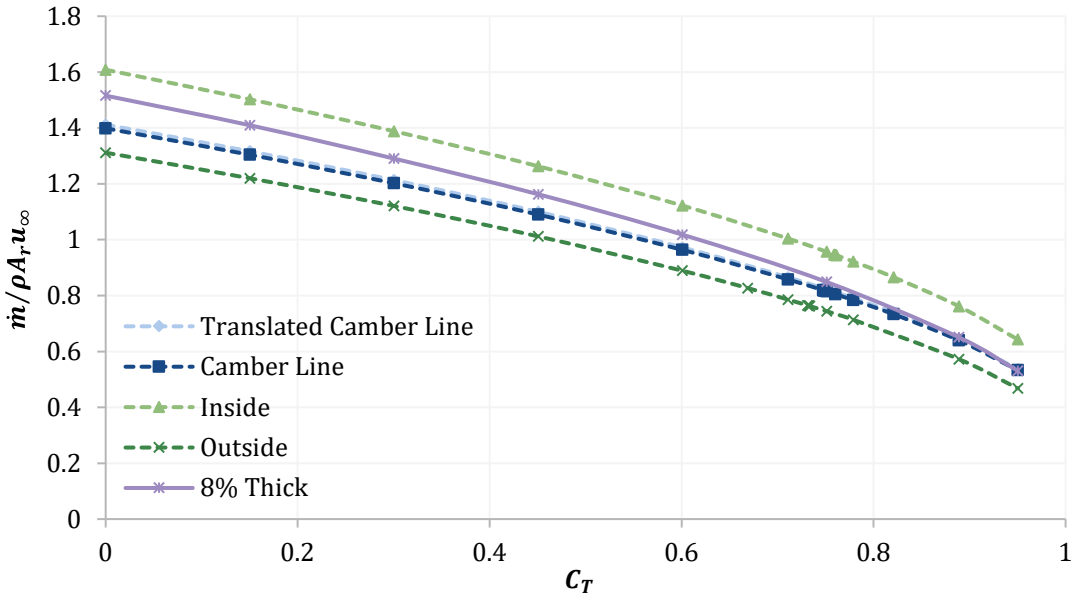

Figure 3.22: Dimensionless mass flow $\dot{m}/\rho A_r u_\infty$ for the translated and actual camber line ducts, the inside surface duct, and the thick duct the others were based on.

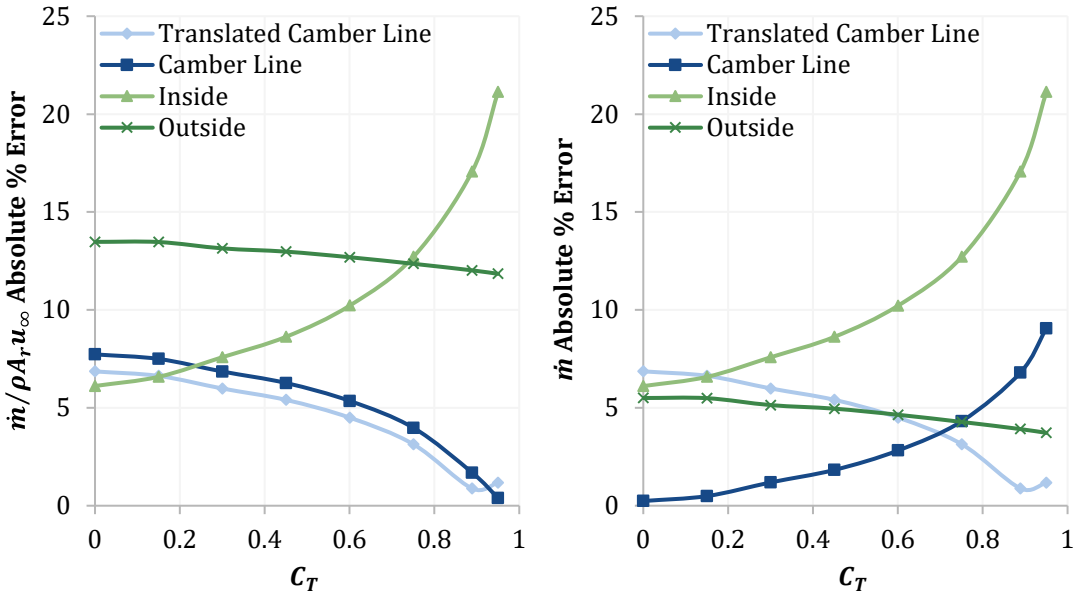

Figure 3.23: Absolute percentage difference from the thick duct results for dimensionless mass flow $\dot{m}/\rho A_r u_\infty$ and actual mass flow $\dot{m}$ through the thin ducts. $\dot{m}/\rho A_r u_\infty$ and C_P differences are equal, while the same is true of $\dot{m}$ and P.

3.3.2 Thin Ducts Can Approximate Thick Ducts

Taking the camber line as the base thin shape, this section assesses the accuracy of the thin duct approximation to ducts of thickness between 2% and 10%. NACA 4 digit thickness profiles were added to the fixed camber line with some additional thickness near the leading edge, as in the previous section, and the thin shape reached C_{Pmax} = 0.61 at C_T = 0.75 and C_D = 0.07. Discretisation convergence not discussed previously for the thin shape is shown in Table 3.14, with only drag at C_T = 0.95 exceeding a 1% change with increased discretisation.

Table 3.14: Change in results with finer discretisation for the thin duct shape, where discretisation was changed from last duct panel length = 0.0013D and expanding wake = 8.3D.

	% Difference with					
	Halved Panel Length			Doubled Wake Length		
	C_T = 0	C_{Topt}	C_T = 0.95	C_T = 0	C_{Topt}	C_T = 0.95
F_D	-	-0.79	3.71	-	-0.01	0.12
Γ_d	-0.12	-	-	0.00	-	-

The impact of changes in rotor area due to thickness is illustrated in Figure 3.24, which shows that thickness broadly increased dimensionless mass flow despite decreasing the actual mass flow. These changes are equal to those for power coefficient and power respectively. Both measures of drag increased in Figure 3.25, however, with differences large enough to partly alleviate the discretisation concerns. Note the reversal at high rotor loadings is misleading: the value of drag became negative, with thickness continuing to act in the same direction to make it less negative.

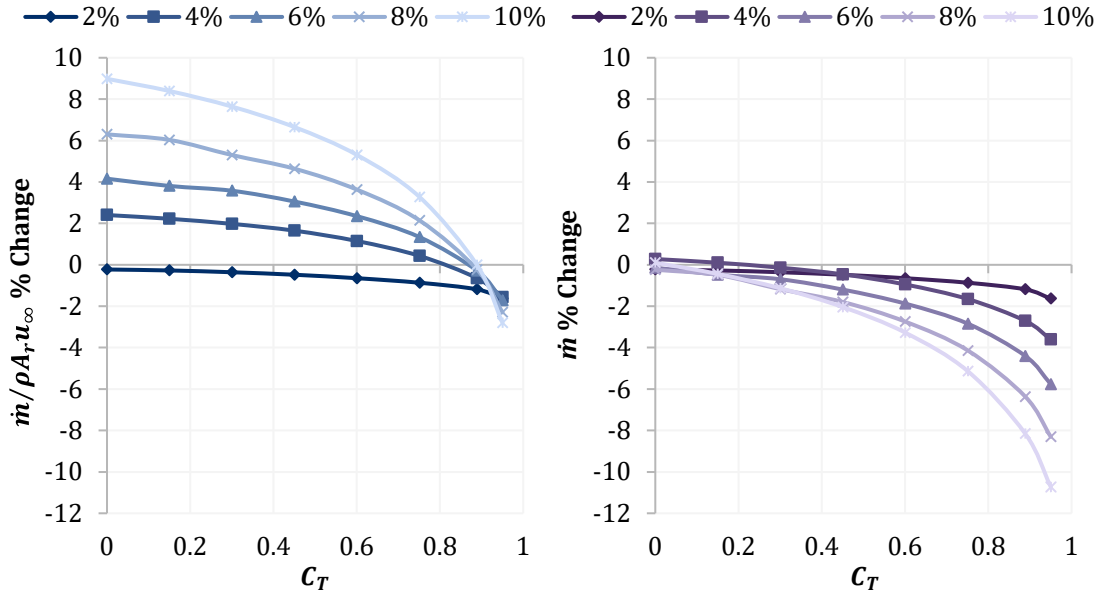

Figure 3.24: Percentage change in dimensionless mass flow rate $\dot{m}/\rho A_r u_\infty$ and actual mass flow rate $\dot{m}$ compared to a thin duct, for ducts with thicknesses of 2% to 10%.

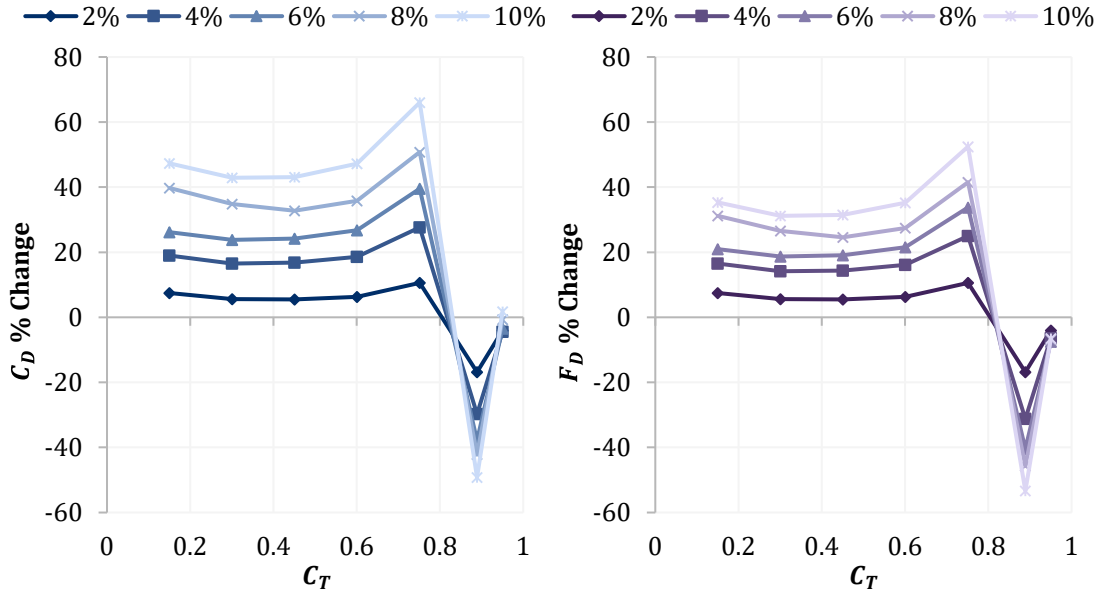

Figure 3.25: Percentage change in dimensionless duct drag C_D and actual duct drag F_D compared to a thin duct, for ducts with thicknesses of 2% to 10%.

Changes in the dimensionless results can also be thought of as the change in dimensional results where the duct has been scaled to hold the rotor area constant, in contrast with the actual dimensional results where the rotor area decreases with thickness. A third option exists for investigating the influence of thickness that is more appropriate for economic comparisons: a duct scaled to hold the rated power constant. It was not possible to correctly carry out this comparison here, as C_{Pmax} was unknown for the thick ducts, but approximating by scaling the ducts to achieve equal power at C_T = 0.75 gave Figure 3.26. These results fell between the other two approaches.

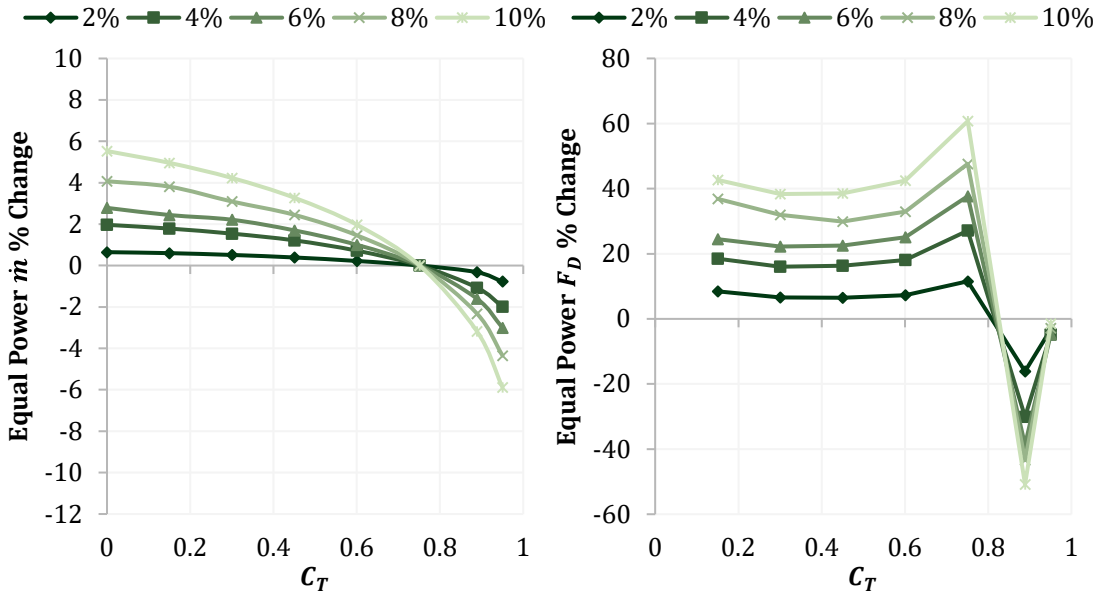

Figure 3.26: Percentage change in actual mass flow $\dot{m}$ and duct drag F_D compared to a thin duct, for ducts with thicknesses of 2% to 10% and where the thick ducts have been scaled to provide the same power as the thin duct at C_T = 0.75.

Figure 3.27 looks at mass flow for $C_T = 0$, as the influence of thickness was unclear from Figure 3.24. No clear impact existed on the zero loading mass flow, with the scatter perhaps numerical error, while somewhat larger errors prevented the dimensionless mass flow passing through zero. Duct bound circulation, which could not be calculated at $C_T > 0$ for the thick ducts, is given by Figure 3.28. Both measures increased with thickness, despite no change in mass flow, and possibly varied linearly.

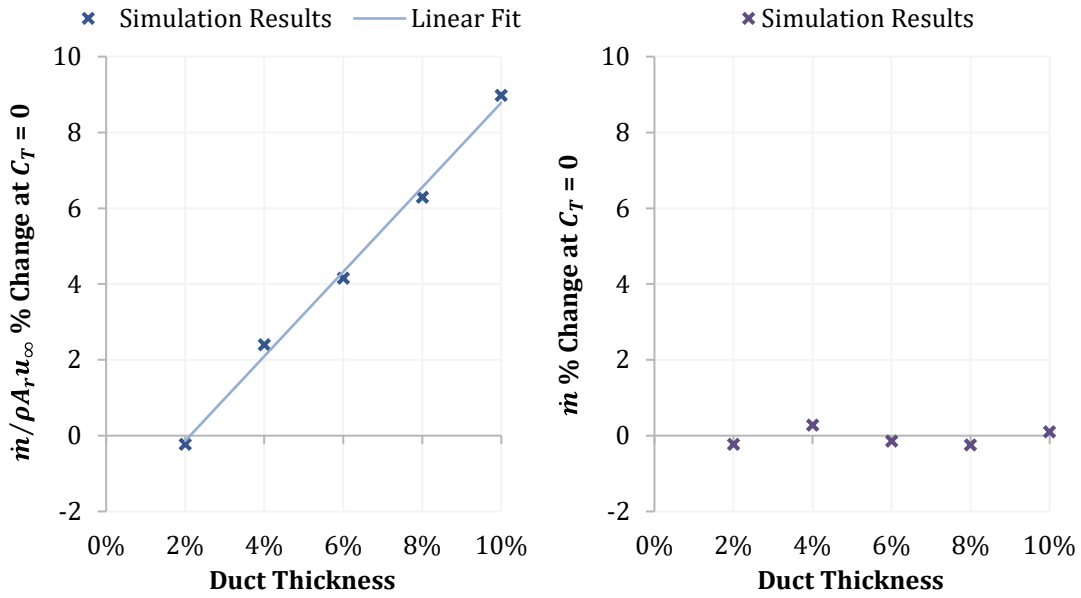

Figure 3.27: Percentage change in dimensionless mass flow rate $\dot{m}/\rho A_r u_\infty$ and actual mass flow rate $\dot{m}$ with duct thickness, at $C_T = 0$.

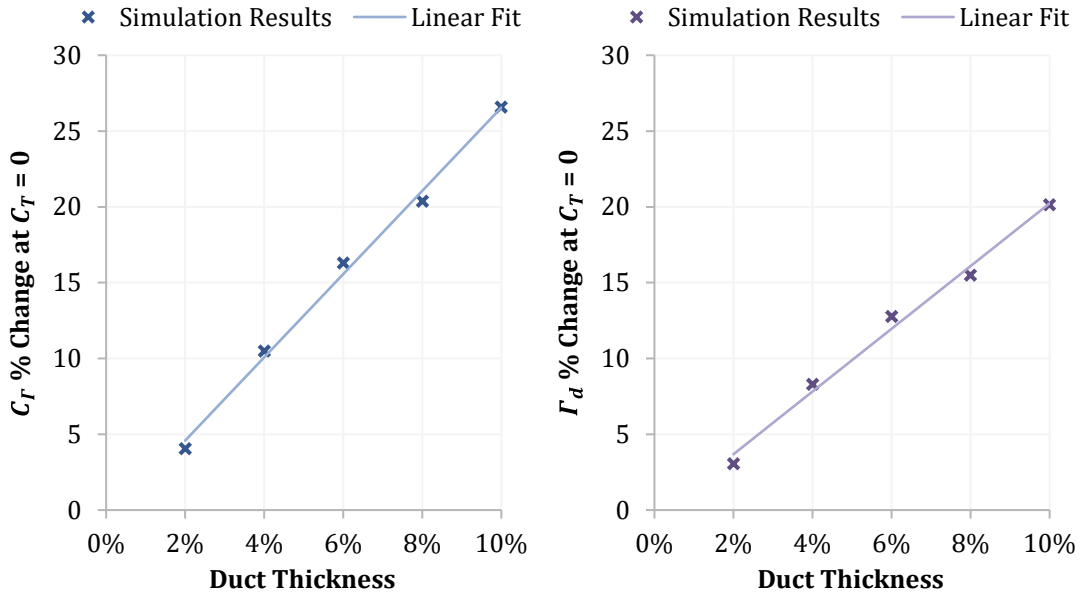

Figure 3.28: Percentage change in dimensionless circulation C_Γ and actual circulation Γ_d with duct thickness, at $C_T = 0$. Circulation was made dimensionless with rotor diameter, but note that the percentage change in actual circulation is equal here to the change in circulation made dimensionless with duct or chord length.

This investigation shows that thickness does influence inviscid ducted turbine performance, but the impact on mass flow was less than 6% for thicknesses up to 6% of chord. A thin duct may therefore be a reasonable approximation for ducts with moderate thickness, although not for drag where much larger differences existed. While increasing thickness did not appear to be advantageous in inviscid flow, it may be beneficial in viscous flow to reduce the chance of separation near the leading edge.

3.3.3 Inlets Influence Performance

Another difference between real ducts and the designs Sections 3.1 and 3.2 is the absence of a contracting inlet section, although the review in Section 1.5.3 identified that an inlet section would not be expected to affect performance in inviscid flow. That theory was tested for C_{Topt} and C_{Pmax} by combining the three diffuser sections in Figure 3.29 with the inlet sections illustrated by Figure 3.30 into a range of duct shapes. Discretisation convergence was good for the diffuser sections alone, with a maximum change of 0.92% reported in Table 3.15, and was improved in most cases tested with the addition of an inlet.

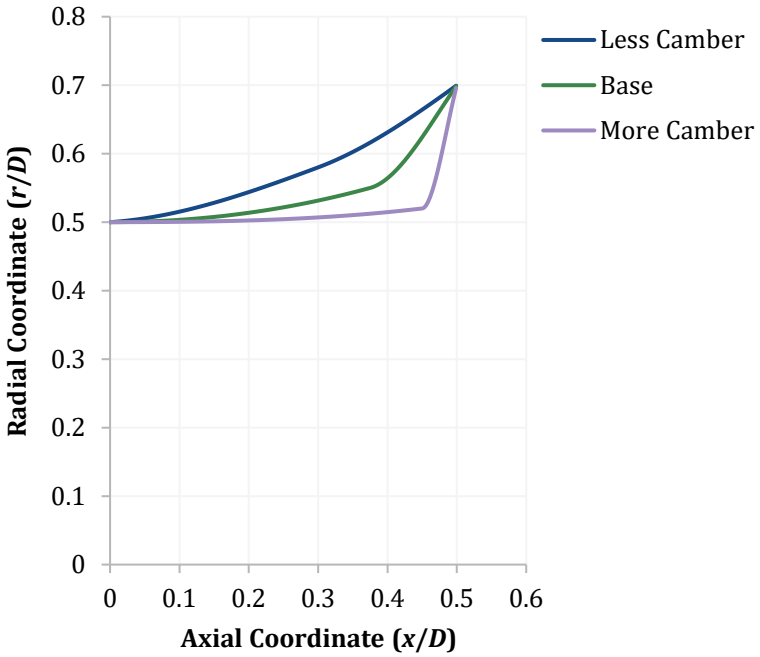

Figure 3.29: Coordinates for the diffuser sections to which inlets were attached.

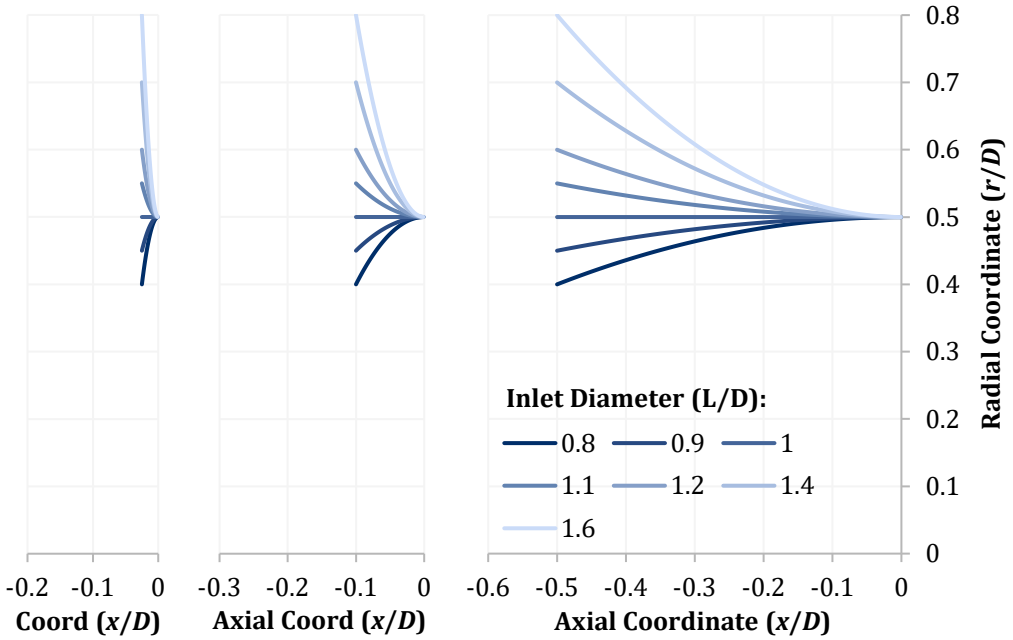

Figure 3.30: Coordinates for the inlet sections of length $0.025D$, $0.1D$, and $0.5D$.

Table 3.15: Change in C_{Pmax} and C_{Topt} with a finer discretisation for the inlet study shapes. Discretisation was changed from a last duct panel length of $0.005D$ and an expanding wake section of $8D$.

Duct Shape			Less Camber	Base	More Camber	Base	Base	Base	Base
Inlet Section Length (L/D)			0	0	0	0.025	0.025	0.5	0.5
Inlet Diameter (L/D)			1	1	1	0.8	1.6	0.8	1.6
% Difference with	**Halved Panel Length**	C_{Pmax}	-0.86	-0.80	-0.92	-0.41	0.02	-0.36	-0.37
		C_{Topt}	-0.02	-0.01	-0.02	-0.28	-0.01	-0.02	-0.01
	Doubled Wake Length	C_{Pmax}	-0.20	-0.21	-0.11	-0.02	-0.28	-0.29	-0.23
		C_{Topt}	-0.08	-0.05	-0.09	-0.08	-0.03	-0.09	0.00

In general, Figure 3.31 to Figure 3.33 show that increases in inlet diameter led to a reduction in C_{Pmax}, including for inlets smaller than the rotor, while longer inlet sections increased performance. As the camber and hence performance of the bare diffuser sections increased, so did the performance of the inlets. With increased inlet diameter came a reduction in optimum loading in Figure 3.34 to Figure 3.36, but the behaviour with increased inlet section length was more complex and depended on the relative size of the inlet and exit diameters.

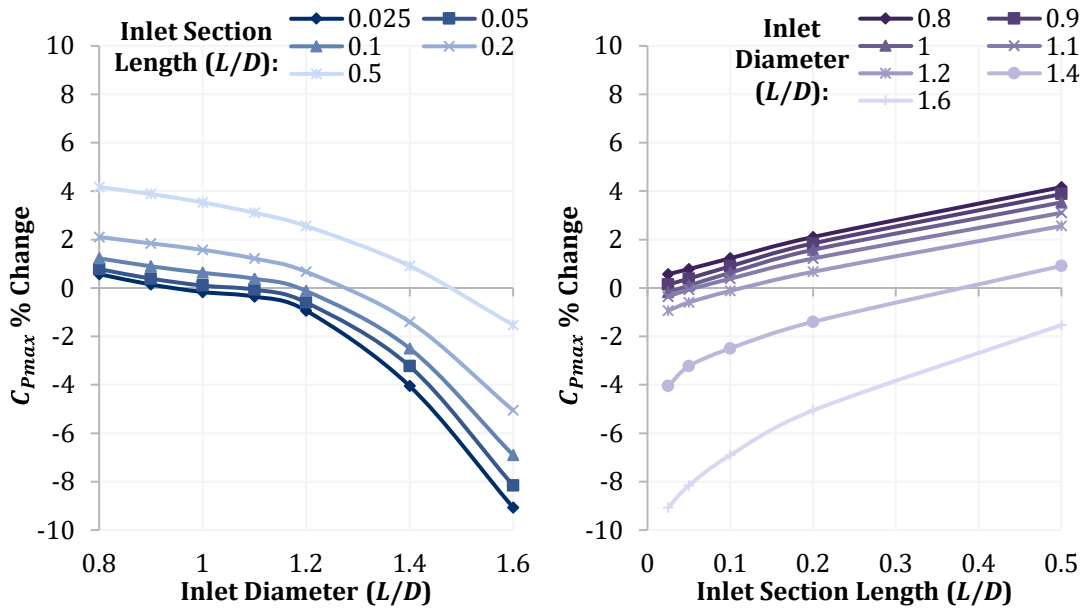

Figure 3.31: Influence of inlet size on C_{Pmax} when combined with Less Camber diffuser section.

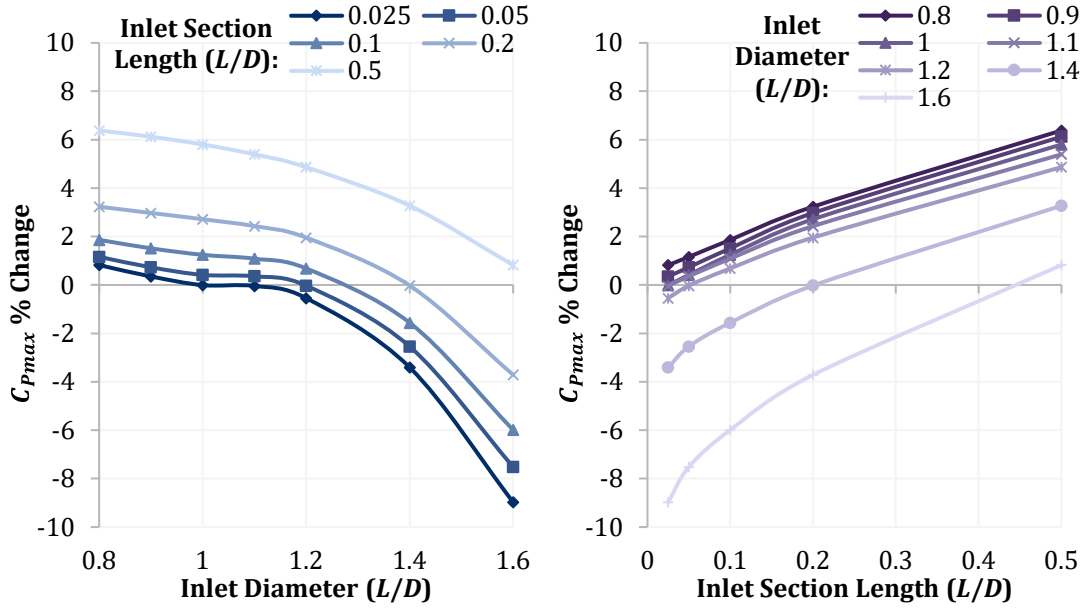

Figure 3.32: Influence of inlet size on C_{Pmax} when combined with Base diffuser section.

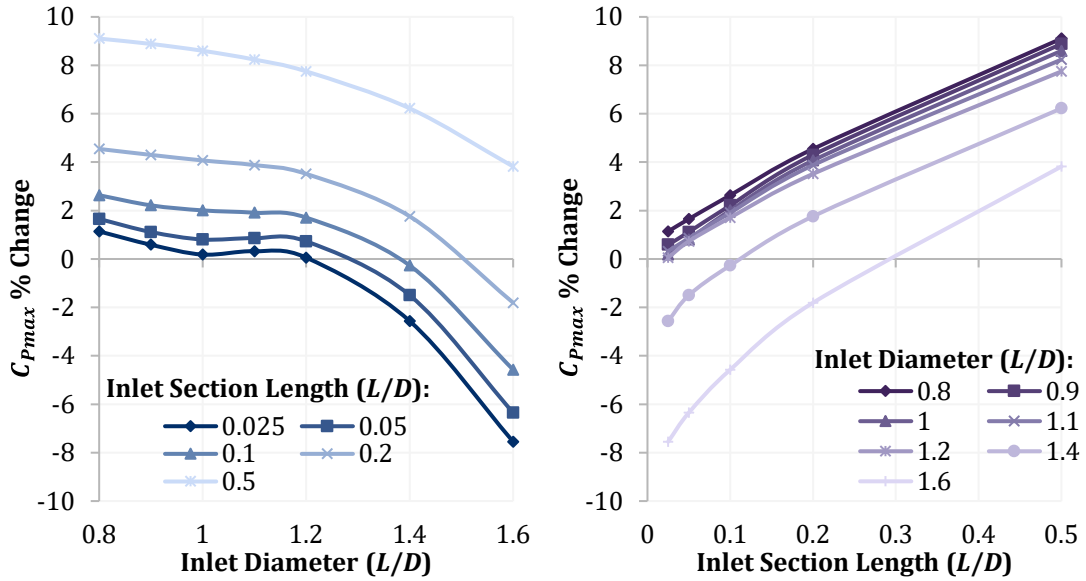

Figure 3.33: Influence of inlet size on C_{Pmax} when combined with More Camber diffuser section.

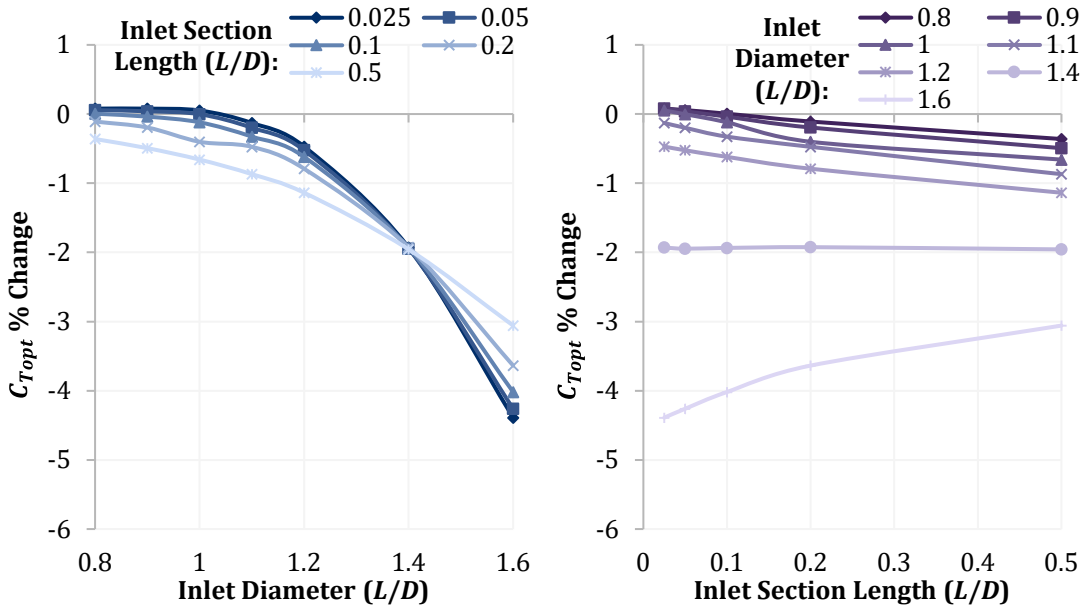

Figure 3.34: Influence of inlet size on C_{Topt} when combined with Less Camber diffuser section.

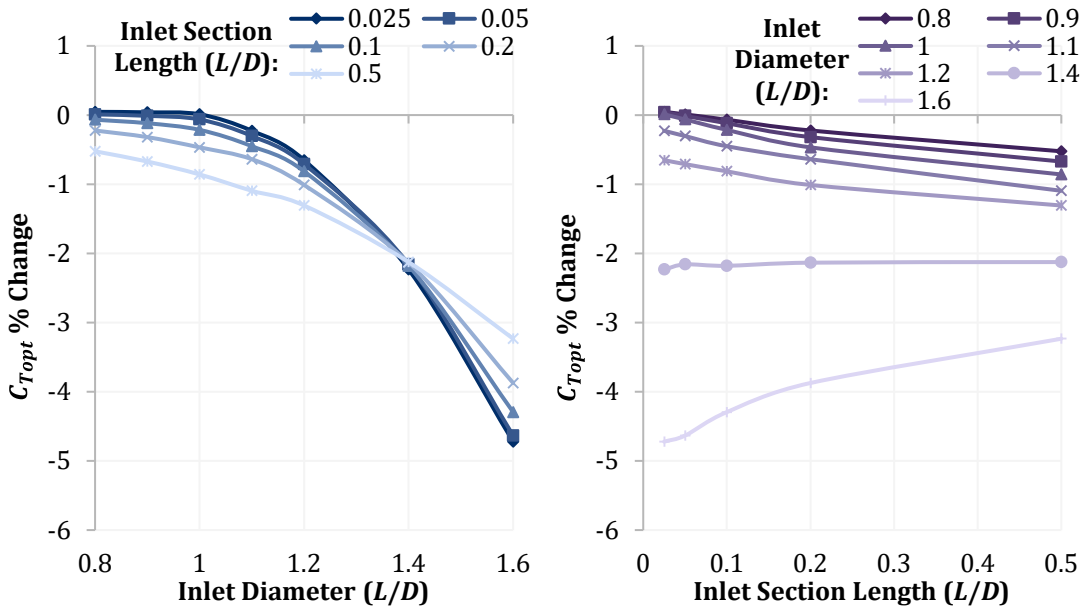

Figure 3.35: Influence of inlet size on C_{Topt} when combined with Base diffuser section.

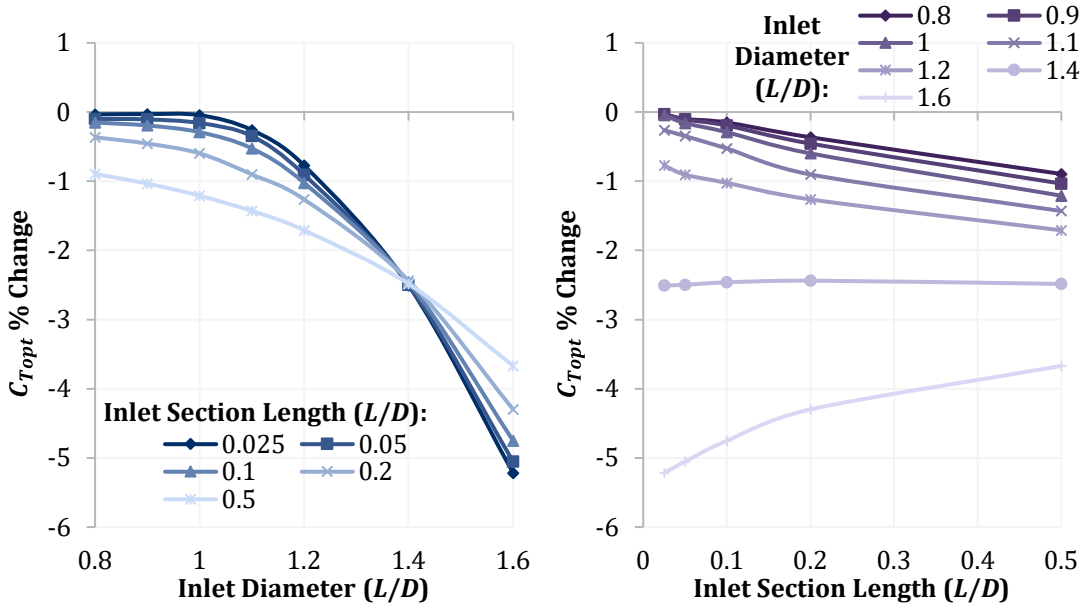

Figure 3.36: Influence of inlet size on C_{Topt} when combined with More Camber diffuser section.

Differences with the addition of an inlet section of up to 9% for C_{Pmax} and 5% for C_{Topt} were found for these designs, with the influence of inlets reducing substantially when restricted to more reasonable dimensions. The results here therefore support an approximation of inlet design not affecting performance outside of viscous effects. However, it is an approximation only: the theoretically correct point of view is that inlet section design affects the inviscid component of ducted turbine performance.

3.3.4 Agreement between Viscous and Inviscid Performance

Examining the underlying inviscid performance of ducted turbines has been valuable throughout this chapter, but inviscid modelling may also predict viscous performance reasonably accurately when separation is avoided. This result was demonstrated using a 4-digit NACA aerofoil [178], with 5% camber maximum at 40% of chord, 4% and 0% thickness for the viscous and inviscid results respectively, and a slightly thickened leading edge in the viscous case. The aerofoils were rotated to between 5° and 35° from axial before being scaled and radially translated to maintain a duct length to inlet diameter ratio of 0.4, and were modelled at C_T = 0.75.

Viscous results were obtained using ANSYS Fluent 15.0, the k-ω turbulence model and the simulation setup described in Section 2.3.1, with Reynolds numbers of around 3×10^6 based on duct chord length. Discretisation error, shown in Table 3.16, and domain size convergence, shown in Table 3.17, were generally reasonable. Concerning grid convergence index values did exist, however, for F_D with the 25° duct and $\dot{m}$ with the 35° duct. Relatively large percentage changes occurred for drag in the thin 5° duct, shown in Table 3.18, but the magnitude of the drag was very small at less than 4% of that for the 35° duct.

Table 3.16: Discretisation error estimates for 5° to 35° duct wall Fluent simulations, calculated from simulations with 157,000 to 174,000, 370,000 to 408,000, and 875,000 to 941,000 cells. The number of cells differed in each discretisation stage between ducts.

Duct Wall Angle	5°	15°	25°	35°
Approximate Relative Error (%)				
$\dot{m}$	0.04	0.00	1.43	1.05
F_D	0.07	0.03	0.44	0.16
Grid Convergence Index (%)				
$\dot{m}$	0.06	0.00	0.78	6.96
F_D	0.00	0.01	7.74	0.26

Table 3.17: Change in Fluent results for 5° to 35° wall ducts with doubled domain length and radius.

	% Difference with Doubled Domain Dimensions			
Duct Wall Angle	5°	15°	25°	35°
$\dot{m}$	-0.32	0.15	-0.12	-0.28
F_D	-1.82	-0.64	-1.03	-1.25

Table 3.18: Change in results with finer discretisation for the thin walled 5° and 35° ducts in inviscid flow. Base last duct panel length = $0.00125D$ and base expanding wake length = $8D$.

	% Difference with			
	Halved Panel Length		Doubled Wake Length	
	5° Shape	35° Shape	5° Shape	35° Shape
$\dot{m}$	-0.30	-0.51	-0.31	-0.24
F_D	-7.04	-0.34	-6.36	-0.33

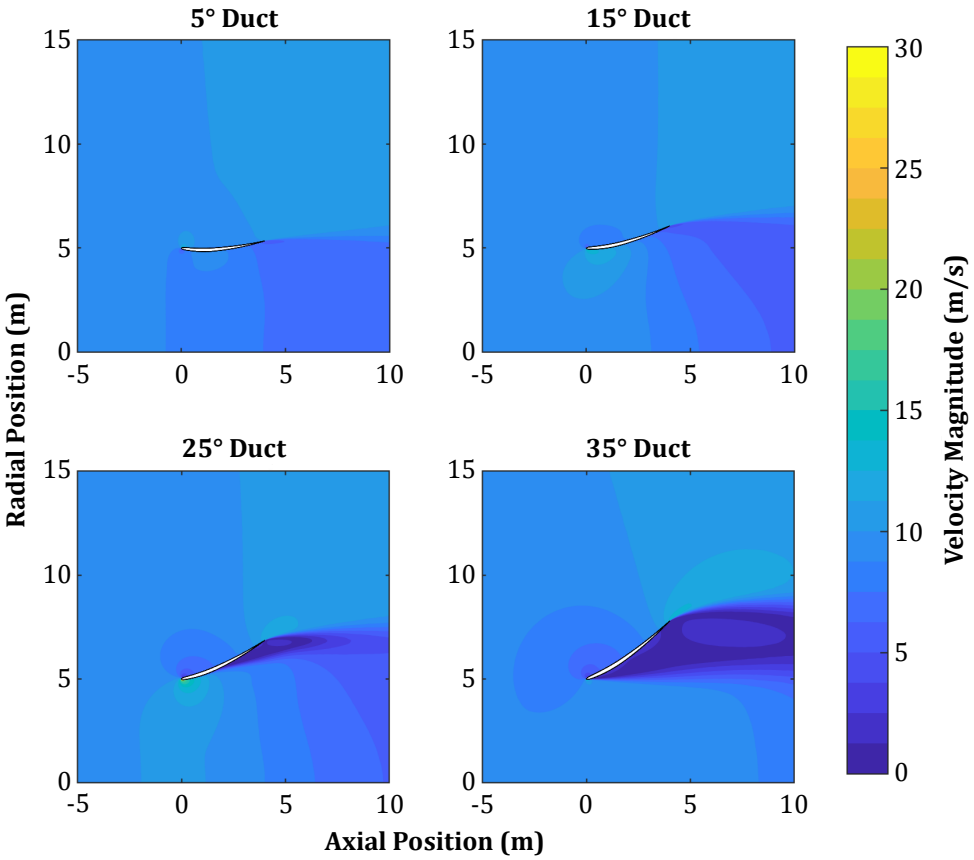

Figure 3.37: Contours of velocity magnitude for ducts with wall angles of 5° to 35° in viscous flow.

Velocity magnitude contours in Figure 3.37 show that separated flow was apparent by the 25° duct and encompassed the entire inside surface at 35°. These are not predictions of the actual flow through the ducts modelled: rotor swirl was neglected, which reduces separation [79], and the results were not validated. The comparison is between duct shapes with particular levels of separation, not a particular duct shape in inviscid and viscous flow.

As the duct wall thicknesses were not equal, dimensionless and dimensional results were again different. Comparative power was used to compare dimensional results, calculated using the fixed reference A_{ref} of the 5° duct's rotor area and Equation 3.4.

$$\text{Comparative Power} = \frac{P}{{}^{1}/_{2}\,\rho A_{ref} u_{\infty}^{3}} \qquad \textbf{Equation 3.4}$$

Reasonable agreement between viscous and inviscid results is visible in Figure 3.38 where separation was absent, with an apparent reduction in gradient for the viscous curve in the no separation region. The inviscid and viscous drags were surprisingly close in separated flow, as shown in Figure 3.39, but without more evidence this is likely only coincidence. Inviscid drag was within 13% of viscous at 15°, but rose above 50% by 5°. The inviscid power coefficient performed better, being within 10% of the viscous values for attached flow, suggesting that inviscid modelling may be directly relevant to ducted turbine design.

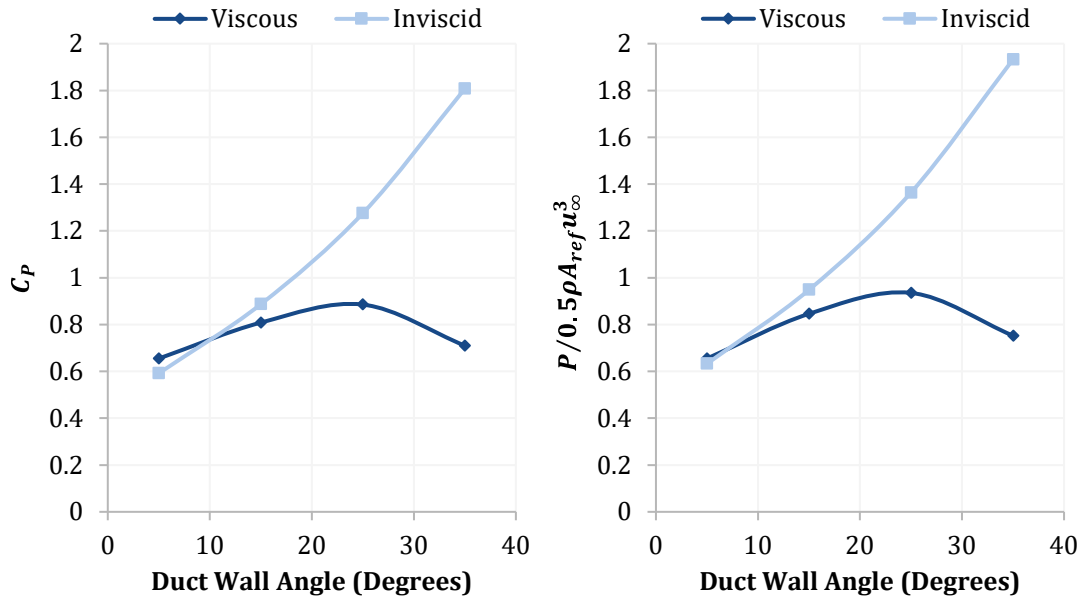

Figure 3.38: Variation of dimensionless power C_P and comparative power $P/0.5\rho A_{ref} u_{\infty}^{3}$ with duct wall angle, for viscous and inviscid flow.

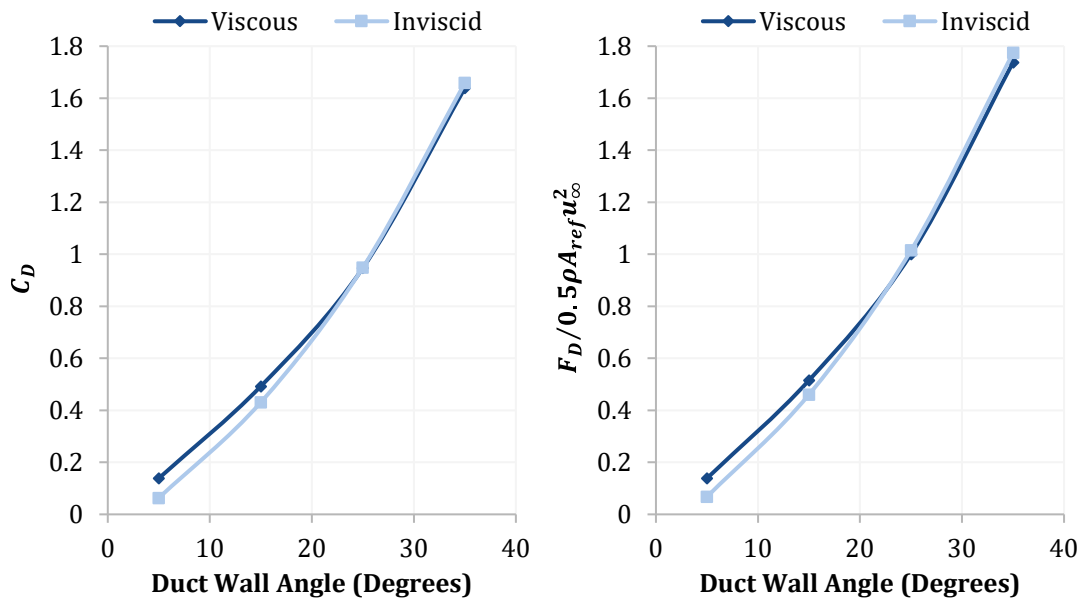

Figure 3.39: Variation of dimensionless drag C_D and comparative drag $F_D/0.5\rho A_{ref}u_\infty^2$ with duct wall angle, for viscous and inviscid flow.

3.4 Conceptual Model: A Diffuser or an Aerofoil?

Each of the investigations in this chapter has had particular theoretical or practical implications, but they can also be drawn together to address a question from Section 1.6: does an aerofoil or a diffuser make a better conceptual model for a ducted turbine? The results do not provide a clear answer, but do contain various hints when considered in terms of how aerofoils and diffusers could be expected to behave.

This topic was touched on in Section 3.1.2, which considered the influence of shape on performance and concluded that both conceptual models are consistent with the results. Increases in camber led to increased circulation [69] and hence velocity from the aerofoil point of view, while increased exit angle forced greater expansion of the flow thereby reducing exit pressure and increasing augmentation for the diffuser concept.

The viscous results in Section 3.3.4 are also well explained by both viewpoints. The reduced mass flow gradient with duct wall angle in viscous flow is consistent with increasing viscous losses, and with the presence of a boundary layer changing an aerofoil's effective shape to reduce performance [179].

A more speculative approach is needed to explain the reduction in augmentation ratio with loading in Section 3.1.5. Exit angle alone cannot explain the result, but the difference between exit angle and the expansion of an unaugmented flow might. An aerofoil explanation could be the rotor causing a reduction in the velocity magnitude

local to the duct and a reduction in the effective wall angle of attack, with a consequent reduction in duct circulation. This explanation will be considered further in Chapter 7.

The expectation from the diffuser conceptual model that performance should be a function of duct exit angle did not correspond to results from the right angle, small flange, and thickness studies in Sections 3.2.2, 3.2.4, and 3.3.1 respectively. Performance varied in the right angle results even though exit angle and all the other diffuser parameters identified by Phillips [4] and Shives and Crawford [57] were fixed, and also in the flange size results where the only change in the diffuser parameters were minor exit area ratio variations. Finally, Phillips identified that exit angle should be measured on a duct's external surface. However, adding thickness reduced this angle without a corresponding reduction in mass flow or velocity at C_T = 0.

All three of these results are consistent with aerofoil behaviour. Performance was unique for camber with fixed length and area ratios, and the percentage lift increase from Gurney flaps [180] is comparable to the change in mass flow here. Circulation at C_T = 0 increased linearly with thickness, matching expectations from a Joukowski transformation [179] of an aerofoil and explaining the increased velocity. Further, the identification of the camber line as the best thin approximation of a thick duct wall supports the aerofoil point of view.

Neither length nor inlet sections were expected to affect inviscid diffuser performance from the literature surveyed in Section 1.5.3, but were shown to do exactly that in Sections 3.2.2 and 3.3.3 where the other diffuser parameters were held constant. It is not clear why either would force a greater flow expansion, but both results are expected from aerofoil performance. Adding inlets modified the wall angle of attack and chord, as did changing the length of the duct, leading to changes in circulation.

Both conceptual models are imperfect when their direct influence on augmentation is examined: general associations were found between augmentation and both exit pressure and circulation in Section 3.1.6, but they were not single valued. Both performed roughly as well as each other despite more flaws in the diffuser viewpoint, suggesting a closer connection between aerofoil parameters and circulation than between diffuser parameters and exit pressure. Although it did not provide the correct intuition in every case, however, the aerofoil conceptual model better matched the numerical results across the full range of studies and may be more helpful in practice.

3.5 Summary

A number of useful conclusions were drawn from inviscid modelling of a set of ducted turbines, where the area and length ratios were held constant. Duct shape had a significant impact: power coefficient more than doubled from the least to most cambered duct, with even larger changes for exit pressure coefficient and the radial variation of exit pressure. The augmentation occurred due to an increased flow rate, and decreased with rotor loading as the ducts became less effective. C_{Topt} therefore dropped by between 10% and 20% from 8/9, and C_{Pmax} was not single valued for C_{Topt}.

These ducted turbines were also capable of exceeding the Betz limit, even when calculated on the basis of exit area. Indeed, the largest power coefficient based on exit area was 1.04. However, the ducted turbines actually captured a smaller proportion of the available power than a bare actuator disc, and $C_P > 1$ only indicates an abundance of available power combined with a power coefficient definition based on the power available to a bare rotor.

Within the constraints of fixed length and fixed inlet and outlet radii, with the throat at the inlet, the best performing shape was found to be a right angle. Even for such a duct sized at 2.5% of rotor diameter, C_{Pmax} was raised by 23%. Adding a radial rim of the same size to an existing duct increased C_{Pmax} by 34%. Performance would likely reduce in viscous flow, but these results still have significance if taken as limiting values. Comparing less extreme shapes, the inviscid power coefficient was within 10% of the viscous value for attached flow.

Adding thickness to a thin walled duct broadly increased dimensionless mass flow and power coefficient despite decreasing the actual mass flow and power. However, differences were within 6% for a 6% thick duct; a thin duct may still serve as a reasonable approximation for a thick one. Setting such a thin duct as the inside or outside surface of a thick duct gave worse agreement than using the camber line, but cases were split between the camber line in its natural position and translated to achieve the same rotor area.

An aerofoil appears to make a better conceptual model for a ducted turbine than a diffuser, although neither was perfect. The influence of length and inlet sections on performance did not tie in with diffuser based expectations, and changes in exit angle did not explain some of the shape optimisation, small flange, and thickness results. One further flaw applied to both models in testing their direct influence on augmentation: general associations exited between augmentation and both exit pressure and circulation, but they were not single valued.

4 Chapter

Parameters for Duct Shape

An important part of a conceptual model for ducted turbines is selection of the parameters defining duct shape. Both the aerofoil and diffuser based models are used in this chapter to select sets of geometrical parameters, which are compared on the basis of practicality and whether the actual performance matches expectations. Each approach is examined in turn using results from the inviscid panel method, before a comparison suggests that the aerofoil approach is again superior. Preliminary investigations in the aerofoil section also compare performance measurement stations and various definitions of length to diameter ratio and dimensionless circulation.

4.1 Diffuser Parameters

A set of parameters was selected for the diffuser approach based on those found in the literature in Section 1.5.2, with the thin duct walls modelled giving equal inside and outside exit angles. Duct length was also added as a parameter given the discovery of its influence in Section 3.4. The complete list was therefore: the exit area ratio A_e/A_r, the inlet area ratio A_i/A_r, the duct length ratio L_d/D, and the exit angle θ_e in degrees measured from a point 0.5% along the duct surface from the exit.

Generation of duct geometry followed the process used by Shives & Crawford [57] and Hansen et al [55]. A cylindrical duct of given length was specified, followed by cambering of the duct wall by rotating each point around the upstream end with an angle varying linearly between zero at the inlet and the specified camber angle at the exit. The wall was then rotated as a solid body by the rotation angle, and translated radially to achieve the desired ratio of rotor diameter to initial cylindrical length.

These geometry generation parameters differ substantially from the diffuser parameters that are used to measure the output geometry and thought to control duct performance. An attempt to derive exact relationships between these parameter sets failed, and no reliable way was found to select geometry generation parameters that would give particular diffuser parameters. It was therefore not possible to vary each diffuser parameter in isolation. Geometry generation parameters were instead selected randomly and, similar to Shives and Crawford's approach, a regression analysis was used to estimate the influence of the diffuser parameters.

4.1.1 Regression Models

A set of 800 duct shapes formed the sample to which polynomial relationships were fitted using stepwise least-squares regression. Geometrical limits were set at 0.1 to 1.2 for the cylindrical length ratio, 0° to 30° for the camber angle, and −20° to 20° for the solid rotation angle. Discretisation convergence for shapes with all combinations of these limits is given in Table 4.1, with a 0.75% change exceeded only once in a case of a small valued C_{Pmax}, and the shapes themselves are shown in Figure 4.1. These limits led to the range of diffuser parameters in Table 4.2 for the sample shapes.

Table 4.1: Worst and median magnitude change in result when discretisation was changed for the discretisation checking duct shapes.

	% Difference with			
	Halved Panel Length		Doubled Wake Length	
	Worst	Median	Worst	Median
C_{Pmax}	1.86	0.22	0.24	0.01
C_{Topt}	0.48	0.11	0.71	0.04

Table 4.2: Minimum and maximum values for diffuser parameters in the 800 duct shape regression sample.

	Inlet Area Ratio	Exit Area Ratio	Length Ratio	Exit Angle
Minimum	1	1	0.05	-16.8°
Maximum	2.37	3.54	0.82	74.9°

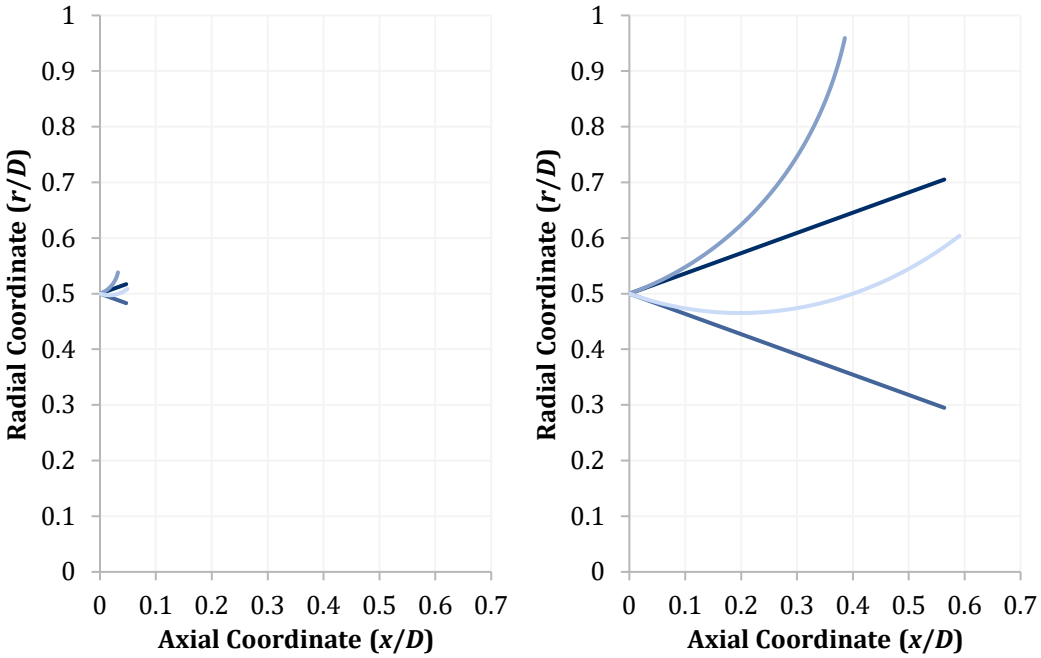

Figure 4.1: Duct shapes at the limiting combinations of the geometry generation parameters. Short and long ducts shown separately for clarity.

Each regression fitting began with linear terms relating the predictor and response variables. An automatic method then added and removed terms, by comparing the model with and without the term in question: a term was included when its coefficient had a statistically significant difference from zero, based on the p-value of an F-statistic [181]. This process continued in a stepwise fashion until no further statistically significant changes were possible or the upper limit on the model terms was reached.

Separate models were fitted with C_{Pmax} and C_{Topt} as the response variable, where the diffuser parameters listed at the start of Section 4.1 were the predictor variables. Two different upper limits on the model terms were applied to give two models each for C_{Pmax} and C_{Topt}: one limited to quadratic terms and one limited to 5th degree polynomial terms, both including interaction terms. All four fits were tested against 220 random validation duct shapes and also against shapes with the geometry generation parameter limits. The fit limited to 5th order terms was selected as superior in both C_{Pmax} and C_{Topt} predictions, as shown in Table 4.3 with more detail for the 5th order fit in Figure 4.2 and Figure 4.3.

Table 4.3: Worst and median magnitude errors from the regression models, for 220 randomly generated validation duct shapes and shapes with the geometry generation parameter limits.

		% Prediction Errors for			
		2nd Order Fit Limit		5th Order Fit Limit	
		Worst	Median	Worst	Median
Validation Shapes	C_{Pmax}	6.67	0.42	0.31	0.04
	C_{Topt}	1.77	0.28	0.25	0.03
Limit Shapes	C_{Pmax}	34.1	1.09	4.71	0.13
	C_{Topt}	9.39	0.70	5.78	0.12

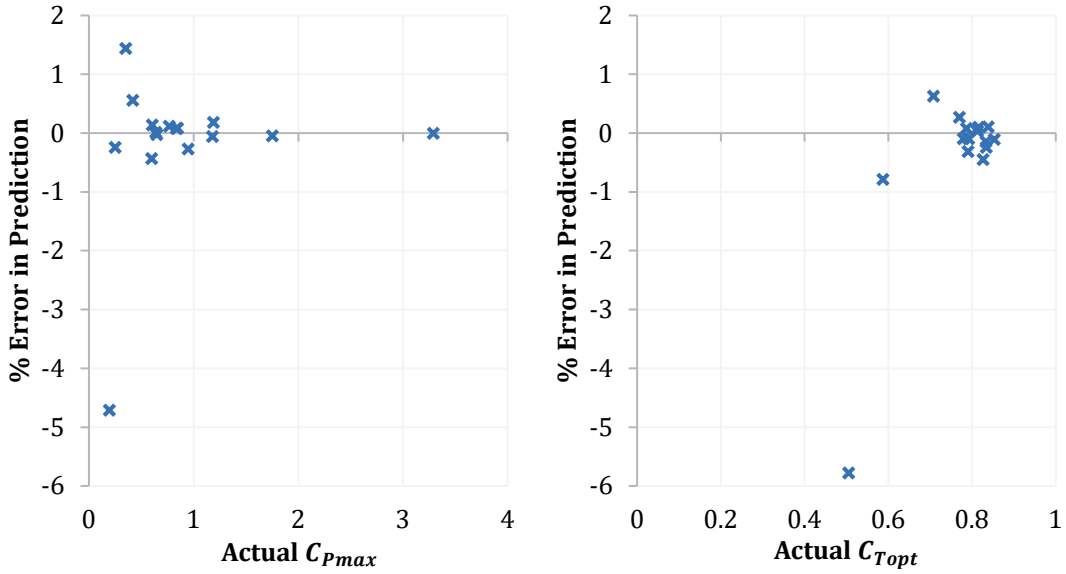

Figure 4.2: Validation of selected regression model against simulation results at the limits of the duct geometry generation parameters.

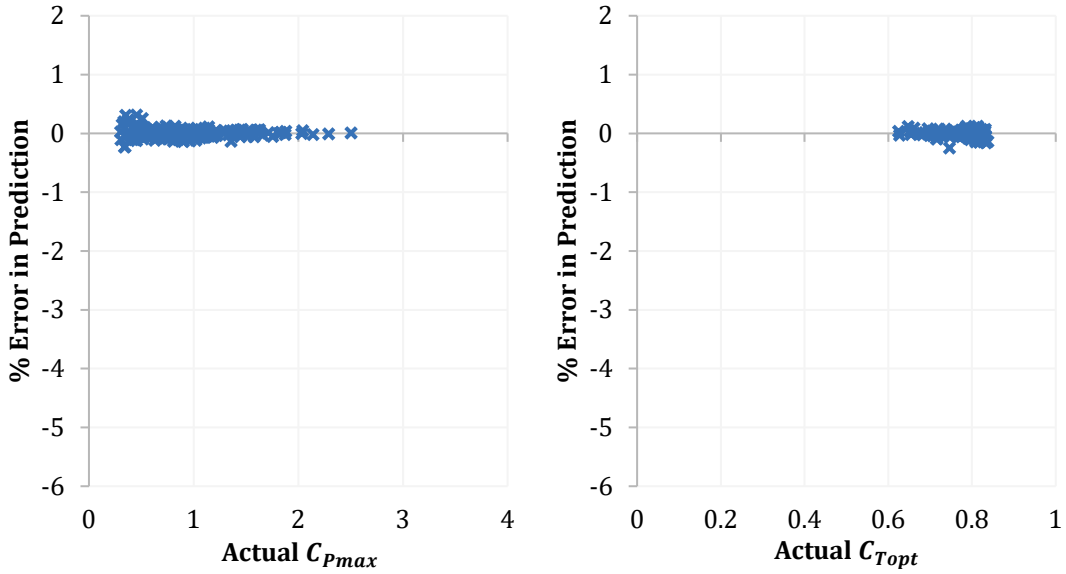

Figure 4.3: Validation of selected regression model against simulation results for 220 randomly generated duct shapes.

4.1.2 Restrictions on Duct Geometry

Even within the sample range seen in Table 4.2, it may be impossible to generate shapes with particular diffuser parameter combinations. A multi-objective optimisation algorithm [182] tested the feasibility of particular duct shapes by attempting to find a suitable set of geometry generation parameters, beginning from initial guesses provided by a regression analysis of the parameters in the 800 shape sample. Figure 4.4 shows the possible duct shapes, defined as all diffuser parameters being within 2% of their target. Those not found are not definitively impossible because the optimisation was sensitive to the initial guess, but the feasibility of such shapes is in serious doubt. These results suggest that the shape generation algorithm may only provide a limited subset of the full set of all possible shapes.

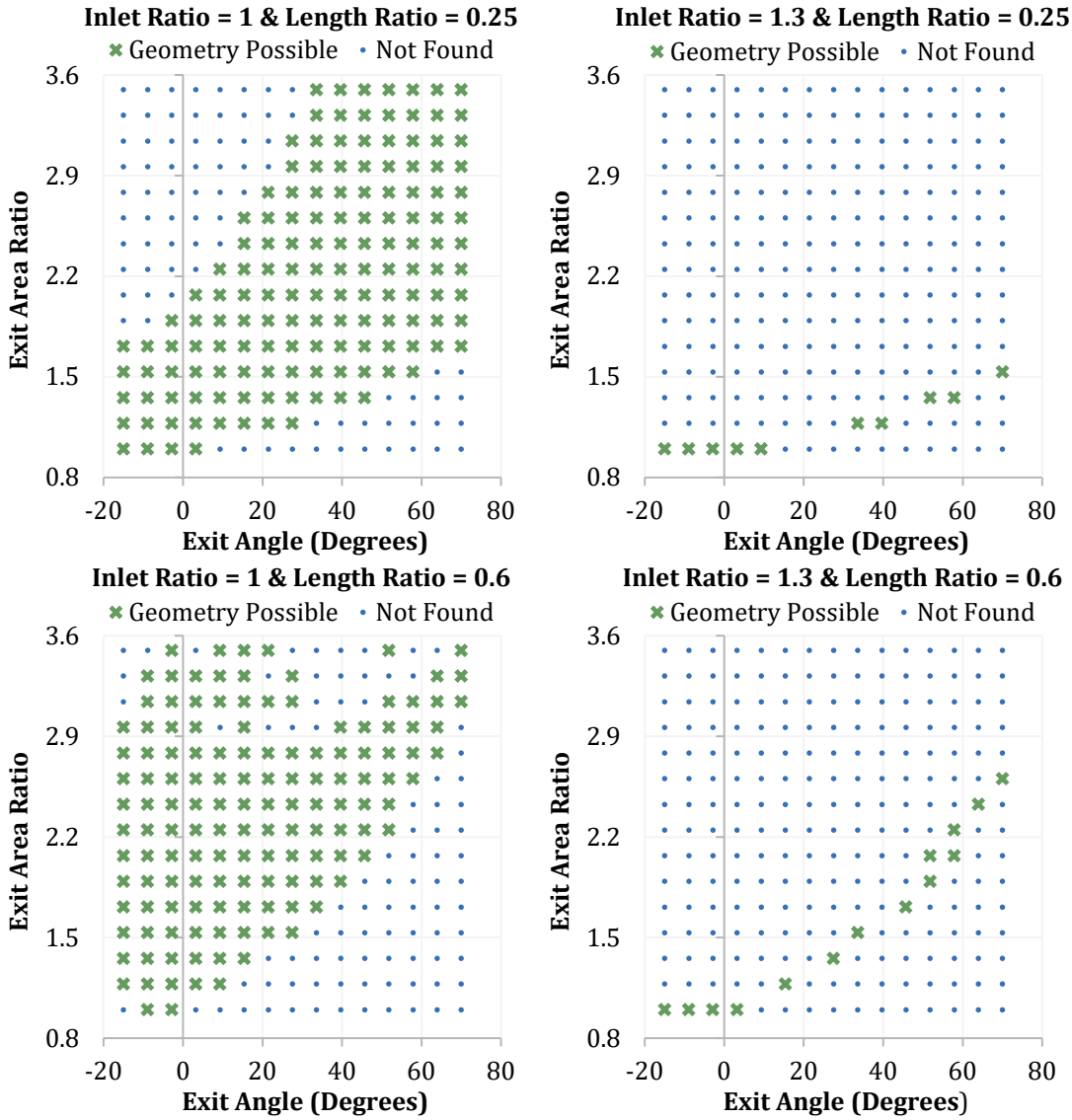

Figure 4.4: Results of the search for possible duct geometries for a range of exit area ratios A_e/A_r and exit angles θ_e, for the combinations of 1 and 1.3 for inlet ratio A_i/A_r and 0.25 and 0.6 for length ratio L_d/D.

4.1.3 Performance Predictions

Predictions for C_{Pmax} and C_{Topt} were generated from the regression models in Section 4.1.1 for duct shapes within the bounds of Table 4.2. Although the aim was to examine all the diffuser parameters, inlet ratio was fixed at 1: Figure 4.4 indicates very few shapes found above that value, and 50% of the sample shapes had a ratio of 1 with 86% at 1.1 or less. Predictions for maximum power are given in Figure 4.5 to Figure 4.7 and optimum rotor loading in Figure 4.8 to Figure 4.10. Although simultaneous prediction intervals are shown, it must be remembered that some points on these plots may represent impossible duct geometries and that the predictions are reliant on the quality of the regression analysis.

Predictions for Maximum Power

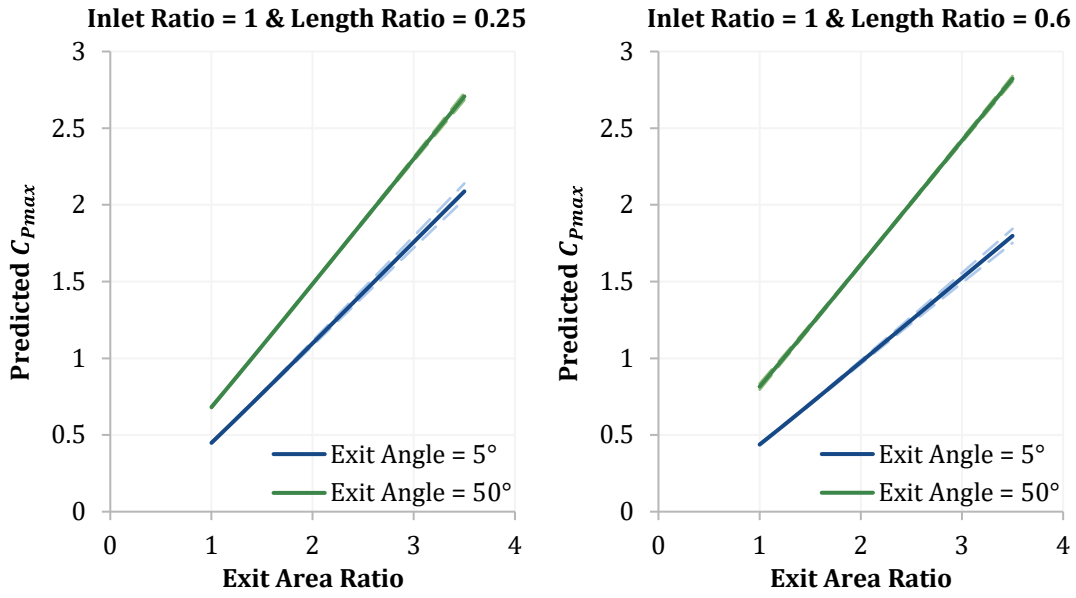

Figure 4.5: Variation of predicted C_{Pmax} with exit area ratio A_e/A_r, at selected inlet area ratio A_i/A_r, length ratios L_d/D, and exit angles θ_e. Dashed lines indicate 95% prediction intervals.

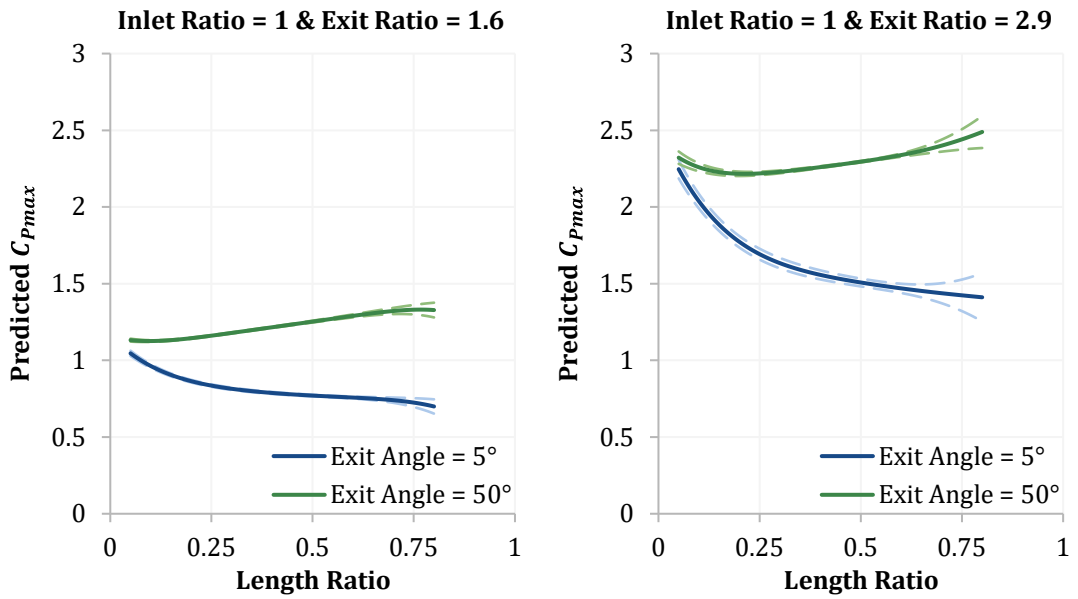

Figure 4.6: Variation of predicted C_{Pmax} with length ratio L_d/D, at selected inlet area ratio A_i/A_r, exit area ratios A_e/A_r, and exit angles θ_e. Dashed lines indicate 95% prediction intervals.

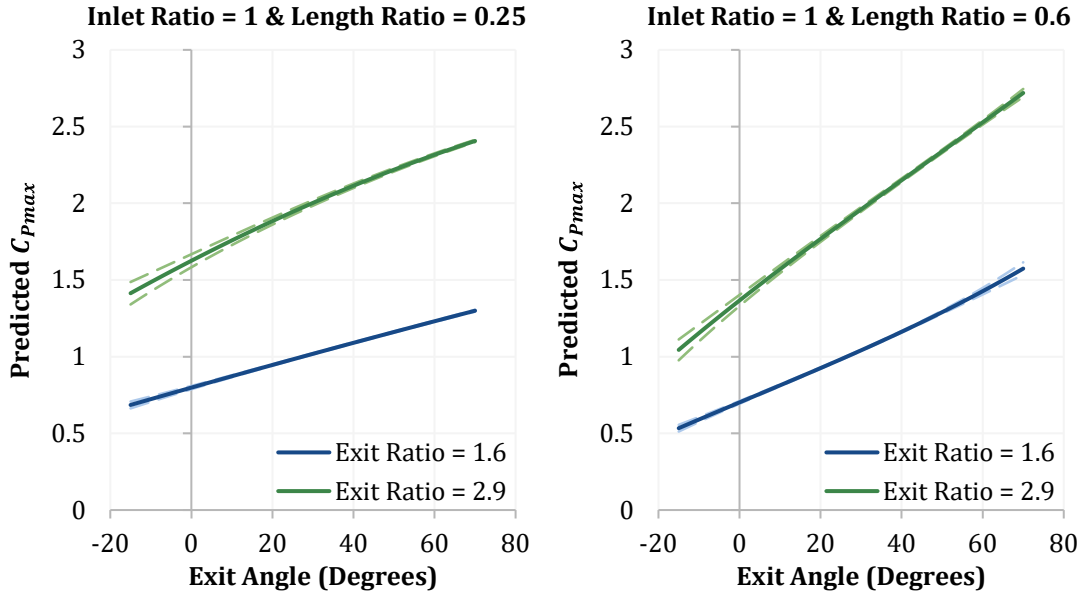

Figure 4.7: Variation of predicted C_{Pmax} with exit angle θ_e, at selected inlet area ratio A_i/A_r, length ratios L_d/D, and exit area ratios A_e/A_r. Dashed lines indicate 95% prediction intervals.

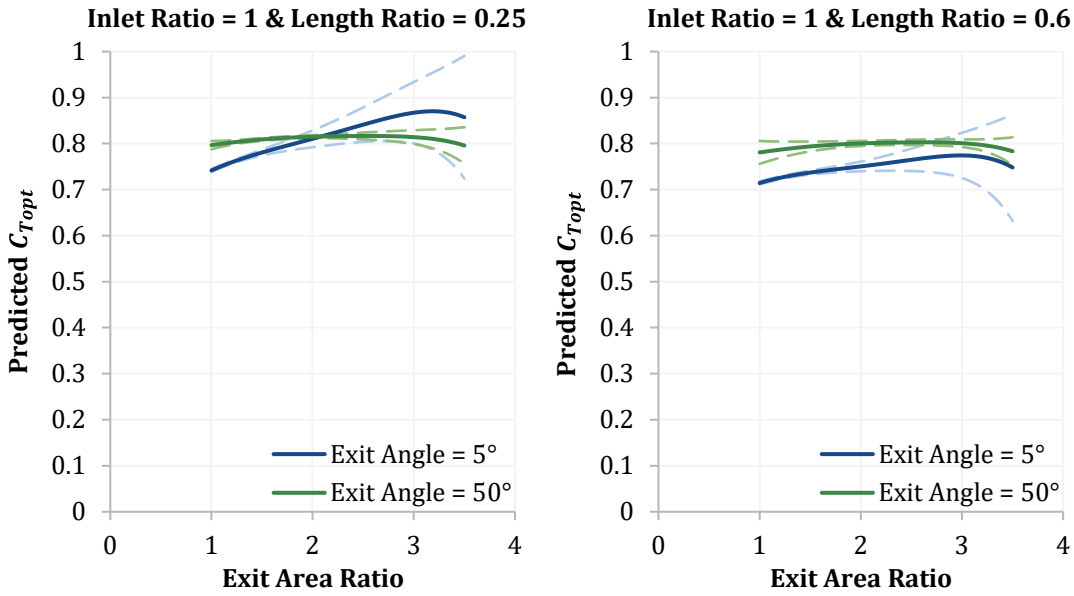

Figure 4.8: Variation of predicted C_{Topt} with exit area ratio A_e/A_r, at selected inlet area ratio A_i/A_r, length ratios L_d/D, and exit angles θ_e. Dashed lines indicate 95% prediction intervals.

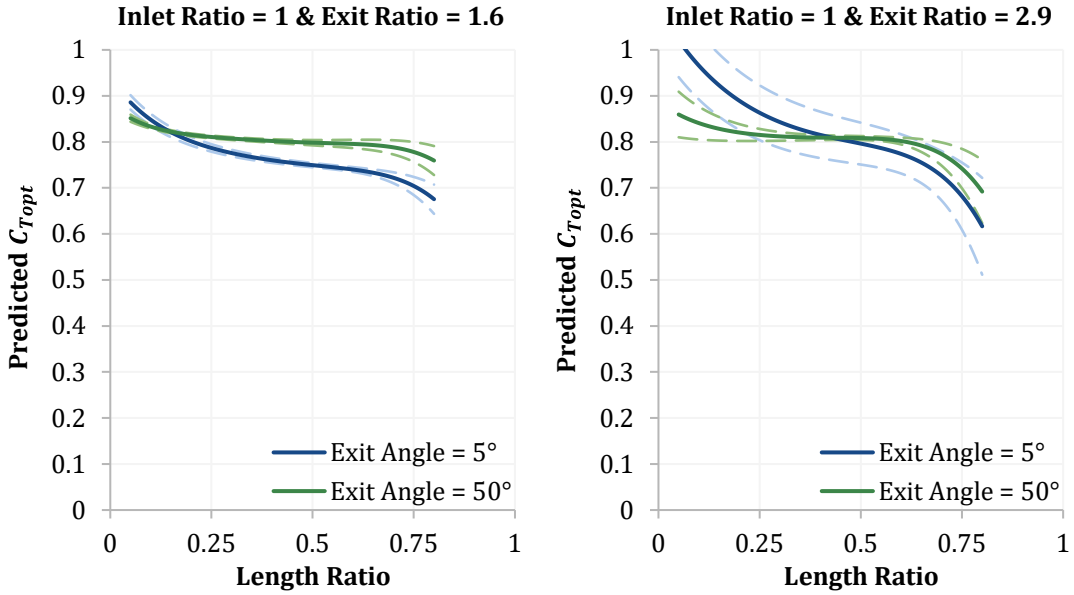

Figure 4.9: Variation of predicted C_{Topt} with length ratio L_d/D, at selected inlet area ratio A_i/A_r, exit area ratios A_e/A_r, and exit angles θ_e. Dashed lines indicate 95% prediction intervals.

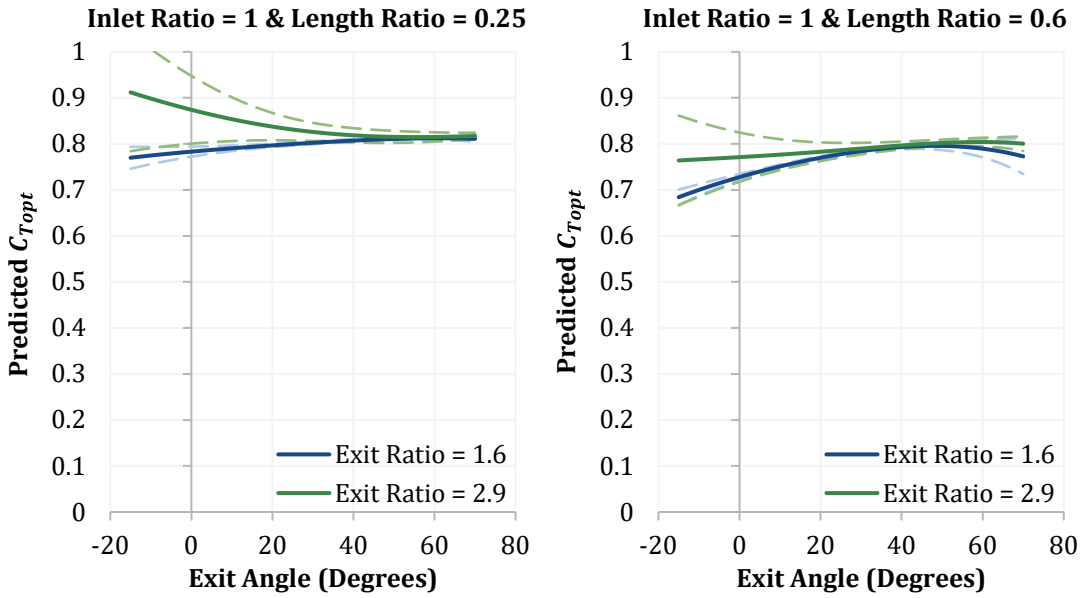

Figure 4.10: Variation of predicted C_{Topt} with exit angle θ_e, at selected inlet area ratio A_i/A_r, length ratios L_d/D, and exit area ratios A_e/A_r. Dashed lines indicate 95% prediction intervals.

4.1.4 A Limited Approach

A cursory assessment would suggest that the diffuser approach performed reasonably well for maximum power: variations with exit area ratio and exit angle were fairly linear, and behaved as expected. The relationship with length ratio was more complex, with no consistent influence on performance, although the results do confirm that length should not be excluded from the standard diffuser conceptual model. Relative certainty is indicated by the prediction intervals, suggesting a high degree of confidence in the mean value of C_{Pmax} for each diffuser parameter combination, and that there is little scatter around that mean. In other words, it would appear that the set of diffuser parameters is sufficient to uniquely determine C_{Pmax}.

However, these findings are not universal. They apply only to duct geometries generated using the approach detailed near the start of Section 4.1. While it is possible to imagine a range of duct shapes that would produce a given set of diffuser parameters, the geometry generation approach limits the possibilities. Indeed, it seems there was little variation in shape at a given combination of diffuser parameters: Figure 4.11 shows that reasonably accurate predictions can be made for the camber and rotation angles used in geometry generation from a regression analysis of the four diffuser parameters, using the methodology described in Section 4.1.1.

Instead of a diffuser parameter set being associated with a single value of C_{Pmax}, it may simply be that the geometry generation approach gives little choice in how to achieve the parameter set. Where only limited variation in the physical shape of the duct is possible, there can be little variation in performance. This analysis therefore only shows

that C_{Pmax} is uniquely specified using the diffuser parameters when restrictions are placed on duct shape.

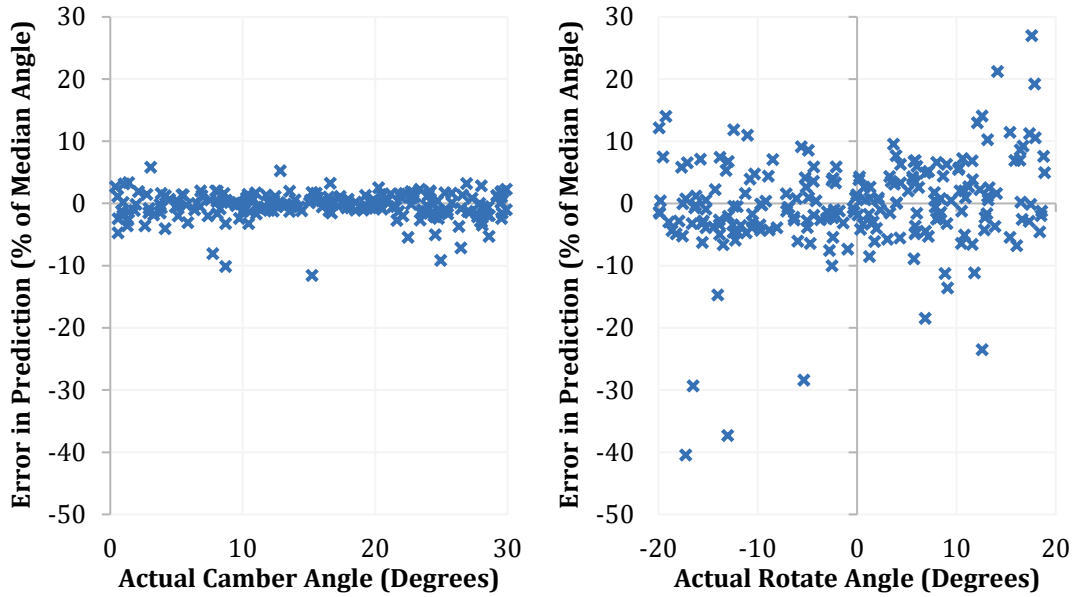

Figure 4.11: Error in predictions of camber and rotation angles from the regression models when tested against 220 randomly generated duct shapes. Errors are given as a percentage of the median absolute value of the angles in each case: 16.3° (left) and 9.1° (right).

In contrast to maximum power, the optimum rotor loading predictions had prediction intervals that suggested substantial uncertainty. From the definition of a prediction interval, this could indicate either a wide distribution of results around the mean value at a given point or uncertainty in the value of the mean itself. Comparison with confidence intervals, which measure only the uncertainty in the mean value, showed the uncertainty to be concentrated on the value of the mean. While the physically impossible predictions of C_{Topt} greater than 1 in inviscid flow can therefore be dismissed on the basis that the prediction is probably inaccurate, even the lower prediction interval reaches peak values greater than any result seen in the simulations carried out for this work.

These unlikely findings highlight that it is unknown whether particular features in the predictions are real or an artefact of the regression. Be it due to errors in the fitting process, insufficient data for certain ranges of shape, or impossible geometries, incorporating a regression analysis into the results can only add uncertainty. Although the prediction intervals attempt to quantify that uncertainty they themselves must rely on the quality of the regression.

4.2 Aerofoil Parameters

Standard aerofoil parameters were used as a base for setting the duct geometry in the aerofoil approach, illustrated in Figure 4.12, beginning with the selection of the NACA 4 digit aerofoil family [183]. An aerofoil shape was then uniquely specified with camber, point of maximum camber, and thickness, all defined as a fraction of the aerofoil chord length. Forming that shape into a particular duct design required setting a length to diameter ratio and the angle of the aerofoil to the flow axis. Although they may be important to performance, it was not feasible to investigate the influences of aerofoil family, thickness, and point of maximum camber here. Zero thickness was instead used throughout, with the point of maximum camber at 40% of chord.

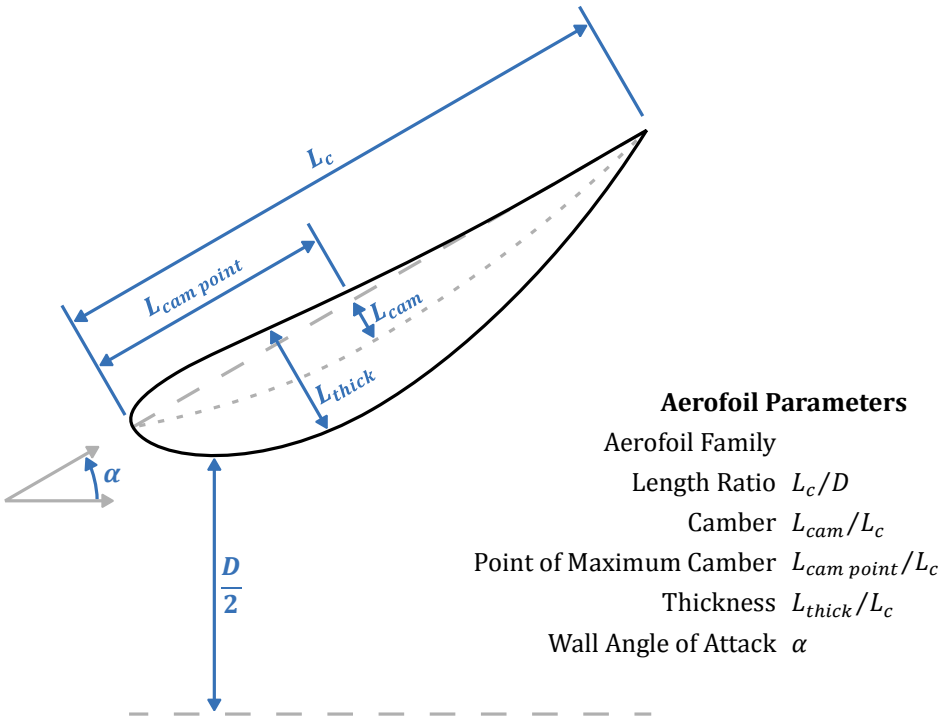

Figure 4.12: Illustration of the parameters used to set duct shape in the aerofoil approach.

Before assessing the aerofoil parameters, three preliminary studies will be described. In the first, the duct throat was found to be the most appropriate station for calculating performance results rather than inlet or exit. The parameters used in the length to diameter ratio were then selected, with aerofoil chord length chosen over duct length and throat diameter over inlet diameter. Finally, throat diameter was chosen for the definition of dimensionless circulation.

The linearity of the relationships involved was considered an important criterion for decision making in these three studies, in the hope of minimising the number of experiments or simulations required to characterise duct performance in future. While the relationships weren't truly linear, choosing the least non-linear option perhaps

makes linearity more often a reasonable approximation. When selecting the performance measurement station and the length to diameter ratio, the relevant relationships were between duct performance and the aerofoil parameters. For dimensionless circulation, it was between that parameter and velocity ratio.

There are many possible measures of linearity that could reasonably be used for these studies, with the adjusted coefficient of determination R^2 [184] for linear fits to the data chosen for assessing the measurement station and length ratio. The adjustment of this parameter removes the statistical bias seen in the standard R^2 with small sample sizes. For the dimensionless circulation study, where the sample size was much larger, Pearson's correlation coefficient was used to quantify the linear relationships along with Spearman's correlation coefficient to provide the wider context of the monotonic relationship strength.

When interpreting the adjusted R^2 values, the demonstration in Figure 4.13 should be kept in mind: even small differences could represent significant changes in subjective linearity. It is also important that fits for certain different parameters at the same measurement station produced identical adjusted R^2 values. At fixed rotor loadings, adjusted R^2 values were equal for C_P, velocity ratio, and axial induction, while velocity ratio and axial induction adjusted R^2 values matched at C_{Topt}. Therefore only one value was considered from each of these sets.

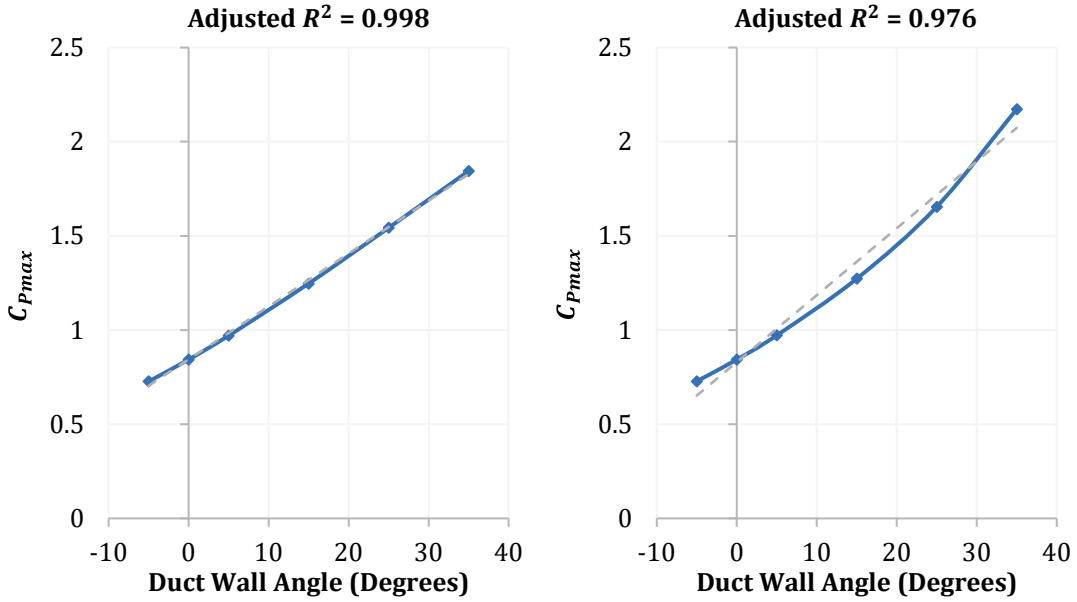

Figure 4.13: Comparison of subjective linearity for two values of adjusted R^2, with linear best fits shown by the dashed lines.

A total of 576 duct shapes were modelled for this investigation, chosen to test the influence on performance of each aerofoil parameter in turn while the others were held constant at a range of values. Discretisation convergence was tested using all four

length to diameter ratio approaches, at all eight combinations of the limiting aerofoil parameters shown in Table 4.4. Excluding one set of aerofoil parameters leading to small values of drag, the changes in result summarised in Table 4.5 were all less than 0.6%.

Table 4.4: Range of parameters used in aerofoil approach investigation.

	Length Ratio	Camber	Angle
Minimum	0.1	0%	-5°
Maximum	1	25%	35°

Table 4.5: Worst and median magnitude change in result when discretisation was changed for the discretisation checking duct shapes. Last duct panel length began at 0.00125 times the fixed diameter, and expanding wake length at 8 times the fixed diameter.

		% Difference with			
		Halved Panel Length		Doubled Wake Length	
Loading	**Result**	**Worst**	**Median**	**Worst**	**Median**
C_{Topt}	C_P	0.37	0.28	0.20	0.00
	C_{Topt}	0.16	0.07	0.58	0.02
	C_D	2.23	0.28	0.35	0.02
$C_T = 0$	u/u_∞	0.39	0.17	0	0

4.2.1 Choosing a Measurement Station

The performance parameters examined in this study vary depending on where they are computed within a duct; this section identifies the most appropriate measurement station before the length to diameter ratio approaches are assessed. The inlet, throat, and exit stations were tested to find which gave the most linear variation of C_P and u/u_∞ as each aerofoil parameter was varied in isolation. This process was repeated with a range of values for the unvaried remaining aerofoil parameters, and median values of adjusted R^2 were calculated for the linear fits.

All four combinations of length and diameter approaches were examined, with the values in Table 4.6 to Table 4.8 being the largest median of the four. The choice of station did not often have a large influence, although the exit station was noticeably worse than the alternatives with length ratio. While it is not known if the differences were statistically significant, it appears that the strongest linear relationships overall were found by calculating power coefficient and velocity at the throat. That station was therefore used when comparing the length and diameter approaches.

Table 4.6: Median adjusted R^2 values for linear fits of selected results to wall angle α, with results computed at the duct inlet, throat, and exit. The largest of the four geometry approach medians are shown.

		Median Adjusted R^2 for Wall Angle		
Loading	**Result**	**Inlet**	**Throat**	**Exit**
C_{Topt}	C_P	0.990	0.994	0.993
	u/u_∞	0.991	0.994	0.997
C_T = 0.75	C_P	0.991	0.994	0.992
C_T = 0	u/u_∞	0.989	0.994	0.999

Table 4.7: Median adjusted R^2 values for linear fits of selected results to length ratio L_c/D, with results computed at the duct inlet, throat, and exit. The largest of the four geometry approach medians are shown.

		Median Adjusted R^2 for Length Ratio		
Loading	**Result**	**Inlet**	**Throat**	**Exit**
C_{Topt}	C_P	0.990	0.993	0.882
	u/u_∞	0.992	0.998	0.867
C_T = 0.75	C_P	0.993	0.994	0.889
C_T = 0	u/u_∞	0.991	0.996	0.840

Table 4.8: Median adjusted R^2 values for linear fits of selected results to camber L_{cam}/L_c, with results computed at the duct inlet, throat, and exit. The largest of the four geometry approach medians are shown.

		Median Adjusted R^2 for Camber		
Loading	**Result**	**Inlet**	**Throat**	**Exit**
C_{Topt}	C_P	0.996	0.993	0.996
	u/u_∞	0.998	0.990	0.998
C_T = 0.75	C_P	0.996	0.994	0.996
C_T = 0	u/u_∞	1.000	0.987	1.000

4.2.2 Defining Length to Diameter Ratio

A similar approach to the previous section was used in assessing the length to diameter ratio, extended to include C_{Topt} and C_D in Table 4.9 to Table 4.11. C and D designate results where duct geometry was generated with the chord and duct length approaches respectively, while I and T represent inlet and throat diameter. Only the overall medians of the R^2 values at each loading were considered in judging the best approach, with the most linear results highlighted in each table. A tolerance of 0.01 was applied, within which results were considered equal. Note that the median R^2 values for C_P were equal to those for C_D to three decimal places at C_T = 0.75.

Table 4.9: Median adjusted R^2 values for linear fits of selected results to wall angle α, used in comparing the CI, CT, DI, and DT approaches. The best approaches are highlighted in the rows for the overall medians at each loading, using a tolerance of 0.01.

		Median Adjusted R^2 for Wall Angle			
Loading	**Result**	**CI**	**CT**	**DI**	**DT**
C_{Topt}	C_P	0.994	0.992	0.973	0.960
	u_r/u_∞	0.994	0.991	0.970	0.957
	C_D	0.992	0.990	0.971	0.956
	C_{Topt}	0.901	0.907	0.899	0.904
	Overall	**0.984**	**0.979**	0.952	0.946
C_T = 0.75	C_P & C_D	**0.994**	**0.992**	0.973	0.960
C_T = 0	u_r/u_∞	**0.994**	**0.988**	0.965	0.952

Table 4.10: Median adjusted R^2 values for linear fits of selected results to length ratio L_c/D, used in comparing the CI, CT, DI, and DT approaches. The best approaches are highlighted in the rows for the overall medians at each loading, using a tolerance of 0.01.

		Median Adjusted R^2 for Length Ratio			
Loading	**Result**	**CI**	**CT**	**DI**	**DT**
C_{Topt}	C_P	0.979	0.993	0.975	0.992
	u_r/u_∞	0.988	0.998	0.986	0.998
	C_D	0.983	0.995	0.982	0.994
	C_{Topt}	0.401	0.417	0.292	0.316
	Overall	0.967	**0.992**	0.963	**0.991**
C_T = 0.75	C_P & C_D	0.980	**0.994**	0.976	**0.993**
C_T = 0	u_r/u_∞	0.990	**0.996**	0.987	**0.996**

Table 4.11: Median adjusted R^2 values for linear fits of selected results to camber L_{cam}/L_c, used in comparing the CI, CT, DI, and DT approaches. The best approaches are highlighted in the rows for the overall medians at each loading, using a tolerance of 0.01.

		Median Adjusted R^2 for Camber			
Loading	**Result**	**CI**	**CT**	**DI**	**DT**
C_{Topt}	C_P	0.972	0.994	0.963	0.993
	u_r/u_∞	0.964	0.990	0.956	0.989
	C_D	0.967	0.992	0.961	0.991
	C_{Topt}	0.870	0.866	0.871	0.867
	Overall	0.941	**0.989**	0.933	**0.986**
C_T = 0.75	C_P & C_D	0.970	**0.994**	0.962	**0.993**
C_T = 0	u_r/u_∞	0.959	**0.987**	0.953	**0.987**

In every case a draw existed for most linear, but the combination of chord length with throat diameter was the only option to be jointly most linear in every test. Removing the threshold and counting only the greatest medians left CT the most linear in 6 cases, CI in 3, and the others in 0. Chord length and throat diameter therefore appear to be the best approaches, with chord length also avoiding a variation in aerofoil scaling as the aerofoil angle is varied at fixed length ratio. Based on this conclusion, a repeat of the analysis carried out in Section 4.2.1 using only the CT results – instead of all of the length to diameter ratio approaches – confirmed the selection of the throat as the measurement station.

4.2.3 Making Circulation Dimensionless

A close association between circulation and duct performance was desired for the analysis of the aerofoil parameters discussed later in Section 4.2.5, but an appropriate length parameter had not previously been determined for dimensionless circulation. Chord length, duct length, and inlet, throat, and exit diameter were all therefore tested. The performance measurement station was also reassessed in case the best choice for the relationship between performance and circulation differed from that in Section 4.2.1 for performance and the geometrical parameters.

Choosing velocity ratio as the performance measure, Figure 4.14 illustrates the resulting strength of association with circulation at C_{Topt}. 200 randomly generated duct shapes provided the required data, using the length to diameter approach selected in Section 4.2.2 and the limits in Table 4.4. The pattern seen was not affected by rotor loading or by measuring performance with C_P, while the order of the top three coefficients was the same using the four sets of non-randomly generated shapes from the length and diameter approach tests.

Using the diffuser parameter shapes from Section 4.1, however, saw a change in the measurement station for the greatest Pearson's coefficient from the duct's throat to the exit with dimensionless circulation defined using chord length. Figure 4.15 shows a kink in the throat results for the diffuser shapes, absent from the aerofoil results, reducing the overall linearity but not the monotonic relationship strength. Throat measurement nevertheless led to greater linearity in the augmentation region, as seen by comparison with the exit measurement results in Figure 4.16.

Explaining with any certainty the change in slope seen for the diffuser results must be left to future work, but it is possible that it relates to the change in rotor position with changes in duct shape; the rotor was always placed in the smallest cross-sectional area in Figure 4.15. Both rotor position and duct shape should influence the velocity at the rotor, but the most poorly performing diffuser shapes had rotors in the exit plane. Additional changes in duct shape could not therefore move the rotor any further downstream, perhaps changing the relationship between circulation and velocity.

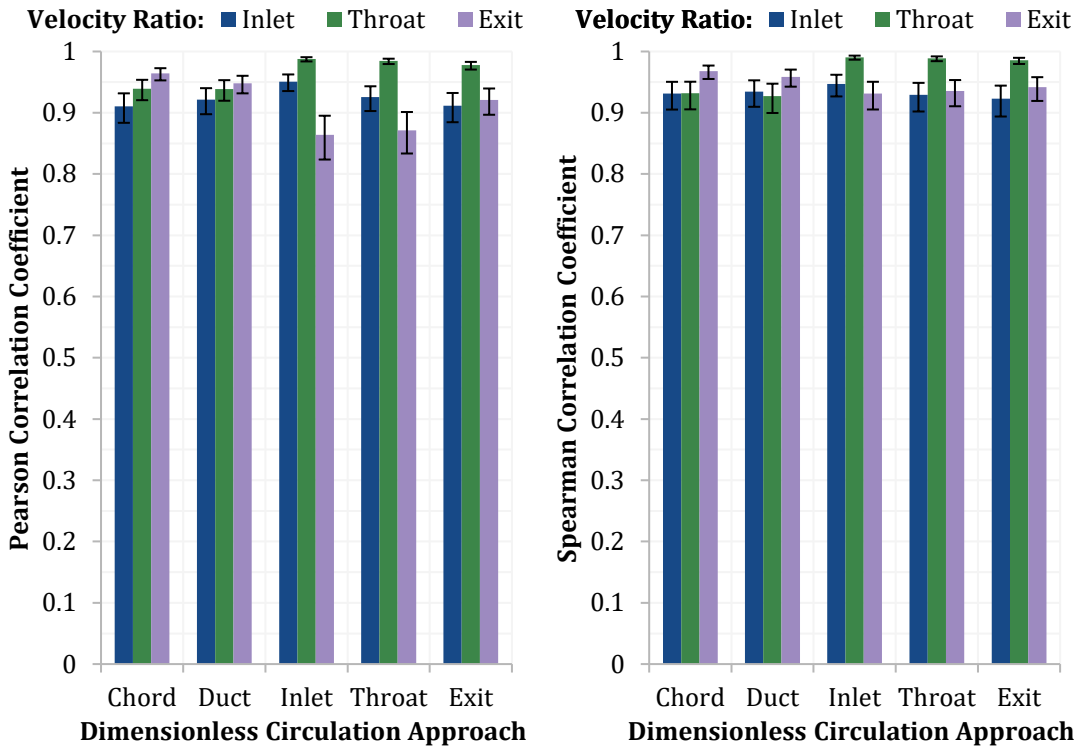

Figure 4.14: Correlation between performance at C_{Topt} – computed using the velocity ratio u/u_∞ at the inlet, throat, and exit – and circulation Γ_d – made dimensionless with chord length, duct length, and inlet, throat, and exit diameters. 95% confidence intervals are shown.

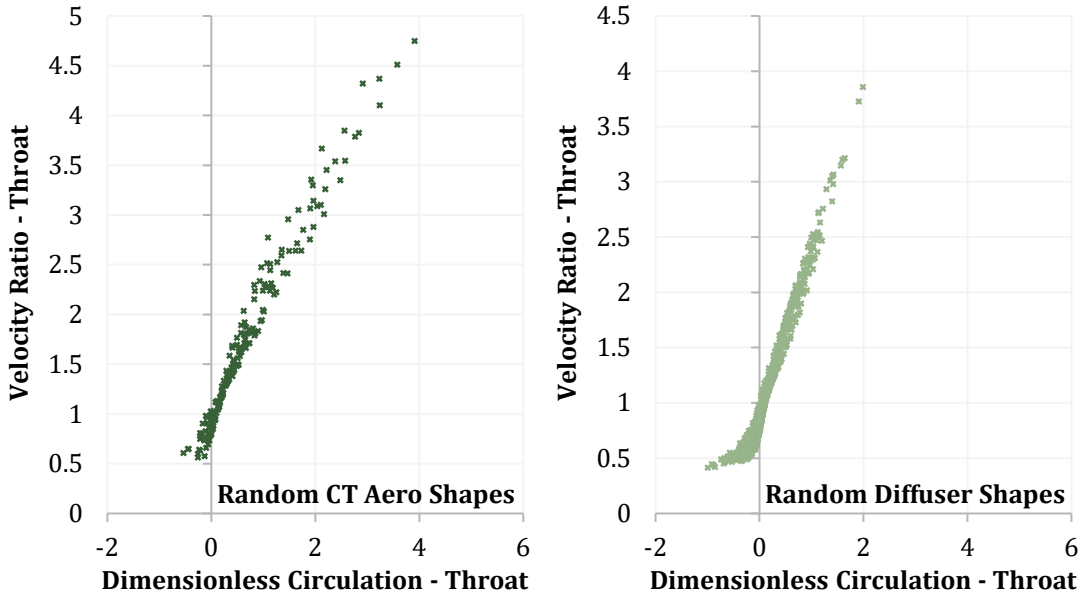

Figure 4.15: Variation of the throat velocity ratio u_r/u_∞ with circulation made dimensionless using the throat diameter $\Gamma_d/u_\infty D$ at C_{Topt} for 200 duct shapes randomly generated using the Chord and Throat aerofoil approach (left) and 1000 shapes randomly generated using the diffuser approach (right).

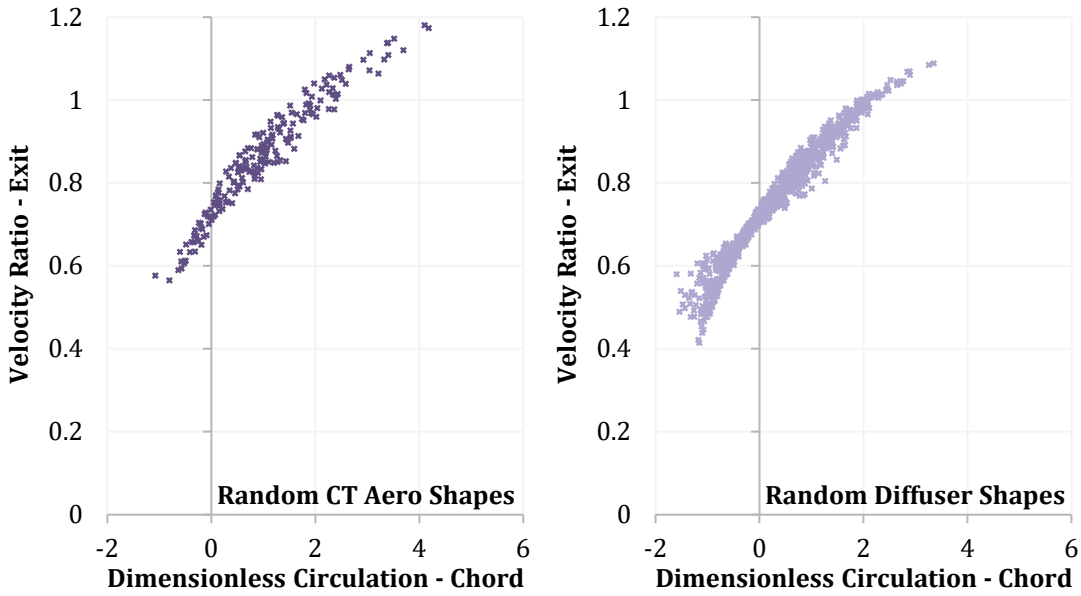

Figure 4.16: Variation of the exit velocity ratio u_e/u_∞ with circulation made dimensionless using the chord length $\Gamma_d/u_\infty L_c$ at C_{Topt} for 200 duct shapes randomly generated using the Chord and Throat aerofoil approach (left) and 1000 shapes randomly generated using the diffuser approach (right).

Overall, measuring performance at the throat appears to give the strongest association between performance and circulation. The data for defining dimensionless circulation is less clear cut: inlet diameter gave the greatest correlation coefficients, but the values did not reach outside the 95% confidence intervals for throat diameter. Although formal hypothesis testing was not used, any difference seems slight at most. Throat diameter was therefore chosen as it also has the advantage of being consistent with the power and drag coefficient definitions, giving the definition of dimensionless duct circulation C_Γ in Equation 4.1.

$$C_\Gamma = \frac{\Gamma_d}{u_\infty D} \qquad \textbf{Equation 4.1}$$

An explanation for the stronger association with the diameter approaches may come from considering two situations where u/u_∞ could vary without a corresponding change in C_Γ: changes in Γ_d could affect u/u_∞ but not C_Γ if there were a linear relationship between the length parameter and Γ_d, while changes in the cross sectional area A could affect u/u_∞ but not C_Γ if there were no connection between the length parameter and A. Both of these seem less likely to occur for diameter than for chord and duct length.

4.2.4 Performance Results

With the preliminary studies complete, simulation results showing the influence of the aerofoil parameters on maximum power coefficient are given by Figure 4.17 to Figure 4.19 and optimum rotor loading by Figure 4.20 to Figure 4.22. Duct geometry was generated using a length to diameter ratio defined with chord length and throat diameter L_c/D. Only a subset of the results used to calculate the linearity in the earlier sections is shown here.

Results for Maximum Power

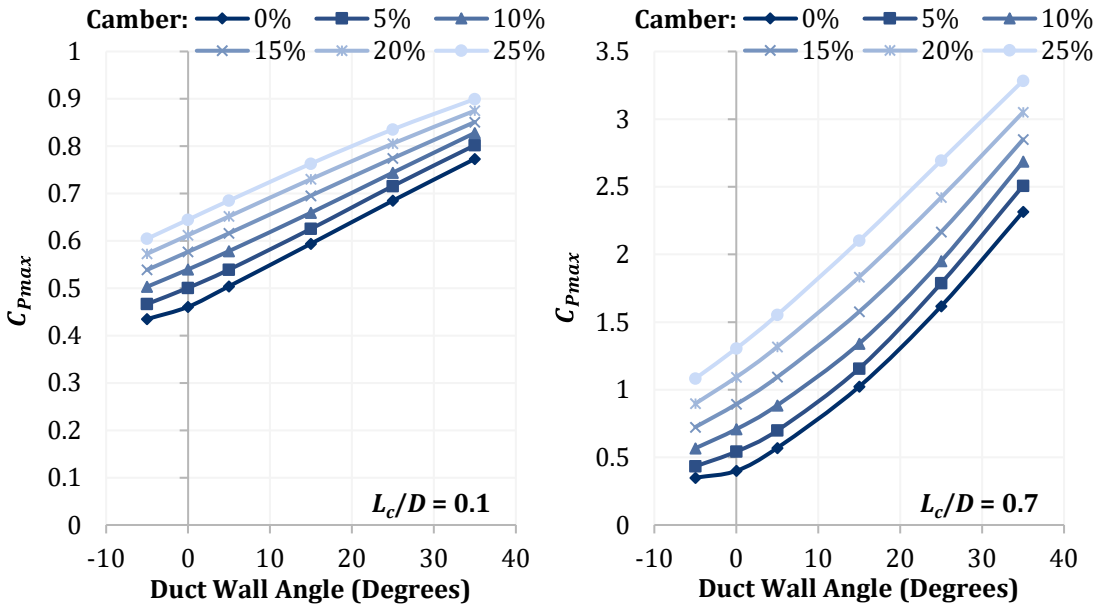

Figure 4.17: Variation of maximum power coefficient C_{Pmax} with duct wall angle α, at selected cambers L_{cam}/L_c and chord length ratios L_c/D.

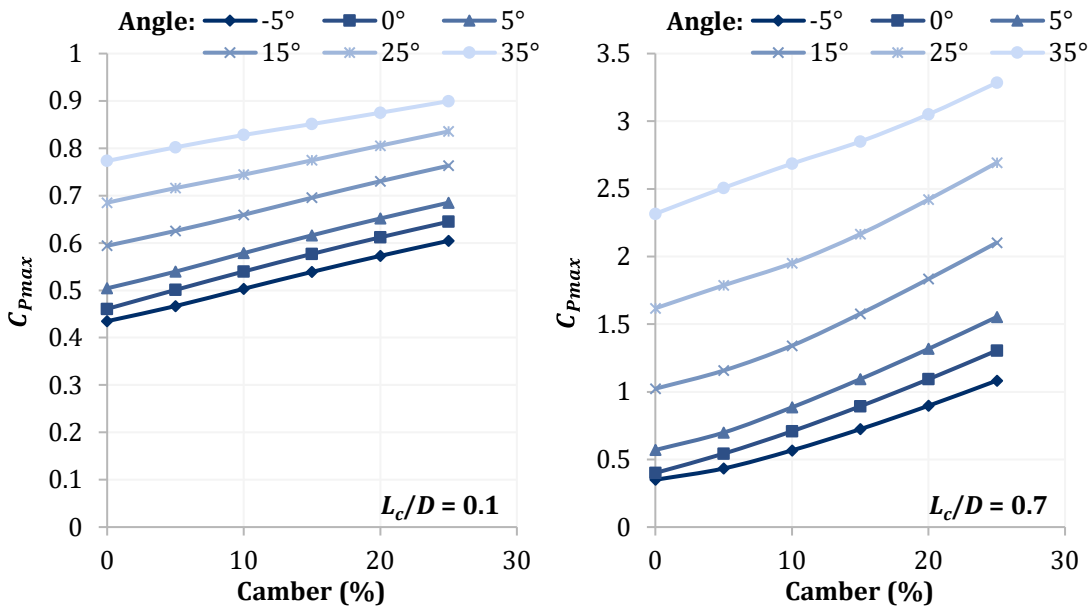

Figure 4.18: Variation of maximum power coefficient C_{Pmax} with camber L_{cam}/L_c, at selected duct wall angles α and chord length ratios L_c/D.

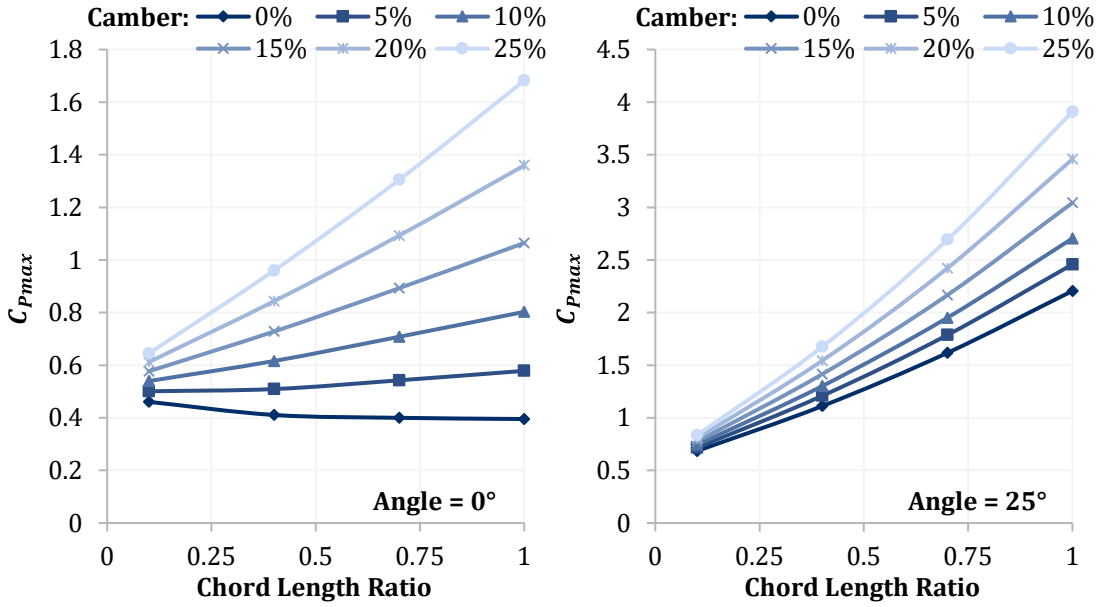

Figure 4.19: Variation of maximum power coefficient C_{Pmax} with chord length ratio L_c/D, at selected cambers L_{cam}/L_c and duct wall angles α.

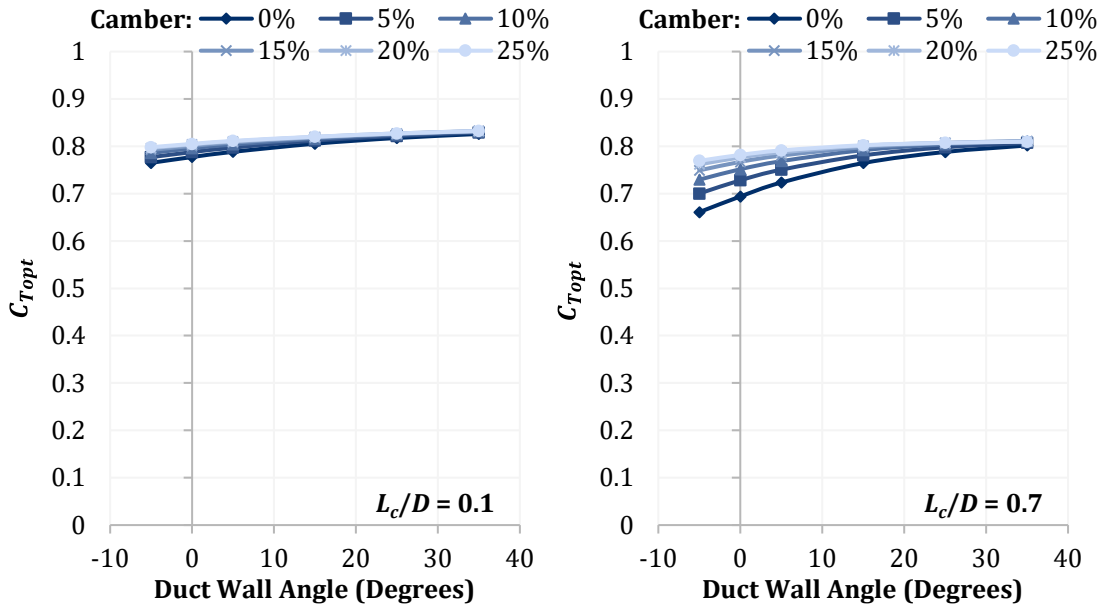

Figure 4.20: Variation of optimum rotor loading C_{Topt} with duct wall angle α, at selected cambers L_{cam}/L_c and chord length ratios L_c/D.

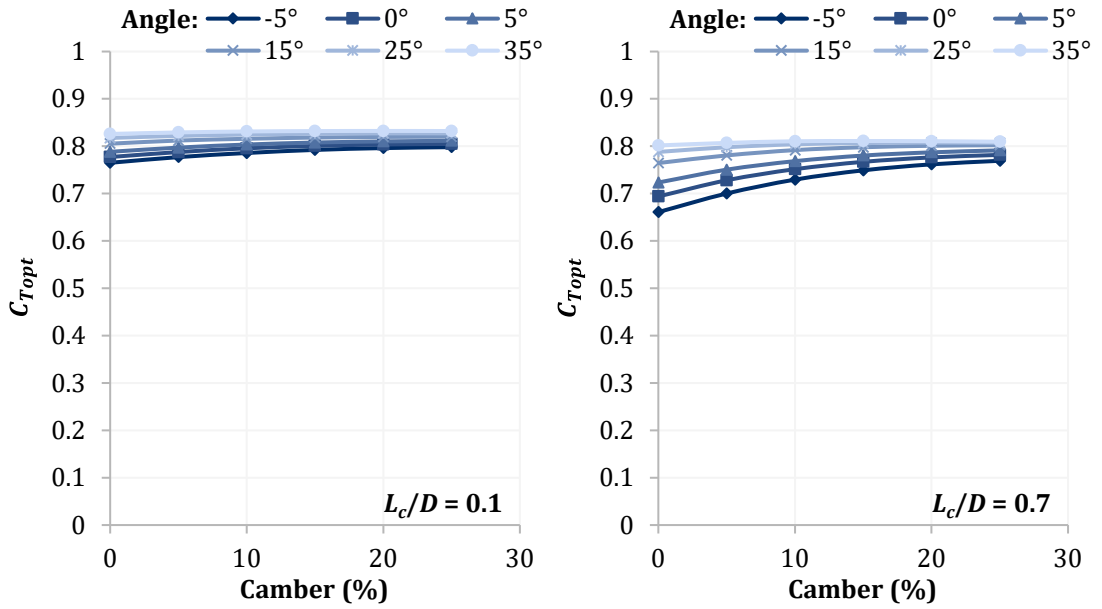

Figure 4.21: Variation of optimum rotor loading C_{Topt} with camber L_{cam}/L_c, at selected duct wall angles α and chord length ratios L_c/D.

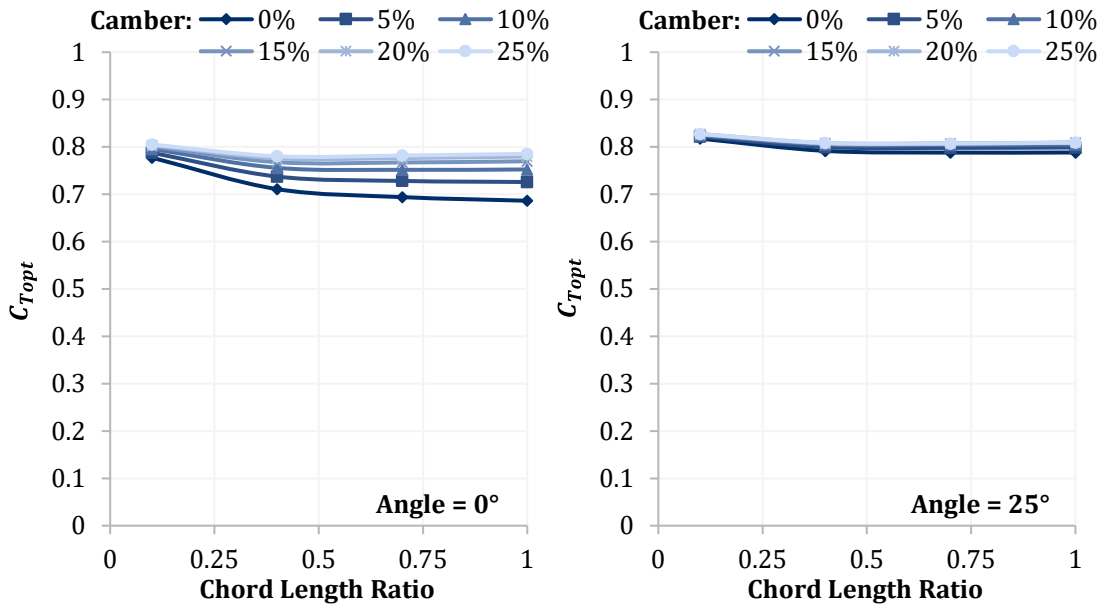

Figure 4.22: Variation of optimum rotor loading C_{Topt} with chord length ratio L_c/D, at selected cambers L_{cam}/L_c and duct wall angles α.

4.2.5 A Useful Approach

Although the chosen length to diameter ratio and performance measurement approaches gave the most linear set of results, the linearity in Figure 4.17 to Figure 4.22 was far from universal. Maximum power coefficient, however, was visibly linear with angle and camber for short ducts and with chord length ratio for low angle ducts above zero camber. At L_c/D = 0.1, the median adjusted R^2 for linear fits to the angle results was 0.9989 and to the camber results was 0.9993, while the corresponding value for the chord length ratio results above zero camber and at angles of 0° and 5° was 0.9976. It may well be feasible to make an assumption of linearity if short ducts prove to be the path to economic viability.

It would be advantageous if thin aerofoil theory [69], used to calculate aerofoil circulation in inviscid flow, could be applied to ducted turbines. To test this possibility, the thin aerofoil circulation was made dimensionless with the free stream velocity and rotor diameter in Equation 4.2.

$$C_\Gamma = \frac{\Gamma}{u_\infty D} = \frac{\pi L_c}{D}\left[\alpha + \frac{1}{\pi}\int_0^\pi \frac{\mathrm{d}r}{\mathrm{d}x}(\cos\theta_0 - 1)\mathrm{d}\theta_0\right] \qquad \textbf{Equation 4.2}$$

α is the angle of the duct wall chord line to the axial direction, $\mathrm{d}r/\mathrm{d}x$ is the gradient of the camber line at a given location, and θ_0 corresponds to a particular axial location on the chord line x through the transformation $x = (L_c/2)(1 - \cos\theta_0)$. Circulation varies linearly with angle and the integral camber term, which itself increases with camber [69]. The chord length ratio then acts as a multiplier, linearly increasing or decreasing circulation depending on the sum of the angle and camber terms.

It has already been noted that maximum power did not always vary in a linear fashion. Another difference is that chord length ratio did not seem to act perfectly as a multiplier, with two cases of a duct shape curtailing the flow experiencing increased performance with increased length. Removing the influence of the rotor by examining C_T = 0 in Figure 4.23, and therefore modelling the case of an axisymmetric aerofoil, reveals the expected variation.

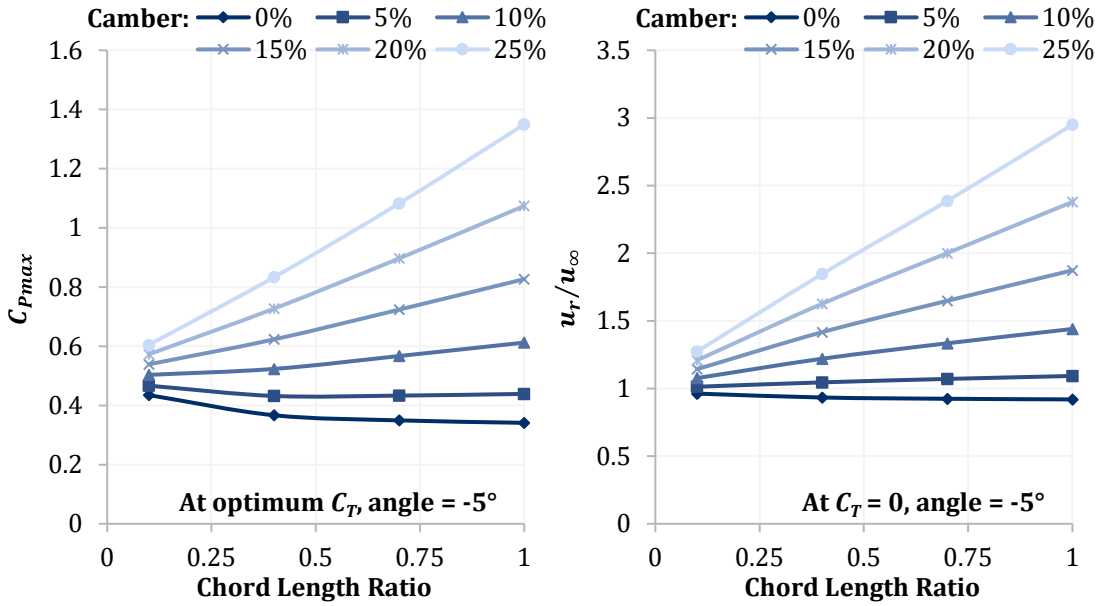

Figure 4.23: Variation of maximum power coefficient C_{Pmax} (left) and dimensionless velocity u_r/u_∞ at C_T = 0 (right) with chord length ratio.

The inclusion of the rotor model is only one of the differences from thin aerofoil theory. Ducts are not two-dimensional aerofoils, and some of the shapes here violate the assumptions of small angles and camber. Comparing power with circulation makes the further assumption that both parameters are directly proportional. Nevertheless, the maximum power results did match expectations from thin aerofoil theory in a general sense: performance increased with angle and camber, and increased length tended to amplify the augmentation or diminution of the flow.

4.3 The Benefits of an Aerofoil Approach

Aerofoil parameters for the specification of duct shape offer significant advantages over a diffuser approach. Even choosing a duct shape is not straightforward for the latter, as the parameters which generate the shape differ from the set of diffuser parameters used to measure the shape and thought to control duct performance. While that may only be a limitation of the particular shape generation method tested, it is unclear if the diffuser parameters themselves could be used directly for shape generation. The aerofoil parameters, however, both generate and measure the duct shape, making shape generation straightforward.

A much greater degree of certainty exists for the aerofoil results because of the straightforward shape generation, as there was no regression step in which additional errors could have been introduced and no doubt over whether a particular duct shape is possible. The unrealistically high C_{Topt} predictions with the diffuser parameters are a likely consequence of these problems, while results for the aerofoil approach were in line with all other simulations in this work. Difficulty generating duct shapes with the diffuser parameters also led to inlet area ratio not being assessed.

While the assumptions underlying thin aerofoil theory prevented an exact match with maximum power coefficient, the variation in performance was generally as expected. A traditional diffuser conceptual model, however, would not have predicted the changes seen with duct length. While the variations with exit area ratio and exit angle were predictable, it is important to note that these findings apply only to the shape generation method tested: one which placed implicit limitations on duct shape for a given set of diffuser parameters. It is not known if performance would vary in the expected way were these limitations removed.

None of these difficulties are fatal for the diffuser model. To be useful, the shape generation approach must become an explicit parameter, not simply a mechanism ignored once the diffuser parameters are generated, and it should use the modification introduced here for duct length. However, the advantages of the aerofoil model make it the more attractive option, and there exists a wealth of data on aerofoil performance that could be investigated for applicability to ducted turbines.

4.4 Summary

A conceptual model for ducted turbines should allow easy identification of how performance varies with a limited set of geometrical parameters. Such a model can improve understanding generally, form the basis of a design process, or allow a systematic approach to shape optimisation. An appropriate choice of parameters is key to the usefulness of the model, and two separate sets were tested here: one based on the traditional diffuser set of parameters, and one based on an aerofoil set.

The diffuser parameters used were the exit area ratio, the inlet area ratio, the duct exit angle, and – based on the results from Section 3.2.2 – the length ratio. A separate group of parameters was used to generate the duct shapes, following the process used by Shives & Crawford [57] and Hansen et al [55]. As no reliable way was found of selecting shape generation parameters to provide particular diffuser parameters, geometry generation parameters were selected randomly and regression analysis used to investigate this model.

Stepwise regression was used to automatically fit models to an 800 duct shape sample, with validation against 220 other duct shapes showing the superiority of a fit limited to 5th order terms. Predictions for C_{Pmax} were in line with expectations; however, this finding is not general due to significant restrictions on duct shape. The shape generation approach must therefore be explicitly included in the diffuser parameter set. Unrealistically high values were predicted for C_{Topt}, reflecting either errors introduced by the regression analysis or predictions for duct shapes that are physically impossible with this approach to shape generation.

The NACA 4-digit aerofoil family was used for the aerofoil parameters, with camber, aerofoil angle, and length to diameter ratio tested for their influence. The strongest linear relationships between those parameters and performance were found when measuring performance at the throat and with length to diameter ratio specified using chord length and throat diameter. Further testing also found the strongest association between dimensionless circulation and performance with measurements at the throat, with throat diameter selected as the most appropriate for making circulation dimensionless.

Expectations were met for the C_{Pmax} results: performance increased with angle and camber, while increased length tended to amplify the augmentation or curtailment of the flow. C_{Topt} results were consistent with conclusions from the rest of this work, and did not reach unrealistic values. As the same parameters specified shape and were linked to duct performance, a regression analysis was avoided and there was no uncertainty over the physical feasibility of particular sets of parameters. Being straightforward to use and with less scope for error, the aerofoil approach was selected as the superior option.

5 Chapter

Testing Current Theories

An alternative to simulations for the analysis of ducted turbines is the application of physical laws to create a theoretical model that can help build an understanding of the fundamentals. A number of quasi-one dimensional theories exist in the literature, which have already been used to predict the importance of various parameters to performance, but little validation has been carried out thus far. This chapter will therefore present tests of four theories to determine where trust should be placed.

Both the theories of Sørensen [185] and Werle and Presz [108] were chosen for evaluation because they aimed to eliminate or reduce empirical parameters, a particularly valuable goal if found to be valid. Phillips' [4] theory was selected as the most detailed derivation encountered, along with Jamieson's [186] due to his introduction of the unique ideal diffuser concept and its need for further development. All are quasi-1D theories applied to ducted actuator discs, with derivations from momentum and energy principles.

5.1 Validation Approach

Finding a theory to be valid does not necessarily mean that it closely matches reality: its equations are simply correct on a chosen level of simplification, as discussed in Section 1.5.1. Both the theories investigated and the inviscid panel code are designed to be valid for ducted actuator discs in inviscid axisymmetric flow, with the simulation code suitable for validating the theories due to the high accuracy demonstrated in Sections 2.2.5 and 2.2.6.

To test the validity of an equation, the left and right sides were calculated independently from numerical results, with a small inequality suggesting a valid relationship. Each theory was examined equation by equation to determine exactly where any inconsistencies arose, with alternative versions of some equations introduced to allow further testing. While reasonable approximations have their place in improving understanding, the aim here was to find theoretically correct relationships only.

Each equation was assessed individually, but in general a difference of less than 1% between the sides implied validity: a perfect agreement could not be expected due to numerical error in the simulation results. Care was taken to differentiate between inequalities due to numerical error and those from an invalid relationship by

considering the inequalities at all rotor loadings and the level of discretisation convergence of each parameter.

To prevent misleadingly large errors when the value of an equation tended towards zero, inequalities were calculated as a percentage of the median right hand side magnitude. Any large percentages therefore represent large absolute inequalities and are not due to normalisation with respect to small values. With simulations at N values of C_T for a particular duct, the percentage inequality at a particular rotor loading j between the right hand side RHS and left hand side LHS of the equation was calculated using Equation 5.1.

$$Inquality_j = \frac{\left|LHS_j - RHS_j\right|}{\text{Median}\begin{pmatrix}|RHS_1| \\ \vdots \\ |RHS_N|\end{pmatrix}} \times 100 \qquad \textbf{Equation 5.1}$$

5.2 Simulations Suitable for Testing Theories

The simulation results selected for this analysis were required to have a very low level of numerical error, so that the approach was sensitive to small differences between theory and simulation, and were chosen to minimise the chance of any coincidental agreement occurring for all the cases modelled. The latter requirement was met by using results at a range of rotor loadings from three duct shapes, VA to VC, with substantially differing performance and where multiple geometrical parameters were varied between shapes. Both the shapes and performance can be seen in Figure 5.1, and all the plotted C_T values were used for validation.

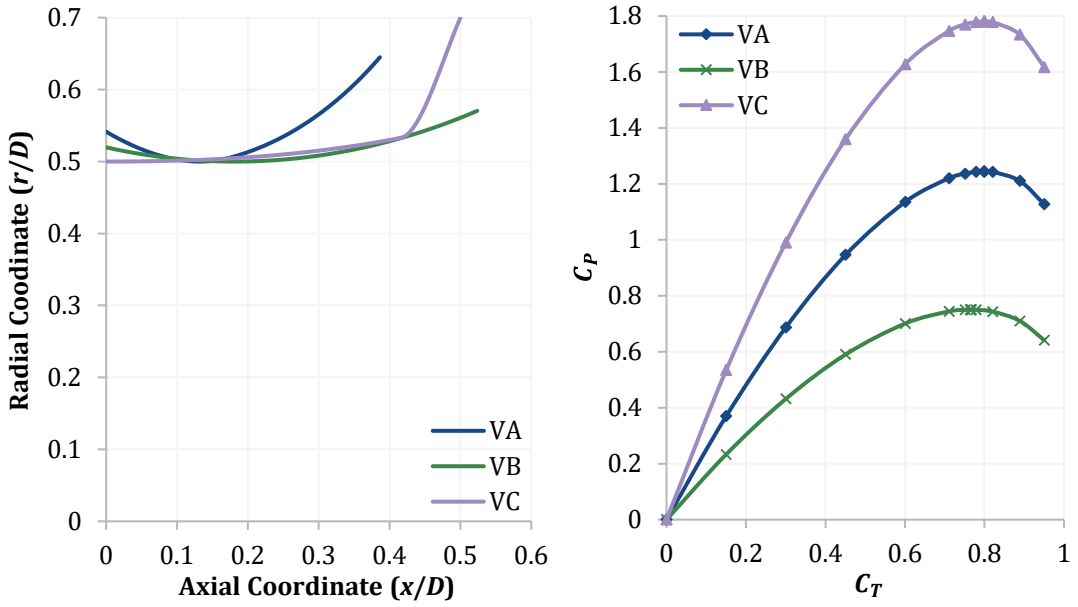

Figure 5.1: Shape of validation ducts VA to VC in terms of each duct's rotor diameter D (left), and the power performance of each duct (right).

Discretisation error was found to be the primary component of numerical error for the panel method code in Sections 2.2.5 and 2.2.6; actuator disc theory values for C_{Topt} and C_{Pmax} were matched to within 0.36% and 0.27% respectively with the discretisation convergence shown in Table 5.1. Similar or better convergence was achieved with the validation ducts, using half cosine spacing for the duct and the variable panel length wake approach, as shown in Table 5.2 to Table 5.4. Comparisons were to a coarser discretisation to match the actuator disc study. The worst case found was 1.3% for far wake radius R_w, compared to the bare rotor's 0.9%.

Table 5.1: Discretisation dependence results from the code validation with actuator disc theory study. Change is from a coarser discretisation for panel length = $0.00125D$ and wake length = $32D$.

	% Difference from			
	Doubled Panel Length		Halved Wake Length	
	C_{Topt}	$C_T = 0.95$	C_{Topt}	$C_T = 0.95$
C_P	-0.23	-0.41	0.00	0.00
C_{Topt}	-0.28	-	0.00	-
R_w	-0.03	0.92	0.18	0.88

Table 5.2 Change in duct VA results from a coarser discretisation, for last duct panel length = $0.000625D$ and wake length = $64.0D$.

	% Difference from					
	Doubled Panel Length			Halved Wake Length		
	$C_T = 0$	C_{Topt}	$C_T = 0.95$	$C_T = 0$	C_{Topt}	$C_T = 0.95$
$\dot{m}$ & C_P	-0.19	-0.21	-0.53	0	0.00	0.00
C_{Topt}	-	-0.12	-	-	0.00	-
R_w	-0.03	0.12	1.16	0	0.03	0.34

Table 5.3: Change in duct VB results from a coarser discretisation, for last duct panel length = $0.000571D$ and wake length = $58.5D$.

	% Difference from					
	Doubled Panel Length			Halved Wake Length		
	$C_T = 0$	C_{Topt}	$C_T = 0.95$	$C_T = 0$	C_{Topt}	$C_T = 0.95$
$\dot{m}$ & C_P	-0.11	-0.10	-0.56	0	0.00	0.00
C_{Topt}	-	-0.10	-	-	-0.02	-
R_w	-0.02	0.13	1.31	0	0.01	0.19

Table 5.4: Change in duct VC results from a coarser discretisation, for last duct panel length = $0.000625D$ and wake length = $64.0D$.

	% Difference from					
	Doubled Panel Length			Halved Wake Length		
	$C_T = 0$	C_{Topt}	$C_T = 0.95$	$C_T = 0$	C_{Topt}	$C_T = 0.95$
$\dot{m}$ & C_P	-0.25	-0.29	-0.58	0	0.00	0.00
C_{Topt}	-	-0.13	-	-	-0.07	-
R_w	-0.03	0.10	1.00	0	0.01	0.53

An expanded discretisation study was carried out including the duct drag coefficient C_D, the gauge pressure p at the inlet i, rotor downstream side rd, and exit e, as well was the change in momentum from far upstream to far downstream ΔM. Comparisons to a finer discretisation are shown in Table 5.5 to Table 5.7, where large percentage differences for p_i and C_D at C_T = 0.95 for ducts VA and VB respectively can be ignored due to pressure and drag approaching zero. The largest changes with halved panel length otherwise were 0.3% at C_T = 0 and 0.5% at C_{Topt}, although they did approach 1% at C_T = 0.95. Changes with doubled wake length were less than 0.25%.

Overall, discretisation convergence was both good and in line with the bare rotor study that achieved close agreement to actuator disc theory. However, the results of these simulations were used to test equations that sometimes amplified numerical inaccuracies, so it is important to note where convergence was least good: far wake radius, static pressure, and duct drag, all at high rotor loadings. By examining these equations at all rotor loadings, and sometimes directly accounting for numerical error, the validity of each theory could still be assessed with confidence.

Table 5.5: Change in duct VA results with a finer discretisation, for last duct panel length = $0.000625D$ and wake length = $64.0D$.

	% Difference with					
	Halved Panel Length			Doubled Wake Length		
	$C_T = 0$	C_{Topt}	$C_T = 0.95$	$C_T = 0$	C_{Topt}	$C_T = 0.95$
$\dot{m}$ & C_P	-0.1	-0.11	-0.30	0	0.00	0.00
C_{Topt}	-	-0.13	-	-	0.00	-
C_D	-	-0.10	-0.29	-	0.00	0.00
p_i	-0.01	0.20	-10.36	0	0.00	-0.02
p_{rd}	-0.08	0.07	-0.62	0	0.00	0.00
p_e	-0.10	0.00	-0.64	0	0.00	0.00
ΔM	-	0.06	0.28	-	0.00	0.02
R_w	-0.01	0.05	0.72	0	0.01	0.06

Table 5.6: Change in duct VB results with a finer discretisation, for last duct panel length = $0.000571D$ and wake length = $58.5D$.

	% Difference with					
	Halved Panel Length			Doubled Wake Length		
	$C_T = 0$	C_{Topt}	$C_T = 0.95$	$C_T = 0$	C_{Topt}	$C_T = 0.95$
$\dot{m}$ & C_P	-0.05	-0.05	-0.32	0	0.00	0.00
C_{Topt}	-	-0.03	-	-	0.03	-
C_D	-	-0.17	-14.71	-	-0.05	0.08
p_i	-0.40	0.47	0.93	0	0.25	0.00
p_{rd}	-0.06	-0.13	-0.89	0	-0.05	0.01
p_e	-0.09	-0.19	-0.97	0	-0.03	0.01
ΔM	-	0.20	0.33	-	0.02	0.03
R_w	-0.01	0.09	0.79	0	0.01	0.02

Table 5.7: Change in duct VC results with a finer discretisation, for last duct panel length = $0.000625D$ and wake length = $64.0D$.

	% Difference with					
	Halved Panel Length			Doubled Wake Length		
	$C_T = 0$	C_{Topt}	$C_T = 0.95$	$C_T = 0$	C_{Topt}	$C_T = 0.95$
$\dot{m}$ & C_P	-0.13	-0.15	-0.32	0	0.00	0.00
C_{Topt}	-	-0.14	-	-	0.00	-
C_D	-	-0.10	-0.13	-	0.00	0.00
p_i	0.29	0.47	-0.61	0	0.00	0.00
p_{rd}	0.29	0.41	-0.47	0	0.00	0.00
p_e	-0.07	0.08	-0.53	0	0.00	0.00
ΔM	-	-0.04	0.18	-	0.00	0.04
R_w	-0.01	0.04	0.64	0	0.01	0.09

5.3 A Correction for Radial Variations and Radial Velocity

5.3.1 Derivation of Correction Factor

Unlike the panel method code used for the simulation results, each of the theories undergoing validation treats the flow through a duct as radially uniform. Comparing results from the two approaches was usually straightforward, with the average across the duct cross section used in place of a radially invariant value. In Bernoulli's equation applied to a cross section, however, the velocity magnitude $|\boldsymbol{U}|$ is first squared at each point before being averaged, so a correction factor must be introduced when replacing $\overline{|\boldsymbol{U}|^2}$ with $\overline{|\boldsymbol{U}|}^2$.

It was also convenient to make a further correction and replace the velocity magnitude with the axial velocity u to match the 1D theories. With a correction factor γ_x, the resulting form of Bernoulli's equation is given by Equation 5.2.

$$\frac{p_1}{\rho} + \gamma_{x,1}\frac{\bar{u}_1^2}{2} = \frac{p_2}{\rho} + \gamma_{x,2}\frac{\bar{u}_2^2}{2} \qquad \textbf{Equation 5.2}$$

Throughout this work, properties such as pressure p_j and velocity u_j at a particular station j refer to the mean value in that cross section. For clarity, however, velocity is treated differently in this section and overbars are used to indicate the mean value.

From the definition of $\overline{|\boldsymbol{U}|^2}$ and the standard form of Bernoulli's equation, the correction factor in Equation 5.3 can be derived.

$$\gamma_x = \frac{1}{\bar{u}^2 A}\iint_A |\boldsymbol{U}|^2 \,\mathrm{d}A \qquad \textbf{Equation 5.3}$$

Where it is preferred to correct only for radial variations and so use velocity magnitude rather than axial velocity, the correction factor γ in Equation 5.4 should be used.

$$\gamma = \frac{1}{\overline{|\boldsymbol{U}|}^2 A}\iint_A |\boldsymbol{U}|^2 \,\mathrm{d}A \qquad \textbf{Equation 5.4}$$

5.3.2 Difference from Boussinesq's Momentum Coefficient

The limited discussion found in the general engineering literature suggested that the kinetic energy correction coefficient is sometimes incorrectly used for non-uniform velocity in Bernoulli's equation, and that the momentum correction coefficient β should be used instead [187, 188]. It will be shown here, however, that γ or γ_x should be used when the velocity has more than one component, rather than β. Also known as the Boussinesq coefficient, this factor is given for a purely axial flow by Equation 5.5.

$$\beta = \frac{1}{\rho\bar{u}^2 A}\iint_A \rho u^2 \,\mathrm{d}A \qquad \textbf{Equation 5.5}$$

The Boussinesq coefficient is derived from the momentum equation rather than from Bernoulli's equation itself [189]. As Boussinesq wrote his work [190] in French, it was necessary to re-derive β to find a form applicable to a flow with multiple velocity components for the proper comparison with γ. To begin, the momentum flow term from the momentum equation [69] for the flow through a surface S was applied to an arbitrary cross section of flow perpendicular to the axial direction and with area A in Equation 5.6.

$$\left|\oiint_S (\rho\boldsymbol{U}\cdot\mathbf{d}\boldsymbol{S})\boldsymbol{U}\right| = \left|\iint_A \rho u\boldsymbol{U}\,\mathrm{d}A\right| = \rho|\bar{u}|\beta|\overline{\boldsymbol{U}}|A \qquad \textbf{Equation 5.6}$$

To obtain a single value for β, the magnitude was taken for the momentum flow term, with the right hand side showing a version with mean values and β. Although $\bar{u}$ is not vector valued, $|\bar{u}|$ is still used to account for negative values. Rearranging gives Equation 5.7.

$$\beta = \frac{1}{\rho|\bar{u}||\overline{\boldsymbol{U}}|A}\left|\iint_A \rho u \boldsymbol{U}\,\mathrm{d}A\right| \qquad \textbf{Equation 5.7}$$

Comparison with Equation 5.4 shows that γ and β are different where non-axial velocity components exist; in general, they are two distinct correction factors that are equal when the velocity vector is normal to a surface. Pressure predictions support the use of γ: values of each correction factor for the duct exit velocity profile in Figure 5.2 are shown in Table 5.8, and only the γ approaches gave the correct $C_{p,e}$ of -5.02 when calculated using the appropriate forms of Bernoulli's equation. γ is therefore the theoretically correct coefficient generally, and γ_x here when using axial velocity rather than velocity magnitude.

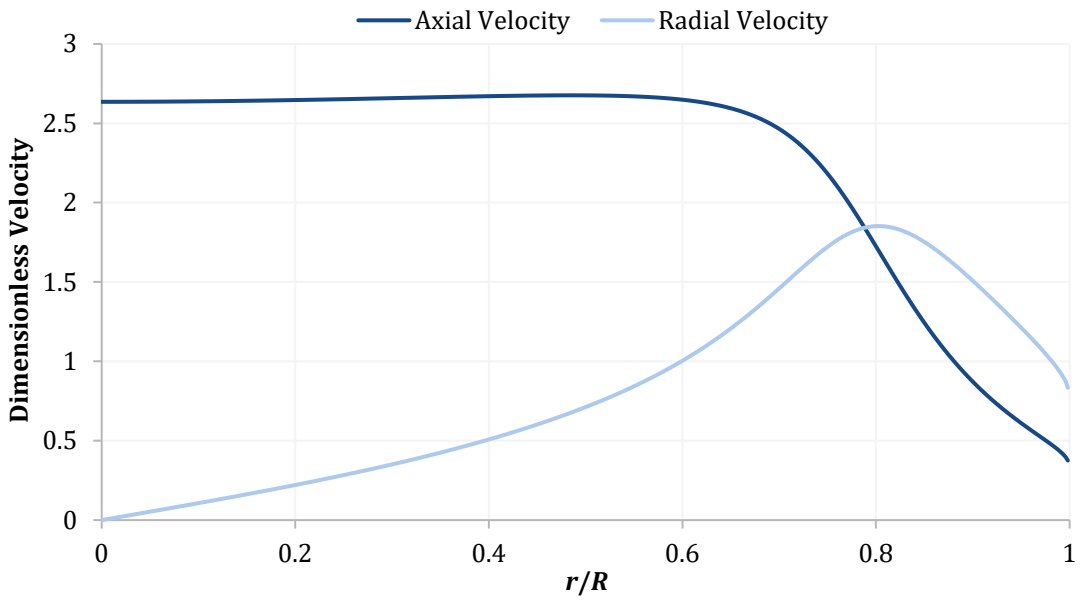

Figure 5.2: Velocity profiles u_e/u_∞ and v_e/u_∞ used in comparison of correction factors, computed for a duct exit by the panel method code.

Table 5.8: Pressure coefficients $C_{p,e}$ calculated using the correction factors. Both β values and γ were used with velocity magnitude, while γ_x was used with axial velocity.

	Factor Value	Calculated $C_{p,e}$	% Error
β (Axial)	1.18	-5.72	13.9
β (Magnitude)	0.96	-4.48	-10.8
γ	1.06	-5.02	0.0
γ_x	1.59	-5.02	0.0

5.3.3 Importance of Correction Factor

Values of γ_x for the three ducts chosen in Section 5.2 are given in Figure 5.3, with rotor loading, position in the duct, and duct shape all showing a significant influence. Although $\gamma_{x,e}$ was relatively constant with C_T, the changing exit pressure distribution seen in Section 3.1.7 suggests a greater variation with other ducts. Neglecting radial variations and radial velocities leads to larger equation inequalities than a peak value of 2 for γ_x would suggest, as seen in Figure 5.4 for the equations requiring γ_x in Phillips' theory. Introducing the correction factor reduced inequalities by up to 950 percentage points, where percentage points measure the arithmetic difference between percentage values, with only 14% of the 242 cases improved by less than 5 points.

The largest inequality reduction was for Equation 5.9, which states that the total pressures at the duct exit and in the far wake are equal, with an inequality reduction from 946% to 3×10^{-10}%. While using absolute pressure instead of gauge pressure in the uncorrected equation saw the inequality drop to around 0.1%, the inequality magnitude was still large compared to the rotor pressure drop, and rearranging the equation for the static pressure difference would see large percentage inequalities return. Inequality reductions still reached 865 points when using absolute pressure in all of Phillips' equations, the maximum reduction then being for Equation 5.16, with an improvement greater than 5 points in 58% of the cases.

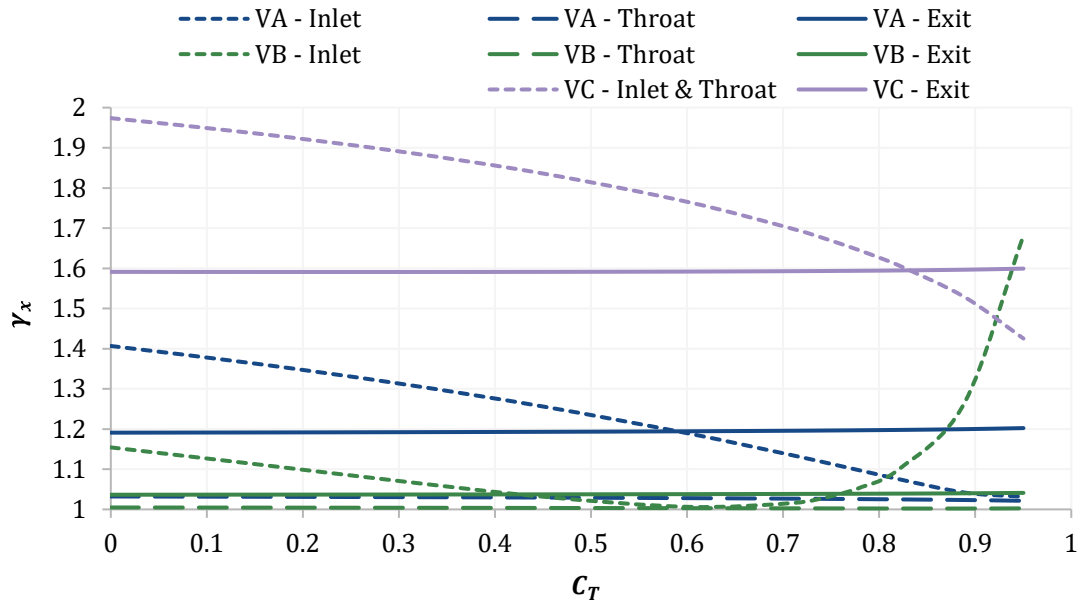

Figure 5.3: Values of correction factor γ_x calculated at the inlet, throat, and exit for ducts VA to VC.

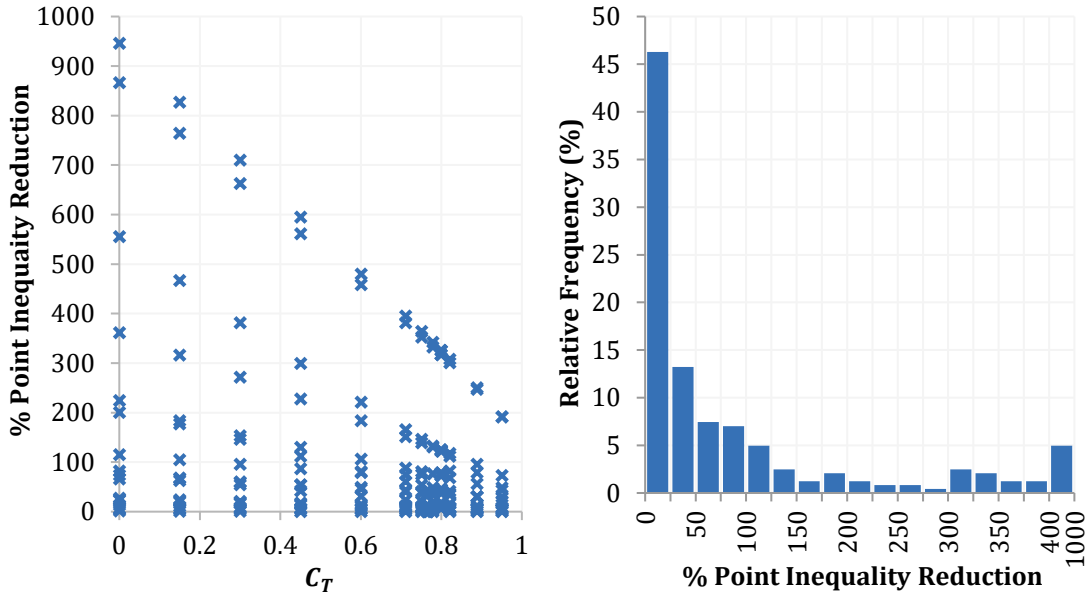

Figure 5.4: Inequality reduction from the introduction of γ_x for Phillips' equations, measured by the percentage point change in the inequality of each equation where γ_x was required. Inequalities were calculated as a percentage of the median right hand side magnitude across rotor loadings.

5.4 Phillips' Theory

Phillips [4] described an analysis of ducted turbines in his thesis that he credited to a confidential report by Snel [191]; the analysis here is based on Phillips' description. He split this theory into two parts, one calculating an energy balance and the other an axial momentum balance, and also set out relationships using Bernoulli's equation before the main analysis. In keeping with the rest of this chapter, velocity correction factors were added to Phillips' equations where needed.

The first relationship links the far upstream pressure p_∞ and velocity u_∞ to the values at the upstream side of the rotor, p_{ru} and u_{ru}, assuming no losses in the inlet. Although the velocity is equal at the upstream side of the rotor ru, in the rotor plane r, and on the downstream side rd, velocity is specified at station station ru to stay consistent with Phillips. Adding the velocity correction factor $\gamma_{x,ru}$ to Equation 4.21 in Phillips' work gave Equation 5.8.

$$p_\infty + \frac{1}{2}\rho u_\infty^2 = p_{ru} + \frac{1}{2}\rho \gamma_{x,ru} u_{ru}^2 \qquad \textbf{Equation 5.8}$$

Table 5.9 shows the results of the validation exercise for this equation, where the inequality values listed are the worst for each duct across all the rotor loadings simulated. With the addition of the correction factor, the relationship is valid for radially varying flow. It should also be valid in one-dimensional flow without the correction factor: as discussed in Section 5.1, the validity of an equation can change depending on the chosen level of simplification.

Table 5.9: Largest absolute inequalities found for Equation 5.8, as a percentage of the median right hand side magnitude across rotor loadings. Phillips designated this relationship, without the correction factor, 4.21.

Inequality for	Duct VA	Duct VB	Duct VC
Equation 5.8	$5\times10^{-12}\%$	$2\times10^{-12}\%$	$2\times10^{-11}\%$

The next relationship connects properties at the duct exit e to those in the far wake w, given by Equation 5.9.

$$p_e + \frac{1}{2}\rho\gamma_{x,e}u_e^2 = p_\infty + \frac{1}{2}\rho u_w^2 \qquad \textbf{Equation 5.9}$$

Numerical inaccuracies meant that the pressure in the far wake did not exactly equal the free stream pressure, with differences of up to 0.41% of the pressure drop across the rotor. To remove the resulting inequalities, p_∞ was replaced with the computed far wake pressure, found at a distance sufficiently far from the rotor that further increases had a negligible effect. The inequality then reduced to zero, as seen in Table 5.10, showing the relationship to be valid.

Table 5.10: Largest absolute inequalities found for Equation 5.9, as a percentage of the median right hand side magnitude across rotor loadings. Phillips designated this relationship, without the correction factor, 4.22.

Inequality for	Duct VA	Duct VB	Duct VC
Equation 5.9	$1\times10^{-11}\%$	$7\times10^{-12}\%$	$1\times10^{-11}\%$

5.4.1 Power from an Energy Balance

The first step Phillips reported for calculating the energy balance was a relationship for the losses in the diffuser section of the duct p_{loss}, given in Equation 5.10.

$$p_{loss} = p_{rd} - p_e + \frac{1}{2}\rho\left(\gamma_{x,rd}u_{rd}^2 - \gamma_{x,e}u_e^2\right) \qquad \textbf{Equation 5.10}$$

As the panel method code models inviscid flow, p_{loss} = 0 in all cases. To provide useful percentage values in Table 5.11, each inequality was divided by the pressure drop across the rotor; results at C_T = 0 were excluded to avoid dividing by zero. The results show that the relationship is a valid one.

Table 5.11: Largest absolute inequalities found for Equation 5.10, as a percentage of the pressure drop across the rotor. Phillips designated this relationship, without the correction factors, 4.24.

Inequality for	Duct VA	Duct VB	Duct VC
Equation 5.10	$1\times10^{-11}\%$	$5\times10^{-12}\%$	$7\times10^{-11}\%$

Phillips then used p_{loss} in the energy balance for a ducted turbine, shown with volume flow rate Q in Equation 5.11.

$$Q\left(\frac{1}{2}\rho u_\infty^2 - \frac{1}{2}\rho u_w^2\right) = u_r F_T + Q p_{loss} \qquad \textbf{Equation 5.11}$$

Small inequalities were found for this equation, as seen in Table 5.12, but they appear to be numerical error. The inequality was largest at the greatest loadings and the relationship depends on velocity in the far wake; the discretisation dependence study showed comparable changes for far wake radius at high rotor loading. This relationship was therefore judged valid.

Table 5.12: Largest absolute inequalities found for Equation 5.11, as a percentage of the median right hand side magnitude across rotor loadings. Phillips designated this relationship 4.25.

Inequality for	Duct VA	Duct VB	Duct VC
Equation 5.11	0.32%	0.36%	0.26%

Phillips next defined diffuser efficiency η_{diff} with Equation 5.12.

$$\eta_{diff} = \frac{p_e - p_{rd}}{\frac{1}{2}\rho\left(\gamma_{x,rd} u_{rd}^2 - \gamma_{x,e} u_e^2\right)} \qquad \textbf{Equation 5.12}$$

Using p_{loss} redefined with η_{diff} and Equation 5.11, the expression for power extracted by the rotor P in Equation 5.13 was derived.

$$P = Q\frac{1}{2}\rho\left(u_\infty^2 - u_w^2 - \left(1-\eta_{diff}\right)\left(\gamma_{x,rd} u_{rd}^2 - \gamma_{x,e} u_e^2\right)\right) \qquad \textbf{Equation 5.13}$$

Phillips then reformulated this equation into the power coefficient C_P using the ratio of velocity at the rotor to free stream velocity $\mathcal{U}_r$ and the ratio of exit area to rotor area $\mathcal{A}_e$. The result is given by Equation 5.14.

$$C_P = \mathcal{U}_r\left(1 - \frac{u_w^2}{u_\infty^2} - \left(1-\eta_{diff}\right)\left(\gamma_{x,rd} - \gamma_{x,e}\mathcal{A}_e^{-2}\right)\mathcal{U}_r^2\right) \qquad \textbf{Equation 5.14}$$

Table 5.13 shows that the previous three equations are valid, although the loss term in Equation 5.13 could not be tested.

Table 5.13: Largest absolute inequalities found for Equation 5.12 to Equation 5.14, as a percentage of the median right hand side magnitude across rotor loadings. Phillips designated these relationships, without the correction factors, 4.26, 4.28, and 4.29.

Inequality for	Duct VA	Duct VB	Duct VC
Equation 5.12	1×10^{-12}%	3×10^{-12}%	1×10^{-12}%
Equation 5.13	0.32%	0.36%	0.26%
Equation 5.14	0.32%	0.36%	0.26%

At this point, Philips noted that it would be more convenient to express power in terms of the duct exit pressure rather than the far wake velocity, and began by using mass flow continuity to define the velocity at the exit with Equation 5.15.

$$u_e = \mathcal{A}_e^{-1} \mathcal{U}_r u_\infty \qquad \textbf{Equation 5.15}$$

Table 5.14 highlights a small error in the numerical results where the mass flow rate was not exactly the same at the rotor and exit. While the difference of 0.34% or less appears insignificant, it is actually important for the remaining equations in this section.

Table 5.14: Largest absolute inequalities found for Equation 5.15, as a percentage of the median right hand side magnitude across rotor loadings. Phillips designated this relationship 4.31.

Inequality for	Duct VA	Duct VB	Duct VC
Equation 5.15	0.01%	0.01%	0.34%

Substituting Equation 5.15 into Equation 5.9 – which was Bernoulli's equation applied between the duct exit and far downstream – then using the definition of exit pressure coefficient led to Equation 5.16.

$$\left(\frac{u_w}{u_\infty}\right)^2 = \gamma_{x,e} \mathcal{A}_e^{-2} \mathcal{U}_r^2 + C_{p,e} \qquad \textbf{Equation 5.16}$$

The small inaccuracy in the far wake pressure seen with Equation 5.9 also affected this equation through $C_{p,e}$, but inequalities remained above 10% even after correction. $\mathcal{U}_r$ was therefore also calculated from the velocity at the exit and mass continuity to compensate for the slight variation in mass flow rate seen in Table 5.14. Table 5.15 then shows the equation to be valid.

Table 5.15: Largest absolute inequalities found for Equation 5.16, as a percentage of the median right hand side magnitude across rotor loadings. Phillips designated this relationship, without the correction factor, 4.32.

Inequality for	Duct VA	Duct VB	Duct VC
Equation 5.16	1×10^{-11}%	7×10^{-12}%	1×10^{-11}%

With an expression relating the far wake velocity to exit pressure derived, it was substituted into Equation 5.14 to achieve the desired relationship between power coefficient and exit pressure, giving Equation 5.17.

$$C_P = \left(1 - C_{p,e}\right)\mathcal{U}_r + \left(\eta_{diff}\left(\gamma_{x,rd} - \gamma_{x,e}\mathcal{A}_e^{-2}\right) - \gamma_{x,rd}\right)\mathcal{U}_r^3 \qquad \textbf{Equation 5.17}$$

Calculating $\mathcal{U}_r$ based on the velocity at the exit and $C_{p,e}$ using the computed far wake pressure, Table 5.16 shows the relationship to be valid.

Table 5.16: Largest absolute inequalities found for Equation 5.17, as a percentage of the median right hand side magnitude across rotor loadings. Phillips designated this relationship, without the correction factors, 4.33.

Inequality for	Duct VA	Duct VB	Duct VC
Equation 5.17	0.33%	0.36%	0.14%

5.4.2 Forces from an Axial Momentum Balance

With an expression for the power coefficient found, Phillips then went on to describe an application of the momentum equation to a ducted turbine. A control volume was defined following the streamtube from far upstream, through the duct, to far downstream, as shown in Figure 5.5. The control volume was considered in parts, with the force acting on it considered separately for the portion upstream of the duct, through the duct, and downstream of the duct, plus the force from the rotor.

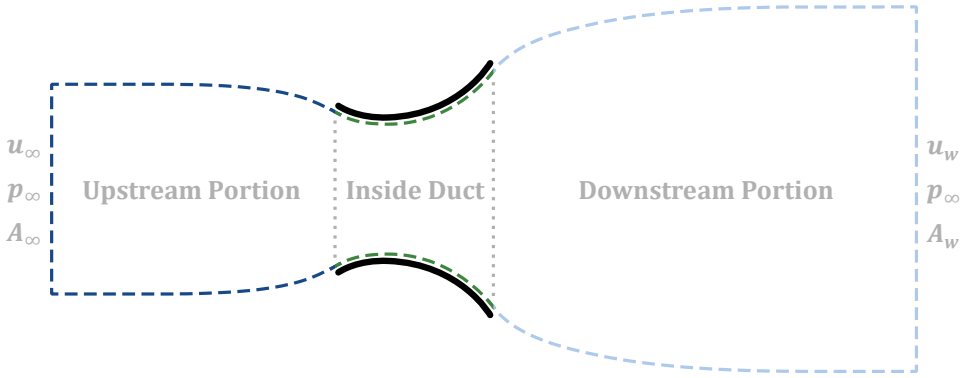

Figure 5.5: Illustration of control volume passing through duct.

Force Calculation for Validation

The aim here was to test the particular formulations of the momentum equation that Phillips described, rather than any sort of test of the momentum equation itself, so different forms of the momentum equation could be used to calculate the control volume forces. Being interested in axial forces only, the derivation of alternatives began with the momentum equation for steady inviscid flow with no body forces. Applying it to the upstream portion of the control volume led to Equation 5.18.

$$-\iint_{A_\infty} \rho u^2 \,\mathrm{d}A + \iint_{A_i} \rho u^2 \,\mathrm{d}A = \iint_{A_\infty} p \,\mathrm{d}A - \iint_{A_i} p \,\mathrm{d}A - \left(\iint_{S_{rad}} p \,\mathbf{dS}\right)_x \qquad \textbf{Equation 5.18}$$

In this equation, the x subscript indicates that only the axial component of the result is used, and the rad subscript signifies the radial surface S of the control volume. It is the pressure on that radial surface combined with the pressure on the upstream end that

constitutes the force on the upstream portion of the control volume F_{us}, as defined in Equation 5.19.

$$F_{us} = \iint_{A_\infty} p \, \mathrm{d}A - \left(\iint_{S_{rad}} p \, \mathbf{dS} \right)_x \qquad \textbf{Equation 5.19}$$

Combining Equation 5.18 and Equation 5.19 gave the calculation procedure for finding F_{us} from the panel method code results, as shown in Equation 5.20.

$$F_{us} = -\iint_{A_\infty} \rho u^2 \, \mathrm{d}A + \iint_{A_i} \rho u^2 \, \mathrm{d}A + \iint_{A_i} p \, \mathrm{d}A \qquad \textbf{Equation 5.20}$$

This procedure required the flow to be computed only at the outlet of the control volume portion, as the far upstream end was at free stream conditions.

Following a similar derivation, the force on the control volume section inside the duct $F_{d,in}$ was calculated using Equation 5.21.

$$F_{d,in} = -\iint_{A_i} \rho u^2 \, \mathrm{d}A + \iint_{A_e} \rho u^2 \, \mathrm{d}A - \iint_{A_i} p \, \mathrm{d}A + \iint_{A_e} p \, \mathrm{d}A + \Delta p A_r \qquad \textbf{Equation 5.21}$$

Finally, the force on the downstream section F_{ds} was calculated assuming a return to free stream pressure rather than with a directly computed downstream pressure, giving Equation 5.22.

$$F_{ds} = -\iint_{A_e} \rho u^2 \, \mathrm{d}A + \iint_{A_w} \rho u^2 \, \mathrm{d}A - \iint_{A_e} p \, \mathrm{d}A \qquad \textbf{Equation 5.22}$$

Validation of Momentum Relationships

Modifying Phillips' expression for the upstream portion force to include the correction factors, with β defined using axial velocity only as in Equation 5.5, gave Equation 5.23.

$$F_{us} = \frac{1}{2} \rho u_\infty^2 A_{ru} \left[(1 - \mathcal{U}_r)^2 + \left(2\beta_{ru} - \gamma_{x,ru} - 1 \right) \mathcal{U}_r^2 \right] \qquad \textbf{Equation 5.23}$$

In this equation, the downstream end of the control volume portion is placed at the rotor and the momentum balance therefore includes any section of duct upstream of the rotor. Phillips, however, also stated that the relation is for the upstream free streamtube, suggesting that no part of the duct is included. It appears that the rotor is assumed to be at the inlet; rewriting to accommodate a duct where it is not gave Equation 5.24.

$$F_{us} = \frac{1}{2} \rho u_\infty^2 A_i \left[(1 - \mathcal{U}_i)^2 + \left(2\beta_i - \gamma_{x,i} - 1 \right) \mathcal{U}_i^2 \right] \qquad \textbf{Equation 5.24}$$

Table 5.17 shows the results of testing this relationship. Equation 5.23 had a large inequality for ducts VA and VB but was valid for duct VC due to the presence and lack of an inlet respectively. Once the equation had been modified to account for an inlet section, it matched in all cases.

Table 5.17: Largest absolute inequalities found for Equation 5.23 and Equation 5.24, as a percentage of the median right hand side magnitude across rotor loadings. Phillips designated this relationship, without the correction factors, 4.40.

Inequality for	Duct VA	Duct VB	Duct VC
Equation 5.23	563.6%	2853%	1×10^{-11}%
Equation 5.24	0.25%	9×10^{-11}%	1×10^{-11}%

The force on the flow from the rotor F_r was defined with Equation 5.25, which was also the method used to calculate F_r in the panel method code.

$$F_r = -(p_{ru} - p_{rd})A_r \qquad \textbf{Equation 5.25}$$

Phillips continued the rotor at inlet assumption in calculating the control volume force on the inside of the duct. With no inlet the duct consists only of a diffuser section, and the force was defined as F_{diff} using Equation 5.26.

$$F_{diff} = \iint_R p \, \mathrm{d}r\mathrm{d}\theta \qquad \textbf{Equation 5.26}$$

Equation 5.27 was then stated, with no details of the derivation supplied and assuming zero losses in the diffuser.

$$F_{diff} = \left(p + \frac{1}{2}\rho u^2\right)(A_e - A_{rd}) - \frac{1}{2}\rho Q^2 \left(\frac{A_e - A_{rd}}{A_{rd}A_e}\right) \qquad \textbf{Equation 5.27}$$

The first term on the right hand side is the total pressure in the flow, calculated for validation as the free stream total pressure minus the rotor pressure drop.

As it was derived assuming no inlet, Equation 5.27 was expected to be invalid for ducts VA and VB. However, Table 5.18 shows a large inequality even for duct VC, which remained above 16% for all rotor loadings. It seems likely that velocity correction factors are required to make this relationship valid outside one-dimensional flow, but the correct re-derivation could not be found in the time available.

Table 5.18: Largest absolute inequalities found for Equation 5.27, as a percentage of the median right hand side magnitude across rotor loadings. Phillips designated this relationship 4.43.

Inequality for	Duct VA	Duct VB	Duct VC
Equation 5.27	207.2%	137.0%	90.0%

The final section of control volume was the downstream portion, with the force given by Phillips as Equation 5.28.

$$F_{ds} = \frac{1}{2}\rho u_\infty^2 A_{ru}\left\{2\mathcal{U}_r\left[\left(\gamma_{x,e}\mathcal{A}_e^{-2}\mathcal{U}_r^2 + C_{p,e}\right)^{1/2} - \beta_e\mathcal{A}_e^{-1}\mathcal{U}_r\right] - \frac{C_{p,e}}{\mathcal{A}_e^{-1}}\right\} \quad \textbf{Equation 5.28}$$

The small variation in mass flow through the duct was compensated for by calculating $\mathcal{U}_r$ from the velocity at the duct exit using Equation 5.15. Inequalities above 6% were then reduced to those in Table 5.19, showing the equation to be valid.

Table 5.19: Largest absolute inequalities found for Equation 5.28, as a percentage of the median right hand side magnitude across rotor loadings. Phillips designated this relationship, without the correction factors, 4.45.

Inequality for	Duct VA	Duct VB	Duct VC
Equation 5.28	0.03%	0.03%	0.02%

At this point, an expression exists for all the forces acting on the control volume. Phillips gave Equation 5.29 as the final axial momentum balance for the turbine.

$$F_{us} + F_r + F_{d,in} + F_{ds} = \rho\mathcal{U}_r u_\infty A_{ru}(u_w - u_\infty) \quad \textbf{Equation 5.29}$$

While Phillips used F_{diff} in this equation, $F_{d,in}$ was used instead here so that the force was calculated for the entire duct and not just the diffuser section. With this change made, Table 5.20 shows that the relationship matched moderately well. The inequalities were at their maximum at the largest rotor loading, and by C_T = 0.8 they had more than halved. This behaviour is likely due to the reduced discretisation convergence at the wake end with high rotor loading, so the relationship appears valid.

Table 5.20: Largest absolute inequalities found for Equation 5.29, as a percentage of the median right hand side magnitude across rotor loadings. Phillips designated this relationship 4.46.

Inequality for	Duct VA	Duct VB	Duct VC
Equation 5.29	1.10%	1.35%	0.85%

5.4.3 Summary: A Valid Theory

Despite some difficulties with relationships that are sensitive to numerical error, almost all are valid once the appropriate velocity correction factors are in place. Table 5.21 shows that only the relationship tested in Table 5.18 could not be validated, and that was more likely due to a lack of correction factors rather than an error in the equation itself. While the final equations derived through the energy and axial momentum approaches are valid, however, they rely on a number of empirical parameters.

Table 5.21: Summary of conclusions for Phillips' Equations.

Table of Inequalities	Phillips' Designation	Conclusion for Relationship
Table 5.9	4.21	Valid with correction factor
Table 5.10	4.22	Valid with correction factor
Table 5.11	4.24	Valid with correction factors
Table 5.12	4.25	Valid
Table 5.13	4.26, 4.28, 4.29	Valid with correction factors
Table 5.14	4.31	Valid
Table 5.15	4.32	Valid with correction factor
Table 5.16	4.33	Valid with correction factors
Table 5.17	4.40	Valid with correction factors
Table 5.18	4.43	Could not validate
Table 5.19	4.45	Valid with correction factors
Table 5.20	4.46	Valid

5.5 Sørensen's Theory

In his work, Sørensen [185] set out to develop a theoretical description of ducted turbines that could predict the maximum power extracted without empirical measurements. He reached an equation that calculates C_{Pmax} only from geometrical measurements of a duct, but made several assumptions that he acknowledged were untested. Such a theory would be invaluable to the development of ducted turbines, but unfortunately this section will show that it cannot correctly predict C_{Pmax} for the ducts tested.

5.5.1 Calculations with Exit Pressure

To begin, Sørensen used a control volume analysis to derive Equation 5.30.

$$Q\left(\frac{1}{2}\rho u_\infty^2 - \frac{1}{2}\rho u_w^2\right) = P + Qp_{loss} \qquad \textbf{Equation 5.30}$$

Rearranging for the power extracted by the rotor gave Equation 5.31.

$$P = \frac{1}{2}\,\rho u_r A_r\left(u_\infty^2 - u_w^2 - 2\frac{p_{loss}}{\rho}\right) \qquad \textbf{Equation 5.31}$$

In Equation 5.32, the p_{loss} term was replaced by one involving the diffuser efficiency η_{diff}.

$$P = \frac{1}{2}\,\rho u_r A_r\left[u_\infty^2 - u_w^2 - \left(1-\eta_{diff}\right)\left(\gamma_{x,r}u_r^2 - \gamma_{x,e}u_e^2\right)\right] \qquad \textbf{Equation 5.32}$$

At this point the velocity and area ratios were introduced, giving an equation for the power coefficient in Equation 5.33.

$$C_P = \mathcal{U}_r\left[1 - \mathcal{U}_w^2 - \left(1 - \eta_{diff}\right)\left(\gamma_{x,r} - \gamma_{x,e}\mathcal{A}_e^{-2}\right)\mathcal{U}_r^2\right] \qquad \textbf{Equation 5.33}$$

While Sørensen assumed the rotor to be at the inlet when calculating losses, the equations could be tested here without modification due to the zero loss simulations. Table 5.22 shows the results. All are valid based on the small inequalities found, although the equations were not tested in the presence of viscous losses so results may differ in that case.

Table 5.22: Largest absolute inequalities found for Equation 5.30 to Equation 5.33, as a percentage of the median right hand side magnitude across rotor loadings. Sørensen designated these relationships, without the correction factors, 3.23, 3.24, 3.28, and 3.29.

Inequality for	Duct VA	Duct VB	Duct VC
Equation 5.30	0.32%	0.36%	0.26%
Equation 5.31	0.32%	0.36%	0.26%
Equation 5.32	0.32%	0.36%	0.26%
Equation 5.33	0.32%	0.36%	0.26%

Beginning the process of removing the far wake velocity from the C_P equation, Bernoulli's equation was applied between the duct exit and far downstream in Equation 5.34.

$$p_e + \gamma_{x,e}\frac{1}{2}\rho u_e^2 = p_\infty + \frac{1}{2}\rho u_w^2 \qquad \textbf{Equation 5.34}$$

Equation 5.35 is then a dimensionless form of Equation 5.34.

$$\mathcal{U}_w^2 = \gamma_{x,e}\mathcal{U}_e^2 + \frac{p_e - p_\infty}{1/2\,\rho u_\infty^2} \qquad \textbf{Equation 5.35}$$

As was discussed in Section 5.4, there was a small numerical inaccuracy in the far wake simulation results. Compensating by using the computed far wake pressure rather than assuming the free stream value showed the equations to be valid with the inequalities in Table 5.23.

Table 5.23: Largest absolute inequalities found for Equation 5.34 and Equation 5.35, as a percentage of the median right hand side magnitude across rotor loadings. Sørensen designated these relationships, without the correction factors, 3.30 and 3.31.

Inequality for	Duct VA	Duct VB	Duct VC
Equation 5.34	1×10^{-11}%	7×10^{-12}%	1×10^{-11}%
Equation 5.35	1×10^{-11}%	7×10^{-12}%	1×10^{-11}%

Using the relationship for far wake velocity, Equation 5.33 was modified to give Equation 5.36.

$$C_P = \mathcal{U}_r\{1 - C_{p,e} + [\eta_{diff}(\gamma_{x,r} - \gamma_{x,e}\mathcal{A}_e^{-2}) - \gamma_{x,r}]\mathcal{U}_r^2\} \quad \textbf{Equation 5.36}$$

Small numerical inaccuracies also affected this equation. These were compensated for by replacing the computed value of the duct exit pressure coefficient by one calculated from the mass flow rate at the rotor, mass continuity, and the velocity correction factor at the duct exit. Although the differences for $C_{p,e}$ were less than 0.5%, Table 5.24 shows a large impact existed on the inequalities for duct VC. It also appears that the relationship is valid.

Table 5.24: Largest absolute inequalities found for Equation 5.36, as a percentage of the median right hand side magnitude across rotor loadings. Sørensen designated this relationship, without the correction factors, 3.32.

Inequality for Equation 5.36	Duct VA	Duct VB	Duct VC
Using $C_{p,e}$ as computed	0.11%	0.04%	5.32%
Using calculated $C_{p,e}$	2×10^{-13}%	1×10^{-13}%	2×10^{-13}%

With an appropriate equation for the power coefficient developed, Sørensen made simplifying assumptions in an attempt to find the optimum operating condition. By assuming that $C_{p,e}$ and η_{diff} do not vary strongly with mass flow rate near the optimum, Equation 5.36 could be differentiated with $C_{p,e}$ and η_{diff} set as constants. This led to the optimum value for $\mathcal{U}_r$ shown in Equation 5.37.

$$\mathcal{U}_{r,opt} = \sqrt{\frac{1 - C_{p,e}}{3[\gamma_{x,r} - \eta_{diff}(\gamma_{x,r} - \gamma_{x,e}\mathcal{A}_e^{-2})]}} \quad \textbf{Equation 5.37}$$

It was necessary to assume here that the velocity correction factors were also constant near the optimum. The computed values, however, supported this assumption for all factors included except $\gamma_{x,r}$ for duct VC.

Based on his result for the optimum rotor velocity, Sørensen derived the maximum power coefficient in Equation 5.38 and associated rotor loading in Equation 5.39.

$$C_{Pmax} = \frac{2}{3}\sqrt{\frac{1 - C_{p,e}}{3[\gamma_{x,r} - \eta_{diff}(\gamma_{x,r} - \gamma_{x,e}\mathcal{A}_e^{-2})]}}(1 - C_{p,e}) \quad \textbf{Equation 5.38}$$

$$C_{Topt} = \frac{2}{3}(1 - C_{p,e}) \quad \textbf{Equation 5.39}$$

Table 5.25 shows that large inequalities existed for these relationships, and using the calculated value for $C_{p,e}$ as in Equation 5.36 did not reduce them. The relationships are therefore not valid, likely due to the assumptions being invalid.

Table 5.25: Absolute inequalities found at $C_{T_{opt}}$ for Equation 5.37 to Equation 5.39, as a percentage of the right hand side. Sørensen designated these relationships, without the correction factors, 3.33 to 3.35.

Inequality for	Duct VA	Duct VB	Duct VC
Equation 5.37	30.5%	14.1%	46.8%
Equation 5.38	15.3%	3.12%	38.6%
Equation 5.39	35.1%	15.1%	58.2%

5.5.2 Calculations with Duct Force

Sørensen then began investigating the role of the force on the duct. Beginning with Bernoulli's equation applied from far upstream to far downstream, and assuming no losses inside the duct, he found Equation 5.40.

$$\Delta p = \frac{1}{2}\rho(u_\infty^2 - u_w^2) \qquad \textbf{Equation 5.40}$$

Table 5.26 confirms the validity of this relationship.

Table 5.26: Largest absolute inequalities found for Equation 5.40, as a percentage of the median right hand side magnitude across rotor loadings. Sørensen designated this relationship 3.36.

Inequality for	Duct VA	Duct VB	Duct VC
Equation 5.40	0.43%	0.52%	0.35%

Applying the momentum equation to a control volume extending from far upstream to far downstream gave Equation 5.41, where F_T is the thrust force on the rotor and F_D is the axial force on the duct.

$$F_T + F_D = \rho u_r A_r (u_\infty^2 - u_w^2) \qquad \textbf{Equation 5.41}$$

Although the control volume being analysed passes through the inside of the duct, personal communication with Sørensen confirmed that F_D is the total force acting on the duct and not just the force on the portion in contact with the control volume. Table 5.27 shows that the equation is indeed valid, with reduced discretisation convergence for duct drag and far wake conditions at high rotor loadings likely explaining the 0.76% result. Around C_T = 8/9, the inequality drops below 0.5% for duct VB and continues to drop as the rotor loading decreases.

Table 5.27: Largest absolute inequalities found for Equation 5.41, as a percentage of the median right hand side magnitude across rotor loadings. Sørensen designated this relationship 3.37.

Inequality for	Duct VA	Duct VB	Duct VC
Equation 5.41	0.58%	0.76%	0.58%

Combining Equation 5.40 and Equation 5.41, and making the result dimensionless, gave Equation 5.42.

$$\mathcal{U}_r = \frac{1}{2}(1 + \mathcal{U}_w)\left(1 + \frac{F_D}{F_T}\right) \qquad \textbf{Equation 5.42}$$

Assuming zero losses in the duct, Equation 5.42 was substituted into Equation 5.33 to give Equation 5.43.

$$C_P = \frac{1}{2}(1 + \mathcal{U}_w)(1 - \mathcal{U}_w^2)\left(1 + \frac{F_D}{F_T}\right) \qquad \textbf{Equation 5.43}$$

Table 5.28 shows that both of these relationships are valid.

Table 5.28: Largest absolute inequalities found for Equation 5.42 and Equation 5.43, as a percentage of the median right hand side magnitude across rotor loadings. Sørensen designated these relationships 3.39 and 3.40.

Inequality for	Duct VA	Duct VB	Duct VC
Equation 5.42	0.13%	0.22%	0.30%
Equation 5.43	0.19%	0.18%	0.08%

Sørensen then assumed that F_D/F_T was independent of the far wake velocity in order to differentiate Equation 5.43 and find the maximum power in Equation 5.44.

$$C_{Pmax} = \frac{16}{27}\left(1 + \frac{F_D}{F_T}\right) \qquad \textbf{Equation 5.44}$$

With changes of less than 0.2% with increased discretisation for the included variables, the inequalities in Table 5.29 suggest that the equation is not valid. Sørensen also derived the value of 1/3 for $\mathcal{U}_{w,opt}$ under the same assumption, which was in error by 10-14% for ducts VA-VC. While there is some agreement for Equation 5.44, its usefulness as an approximation is limited: one must already know C_{Pmax} so that the optimum F_D/F_T can be used, and using F_D/F_T at C_T = 0.15 gave inequalities ≈20%.

Table 5.29: Absolute inequalities found at C_{Topt} for Equation 5.44, as a percentage of the right hand side. Sørensen designated this relationship 3.42.

Inequality for	Duct VA	Duct VB	Duct VC
Equation 5.44	2.25%	4.03%	2.41%

5.5.3 Final Simplifications

Beginning an alternative approach, Sørensen applied the assumption of no losses in the duct to Equation 5.36 and found Equation 5.45.

$$C_P = \mathcal{U}_r\left(1 - C_{p,e} - \gamma_{x,e}\mathcal{A}_e^{-2}\mathcal{U}_r^2\right) \qquad \textbf{Equation 5.45}$$

With the simulation results having zero viscous losses, the inequalities for this equation were identical to those for Equation 5.36. Table 5.30 confirms that the relationship is valid.

Table 5.30: Largest absolute inequalities found for Equation 5.45, as a percentage of the median right hand side magnitude across rotor loadings. Sørensen designated this relationship, without the correction factor, 3.43.

Inequality for Equation 5.45	Duct VA	Duct VB	Duct VC
Using $C_{p,e}$ as computed	0.11%	0.04%	5.32%
Using calculated $C_{p,e}$	2×10^{-13}%	1×10^{-13}%	4×10^{-13}%

Assuming now that the duct exit pressure was independent of mass flow near the optimum rotor loading, Sørensen derived the optimum operating conditions in Equation 5.46 to Equation 5.48.

$$\mathcal{U}_{r,opt} = \sqrt{\frac{1 - C_{p,e}}{3\gamma_{x,e}\mathcal{A}_e^{-2}}} \qquad \textbf{Equation 5.46}$$

$$C_{Pmax} = \frac{2}{3\sqrt{3\gamma_{x,e}}\mathcal{A}_e^{-2}}\left(1 - C_{p,e}\right)\sqrt{1 - C_{p,e}} \qquad \textbf{Equation 5.47}$$

$$C_{Topt} = \frac{2}{3}\left(1 - C_{p,e}\right) \qquad \textbf{Equation 5.48}$$

Table 5.31 shows that none of these relationships are valid, and the inequalities were not improved by using the calculated value for $C_{p,e}$.

Table 5.31: Absolute inequalities found at C_{Topt} for Equation 5.46 to Equation 5.48, as a percentage of the right hand side. Sørensen designated these relationships, without the correction factors, 3.44 to 3.46.

Inequality for	Duct VA	Duct VB	Duct VC
Equation 5.46	30.5%	14.1%	46.8%
Equation 5.47	15.3%	3.12%	38.6%
Equation 5.48	35.1%	15.1%	58.2%

As a final step, Sørensen assumed that both the duct exit pressure and F_D/F_T were independent of mass flow at the optimum rotor loading. Using C_{Topt} = 8/9, derived from the optimum $\mathcal{U}_w$ = 1/3, with Equation 5.48 gave $C_{p,e}$ = -1/3. Inserting this value into Equation 5.47 gave Equation 5.49.

$$C_{Pmax} = \frac{16}{27\sqrt{\gamma_{x,e}}}\left(\frac{A_e}{A_r}\right) \qquad \textbf{Equation 5.49}$$

It has already been shown in Section 3.1.2 that the area ratio alone is not sufficient to characterise the performance of a duct, and Table 5.32 shows that the addition of $\gamma_{x,e}$ does not make this relationship valid.

Table 5.32: Absolute inequalities found at C_{Topt} for Equation 5.49, as a percentage of the right hand side. Sørensen designated this relationship, without the correction factor, 3.47.

Inequality for	Duct VA	Duct VB	Duct VC
Equation 5.49	38.1%	0.90%	93.5%

5.5.4 Invalid Assumptions

Sørensen made three important and untested assumptions in an effort to find a simplified ducted turbine theory. These were that the exit pressure coefficient does not vary with mass flow rate and that the ratio of duct drag to rotor thrust does not vary with mass flow rate or far wake velocity. All of these assumptions were applied at the optimum rotor loading to derive the optimum conditions.

Each of these assumptions was tested by plotting against the dimensionless mass flow rate $\dot{m}/(\rho A_r u_\infty)$ and dimensionless far wake velocity u_w/u_∞, although it was not possible to vary these parameters in isolation: C_T was varied to cause the changes in mass flow and velocity. Figure 5.6 and Figure 5.7 show the results of these tests, and all had a clear variation that did not reduce near the optimum conditions. The assumptions therefore do not hold, explaining why the simplified equations derived are not valid.

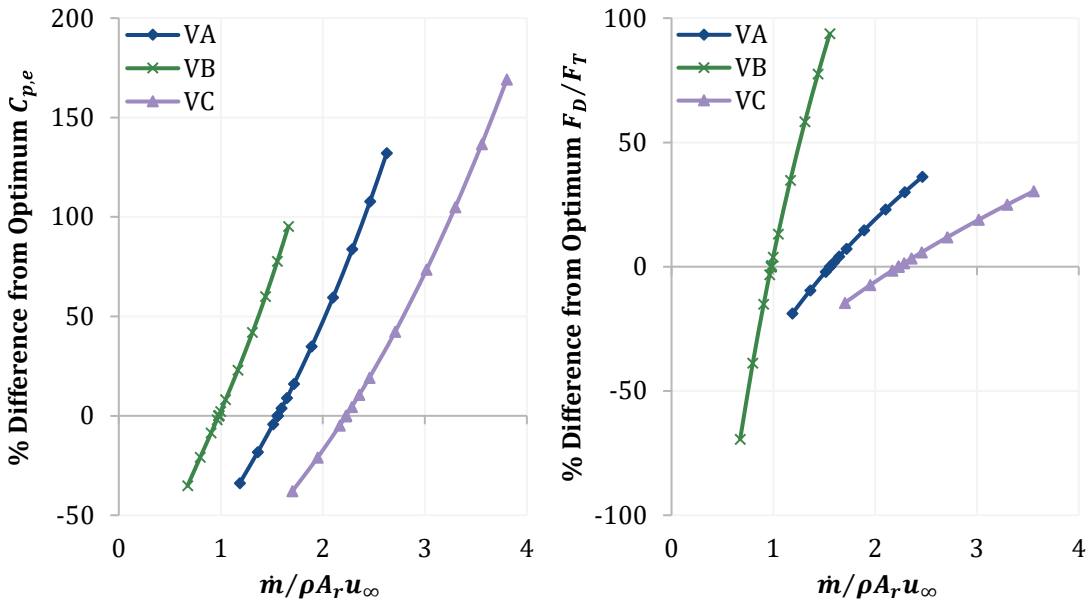

Figure 5.6: Difference from the value at the optimum rotor loading for exit pressure coefficient $C_{p,e}$ (left) and force ratio F_D/F_T (right), for each value of dimensionless mass flow rate $\dot{m}/\rho A_r u_\infty$ and for ducts VA, VB, and VC.

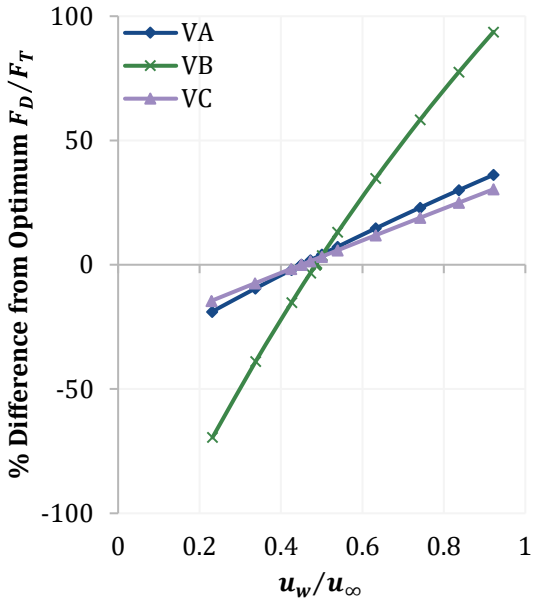

Figure 5.7: Difference from the value at the optimum rotor loading for force ratio F_D/F_T, for each value of dimensionless far wake velocity u_w/u_∞ and for ducts VA, VB, and VC.

5.5.5 Summary: Partly Valid

Sørensen derived a number of valid equations, some of which require the inclusion of correction factors to be valid outside one dimensional flow, as Table 5.33 shows. The relationships resulting from simplifying assumptions, however, were unfortunately found to be invalid; empirical parameters are still required to calculate duct performance.

Table 5.33: Summary of conclusions for Sørensen's Equations.

Table of Inequalities	Sørensen's Designation	Conclusion for Relationship
Table 5.22	3.23, 3.24	Valid
Table 5.22	3.28, 3.29	Valid with correction factors
Table 5.23	3.30, 3.31	Valid with correction factors
Table 5.24	3.32	Valid with correction factors
Table 5.25	3.33 – 3.35	Not valid
Table 5.26	3.36	Valid
Table 5.27	3.37	Valid
-	3.38	Equal to 3.39
Table 5.28	3.39, 3.40	Valid
-	3.41	Equal to 3.36
Table 5.29	3.42	Not valid
Table 5.30	3.43	Valid with correction factor
Table 5.31	3.44 – 3.46	Not valid
Table 5.32	3.47	Not Valid

5.6 Werle and Presz's Theory

Werle and Presz [108] took a different approach to simplifying ducted turbine theory. While not aiming to completely remove empirical parameters as Sørensen did, they drew inspiration from ducted propeller theory to define a duct axial force coefficient meant to be invariant with rotor loading.

5.6.1 Calculating Power from Duct Drag

Their description of a ducted turbine began with the relationship for the power extracted in Equation 5.50, derived from mass, momentum, and energy conservation.

$$P = \left[\frac{1}{2}\rho A_r(u_w^2 - u_\infty^2) + F_D\right]\frac{(u_w + u_\infty)}{2} \qquad \textbf{Equation 5.50}$$

In this equation F_D was modelled in the same way as it has been for ducted propellers. Logically this force should therefore be the total for the duct, although neither Werle and Presz nor their ducted propeller reference [192] show that to be true. Using the total axial force in Table 5.34 nevertheless shows the relationship to be valid. Note that power extraction by the rotor results in a negative value of P in this equation.

Table 5.34: Largest absolute inequalities found for Equation 5.50, as a percentage of the median right hand side magnitude across rotor loadings. Werle and Presz designated this relationship 1.

Inequality for	Duct VA	Duct VB	Duct VC
Equation 5.50	0.07%	0.12%	0.13%

Equation 5.51 defines their duct axial force coefficient C_S.

$$F_D = \frac{1}{2}\rho A_r(u_w^2 - u_\infty^2)C_S \qquad \textbf{Equation 5.51}$$

Using this coefficient in the relationship for velocity at the rotor gave Equation 5.52.

$$u_r = \frac{1}{2}(1 + C_S)(u_w + u_\infty) \qquad \textbf{Equation 5.52}$$

Werle and Presz stated that C_S can be measured at C_T = 0 and used for all rotor loadings, but Table 5.35 shows that large inequalities ensue unless C_S is calculated for each rotor loading individually. While the relationship in Equation 5.52 is therefore valid, the assumption of a constant C_S is not. Note that while the variable C_S was calculated directly from force using Equation 5.51, the constant C_S value had to be calculated from Equation 5.52 itself to avoid a result of $0/0$ at C_T = 0. As inequalities from the C_S assumption were also greater than 10% in the remaining equations, they were tested with a variable C_S to check for other inaccuracies.

Table 5.35: Largest absolute inequalities found for Equation 5.52, as a percentage of the median right hand side magnitude across rotor loadings. Werle and Presz designated this relationship 3a.

Inequality for Equation 5.52	Duct VA	Duct VB	Duct VC
Using C_S at C_T = 0	22.0%	28.3%	22.5%
Using variable C_S	0.26%	0.25%	0.32%

The total drag on the ducted turbine was then given as Equation 5.53, where F_{TD} is the thrust force F_T plus the duct drag force F_D.

$$F_{TD} = \frac{(1 + C_S)P}{u_r} \qquad \textbf{Equation 5.53}$$

A second calculation for F_{TD} was then given using Equation 5.54.

$$F_{TD} = \frac{2P}{(u_w + u_\infty)} \qquad \textbf{Equation 5.54}$$

Table 5.36 shows that Equation 5.53 is valid when using the variable version of C_S, and – with the dependence on C_S removed – that Equation 5.54 is valid without proviso.

Table 5.36: Largest absolute inequalities found for Equation 5.53 and Equation 5.54, as a percentage of the median right hand side magnitude across rotor loadings. Werle and Presz designated these relationships 3b.

Inequality for	Duct VA	Duct VB	Duct VC
Equation 5.53 using variable C_S	0.18%	0.06%	0.20%
Equation 5.54	0.20%	0.33%	0.27%

Werle and Presz asserted at this point that Equation 5.50 to Equation 5.54 can be used to derive the maximum power coefficient in Equation 5.55, which was made positive for power extraction by using $-P$ in the power coefficient definition.

$$C_{Pmax} = \frac{16}{27}(1 + C_S) \qquad \textbf{Equation 5.55}$$

Table 5.37 suggests that this relationship is not valid, even when using C_S at C_{Topt}. All the relationships used to derive it are valid with variable C_S, so the invalid result here comes from an unstated assumption of C_{Topt} = 8/9: this assumption was necessary to re-derive Equation 5.55, and it can also be found by substituting u_w from Equation 5.56 below into a dimensionless form of Equation 5.40. Section 3.1.4 shows that C_{Topt} = 8/9 is not a valid assumption.

Table 5.37: Absolute inequalities found at C_{Topt} for Equation 5.55, as a percentage of the right hand side. Werle and Presz designated this relationship 4.

Inequality for Equation 5.55	Duct VA	Duct VB	Duct VC
Using C_S at C_{Topt}	2.37%	4.09%	2.53%

Werle and Presz then derived the optimum values in Equation 5.56 to Equation 5.58.

$$\mathcal{U}_{w,opt} = \frac{1}{3} \quad \textbf{Equation 5.56}$$

$$\mathcal{U}_{r,opt} = \frac{2}{3}(1 + C_S) \quad \textbf{Equation 5.57}$$

$$\left(\frac{\mathcal{U}_r}{\mathcal{U}_w}\right)_{opt} = 2(1 + C_S) \quad \textbf{Equation 5.58}$$

As expected, Table 5.38 shows that these relationships are not valid.

Table 5.38: Absolute inequalities found at C_{Topt} for Equation 5.56 to Equation 5.58, as a percentage of the right hand side. Werle and Presz designated these relationships 5a, 5b, and 5c.

Inequality for	Duct VA	Duct VB	Duct VC
Equation 5.56	35.0%	45.7%	34.9%
Equation 5.57 using C_S at C_{Topt}	8.58%	11.3%	8.40%
Equation 5.58 using C_S at C_{Topt}	19.6%	23.6%	19.6%

Deriving now a relationship for power coefficient based on rotor loading and duct drag, Werle and Presz found Equation 5.59.

$$C_P = \left(1 + \frac{C_S}{2}\right) C_T\left(1 + \sqrt{1 - C_T}\right) \quad \textbf{Equation 5.59}$$

Despite being derived from the valid Equation 5.50 to Equation 5.54, along with the standard definition for C_T, Table 5.39 shows large inequalities. Perhaps there was another unstated assumption in the derivation. In any case, the relationship is not valid.

Table 5.39: Largest absolute inequalities found for Equation 5.59, as a percentage of the median right hand side magnitude across rotor loadings. Werle and Presz designated this relationship 7.

Inequality for	Duct VA	Duct VB	Duct VC
Equation 5.59 using variable C_S	32.9%	45.3%	25.5%

5.6.2 Calculating Power from Exit Pressure

Werle and Presz then began a derivation for C_{Pmax} from $C_{p,e}$ with Equation 5.60.

$$C_{p,e} = \mathcal{U}_w^2 - \gamma_{x,e}\mathcal{A}_e^{-2}\mathcal{U}_r^2 \quad \textbf{Equation 5.60}$$

This form of Equation 5.60 is different from that shown by Werle and Presz, which instead divided rotor velocity by exit area. A typographical error is the most likely explanation for the version they presented, as correct relationships were derived from it and only a preprint of their paper was accessible.

The inequalities for ducts VB and VC were slightly elevated, as Table 5.40 shows. For VB, this is simply numerical error: the inequality was at its maximum at high C_T, where discretisation convergence was least good, and calculating u_w from C_T through Equation 5.40 reduced the inequality to 0.01%. The inequality was exaggerated at low C_T by the median magnitude calculation for VC, with the largest inequality as a standard percentage being 0.50%. The relationship was therefore judged valid.

Table 5.40: Largest absolute inequalities found for Equation 5.60, as a percentage of the median right hand side magnitude across rotor loadings. Werle and Presz designated this relationship, without the correction factor, 8a.

Inequality for	Duct VA	Duct VB	Duct VC
Equation 5.60	0.35%	1.12%	1.23%

Their alternative calculation for exit pressure coefficient is shown in Equation 5.61.

$$C_{p,e} = \mathcal{U}_w^2 - \gamma_{x,e}\left(\frac{1+C_S}{2}\right)^2 \left(1 - \eta_{diff} + \eta_{diff}\mathcal{A}_e^{-2}\right)(1+\mathcal{U}_w)^2 \quad \textbf{Equation 5.61}$$

Table 5.41 shows that the relationship is valid with the variable C_S.

Table 5.41: Largest absolute inequalities found for Equation 5.61, as a percentage of the median right hand side magnitude across rotor loadings. Werle and Presz designated this relationship, without the correction factor, 8a.

Inequality for	Duct VA	Duct VB	Duct VC
Equation 5.61 using variable C_S	0.21%	0.55%	0.23%

Werle and Presz concluded with the additional relationship for C_{Pmax} in Equation 5.62.

$$\frac{27}{16}C_{Pmax} = \frac{1}{2}\sqrt{\frac{1-9C_{p,e}}{\gamma_{x,e}\left(1-\eta_{diff}+\eta_{diff}\mathcal{A}_e^{-2}\right)}} \quad \textbf{Equation 5.62}$$

The derivation of this equation required the C_{Topt} = 8/9 assumption. Combined with the inequalities in Table 5.42, it is clear that this is not a valid relationship.

Table 5.42: Absolute inequalities found at C_{Topt} for Equation 5.62, as a percentage of the right hand side. Werle and Presz designated this relationship, without the correction factor, 9.

Inequality for	Duct VA	Duct VB	Duct VC
Equation 5.62	5.97%	3.09%	8.22%

5.6.3 Summary: Partly Valid

The validation here followed a similar pattern to that for Sørensen's theory: valid initial equations but invalid simplifying assumptions, although here Equation 5.59 was also invalid despite having no stated assumptions. Werle and Presz assumed that the duct axial force coefficient C_S was constant with rotor loading, which was found to be

incorrect. As Table 5.43 shows, allowing C_S to vary changed some of the relationships to valid ones. The other simplifying assumption made was that C_{Topt} = 8/9. Again this is not the case, and the equations derived for optimum conditions are not valid.

Table 5.43: Summary of conclusions for Werle and Presz's Equations.

Table of Inequalities	Werle and Presz's Designation	Conclusion for Relationship
Table 5.34	1	Valid
Table 5.35	3a	Valid with variable C_S
Table 5.36	3b	Valid with variable C_S
Table 5.36	3b	Valid
Table 5.37	4	Not valid
Table 5.38	5a – 5c	Not valid
Table 5.39	7	Not valid
Table 5.40	8a	Valid with correction factor and typographical correction
Table 5.41	8a	Valid with variable C_S and correction factor
Table 5.42	9	Not valid

5.7 Jamieson's Theory

Jamieson took a unique approach in developing his generalised actuator disc theory [186]. Rather than attacking the problem directly, he introduced the concept of an ideal diffuser: one of infinitely variable shape to account for the changing interaction between the diffuser and a variably loaded rotor. The concept, then, is entirely theoretical in nature and uses a quite different definition of 'ideal' from authors who use it to mean 'without viscous losses'. It is also a concept that has not yet been fully defined. This section therefore seeks not to validate the theory but rather to determine which equations apply to real ducts and which to ideal diffusers, and to understand how the concept of an ideal diffuser is expressed in the equations.

5.7.1 Equations Valid for Real Ducts

Jamieson began with a set of relationships derived from the standard definitions of the power and thrust coefficients. The first of these was Equation 5.63.

$$\frac{P}{F_T} = u_\infty \frac{C_P}{C_T} \qquad \textbf{Equation 5.63}$$

Calculating power extracted as the product of thrust and velocity at the rotor, defined in terms of the axial induction factor at the rotor a_r, gave Equation 5.64.

$$P = F_T u_\infty (1 - a_r) \qquad \textbf{Equation 5.64}$$

From these two relationships, Equation 5.65 was derived.

$$\frac{C_P}{C_T} = (1 - a_r) \qquad \textbf{Equation 5.65}$$

Finally, the thrust coefficient was given as Equation 5.66.

$$C_T = \frac{2\Delta p}{\rho u_\infty^2} \qquad \textbf{Equation 5.66}$$

Application of Bernoulli's equation between far upstream and the upstream side of the rotor gave Equation 5.67.

$$p_\infty + \frac{1}{2}\rho u_\infty^2 = p_{ru} + \gamma_{x,r}\frac{1}{2}\rho u_\infty^2 (1 - a_r)^2 \qquad \textbf{Equation 5.67}$$

Completing the use of Bernoulli's equation was Equation 5.68, applied between the downstream side of the actuator disc and far downstream.

$$p_{ru} - \Delta p + \gamma_{x,r}\frac{1}{2}\rho u_\infty^2 (1 - a_r)^2 = p_\infty + \frac{1}{2}\rho u_\infty^2 (1 - a_w)^2 \qquad \textbf{Equation 5.68}$$

Combining Equation 5.66 to Equation 5.68 then gave Equation 5.69.

$$C_T = 2a_w - a_w^2 \qquad \textbf{Equation 5.69}$$

All of these relationships apply to real ducted turbines, as Table 5.44 shows, although small numerical errors in the far downstream results had to be compensated for in Equation 5.68 by using the computed pressure in the far wake.

Table 5.44: Largest absolute inequalities found for Equation 5.63 to Equation 5.69, as a percentage of the median right hand side magnitude across rotor loadings. Jamieson designated these relationships, without the correction factors, 1 to 7.

Inequality for	Duct VA	Duct VB	Duct VC
Equation 5.63	9×10^{-14}%	9×10^{-14}%	1×10^{-13}%
Equation 5.64	1×10^{-14}%	2×10^{-14}%	2×10^{-14}%
Equation 5.65	1×10^{-13}%	9×10^{-14}%	1×10^{-13}%
Equation 5.66	1×10^{-13}%	9×10^{-14}%	1×10^{-13}%
Equation 5.67	5×10^{-12}%	2×10^{-12}%	2×10^{-11}%
Equation 5.68 using p_∞ in wake	1.37%	1.65%	1.14%
Equation 5.68 using computed p in wake	2×10^{-11}%	4×10^{-12}%	6×10^{-11}%
Equation 5.69	0.43%	0.52%	0.35%

5.7.2 Equations for Ideal Diffusers Only

At this point, one main piece of the puzzle remains for calculating the power extracted: a connection between the axial induction in the far wake and that at the rotor. Jamieson therefore derived the solution in Equation 5.70.

$$a_w = \frac{2(a_r - a_0)}{(1 - a_0)} \qquad \textbf{Equation 5.70}$$

This relationship introduces a_0, which is the axial induction at the rotor without any energy extraction. This parameter is the key to the rest of Jamieson's theory, and serves as the single empirical parameter – measured at only one rotor loading – required to characterise the performance of an ideal diffuser. Table 5.45 makes clear, however, that this is the point where the equations no longer apply to real ducted turbines.

To compare with a relationship that does apply to real ducts, an alternative was derived for this work. An application of the momentum equation, Equation 5.69, and the duct drag coefficient definition, led to Equation 5.71.

$$a_w = a_r + \sqrt{a_r^2 + C_D} \qquad \textbf{Equation 5.71}$$

This relationship, which Table 5.45 confirms is valid for real ducted turbines, has two main differences from Equation 5.70: C_D replaced a_0 as the empirical parameter and the empirical parameter becomes one that varies with C_T. Both of these potentially show how the concept of an ideal diffuser is expressed in the equations.

Table 5.45: Largest absolute inequalities found for Equation 5.70 and Equation 5.71, as a percentage of the median right hand side magnitude across rotor loadings. Jamieson designated this relationship 8.

Inequality for	Duct VA	Duct VB	Duct VC
Equation 5.70	42.8%	51.4%	42.8%
Equation 5.71	0.43%	0.81%	0.74%

Jamieson then substituted for a_w in Equation 5.69. This gave Equation 5.72 for the ideal diffuser and Equation 5.73 using the alternative a_w derived here.

$$C_T = \frac{4(a_r - a_0)(1 - a_0)}{(1 - a_0)^2} \qquad \textbf{Equation 5.72}$$

$$C_T = -2a_r^2 + 2a_r + (2 - 2a_r)\sqrt{a_r^2 + C_D} - C_D \qquad \textbf{Equation 5.73}$$

From this relationship for C_T and Equation 5.65, Jamieson then found Equation 5.74. The alternative a_w version is given in Equation 5.75.

$$C_P = \frac{4(a_r - a_0)(1 - a_0)^2}{(1 - a_0)^2} \qquad \textbf{Equation 5.74}$$

$$C_P = (1 - a_r)\left[-2a_r^2 + 2a_r + (2 - 2a_r)\sqrt{a_r^2 + C_D} - C_D\right] \quad \textbf{Equation 5.75}$$

Table 5.46 shows that the a_0 versions of the last two equations do not apply to a real duct while the alternative versions do.

Table 5.46: Largest absolute inequalities found for Equation 5.72 to Equation 5.75, as a percentage of the median right hand side magnitude across rotor loadings. Jamieson designated these relationships 9 and 10.

Inequality for	Duct VA	Duct VB	Duct VC
Equation 5.72	128.9%	85.6%	151.3%
Equation 5.73	0.04%	0.26%	0.13%
Equation 5.74	123.8%	88.9%	143.6%
Equation 5.75	0.03%	0.18%	0.15%

As a_0 is fixed for a particular ideal diffuser, Equation 5.74 can be differentiated to find the maximum power without any simplifying assumptions. Jamieson found Equation 5.76 to Equation 5.78 for the optimum conditions.

$$a_{r,opt} = \frac{1 + 2a_0}{3} \quad \textbf{Equation 5.76}$$

$$C_{Pmax} = \frac{16}{27}(1 - a_0) \quad \textbf{Equation 5.77}$$

$$C_{Topt} = \frac{8}{9} \quad \textbf{Equation 5.78}$$

As expected, Table 5.47 shows that these relationships do not apply to a real turbine.

Table 5.47: Absolute inequalities found at C_{Topt} for Equation 5.76 to Equation 5.78, as a percentage of the right hand side. Jamieson designated these relationships 11 to 13.

Inequality for	Duct VA	Duct VB	Duct VC
Equation 5.76	25.8%	119.6%	20.1%
Equation 5.77	20.0%	23.9%	21.0%
Equation 5.78	10.1%	13.8%	10.1%

Finally, Jamieson derived Equation 5.79 to relate the power and thrust coefficients using a_0.

$$C_P = \frac{1}{2}C_T(1 - a_0)\left(1 + \sqrt{1 - C_T}\right) \quad \textbf{Equation 5.79}$$

Repeating this process for the alternative equations gave Equation 5.80, which is reasonably similar in form to the ideal version.

$$C_P = \frac{1}{2}(C_T + C_D)\left(1 + \sqrt{1 - C_T}\right) \quad \textbf{Equation 5.80}$$

It can be seen from Table 5.48 that the pattern continued and the ideal diffuser relationship does not apply to real ducts.

Table 5.48: Largest absolute inequalities found for Equation 5.79 and Equation 5.80, as a percentage of the median right hand side magnitude across rotor loadings. Jamieson designated this relationship 14.

Inequality for	Duct VA	Duct VB	Duct VC
Equation 5.79	26.8%	34.5%	27.5%
Equation 5.80	0.30%	0.33%	0.22%

5.7.3 Relating the Real and Ideal

Jamieson proposed an efficiency parameter η_s for applying ideal diffuser results to a real duct. Efficiency here refers only to the reduction in performance associated with a duct being non-ideal in Jamieson's sense, and not to viscous losses. While the efficiency varies with axial induction at the rotor, the approximation that it is fixed was made for the relationship between C_P and C_T. Jamieson found that this approach worked well with simulation results from Hansen et al [143] using the efficiency definition in Equation 5.81.

$$\eta_s = \frac{C_{Topt}}{8/9} \qquad \textbf{Equation 5.81}$$

Equation 5.82 gives the power coefficient using this approximation.

$$C_P = \frac{1}{2} C_T \left(1 - a_0\eta_s + \sqrt{1 - 2a_0\eta_s + a_0^2\eta_s^2 - C_T + 2a_0 C_T - a_0^2 C_T}\right) \qquad \textbf{Equation 5.82}$$

It is important to note that a_0 in this equation still refers to the axial induction at zero loading at the associated ideal diffuser's rotor. It is not the axial induction value for the real duct. In Jamieson's theory, however, the axial induction in the real duct and the associated ideal diffuser will match at a single rotor loading. Jamieson took Hansen's duct as matching its associated ideal diffuser at C_T = 0, so he was able to use the real induction as a_0. To apply Equation 5.82 to the results here, Jamieson suggested in a personal communication using an estimate of a_r at C_T = 0 divided by η_s.

The inequalities in Table 5.49 were found using that estimate, although above C_T = 0.82 the terms inside Equation 5.82's square root summed to a negative number. Those loadings were excluded. It is not surprising that there is not an exact match, as Jamieson stated that the relationship is theoretically incorrect and intended as an approximation only. However, the error in the approximation here is larger than when using Hansen's

results. While the relationship itself may be less accurate than thought, the calculation was also based on an otherwise untested estimate for a_0.

Table 5.49: Largest absolute inequalities and absolute inequalities at C_{Topt} found for Equation 5.82, as a percentage of the median right hand side magnitude across rotor loadings. Jamieson designated this relationship 23.

Inequality for Equation 5.82	Duct VA	Duct VB	Duct VC
Largest	8.92%	14.0%	8.37%
At C_{Topt}	8.40%	13.8%	6.47%

5.7.4 Summary: Increased Understanding

The first half of the equations derived by Jamieson are applicable to real ducted turbines, as Table 5.50 shows. After that point, however, the relationships are valid only for ideal diffusers. While it was clear from the concept of a continually varying shape that the entire theory could not apply to a real duct, it was not clear how this concept was expressed in the equations themselves. Comparison with the alternative form of the theory derived from Equation 5.71 suggests possibilities: that an ideal diffuser is one without drag, or with a variation of shape that allows a fixed empirical parameter, or both.

Table 5.50: Summary of conclusions for Jamieson's Equations.

Table of Inequalities	Jamieson's Designation	Conclusion for Relationship
Table 5.44	1 – 7	Valid for real ducted turbines
Table 5.45	8	Valid for ideal diffuser only
Table 5.46	9, 10	Valid for ideal diffuser only
Table 5.47	11 – 13	Valid for ideal diffuser only
Table 5.48	14	Valid for ideal diffuser only
Table 5.49	23	This approximation may be less accurate than thought

5.8 The Need for Further Development

All of the theories investigated have at least a base of valid equations, but the attractive simplifications aimed at reducing dependence on empirical parameters are not accurate. A wide range of relationships for power extraction were nevertheless found, summarised in Table 5.51 by the parameters needed to calculate C_P for each valid equation. Where a theory had no valid equation for power coefficient, equations for power were used instead. Although this is not a completely fair comparison, as some of these equations assume zero losses while others do not, it does provide a useful overview of the various power calculation methods.

Table 5.51: Parameters required in Equations for C_P, or P where no valid C_P equation existed for a theory, with A_r, u_∞, p_∞, and ρ excluded. Zero losses are assumed in some relationships.

Relationship	u_r	u_w	$\gamma_{x,r}$	$\gamma_{x,e}$	η_{diff}	p_e	$\mathcal{A}_e$	F_D	F_T
Equation 5.14	●	●	●	●	●		●		
Equation 5.33	●	●	●	●	●		●		
Equation 5.43		●						●	●
Equation 5.50		●						●	
Equation 5.17	●		●	●	●	●	●		
Equation 5.36	●		●	●	●	●	●		
Equation 5.45	●			●		●	●		
Equation 5.64	●								●
Equation 5.80								●	●

There is a sharp contrast visible in Table 5.51 between approaches requiring a large number and those requiring a small number of parameters. Some of the difference is due to the zero losses assumption, but – as was argued in Section 1.4 – this assumption is useful if it helps improve understanding. Aside from this, however, it is not clear which approach is more helpful. If a large set of parameters are all independent then they are all required, but the inclusion of interrelated parameters may simply confuse or mislead. It may be impossible to completely remove interrelated parameters, but the reduction from three parameters in Equation 5.43 to two in either Equation 5.50 or Equation 5.80 shows that valid simplification is sometimes possible.

Consider the inclusion of both u_r and p_e in an equation. While they are present for logical reasons – to calculate flow rate and to replace the far wake velocity – one can be calculated from the other using Bernoulli's equation and mass continuity. Does writing the equation with both parameters included anyway subtly imply that they both have some separate influence over power? Even if the link between u_r and p_e is known, the choice of parameters directly included in an equation must surely guide interpretation of it. The question then is not just if the relationships can be simplified in a helpful way, but in what different ways can the equations be expressed? Alternative forms of power equation will be examined in the next chapter to compare various points of view.

Another interesting contrast between the theories came from their application of the momentum equation. Phillips went into the most detail in his examination, and found that the momentum change between far upstream and downstream depended on the rotor thrust, force from the internal surface of the duct, and force acting on the upstream and downstream portions of the control volume. Sørensen and Werle and Presz, however, presented valid equations with only the thrust and total duct forces. While it may have been assumed that the upstream and downstream forces sum to zero, as in the bare rotor case [4, 5], that does not explain the inclusion of the duct outside surface force. No detailed derivation or explanation was found in the literature, so the subject is considered further in Chapter 6.

5.9 Summary

Validation of a theory is required for it to be trusted, but little testing has previously been carried out for ducted turbine theories. Results from the inviscid panel method code suitable for this task were generated by ensuring good discretisation convergence across three duct shapes and a range of rotor loadings. Four theories were selected from the literature for examination: Phillips' for his thorough derivation from the momentum equation, Sørensen's and Werle and Presz's for their proposed simplifications, and Jamieson's to gain increased understanding of the ideal diffuser concept. The equations for each were then tested for validity using the simulation results.

Relationships derived from Bernoulli's equation required modification, however, before they could be verified. The velocity squared term in that equation indicates that a mean value cannot simply replace a radially varying velocity. A correction factor γ was derived to account for the difference, with a modification to γ_x so that axial velocity could replace velocity magnitude. The mean axial velocity could then be inserted along with the correction factor into the theoretical equations, which had avoided the issue by assuming one dimensional flow. Results in this chapter both show the importance of using γ with Bernoulli's equation, and present the correct form of the theories for a radially varying flow.

The investigation of Jamieson's theory had a somewhat different aim from the others; not all of the equations could apply to a real ducted turbine, as they were intended for the theoretical ideal diffuser. However, the equations do apply to real ducts until the point that the empirical parameter a_0 is introduced. It appears that the concept of an ideal diffuser is expressed in the equations through this parameter being invariant with loading, through an absence of duct drag, or through both. Approximations for power for a real ducted turbine and its associated a_0 were also tested and found to be somewhat less accurate than expected.

Testing of the other three theories showed a foundation of valid equations that both Sørensen and Werle and Presz built upon with invalid simplifying assumptions. Simulation results show that the exit pressure coefficient does vary with mass flow rate, and that the ratio of duct drag to rotor thrust does vary with mass flow rate and far wake velocity, contradicting Sørensen's assumptions. For Werle and Presz, the results show their assumptions of an invariant drag coefficient and an optimum rotor loading of 8/9 to be invalid.

Two paths forward were identified based on these results. First, there appears to be an opportunity for some less ambitious simplification work and an examination of different forms of power equation. Second, an interesting contrast exists between

Phillips' detailed derivation of a momentum balance and the less involved derivations in the other theories. The former gave a result in terms of duct inside surface drag and streamtube control volume forces, while the latter were still valid with only total duct drag. A connection between the two is required for a comprehensive theory.

6 Chapter

A Validated Theory

Many theoretical descriptions already exist for ducted turbines, but the evaluation in Section 5.8 identified the need for another: a detailed derivation beginning from general forms of the momentum and energy equations that ends with performance in terms of the total inviscid duct drag. One such derivation is given and shown to be valid here. Returning to topics first examined in Chapter 3, the relationship between drag and augmentation is then explored, and investigations conducted into the power extracted and optimum rotor loading. Finally, various formulations for calculating power coefficient are derived and compared.

6.1 Drag-Based Derivation

6.1.1 Establishing a Momentum Balance

The derivation begins with the general form of the momentum equation for a volume V enclosed by a surface S in Equation 6.1 [69].

$$\frac{\partial}{\partial t}\iiint_V \rho \boldsymbol{U}\,\mathrm{d}V + \oiint_S (\rho \boldsymbol{U}\cdot \mathbf{d}\boldsymbol{S})\boldsymbol{U} = \iiint_V \rho \boldsymbol{f}\,\mathrm{d}V + \boldsymbol{F_{viscous}} - \oiint_S p\,\mathbf{d}\boldsymbol{S} \qquad \textbf{Equation 6.1}$$

To apply this equation to a ducted turbine, the two control volumes shown in Figure 6.1 were specified. Together they make up the streamtube passing through the duct, with control volume 1 extending from the upstream side of the rotor to far upstream and control volume 2 from the rotor downstream side to far downstream. This split was required because Equation 6.1 is not directly applicable to a control volume crossing the rotor.

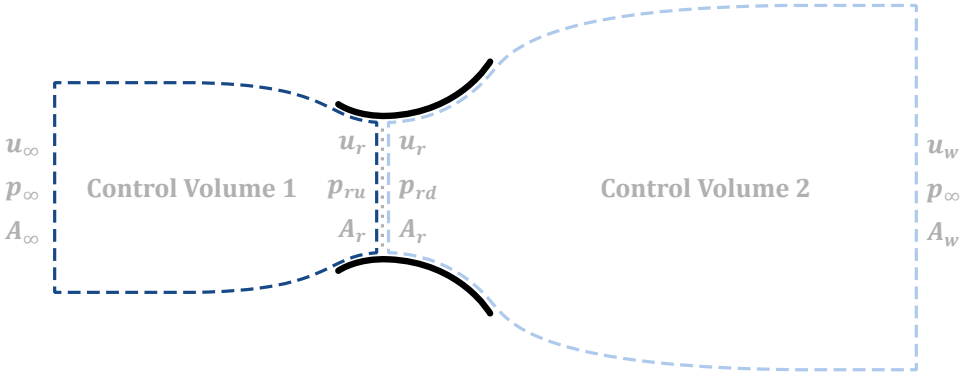

Figure 6.1: Control volumes for the momentum analysis.

Using only the axial component of velocity – as the others are not required to calculate power extraction [5] – the assumption of steady inviscid flow with insignificant body forces $\boldsymbol{f}$ for control volume 1 leads to Equation 6.2.

$$\oiint_{S_1} (\rho \boldsymbol{U} \cdot \mathbf{d}\boldsymbol{S}) u = -\left(\oiint_{S_1} p \, \mathbf{d}\boldsymbol{S} \right)_x \qquad \textbf{Equation 6.2}$$

$\boldsymbol{U} \cdot \mathbf{d}\boldsymbol{S}$ is zero for the circumferential boundary streamtube and equals $-u \, \mathrm{d}A$ far upstream and $u \, \mathrm{d}A$ at the rotor. Splitting the pressure term, however, leaves the contribution from the circumferential surface S_{1c} seen in Equation 6.3.

$$\begin{aligned} &- \iint_{A_\infty} \rho u^2 \, \mathrm{d}A + \iint_{A_{ru}} \rho u^2 \, \mathrm{d}A \\ &= \iint_{A_\infty} p \, \mathrm{d}A - \iint_{S_{1c}} (p\hat{\boldsymbol{n}})_x \, \mathrm{d}S - \iint_{A_{ru}} p \, \mathrm{d}A \end{aligned} \qquad \textbf{Equation 6.3}$$

Applying the same process to control volume 2 gives Equation 6.4.

$$\begin{aligned} &- \iint_{A_r} \rho u^2 \, \mathrm{d}A + \iint_{A_w} \rho u^2 \, \mathrm{d}A \\ &= \iint_{A_{rd}} p \, \mathrm{d}A - \iint_{S_{2c}} (p\hat{\boldsymbol{n}})_x \, \mathrm{d}S - \iint_{A_w} p \, \mathrm{d}A \end{aligned} \qquad \textbf{Equation 6.4}$$

These two equations can be combined using the rotor pressure drop definition in Equation 6.5.

$$\iint_{A_{ru}} p \, \mathrm{d}A - \iint_{A_{rd}} p \, \mathrm{d}A = \Delta p A_r \qquad \textbf{Equation 6.5}$$

It is convenient to recast the control volume pressure forces acting on the resulting single control volume into the forces on the portions of that control volume shown in Figure 6.2, using the definition in Equation 6.6.

$$\begin{aligned} &\iint_{S_{1c}} (p\hat{\boldsymbol{n}})_x \, \mathrm{d}S + \iint_{S_{2c}} (p\hat{\boldsymbol{n}})_x \, \mathrm{d}S - \iint_{A_\infty} p \, \mathrm{d}A + \iint_{A_w} p \, \mathrm{d}A \\ &= -F_{us} - F_{d,in} - F_{ds} \end{aligned} \qquad \textbf{Equation 6.6}$$

F_{us}, $F_{d,in}$, and F_{ds} are the axial forces on the upstream, inside duct, and downstream portions of the streamtube respectively. These forces are defined as positive in the downstream direction, in contrast to the integral terms which become negative for downstream forces.

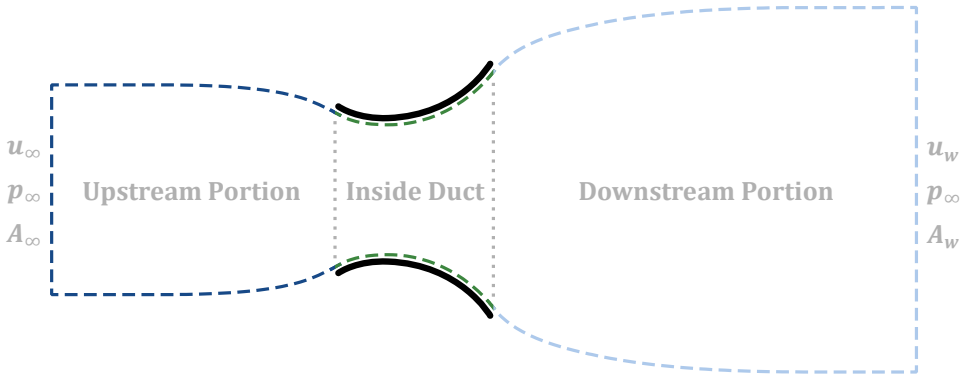

Figure 6.2: Control volume portions for the momentum analysis.

Combining Equation 6.3 and Equation 6.4 using Equation 6.5, reformulating the pressure forces with Equation 6.6, and assuming no radial variation in the flow far upstream and downstream leads to Equation 6.7.

$$\dot{m}(u_\infty - u_w) = \Delta p A_r - F_{us} - F_{d,in} - F_{ds} \qquad \textbf{Equation 6.7}$$

6.1.2 Replacing Far Wake Velocity with Rotor Loading

To develop a useful set of equations, the far wake velocity in Equation 6.7 must be replaced with a less abstract parameter. Both Phillips [4] and Sørensen [185] used a relationship based on the duct's exit pressure, but the approach taken here is similar to Jamieson's [186] in that the far wake velocity is linked to rotor loading. An appropriate relationship can be found by starting with a general form of the energy equation [69] and assuming steady inviscid flow with negligible body forces and volumetric heating. With e as the internal energy per unit mass of the fluid, these assumptions lead to Equation 6.8.

$$-\oiint_S p\boldsymbol{U} \cdot \mathbf{d}\boldsymbol{S} - P = -\oiint_S \rho\left(e + \frac{|\boldsymbol{U}|^2}{2}\right)\boldsymbol{U} \cdot \mathbf{d}\boldsymbol{S} \qquad \textbf{Equation 6.8}$$

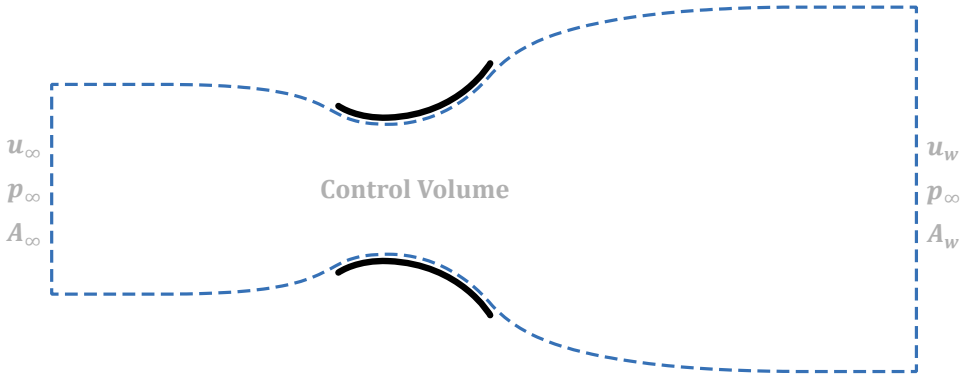

Figure 6.3: Control volume for the energy analysis.

Equation 6.8 is applied to the control volume shown in Figure 6.3, which followed the streamtube passing through the duct from far upstream to far downstream, giving Equation 6.9.

$$\begin{aligned}&\iint_{A_\infty} pu\,\mathrm{d}A - \iint_{A_w} pu\,\mathrm{d}A - P \\ &= -\iint_{A_\infty} \rho\left(e + \frac{|\boldsymbol{U}|^2}{2}\right)u\,\mathrm{d}A + \iint_{A_w} \rho\left(e + \frac{|\boldsymbol{U}|^2}{2}\right)u\,\mathrm{d}A\end{aligned} \qquad \textbf{Equation 6.9}$$

Assuming axial flow with no radial variation at the control volume ends, a return to atmospheric pressure in the far wake, and a calorically perfect gas [69] then gives Equation 6.10.

$$\begin{aligned}&p_\infty u_\infty A_\infty - p_w u_w A_w - P \\ &= -\frac{C_v}{R_s} p_\infty u_\infty A_\infty - \frac{1}{2}\rho u_\infty^3 A_\infty + \frac{C_v}{R_s} p_\infty u_w A_w + \frac{1}{2}\rho u_w^3 A_w\end{aligned} \qquad \textbf{Equation 6.10}$$

C_v is the specific heat at constant volume and R_s is the specific gas constant. Applying mass continuity to this equation and rearranging results in Equation 6.11.

$$-\frac{P}{\dot{m}} = \frac{1}{2}(u_w^2 - u_\infty^2) \qquad \textbf{Equation 6.11}$$

P is then replaced using Equation 6.12 [5].

$$P = \Delta p A_r u_r \qquad \textbf{Equation 6.12}$$

Rearranging the result and using the standard definition for thrust coefficient gives the desired connection between the far wake velocity and rotor loading in Equation 6.13.

$$u_w = u_\infty\sqrt{1 - C_T} \qquad \textbf{Equation 6.13}$$

The derivation from the momentum equation can then be continued by substituting into Equation 6.7 to get Equation 6.14.

$$\dot{m}u_\infty\left(1 - \sqrt{1 - C_T}\right) = \Delta p A_r - F_{us} - F_{d,in} - F_{ds} \qquad \textbf{Equation 6.14}$$

6.1.3 Replacing Control Volume Forces with Drag

Phillips [4] stopped his application of the momentum equation at a point similar to Equation 6.14, pointing out the difficulty of determining the forces on the streamtube. However, it must be possible to continue: numerical results in Section 5.5.2 suggest valid momentum balances exist without the streamtube forces. They included instead a duct drag term, although no supporting derivation was found. It was therefore hypothesised that the total duct drag is equal and opposite to the sum of the control

volume forces. Empirical evidence supporting this hypothesis, gathered from panel method simulation results, is presented in this section.

Approach

Writing the hypothesis in terms of the reaction force on the flow from the duct inside surface $F_{d,in}$ and outside surface $F_{d,out}$ gives Equation 6.15.

$$\begin{aligned} F_{us} + F_{d,in} + F_{ds} &= -F_D \\ &= F_{d,in} + F_{d,out} \end{aligned} \qquad \textbf{Equation 6.15}$$

The inside duct force cancels, leaving the hypothesis in Equation 6.16.

$$F_{us} + F_{ds} = F_{d,out} \qquad \textbf{Equation 6.16}$$

By finding each of these forces from simulation results, the accuracy of the equation can be tested. F_{us} and F_{ds} were calculated using applications of the momentum equation, as in Equation 6.17 and Equation 6.18.

$$F_{us} = -\iint_{A_\infty} \rho u^2 \,\mathrm{d}A + \iint_{A_i} \rho u^2 \,\mathrm{d}A + \iint_{A_i} p \,\mathrm{d}A \qquad \textbf{Equation 6.17}$$

$$F_{ds} = -\iint_{A_e} \rho u^2 \,\mathrm{d}A + \iint_{A_w} \rho u^2 \,\mathrm{d}A - \iint_{A_e} p \,\mathrm{d}A \qquad \textbf{Equation 6.18}$$

The integrations at the duct inlet i and exit e were computed directly from numerical measurements at those locations. For simplicity, however, the far upstream momentum flow was calculated from the mass flow rate computed at the duct inlet and the free stream velocity. Reduced discretisation convergence far downstream was avoided by using the analytical far downstream velocity from Equation 6.13 with the mass flow rate to calculate the momentum flow at w.

$F_{d,out}$ was calculated from the total duct drag F_D and the inside reaction force. This inside force was computed using the momentum relationship in Equation 6.19.

$$F_{d,in} = -\iint_{A_i} \rho u^2 \,\mathrm{d}A + \iint_{A_e} \rho u^2 \,\mathrm{d}A - \iint_{A_i} p \,\mathrm{d}A + \iint_{A_e} p \,\mathrm{d}A + \Delta p A_r \qquad \textbf{Equation 6.19}$$

Numerical results were extracted from the three duct shapes described in Section 5.2, with the hypothesis checked at a range of rotor loadings. Discretisation convergence is shown in Table 6.1 and was acceptable for expanding wake length but poor for changes in panel length. Richardson extrapolation [171, 173] was used to compensate, with results calculated at the panel lengths stated in Table 6.1's caption along with double and half the resolution.

Table 6.1: Worst change in results with finer discretisation for the validation shapes. Discretisation was changed from last duct panel length = $0.00125D$ and expanding wake length = $16.0D$ for duct VA, $0.00114D$ and $14.6D$ for duct VB, and $0.00125D$ and $16.0D$ for duct VC.

	% Difference with			
	Halved Panel Length		Doubled Wake Length	
	$C_T = 0$	$C_T = 0.95$	$C_T = 0$	$C_T = 0.95$
F_{us}	4.67	8.26	0	0.54
$F_{d,in}$	8.41	3.31	0	0.14
F_{ds}	31.2	2.97	0	0.22
F_D	-	4.32	-	0.08

Results

Two forms of the hypothesis are assessed in Figure 6.4: the sum $F_{us} + F_{ds} - F_{d,out}$ is plotted along with each of the forces, while the inequality of $F_{us} + F_{ds} = F_{d,out}$ is given as a percentage. As the magnitudes of some forces were much larger than others, the percentage was calculated using the largest magnitude force as the divisor. A small error in a large force could not therefore cause a misleadingly large percentage imbalance.

In some cases the results in Figure 6.4 were sensitive to the choices made when applying Richardson extrapolation. In testing the force imbalance, for example, $F_{us} + F_{ds}$ could be calculated from individual extrapolations of F_{us} and F_{ds} or from extrapolation of the sum $F_{us} + F_{ds}$. In this case the latter was more reliable, as the former made less consistent predictions with changes in duct discretisation. All other extrapolation choices were made on the same basis, but not all differences had a clearly superior approach.

With an error of 1.2% or less, when calculated on the basis of the largest force, the upstream and downstream control volume forces must indeed equal the reaction force on the flow from the duct outside surface. It therefore follows that the control volume forces can be replaced with the total duct drag using Equation 6.20.

$$F_{us} + F_{d,in} + F_{ds} = -F_D \qquad \textbf{Equation 6.20}$$

Although this result has been found numerically, it is perhaps logical from a theoretical perspective. There is no energy extraction outside of the duct, so an application of the energy equation shows an eventual return to the free stream velocity outside the duct's streamtube. Nevertheless, there is a momentum drop associated with the force on the duct outside surface; this force may be equal to the streamtube forces due to the momentum drop transferring into the streamtube passing through the duct.

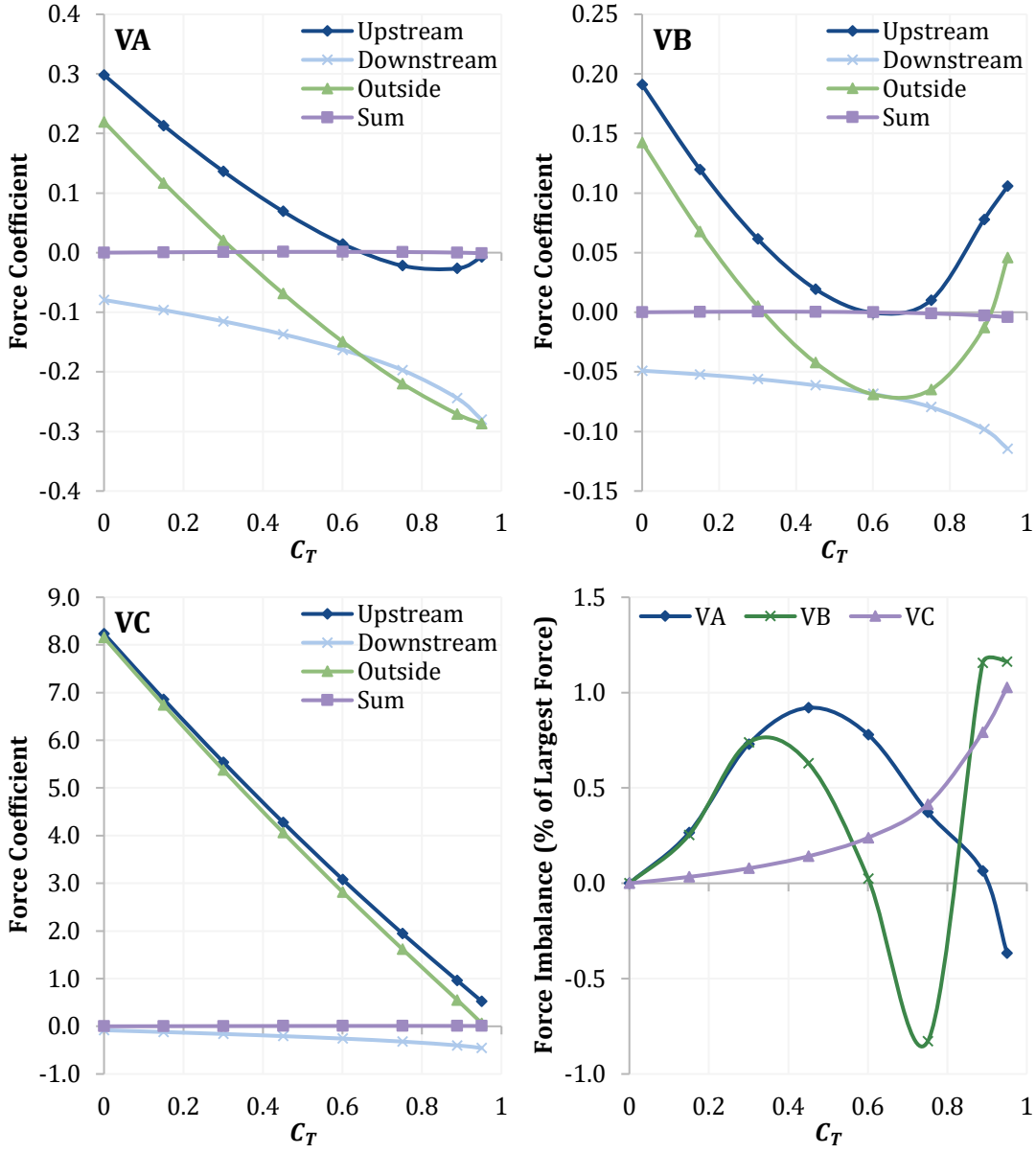

Figure 6.4: Variation of F_{us}, F_{ds}, $F_{d,out}$, and $F_{us} + F_{ds} - F_{d,out}$ with rotor loading, where the forces are given as a coefficient calculated from free stream velocity and rotor area $F/0.5\rho u_\infty^2$ for ducts VA, VB, and VC. The bottom right plot shows the difference between $F_{us} + F_{ds}$ and $F_{d,out}$ as a percentage of the largest force.

6.1.4 Calculating Performance

The final abstract parameters in the momentum equation can now be replaced by substituting Equation 6.20 into Equation 6.14. Dividing through by $0.5\rho u_\infty^2 A_r$ then gives Equation 6.21.

$$\frac{2u_r}{u_\infty}\left(1-\sqrt{1-C_T}\right)=C_T+C_D \qquad \textbf{Equation 6.21}$$

Using Jamieson's approach [186], modified for velocity rather than axial induction, the relationship for power in Equation 6.12 can be combined with the definitions of power and thrust coefficients to derive Equation 6.22.

$$\frac{u_r}{u_\infty}=\frac{C_P}{C_T} \qquad \textbf{Equation 6.22}$$

This equation provides the final piece of the puzzle, and substituting into Equation 6.21 leads to the relationship for a ducted turbine's power coefficient in Equation 6.23.

$$C_P=\frac{1}{2}(C_T+C_D)\left(1+\sqrt{1-C_T}\right) \qquad \textbf{Equation 6.23}$$

Velocity at the rotor, meanwhile, is given by Equation 6.24.

$$\frac{u_r}{u_\infty}=\frac{1}{2}\left(1+\frac{C_D}{C_T}\right)\left(1+\sqrt{1-C_T}\right) \qquad \textbf{Equation 6.24}$$

An alternative perspective is to rearrange Equation 6.23 and calculate drag from performance, as in Equation 6.25.

$$C_D=\frac{2C_P}{1+\sqrt{1-C_T}}-C_T \qquad \textbf{Equation 6.25}$$

Similar to equations previously derived in the literature [e.g. 66, 95, 108, 185], these equations relate the performance of a ducted turbine to the drag force acting on the duct. The previous derivations simply stated that such relationships can be derived from momentum conservation, however, in contrast with the full detail provided here. Starting from an application of the momentum equation to a control volume passing through the duct and showing each subsequent step will hopefully aid understanding of the derivation and provide further confidence in the results.

When interpreting theses equations, it should be remembered that the principle assumption underlying them is that of inviscid flow. While the influence of viscosity must not be forgotten, these equations serve as a base from which the inviscid component of ducted turbine performance can be more fully understood and the viscous component more easily isolated.

Testing the final set of performance equations against inviscid simulation results, using the method described in Section 5.1, gave the results in Table 6.2. Discretisation convergence was reduced for duct VB at high rotor loadings, leading to the elevated inequality seen for Equation 6.25. At $C_T \leq 8/9$ the largest inequality was 0.72% for that duct, leading to the conclusion that the set of equations – and hence the derivation behind them – is valid.

Table 6.2: Largest absolute inequalities found for the performance relationships, as a percentage of the median magnitude of the right hand side across all rotor loadings tested.

Inequality for	Duct VA	Duct VB	Duct VC
Equation 6.23	0.37%	0.33%	0.22%
Equation 6.24	0.30%	0.26%	0.30%
Equation 6.25	0.83%	1.66%	0.39%

6.2 Analytical Investigations

A validated theory may be useful for many investigations, but here the focus is on returning to topics considered in Chapter 3. Numerical results from that chapter concerning the relationship between drag and augmentation, the behaviour of power extraction, and the optimum rotor loading will be supplemented with analytical conclusions.

6.2.1 Augmentation, Drag, and Their Momentum Connection

A very strong correlation was confirmed between inviscid duct drag and augmentation in Section 3.1.6. The equations in Section 6.1.4 and in the previous literature [e.g. 66, 95, 108, 185] already show consistency with that result, but explicitly calculating the augmentation brings further clarity. By setting C_D = 0 for the bare rotor case in Equation 6.23 and Equation 6.24 and comparing to the ducted result, the augmentation can be given by Equation 6.26.

$$\frac{C_D}{C_T} = \frac{u_r - u_{r,bare}}{u_{r,bare}} = \frac{C_P - C_{P,bare}}{C_{P,bare}} \qquad \textbf{Equation 6.26}$$

The link between performance and inviscid drag, then, is straightforward: the ratio of drag to rotor loading C_D/C_T equals the fractional augmentation over a bare actuator disc at the same loading $\left(u_r - u_{r,bare}\right)/u_{r,bare}$. Figure 6.5 confirms that the relationship holds both with the rotor at a duct's throat and at the exit, using the duct shapes from Section 4.2.3. A duct that is augmenting the flow at a given rotor loading will experience drag, one that does not influence the flow will not, and one that is curtailing the flow will experience a force in the upstream direction.

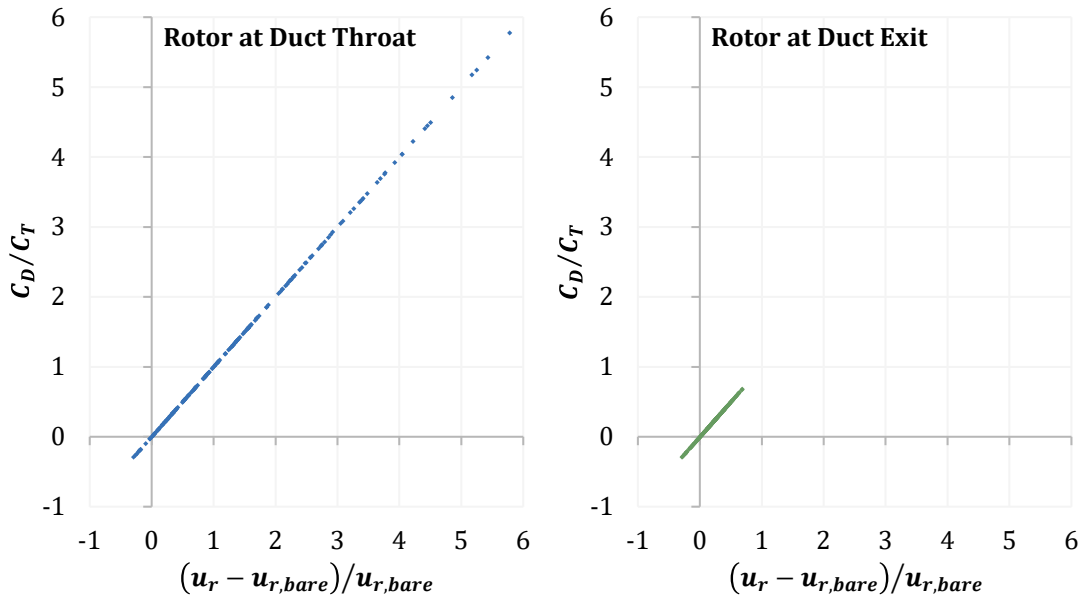

Figure 6.5: Comparison of drag to rotor loading ratio C_D/C_T and fractional augmentation $(u_r - u_{r,bare})/u_{r,bare}$ from simulation results at C_T = 0.75 for 200 duct shapes, with the rotor at the duct throat (left) and at the duct exit (right).

In some ways this is a curious relationship. Recall from Equation 6.20 that a positive duct drag is equal to a force on the streamtube control volume in the upstream direction: as the augmentation of mass flow and hence drag increases, the force on the control volume increasingly opposes the flow. Likewise, a duct that reduces the mass flow through the rotor implies a force on the control volume that intuitively should be accelerating the flow. In other words, the relationship is the opposite of what may be expected. Instead of going from the bare to ducted case by applying a force in the downstream direction to accelerate the flow, there is an additional force in the upstream direction.

Consider the relationship for the momentum drop between far upstream and downstream ΔM in Equation 6.27.

$$\begin{aligned} \Delta M = \dot{m}(u_\infty - u_w) &= \Delta p A_r + F_D \\ &= \Delta p A_r - F_{us} - F_{d,in} - F_{ds} \end{aligned} \qquad \textbf{Equation 6.27}$$

Positive values of $\Delta p A_r$ and F_D imply upstream forces on the flow and a drop in momentum, while positive values of the control volume forces F_{us}, $F_{d,in}$, and F_{ds} imply downstream forces on the flow and a gain in momentum. The method by which momentum can change is constrained, however: u_w is fixed by Δp and u_∞ in Equation 6.13, so the forces on the control volume cannot influence the far wake velocity. To achieve the required change in momentum, therefore, the mass flow rate must vary.

In an operating wind turbine, there is a momentum drop between far upstream and far downstream meaning positive values for $\dot{m}(u_\infty - u_w)$ and $\Delta p A_r$. A force on the control

volume in the upstream direction also reduces the momentum, thereby increasing the magnitude of the drop. This reasoning explains the somewhat counterintuitive result of increased mass flow rate with increased drag: with only the mass flow rate free to vary, it must increase to cause a larger momentum drop for positive drag and negative control volume forces.

The logic here is more straightforward for a rotor increasing the momentum of the flow, as in a ducted propeller. With a momentum gain from the rotor, control volume forces in the upstream direction would decrease the mass flow rate. The influence of forces on the control volume for both ducted turbines and ducted rotors is summarised in Table 6.3, where ΔM_r and ΔM_{cv} are the axial momentum changes caused by the rotor and control volume forces respectively.

Table 6.3: Influence of control volume forces on mass flow rate, for both the momentum drop caused by a rotor and the momentum gain from a propeller.

Momentum Change From Rotor ΔM_r	Control Volume Force		
	Direction	Momentum Change ΔM_{cv}	Influence On Mass Flow $\dot{m}$
Drop	Upstream	Drop	Increase
Drop	Downstream	Gain	Decrease
Gain	Upstream	Drop	Decrease
Gain	Downstream	Gain	Increase

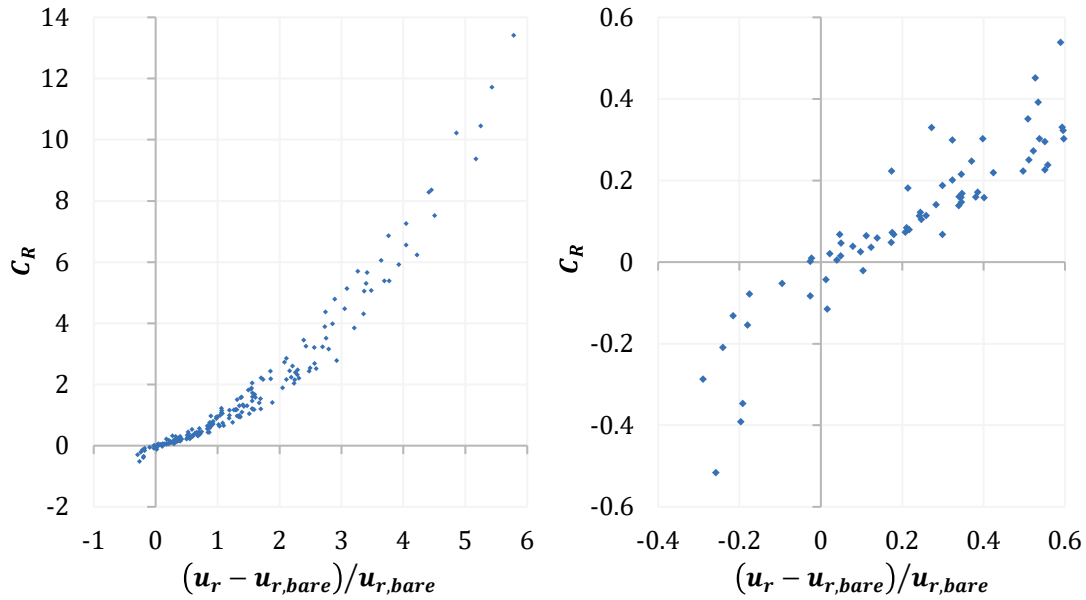

Figure 6.6: Comparison of radial force per unit radian coefficient C_R and fractional augmentation $(u_r - u_{r,bare})/u_{r,bare}$ from simulation results at C_T = 0.75 for 200 duct shapes (left), with a focus on results near zero augmentation (right).

Extending this study to consider radial forces shows that there is not an exact relationship with augmentation, as shown in Figure 6.6, despite many authors viewing

these forces as a cause of augmentation. A significant reduction in scatter is seen as the fractional augmentation approaches zero, however, suggesting an inward force on the duct when the flow is augmented and an outward force when the flow is curtailed. The small values of radial force remaining at zero augmentation could well be numerical error, although further work is needed to confirm this hypothesis.

6.2.2 Power Extraction Matches Numerical Results

The relationships derived in Section 6.1.4 are dependent on an empirical parameter, as they cannot be used to predict the power extracted by a particular ducted turbine without results for the inviscid drag. Nevertheless, certain general conclusions can be reached. Consider first the rearrangement of Equation 6.11 in Equation 6.28.

$$\frac{P}{\dot{m}} = \frac{1}{2}(u_\infty^2 - u_w^2) \qquad \textbf{Equation 6.28}$$

With Equation 6.13 demonstrating that the far wake velocity is fixed by the rotor loading and free stream velocity, there can be no direct augmentation of the power per unit mass flow by a ducted turbine in inviscid flow.

Dividing Equation 6.28 by $0.5\rho u_\infty^3 A_r$ then leads to Equation 6.29.

$$C_P = \frac{u_r(u_\infty^2 - u_w^2)}{u_\infty^3} \qquad \textbf{Equation 6.29}$$

At a particular rotor loading, power increases linearly with the mean axial velocity at the rotor and hence mass flow. This conclusion is consistent with the numerical results in Section 3.1.3 and with previous findings [55, 58].

None of the equations presented in Section 6.1.4 imply any kind of limitation on the inviscid performance of a ducted turbine. With no independent equation for the inviscid drag, it can only be stated that the power extracted will continually increase so long as the drag does. Indeed, the numerical results in Section 3.2.2 exhibited no indication of a limit as the ducts grew to ridiculous proportions.

Modifying Equation 6.23 to instead provide the exit area power coefficient $C_{P,e}$ gives Equation 6.30.

$$C_{P,e} = \frac{A_r}{A_e}\frac{1}{2}(C_T + C_D)\left(1 + \sqrt{1 - C_T}\right) \qquad \textbf{Equation 6.30}$$

Any limitation on performance remains a practical question: as with the standard C_P equation, the limit will be set by how C_D actually varies for a particular duct. The theoretical description is therefore fully consistent with the numerically based conclusion in Section 3.1.8 that the Betz limit does not apply to ducted turbines.

6.2.3 Optimum Rotor Loading Remains Empirical

Of the ducts numerically modelled in Section 3.1.4, all had an optimum rotor loading less than the bare rotor value of C_{Topt} = 8/9. Only a limited subset of the possible duct shapes were examined there, however, leaving open the question: how do ducted turbines affect C_{Topt} in general?

As with maximum power, there is insufficient information to determine the optimum rotor loading from the equations in Section 6.1.4 alone. What can be shown is that the equations themselves do not require a change in C_{Topt} at all. Consider the hypothetical case of a ducted turbine where drag varies according to $C_D = kC_T$, where k is a constant.

Inserting the hypothetical drag relationship into Equation 6.23 gives the power for this particular turbine in Equation 6.31.

$$C_P = \frac{1}{2}(C_T + kC_T)\left(1 + \sqrt{1 - C_T}\right) \qquad \textbf{Equation 6.31}$$

Differentiating C_P with respect to C_T will lead to the optimum rotor loading for this duct, beginning with Equation 6.32.

$$\frac{\mathrm{d}C_P}{\mathrm{d}C_T} = \frac{\mathrm{d}}{\mathrm{d}C_T}\left[\frac{1}{2}(1+k)C_T\right] + \frac{\mathrm{d}}{\mathrm{d}C_T}\left[\frac{1}{2}(1+k)C_T\sqrt{1-C_T}\right] \qquad \textbf{Equation 6.32}$$

Using the product rule for second term on the right hand side and then the chain rule leads to Equation 6.33.

$$\frac{\mathrm{d}C_P}{\mathrm{d}C_T} = \frac{1}{2}(1+k) - \frac{{}^1\!/_4\,(1+k)C_T}{\sqrt{1-C_T}} + \frac{1}{2}(1+k)\sqrt{1-C_T} \qquad \textbf{Equation 6.33}$$

Setting $\mathrm{d}C_P/\mathrm{d}C_T$ = 0, rearranging, and squaring results in Equation 6.34.

$$\frac{(1+k)^2}{4} = \frac{(1+k)^2 C_T^2}{16(1-C_T)} - \frac{(1+k)^2 C_T}{4} + \frac{(1+k)^2(1-C_T)}{4} \qquad \textbf{Equation 6.34}$$

Assuming $k \neq$ -1, Equation 6.34 can be divided by $(1+k)^2$ and rearranged to find Equation 6.35.

$$0 = C_T(9C_T - 8) \qquad \textbf{Equation 6.35}$$

The only valid solution to this equation is C_T = 8/9 for maximum power. It is not known if $C_D = kC_T$ is possible for a ducted turbine, but this result nevertheless demonstrates that the relationships derived in this chapter do not imply that C_{Topt} must change from the bare rotor value.

C_{Topt} consequently remains a practical question, in which augmentation plays a key role: Equation 6.26 shows that in reality C_D and C_T are related by augmentation, itself

found to be a function of C_T in Section 3.1.5. If augmentation reduces with increasing C_T, u_r for the ducted turbine would by definition reduce at a faster rate with C_T than for a bare rotor. So, therefore, would the energy in the flow. As the fraction of energy extracted increases identically with C_T for ducted and bare actuator discs, C_{Topt} would in turn be lower for ducted turbines. Chapter 7 will consider whether augmentation actually does reduce in general with C_T.

6.3 Alternative Relationships

Writing the C_P equation in terms of the thrust and drag coefficients, as in Section 6.1.4, is just one of the possible approaches. Alternatives based on axial induction and exit pressure are derived here, for later comparison in Section 6.4.

6.3.1 Based on Axial Induction

It is common to express the power and thrust coefficients for a wind turbine in terms of the axial induction, rather than a single equation with C_P in terms of C_T. The same can be achieved for ducted turbines, beginning by combining Equation 6.7 and Equation 6.20 then rewriting in terms of the axial induction at the rotor a_r to find Equation 6.36.

$$\Delta p A_r + F_D = (u_\infty - u_w)\rho A_r u_\infty (1 - a_r) \qquad \textbf{Equation 6.36}$$

An application of Bernoulli's equation assuming no losses in the duct, meanwhile, leads to Equation 6.37.

$$\Delta p = \frac{1}{2}\rho(u_\infty^2 - u_w^2) \qquad \textbf{Equation 6.37}$$

Substituting into Equation 6.36 and rearranging to find the far wake velocity using the quadratic formula gives the choice in Equation 6.38.

$$u_w = (1 - a_r)u_\infty \pm u_\infty\sqrt{a_r^2 + C_D} \qquad \textbf{Equation 6.38}$$

Given that $(1 - a_r)u_\infty = u_r$, the second term on the right hand side of this equation must equal the difference between u_r and u_w. It is therefore possible to determine the correct sign: the negative option must be chosen for $u_w < u_r$, which would be expected when the flow is augmented, unaffected, or moderately curtailed. It is theoretically possible to obtain $u_w > u_r$, since Equation 6.13 shows that u_w depends only on u_∞ and C_T, so for severely curtailing ducts the positive option must be used. When $u_w = u_r$, the second term is equal to zero and both signs are equivalent.

Continuing for augmenting ducts leads to Equation 6.39.

$$u_w = u_\infty\left(1 - a_r - \sqrt{a_r^2 + C_D}\right) \qquad \textbf{Equation 6.39}$$

Substituting u_w back into Equation 6.36 and using the relationship for power in Equation 6.12, with the standard definition of power coefficient, gave Equation 6.40.

$$C_P = 2\left(a_r + \sqrt{a_r^2 + C_D}\right)(1 - a_r)^2 - C_D(1 - a_r) \qquad \textbf{Equation 6.40}$$

Similarly, substituting for u_w in Equation 6.36 and using the standard definition of thrust coefficient found the relationship in Equation 6.41.

$$C_T = 2\left(a_r + \sqrt{a_r^2 + C_D}\right)(1 - a_r) - C_D \qquad \textbf{Equation 6.41}$$

Both the C_P and C_T equations directly reduce to standard actuator disc theory when C_D is set to zero. Finally, rearranging Equation 6.36 and using the substitution for u_w led to Equation 6.42.

$$C_D = 2\left(1 - \sqrt{1 - C_T}\right)(1 - a_r) - C_T \qquad \textbf{Equation 6.42}$$

Table 6.4 shows the results of testing the final axial induction relationships against the inviscid simulation results. Reduced discretisation convergence at high C_T for duct VB led to elevated inequalities for the C_D equation, but the difference fell to less than 0.72% for rotor loadings of 8/9 and below. The relationships are therefore valid.

Table 6.4: Largest absolute inequalities found for the axial induction relationships, as a percentage of the median magnitude of the right hand side across all rotor loadings tested.

Inequality for	Duct VA	Duct VB	Duct VC
Equation 6.40	0.17%	0.18%	0.15%
Equation 6.41	0.23%	0.26%	0.23%
Equation 6.42	0.83%	1.66%	0.39%

6.3.2 Based on Exit Pressure

Theoretical descriptions of ducted turbines frequently relate performance to the pressure in the exit plane of the duct. All such cases seen in Section 5.8 included both the exit pressure and the velocity at the rotor, despite the direct relationship between these parameters through Bernoulli's equation and mass continuity. An alternative is derived here that does not involve velocity.

Beginning with an application of Bernoulli's equation, assuming zero losses, leads to Equation 6.43.

$$C_T + C_{p,e} = 1 - \gamma_{x,e}\frac{u_e^2}{u_\infty^2} \qquad \textbf{Equation 6.43}$$

This equation uses the standard definition of exit pressure coefficient $C_{p,e}$ and the velocity correction factor $\gamma_{x,e}$ described in Section 5.3. Using mass continuity to replace the velocity at the exit with the velocity at the rotor then gives Equation 6.44.

$$u_r = \pm \frac{1}{\sqrt{\gamma_{x,e}}} \frac{A_e}{A_r} u_\infty \sqrt{1 - C_T - C_{p,e}} \qquad \textbf{Equation 6.44}$$

The positive option matched simulation results for both augmenting and curtailing ducts. Substituting into Equation 6.22 leads to Equation 6.45.

$$C_P = \frac{1}{\sqrt{\gamma_{x,e}}} \frac{A_e}{A_r} C_T \sqrt{1 - C_T - C_{p,e}} \qquad \textbf{Equation 6.45}$$

Although the aim of relating exit pressure to power without involving velocity has been achieved, it has been replaced by the rotor loading which also has an influence on exit pressure. It seems more reasonable, however, to treat C_T rather than u_r as a design variable held constant to investigate the influence of exit pressure, with velocity and power as objectives to optimise.

An extra empirical parameter has also been introduced in the form of $\gamma_{x,e}$, when comparing with other theoretical descriptions. This addition reflects the change in assumptions away from radially uniform, purely axial flow. It therefore does not represent any real additional complexity in the equation, and can simply be set to 1 if the simplifying assumptions are desired.

The augmentation can be calculated by dividing Equation 6.45 by Equation 6.23 with C_D = 0, giving Equation 6.46.

$$\frac{C_P}{C_{P,bare}} = \frac{2}{\sqrt{\gamma_{x,e}}} \frac{A_e}{A_r} \frac{\sqrt{1 - C_T - C_{p,e}}}{1 + \sqrt{1 - C_T}} \qquad \textbf{Equation 6.46}$$

A relationship between the drag and exit pressure empirical parameters can be found by substituting Equation 6.44 into Equation 6.24, leading to Equation 6.47.

$$C_{p,e} = 1 - C_T - \frac{A_r^2}{A_e^2} \gamma_{x,e} \left(\frac{1}{2} + \frac{C_D}{2C_T} \right)^2 \left(1 + \sqrt{1 - C_T} \right)^2 \qquad \textbf{Equation 6.47}$$

With the other parameters held constant, increased drag is associated with reduced exit pressure. Both are associated with increased power extraction, and are simply alternative ways of representing the underlying performance of the duct.

Good agreement was found in all cases between the equations and simulation results, as seen in Table 6.5.

Table 6.5: Largest absolute inequalities found for the exit pressure relationships, as a percentage of the median magnitude of the right hand side across all rotor loadings tested.

Inequality for	Duct VA	Duct VB	Duct VC
Equation 6.44	0.01%	0.01%	0.34%
Equation 6.45	0.01%	3×10^{-3}%	0.17%
Equation 6.46	0.01%	0.01%	0.24%
Equation 6.47	0.55%	0.60%	0.46%

6.4 Power Equations: Informative or Misleading?

In this chapter, and in the literature generally, various perspectives have been used when formulating equations for ducted turbines. Examples have been presented here for power extraction calculated with velocity, drag, and exit pressure as the empirical parameter. All are equally valid, but this section will consider if all are equally useful.

The simplest equation is found using velocity at the rotor, by rearranging Equation 6.22 into Equation 6.48.

$$C_P = \frac{u_r}{u_\infty} C_T \qquad \textbf{Equation 6.48}$$

An inviscid drag-based approach was derived in Equation 6.23, repeated here as Equation 6.49.

$$C_P = \frac{1}{2}(C_T + C_D)\left(1 + \sqrt{1 - C_T}\right) \qquad \textbf{Equation 6.49}$$

Replacing C_T with the axial induction at the rotor led to Equation 6.40, repeated in Equation 6.50.

$$C_P = 2\left(a_r + \sqrt{a_r^2 + C_D}\right)(1 - a_r)^2 - C_D(1 - a_r) \qquad \textbf{Equation 6.50}$$

Finally the duct exit pressure was used as an empirical parameter in Equation 6.45, repeated as Equation 6.51.

$$C_P = \frac{1}{\sqrt{\gamma_{x,e}}} \frac{A_e}{A_r} C_T \sqrt{1 - C_T - C_{p,e}} \qquad \textbf{Equation 6.51}$$

All of these equations suffer from the same problem: the parameters are interrelated, making their influence difficult to determine. It is logical, however, to examine their influence at a particular rotor loading, as C_T can be chosen by the designer and will have a single optimum value for a particular turbine. Straightforward relationships then exist between C_P and the empirical parameters of velocity and drag in the first two equations.

Interpretation of Equation 6.50 unfortunately remains problematic, as a_r and C_D are correlated even at fixed loading. This relationship is particularly confusing if C_D is considered as representing the performance of the duct: the purpose of increasing C_D is then to reduce a_r, meaning Equation 6.50 cannot be used alone to determine the connection between duct performance and power extraction. In the final equation, $\gamma_{x,e}$, A_e/A_r, and $C_{p,e}$ also remain interrelated at fixed C_T. With these relationships being unknown, Equation 6.51 yields only limited information.

A key question in ducted turbine design is the influence of duct geometry on performance. Only the exit pressure equation involves a geometrical parameter, but that may be misleading rather than useful: it places greater emphasis on area ratio than other geometrical parameters without any evidence that area ratio is actually of more importance, and it does not make explicit the relationship between area ratio and exit pressure. It also implies a use of diffuser-based parameters for ducted turbines when Sections 3.4 and 4.3 suggested that aerofoil parameters are more suitable.

If these equations cannot inform the optimisation of duct geometry, it may be sensible to measure the influence on performance directly. Drag and exit pressure changes could then be considered as consequences of the augmentation rather than as empirical parameters from which to calculate C_P. In some cases power could be calculated directly in experiments or simulations, but otherwise Equation 6.48 keeps the focus on the most direct causes of augmentation: increases in mass flow, and increases in optimum rotor loading if that proves to be possible.

6.5 Summary

Can a detailed derivation lead to ducted turbine performance in terms of total duct drag? That was the question raised at the end of Chapter 5, and addressed here by applying general forms of the momentum and energy equations. An essential result came from a numerical study: the forces acting on the surface of the streamtube passing through the duct are equal and opposite to the total inviscid duct drag. With this information it is possible to go beyond previous detailed derivations and calculate power extracted from rotor loading and duct drag.

Confirmation is provided by the analytical results of the linear relationship between the power and drag coefficients. The equations also lead to the intriguing conclusion that the mass flow through the turbine grows as the forces on the streamtube increasingly oppose the flow. Two factors explain this result. First, the streamtube forces cause a momentum drop over and above that caused by the rotor. Second, the far wake velocity is fixed by the rotor loading and free stream velocity. The additional momentum drop must therefore be associated with an increased mass flow.

Theoretical results for power are also consistent with earlier numerical results: power per unit mass flow is unaffected at fixed rotor loading, power varies linearly with mass flow, and there is no indication that the Betz limit should apply. While the equations themselves do not impose any change from the bare rotor $C_{Topt} = 8/9$, empirical results are needed to calculate the optimum rotor loading for a particular turbine. A further numerical investigation is required to determine how the optimum rotor loading is affected in general.

The inviscid duct drag is not the only basis for calculating the power extracted; formulations with velocity, axial induction, and exit pressure are also possible. All suffer from the problem of interrelated parameters, however, although those based on velocity and drag are straightforward at fixed rotor loading. These equations also give little insight into the geometrical design of ducted turbines, and can even be misleading. It may therefore be better to consider empirical parameters like drag and exit pressure as consequences of augmentation rather than a means to calculate it.

Chapter 7

Optimum Rotor Loading and Augmentation Theory

Both the numerical results in Section 3.1.4 and the analytical examination in Section 6.2.3 confirmed that optimum rotor loading coefficients below 8/9 are possible for ducted turbines in inviscid flow, an important difference from the bare rotor value [5]. Both studies, however, left open the larger question: must C_{Topt} be less than 8/9? A combination of approaches is used here to find the answer, beginning with a much larger scale numerical investigation. The circulation explanation for augmentation is then validated, before being used with numerical results to show that increased rotor loading reduces augmentation and therefore decreases C_{Topt} in inviscid flow.

7.1 Optimum Rotor Loading: Numerical Investigations

7.1.1 A Search with Duct Shape Optimisation

An optimisation approach was the first numerical tactic used, with duct shape modified in search of the maximum C_{Topt} possible. Thirty starting duct shapes were selected to minimise the chance of finding only a sub-optimal local maximum, with the optimisation for each completed using an interior point algorithm [176]. The optimisation was carried out in two stages, first with a coarser discretisation to bring the starting duct shapes closer to optimum and then with a finer discretisation for more accurate results.

Two fixed nodes defined the inlet and outlet for the ducts, and served as bounds for two movable nodes that were adjusted during the optimisation. Nodes were interpolated between using a piecewise cubic Hermite spline [153]. Duct starting shapes were defined using the nodes on the left of Figure 7.1: for each shape, one node was chosen and then the second selected from any of the nodes with an equal or greater axial coordinate and a greater radial coordinate. These constraints gave thirty possible combinations, of which five examples are shown on the right of Figure 7.1.

Most of the starting shapes ended the first stage of optimisation in relatively similar positions, as seen on the left of Figure 7.2. The top 27 ducted turbines all had optimum rotor loadings within 0.32% of the maximum found, with three outliers ranging between 6.2% and 9.4% lower. Some of the duct shapes were subjectively very similar, so only those with the greatest C_{Topt} in a group of alike shapes were kept for the second stage of optimisation. The remaining 16 shapes are shown on the right of Figure 7.2.

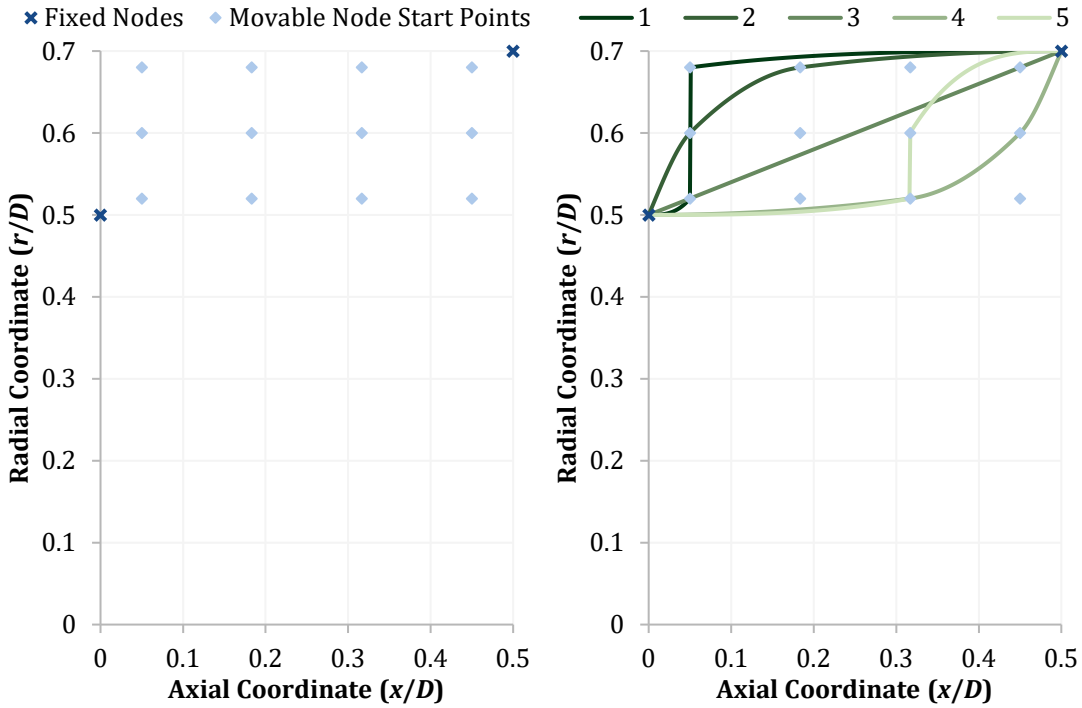

Figure 7.1: Node positions used to generate starting duct shapes (left), and 5 example starting duct shapes (right).

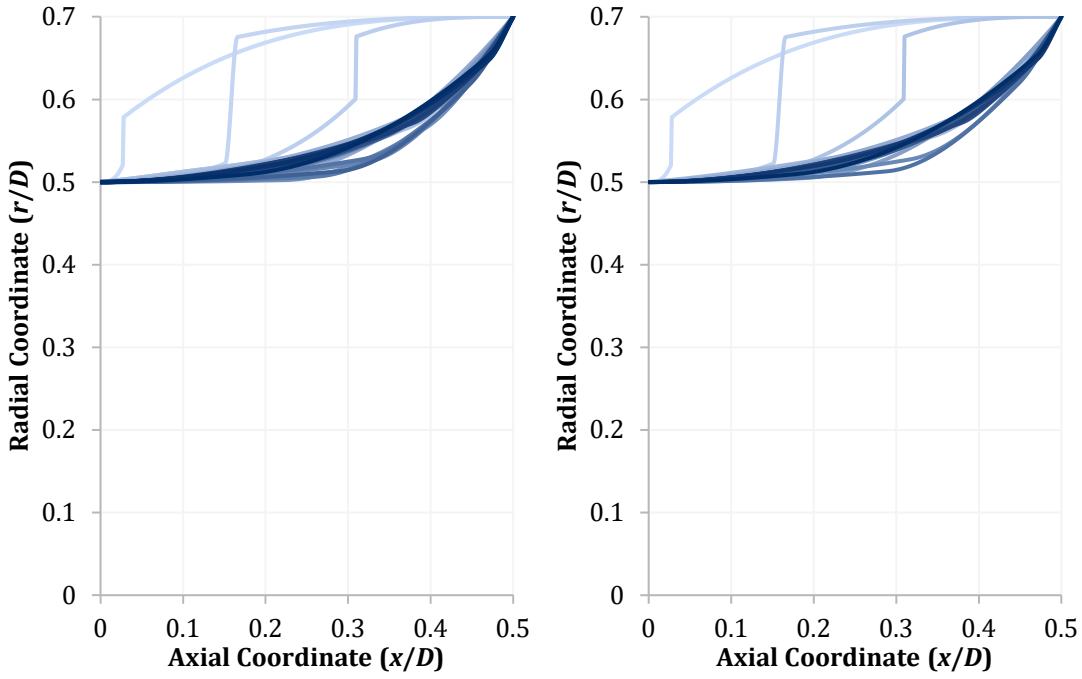

Figure 7.2: Duct shape results from the first optimisation stage (left), and those results grouped into 16 starting duct shapes for the second stage (right). Darker lines indicate a higher C_{Topt} ranking.

A last duct panel length of $0.02D$ and an expanding wake length of $8D$ were chosen for stage 2 of the optimisation, as that gave adequate C_{Topt} discretisation convergence for the best stage 1 shape. The spread of the optimum shapes reduced after optimisation at the increased resolution, as seen on the left of Figure 7.3. C_{Topt} was within 0.11% of the best shape for the top 15 shapes, while the single remaining outlier lay 7.9% lower.

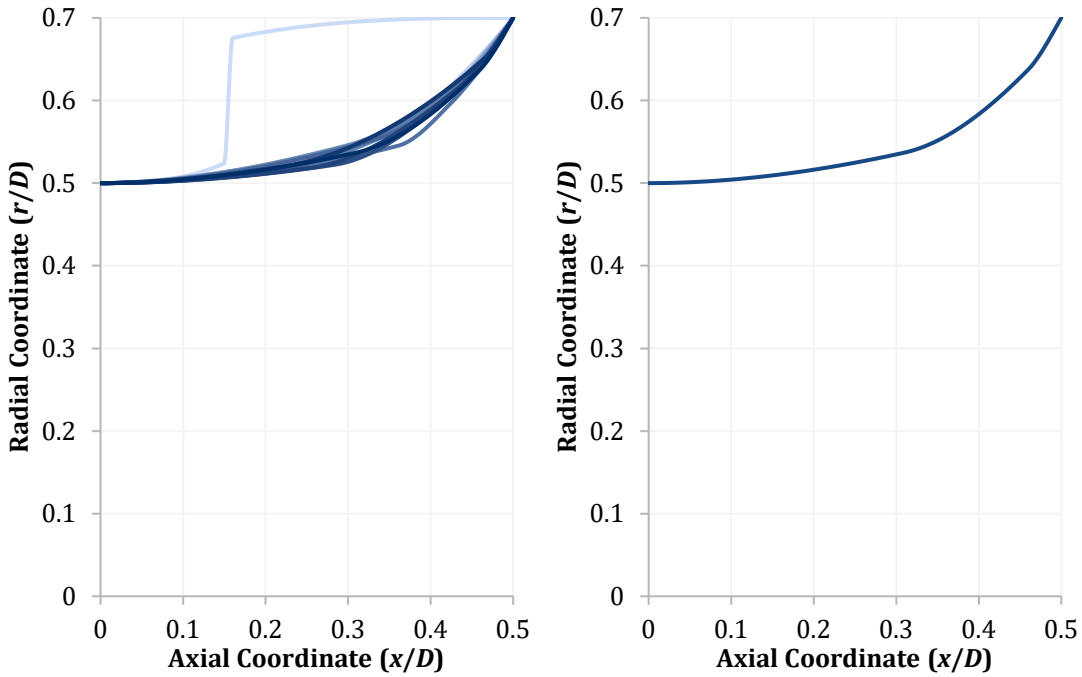

Figure 7.3: Duct shape results from the second optimisation stage (left), where darker lines indicate a higher C_{Topt} ranking, and the duct shape for maximum C_{Topt} (right).

The shape with the largest optimum rotor loading is shown alone on the right of Figure 7.3, and achieved C_{Topt} = 0.81. Notable is the smoothness of the shape, in contrast to the right angled ducts that maximised power extraction in Section 3.2.1. Discretisation convergence for this shape was adequate, with C_{Topt} changed by -0.11% and -0.72% by doubling the expanding wake length and halving the panel lengths respectively. Given the reduced spread between stage 1 and 2, increased resolution also seems unlikely to change the shapes found by the optimisation algorithm. Tightening the optimisation stopping criteria by an order of magnitude did not change the result.

Two important limitations exist for this investigation. First, fixed end points were enforced, only two movable nodes were used, and the movable nodes were constrained within the end point bounds; the optimum found is therefore only the optimum within these restrictions. Second, different start points could have led to a result with a greater C_{Topt}. It is, however, reassuring that the start shapes appeared to be caught in a single basin of attraction with an optimum far from the bounds. While the first limitation still applies, it seems likely that the result is the global optimum within the constraints applied.

7.1.2 A Search with Many Duct Shapes

Some of the shortcomings of the optimisation investigation were addressed by examining the duct shapes used in Chapter 4. Although there was no optimisation algorithm seeking to maximise optimum rotor loading, 1776 duct shapes were modelled with less restrictive constraints on geometry than used in the previous section. All of the diffuser and aerofoil parameter duct shapes from Chapter 4 were inspected here, giving the geometrical limits shown in Table 7.1 and Table 7.2. Full details of the geometry generation and results showing acceptable discretisation convergence for C_{Topt} are presented in Sections 4.1 and 4.2.

Table 7.1: Geometrical limits for the diffuser parameter duct shapes.

	Inlet Area Ratio	Exit Area Ratio	Length Ratio	Exit Angle
Minimum	1	1	0.05	-16.8°
Maximum	2.37	3.54	0.82	74.9°

Table 7.2: Geometrical limits for the aerofoil parameter duct shapes.

	Length Ratio	Camber	Angle
Minimum	0.1	0%	-5°
Maximum	1	25%	35°

All of the results are plotted against C_{Pmax} in Figure 7.4, but a great deal of caution must be used in interpreting this figure: only some of the duct shapes were chosen randomly and the set of shapes is certainly not a representative sample of all possible or feasible duct shapes. The features seen on the plot may simply be artefacts of the duct shapes that happened to be chosen.

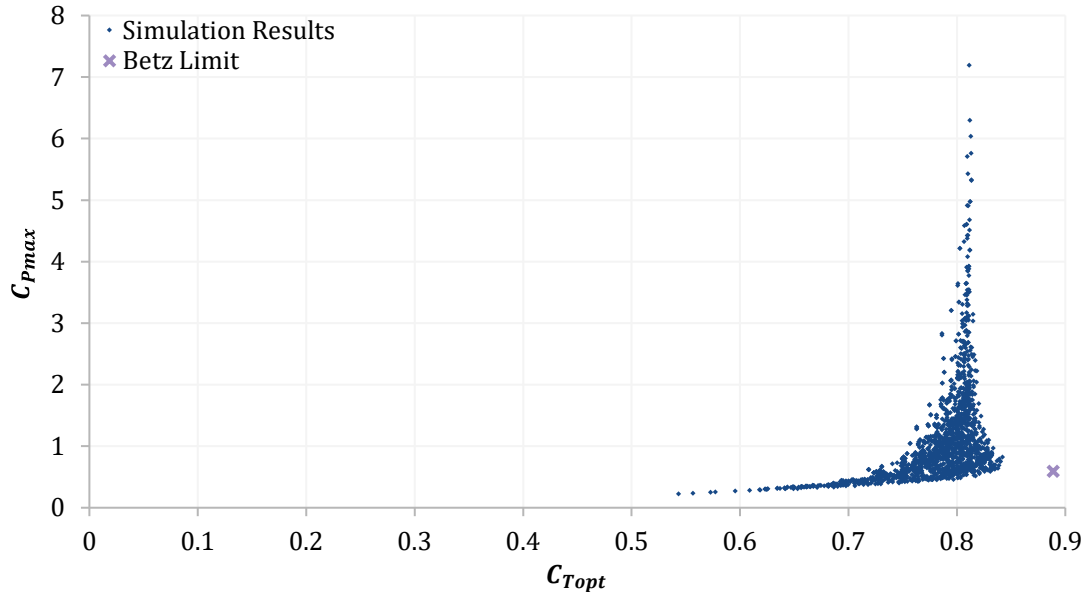

Figure 7.4: Optimum rotor loading for 1776 aerofoil and diffuser parameter duct shapes.

The features in Figure 7.4 can be accounted for, however, so similar results may perhaps be found for other sets of duct shapes. An important factor is the strength of the influence that a particular duct has on the flow. Consider the lower bound to C_{Pmax} that rises with C_{Topt}. Ducts in this region are curtailing the flow compared to a bare rotor, and appear to be approaching the bare rotor values of C_{Topt} and C_{Pmax} as the ducts have less and less influence on the flow.

Similar reasoning can be applied to the C_{Pmax} upper bound on the right of the peak. A duct that causes a large value of C_{Pmax} is by definition having a large influence on the flow. If there is an inherent decrease in C_{Topt} with ducted turbines, the only way to approach C_{Topt} = 8/9 would be to reduce the influence of the duct. A reduced C_{Pmax} would logically follow.

The C_{Pmax} upper bound to the left of the peak can be partially explained by the linear relationship between C_P and C_T at a fixed flow rate through the rotor. As the bound appears to have a much greater than linear relationship, however, some other factor is also involved. An association between increased C_{Topt} and a greater flow rate must exist, if this bound is not simply caused by the duct shapes chosen, albeit one that does not continue all the way to C_{Topt} = 8/9.

Figure 7.5 plots the same optimum rotor loadings against the duct length ratio. Again the results must be interpreted with caution, but they are consistent with an explanation used for the features in Figure 7.4: only the smallest ducts, with the least influence on the flow, approach the highest values of C_{Topt}. The duct for the lowest C_{Topt}, meanwhile, is shown by Figure 7.6 to be relatively large with a shape that will act to reduce flow rate.

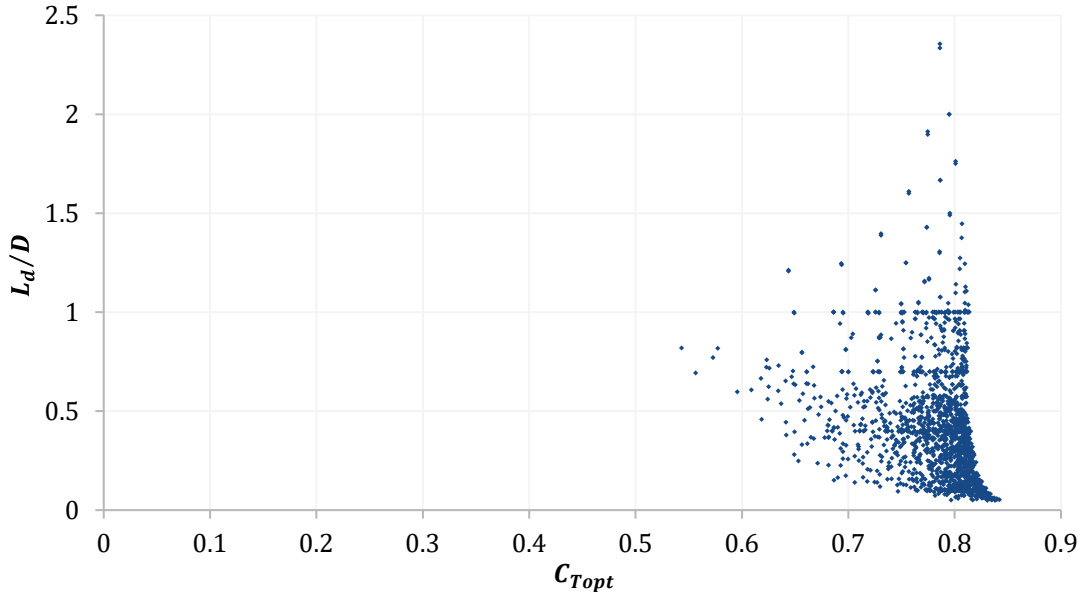

Figure 7.5: Comparison of C_{Topt} and duct length ratio L_d/D for 1776 duct shapes.

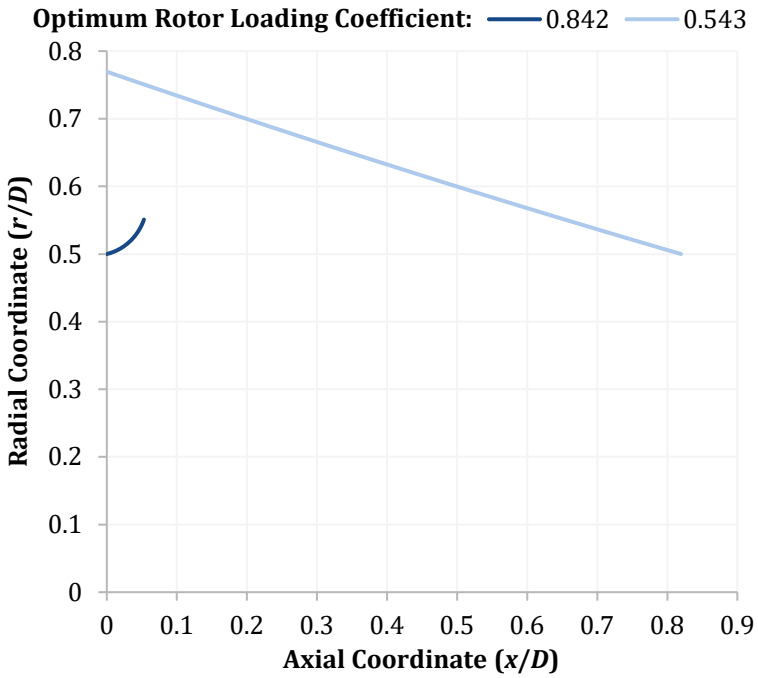

Figure 7.6: Duct shapes found with highest and lowest values for optimum rotor loading coefficient C_{Topt}.

7.1.3 The Failure to Reach 8/9

These studies suggest that ducts decrease the optimum rotor loading in inviscid flow, as an optimisation algorithm modifying duct shape managed only C_{Topt} = 0.81 while a comparison of 1776 duct shapes reached C_{Topt} = 0.84. Smaller ducts in the second case led to the higher C_{Topt}, as in the limit of no duct C_{Topt} must reach the bare rotor value of 8/9. A direct search, however, can never prove that C_{Topt} must be reduced: there will always be other optimisation approaches to try or duct shapes left unexamined. Additional evidence is required, and will be found using an alternative approach where the mechanism of augmentation is considered.

7.2 Augmentation Theory

Throughout this work, an aerofoil conceptual model for the performance of ducted turbines has proven useful, but not flawless: a less than perfect association between circulation and augmentation was found in Section 3.1.6. This inconsistency must be addressed before the mechanism of augmentation can be used to explain the reductions in C_{Topt}. The diffuser conceptual model was not considered for this investigation due to the superiority of the aerofoil model in making performance predictions and for parameterising duct geometry.

7.2.1 Circulation or Force Explanation?

An initial hypothesis for the cause of the aerofoil inconsistency was that the true mechanism of augmentation was the radial or total force acting on the duct, rather than circulation. If circulation and force had an imperfect relationship, this hypothesis could explain both the usefulness of the aerofoil conceptual model and the imperfect relationship between circulation and augmentation. A set of 200 duct shapes randomly generated from the NACA 4-digit aerofoil family, as described in Section 4.2.3, was used to test the hypotheses by calculating the correlations between axial velocity, circulation, and duct forces at C_{Topt}. Discretisation convergence was good, with the changes above 1% seen in Table 7.3 caused only by small valued results.

Table 7.3: Worst and median magnitude change in dimensionless results when discretisation was changed for the discretisation checking duct shapes at C_{Topt}. Last duct panel length began at $0.00125D$ and expanding wake length at $8D$.

	% Difference with			
	Halved Panel Length		Doubled Wake Length	
Result	Worst	Median	Worst	Median
Circulation	1.63	0.11	0.32	0.04
Radial Force – Throat Rotor	17.25	0.12	11.50	0.04
Total Force – Throat Rotor	0.43	0.11	0.54	0.03
Radial Force – Exit Rotor	1.26	0.13	0.56	0.05
Total Force – Exit Rotor	1.30	0.12	0.56	0.05
Velocity Ratio	0.37	0.27	0.13	0.00

Pearson and Spearman correlation coefficients are shown in Figure 7.7 as tests of the linear and monotonic relationship strengths respectively; this approach allowed relationships of any form to be detected. Both throat and exit-based values were tested. In no case was a perfect relationship found, and the force correlations exceeded circulation values in only one case: the combination of radial force with the rotor at the throat, throat velocity ratio, and the Spearman coefficient. Without formal hypothesis testing it is impossible to say if the difference found was statistically significant, but such a small difference is not practically significant either way.

Visually examining the data in Figure 7.8 shows little difference in the scatter, confirming that there is no practical difference in the monotonic relationship strengths. There is a noticeable difference in linearity, however, with the circulation relationship being more linear. A comparison of the radial force and circulation coefficients in Figure 7.9 is consistent with this finding, as there is a close relationship leading to similar Spearman coefficients but it is non-linear leading to dissimilar Pearson coefficients.

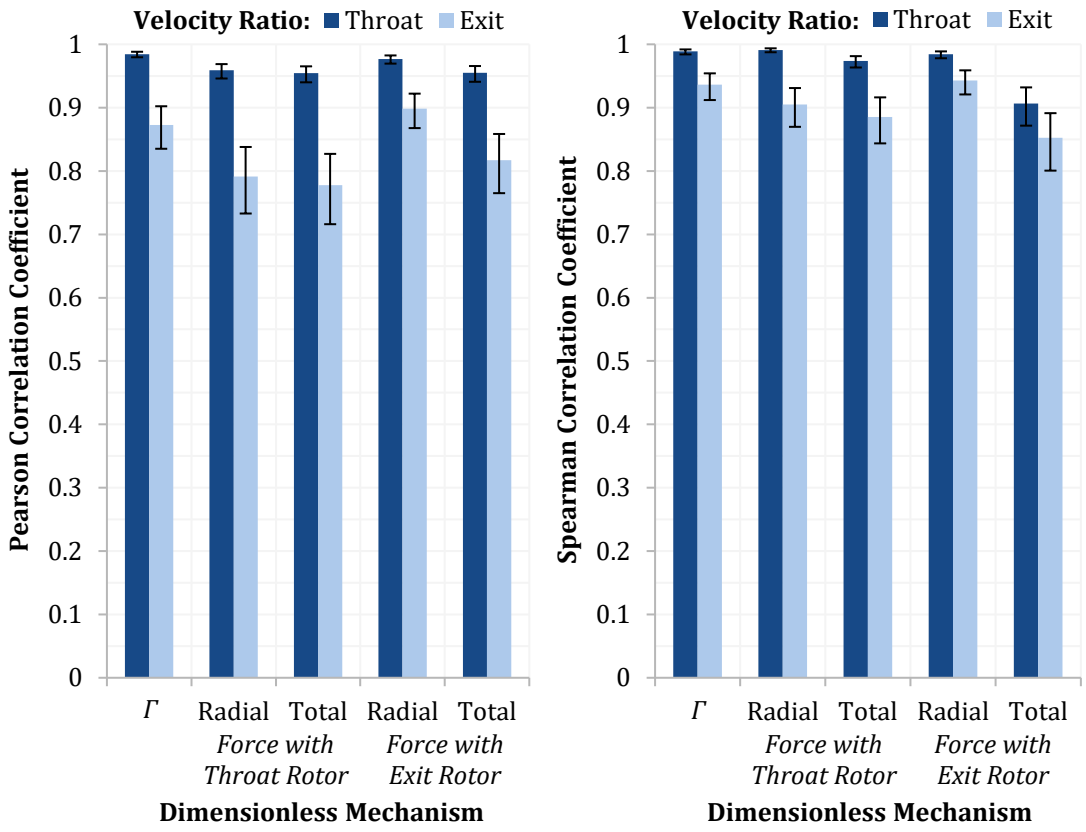

Figure 7.7: Pearson (left) and Spearman (right) correlation coefficients between axial velocity ratios in the duct u/u_∞ and proposed mechanisms of augmentation, with 95% confidence intervals shown. Calculated at C_{Topt} for 200 random duct shapes.

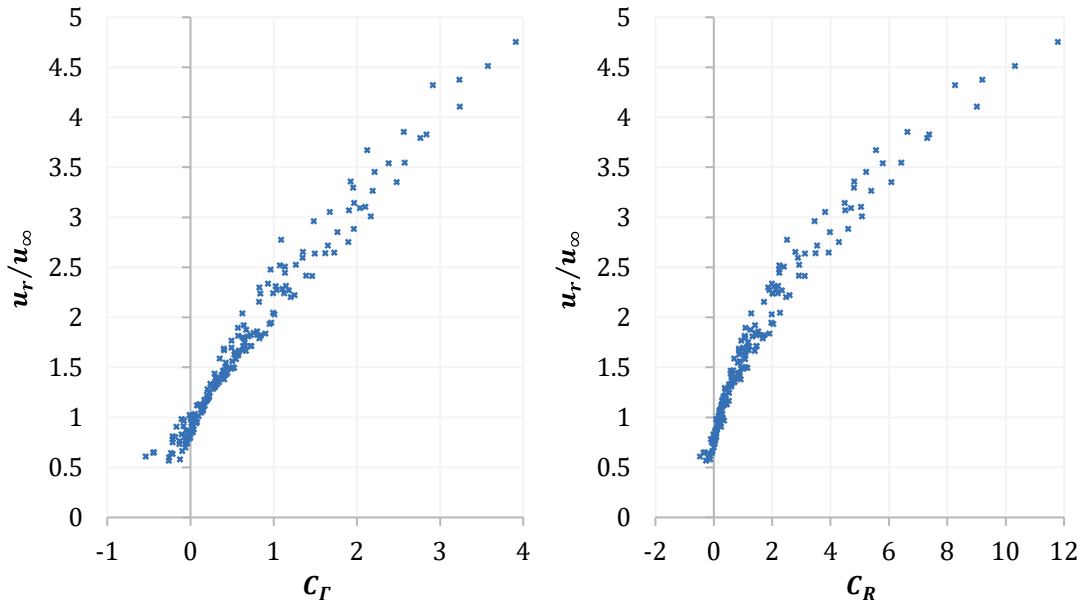

Figure 7.8: Variation of axial velocity at the throat u_r with duct circulation coefficient C_Γ (left) and the coefficient of radial force per radian C_R with throat rotor (right). Calculated at C_{Topt} for 200 random duct shapes.

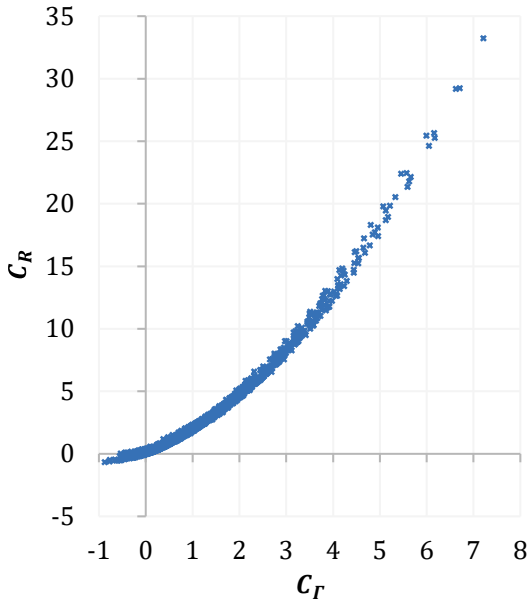

Figure 7.9: Variation of the coefficient of radial force per radian C_R with circulation coefficient C_Γ for 200 random duct shapes at all C_T values modelled and with the rotors at each duct's throat.

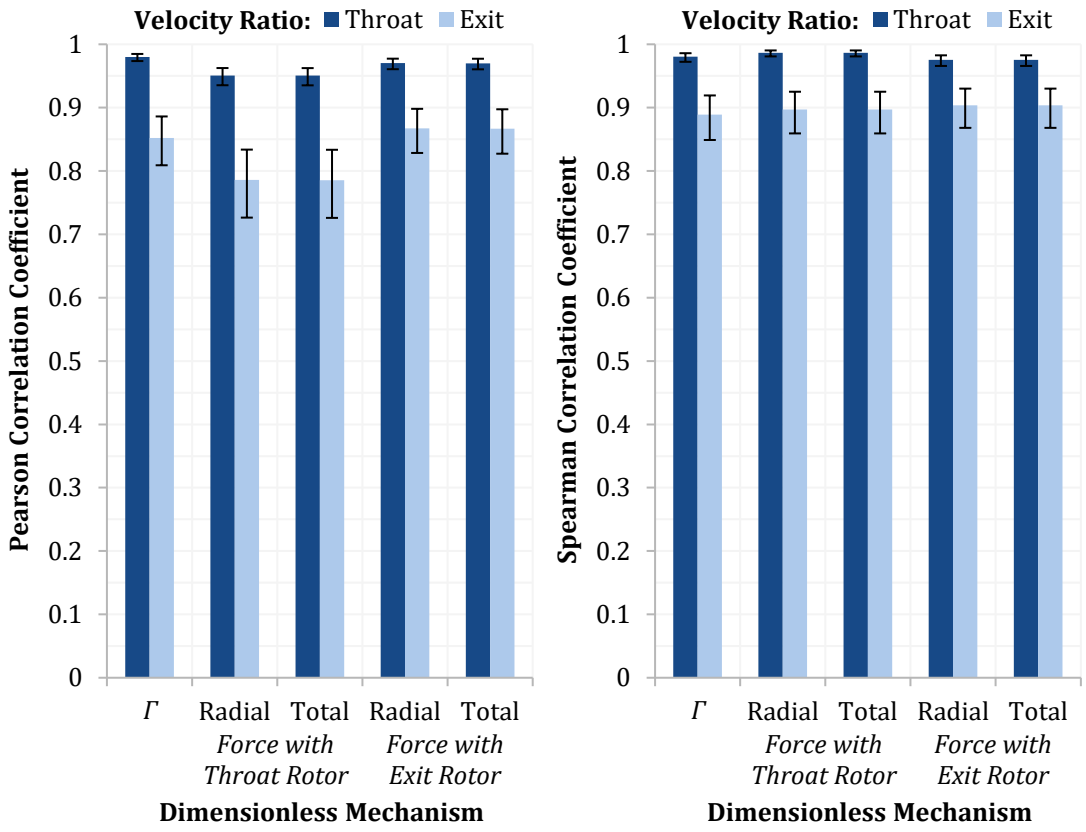

Figure 7.10: Pearson (left) and Spearman (right) correlation coefficients between axial velocity ratios u/u_∞ in the duct and proposed mechanisms of augmentation, with 95% confidence intervals shown. Calculated at C_T = 0 for 200 random duct shapes.

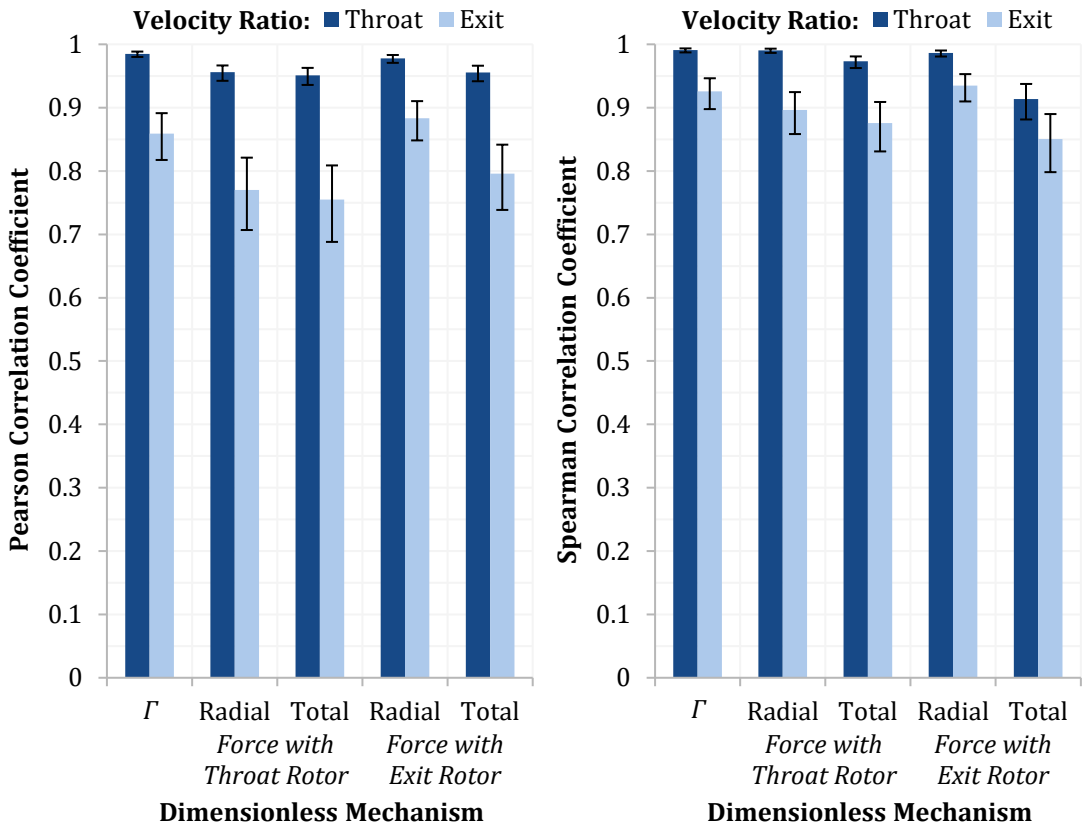

Figure 7.11: Pearson (left) and Spearman (right) correlation coefficients between axial velocity ratios u/u_∞ in the duct and proposed mechanisms of augmentation, with 95% confidence intervals shown. Calculated at C_T = 0.75 for 200 random duct shapes.

None of the force options examined provided a perfect relationship with axial velocity, a finding that also held for fixed C_T values of 0 and 0.75 in Figure 7.10 and Figure 7.11 respectively. As the force relationship was no less inexact than the circulation relationship, the hypothesis that a force-based mechanism of augmentation would resolve the inconsistency in the aerofoil conceptual model must therefore be dismissed. While either could potentially be used to explain augmentation, circulation was chosen due to the seemingly closer to linear relationship.

7.2.2 The Missing Factor: Circulation Dispersion or Effectiveness

While circulation may be the best parameter for explaining the mechanism of augmentation, the results of the previous section suggest that it is not able to characterise duct performance alone. A simple example verifies this conclusion. Consider the case of a duct represented by a single vortex ring, where the axial velocity passing through the duct has been computed and is shown in the 'one ring' column of Table 7.4. With the same total circulation, a second ring can be added to the representation and modified with consequent changes in the velocity induced. Both the vortex strength and the distance between the vorticity and a point of interest affect the velocity.

Table 7.4: Axial velocity u passing through a vortex ring alone, and with a second ring added and modified. Input parameters changed from the previous column are underlined. D is the diameter of the first ring.

	One Ring	Two Rings	C_Γ Weighting Changed	Ring 2 Location Changed
x_1/D	0	0	0	0
r_1/D	0.5	0.5	0.5	0.5
$C_{\Gamma,1}$	0.4	**0.2**	**0.1**	0.1
x_2/D	-	**0.2**	0.2	**0.3**
r_2/D	-	**0.9**	0.9	**1.2**
$C_{\Gamma,2}$	-	**0.2**	**0.3**	0.3
u/u_∞	1.93	1.58	1.40	1.35
η_Γ	1.00	0.82	0.73	0.70
Λ_Γ	1.00	1.22	1.38	1.43

A crucial difference therefore exists between ducted turbines and the aerofoil analogy: only the total circulation must be known to calculate lift, but the distribution of circulation along a duct's surface is also required to calculate velocity. One way of quantifying this distribution is by comparing the axial velocity actually induced at the rotor to the axial velocity induced when the duct is replaced with a single vortex ring of the same total strength that is positioned around the rotor. The resulting circulation effectiveness ratio η_Γ is calculated by Equation 7.1.

$$\eta_\Gamma = \frac{u_d + u_{wake} + u_\infty}{u_{dsr} + u_{wake} + u_\infty} \qquad \textbf{Equation 7.1}$$

Contributions to the velocity at the rotor from the duct, duct as a single ring, wake, and free stream are represented by u_d, u_{dsr}, u_{wake}, and u_∞ respectively. These velocities are defined as averages over the rotor plane, with $u_d + u_{wake} + u_\infty$ being the actual velocity u_r. This parameter is conceptually straightforward, but it has a significant drawback: the denominator can pass through 0 when u_{dsr} becomes negative, which can occur even for sensible duct shapes at high C_T. Plots of η_Γ can therefore reach extremely large values, making them almost impossible to interpret.

A more practically useful parameter can be defined by taking the reciprocal of η_Γ, giving the circulation dispersion ratio Λ_Γ in Equation 7.2.

$$\Lambda_\Gamma = \frac{u_{dsr} + u_{wake} + u_\infty}{u_d + u_{wake} + u_\infty} \qquad \textbf{Equation 7.2}$$

This parameter is a measure of how dispersed the positive contributions to the overall circulation are from the rotor. When Λ_Γ is large, the positive contribtions are far from the rotor and their influence on u_r is reduced. The velocity at the rotor is therefore less than if Λ_Γ were small.

Although u_d alone may still become negative, $u_d + u_{wake} + u_\infty$ will always remain above 0 for a ducted wind turbine. Λ_Γ can therefore be plotted without the problematic values seen for η_Γ, although either parameter may be useful on a conceptual level. Whichever one is used, it must be remembered that the parameters are not intended to represent efficiency or inefficiency values to be optimised. They are intended only as aids to understanding the mechanism of augmentation.

These definitions are not the only possibilities for effectiveness and dispersion parameters. An alternative that is initially attractive would be u_d/u_{dsr} for effectiveness and u_{dsr}/u_d for dispersion, since these directly compare the velocities induced by the vorticity in question. Both, however, suffer from the denominator passing through zero, leading to plots that are impossible to interpret and ruling out their use. There is also merit to using the physically meaningful value of $u_d + u_{wake} + u_\infty$ in the definitions selected above, rather than the somewhat theoretical value of u_d alone.

Figure 7.12 to Figure 7.14 illustrate the behaviour of the circulation dispersion ratio with the NACA 4-digit aerofoil shapes used in Section 4.2.4. Use of the circulation effectiveness ratio in these plots would have led to extreme values. Discretisation convergence tests at C_{Topt} found changes of less than 0.30% with halved panel lengths forΛ_Γ, and less than 0.31% with doubled expanding wake length. Each value of Λ_Γ must fall into one of seven categories, all of which are seen in the plots below:

- $\Lambda_\Gamma > 1$ indicates that positive circulation is dispersed away from the rotor. Concentrating the duct circulation into a single vortex ring at the rotor would give a velocity greater than the actual velocity at the rotor.
- $\Lambda_\Gamma = 1$ signifies that the actual distribution of circulation is equivalent to the single ring case, with $u_d + u_{wake} + u_\infty = u_{dsr} + u_{wake} + u_\infty$ and $u_d = u_{dsr}$.
- $0 < \Lambda_\Gamma < 1$ implies a circulation distribution that is effectively more concentrated than a lumped single ring. Although this may appear to be an illogical statement at first, two explanations do exist. Both were found in the results:
    - A negative contribution to velocity from the duct that is magnified when the circulation is lumped into a single ring.
    - A single ring representing positive circulation contributions near the rotor and negative contributions further from it, leading to a reduced rotor velocity in the single ring case by effectively moving the negative contributions closer to the rotor.
- $\Lambda_\Gamma = 0$ also denotes a greater concentration than in the single ring case, but some care needs to be taken. Any value of $u_d + u_{wake} + u_\infty$ will lead to $\Lambda_\Gamma = 0$ when $u_{dsr} + u_{wake} + u_\infty = 0$, even infinitesimal ones.

- -1 < Λ_Γ < 0 shows that the actual velocity magnitude is greater than the single ring value, but where the sum $u_{dsr} + u_{wake} + u_\infty$ has become negative due to the strength of the single ring duct. Negative values of Λ_Γ could also theoretically stem from the actual rotor velocity becoming negative, but such a device would hardly qualify as a ducted turbine.
- Λ_Γ = -1 can be interpreted as the cut off between concentrated and dispersed for negative $u_{dsr} + u_{wake} + u_\infty$, similar to Λ_Γ = 1, in that $u_d + u_{wake} + u_\infty = -(u_{dsr} + u_{wake} + u_\infty)$. However, note that $-u_{dsr} = u_d + 2u_{wake} + 2u_\infty$.
- $\Lambda_\Gamma \leq$ -1 occurs if the velocity magnitude in the rotor plane would be increased by concentrating the duct circulation into a single vortex ring when $u_{dsr} + u_{wake} + u_\infty$ is negative.

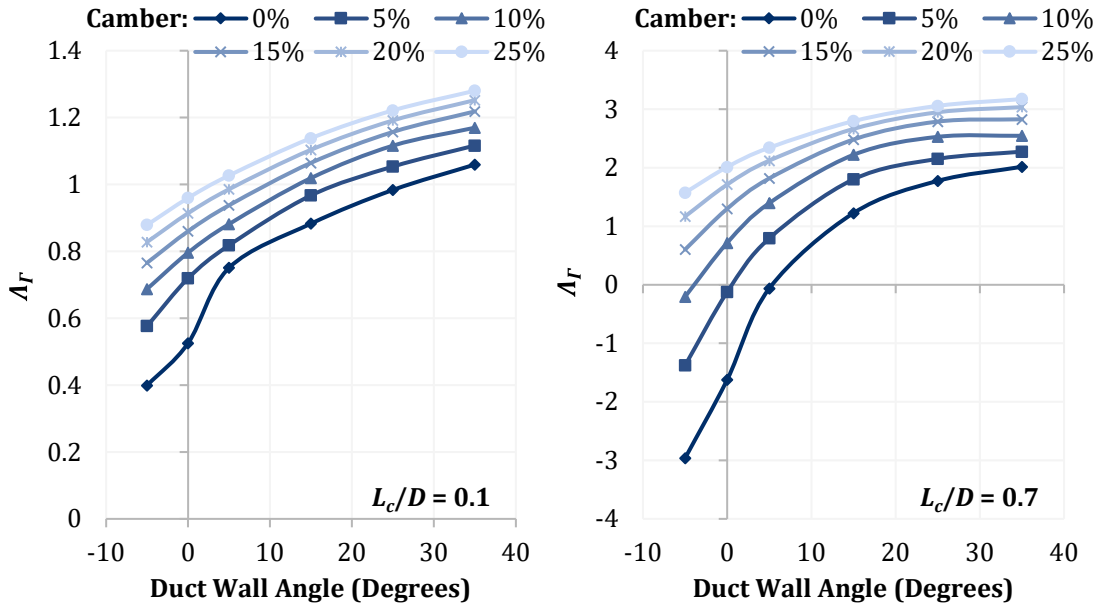

Figure 7.12: Variation of the circulation dispersion ratio Λ_Γ with duct wall angle α, at selected cambers L_{cam}/L_c and chord length ratios L_c/D. Calculated at C_{Topt}.

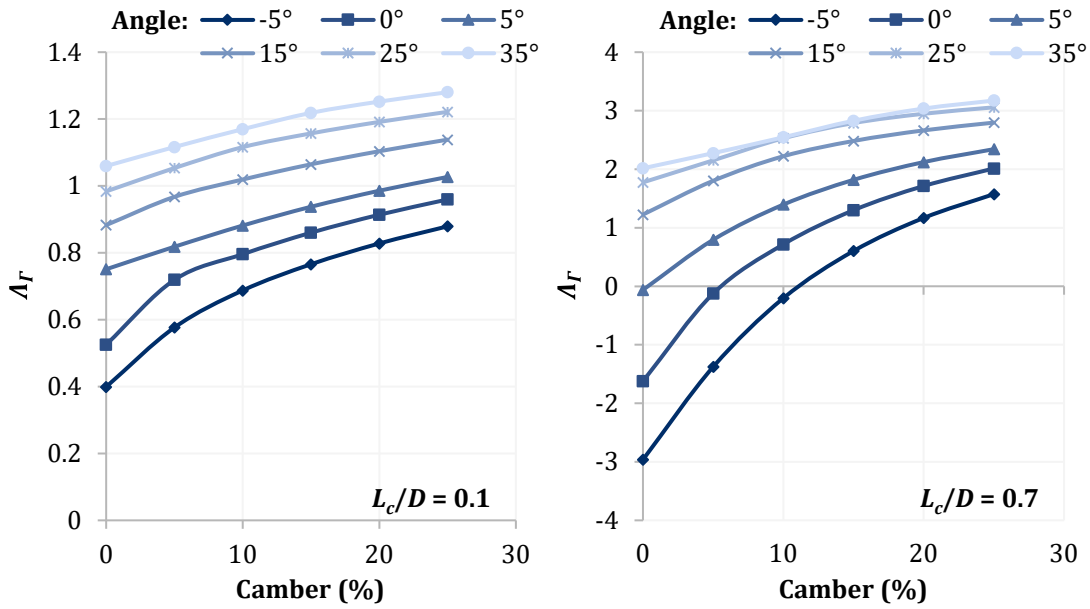

Figure 7.13: Variation of the circulation dispersion ratio Λ_Γ with camber L_{cam}/L_c, at selected duct wall angles α and chord length ratios L_c/D. Calculated at C_{Topt}.

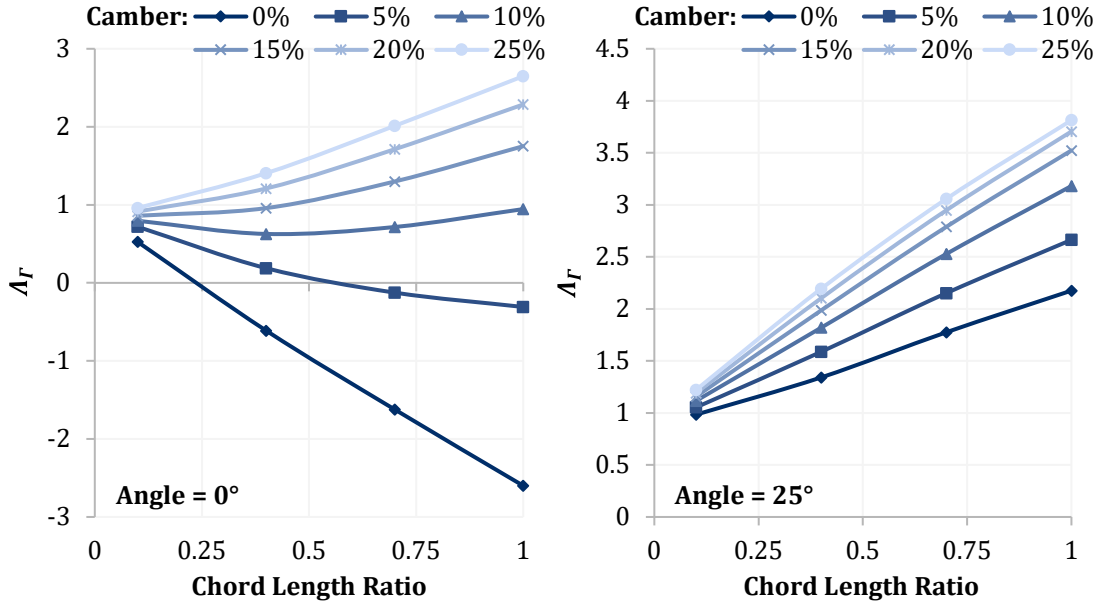

Figure 7.14: Variation of the circulation dispersion ratio Λ_Γ with chord length ratio L_c/D, at selected cambers L_{cam}/L_c and duct wall angles α. Calculated at C_{Topt}.

An explanation has now been found for the imperfect relationship between circulation and velocity at the rotor, the inconsistency in the aerofoil conceptual model that this section aimed to address. It is now clear that the expectation of a perfect relationship was based on a faulty assumption, and that both the total circulation and the distribution of it along a duct's surface are needed for a complete characterisation. By establishing the importance of the circulation dispersion ratio, circulation can now be trusted as an explanation of ducted turbine augmentation.

7.2.3 Suitability of the Aerofoil Conceptual Model

Accurate qualitative predictions from the aerofoil conceptual model have been demonstrated throughout this work, and an important discrepancy has now been resolved by introducing the circulation dispersion ratio. The axisymmetry of a ducted turbine remains an important difference from the aerofoil model, however, necessitating the length to diameter ratio in Section 4.2 and illustrated by the disparity in the velocity induced by a straight vortex segment in Equation 2.12 and a ring vortex in Equation 2.13 and Equation 2.14.

Further confidence in the applicability of the model is given here by testing quantitative predictions. As will be discussed, these predictions cannot reduce the effort needed to characterise a ducted turbine's performance; they are intended only to test the aerofoil conceptual model and to improve understanding of ducted turbine behaviour. In particular, understanding the change in duct performance with rotor loading is desirable before returning to the optimum rotor loading investigation.

It was therefore hypothesised that the aerofoil model could be used to predict duct performance by representing the influence of the rotor's wake on the duct as a change in the free stream velocity. This effective free stream velocity $\boldsymbol{U}_{\infty,\boldsymbol{eff}}$ would differ from the actual value through a change in magnitude and the addition of a radial component, and was calculated using Equation 7.3.

$$\boldsymbol{U}_{\infty,\boldsymbol{eff}} = u_{\infty} + \boldsymbol{U}_{\boldsymbol{wake}} \qquad \textbf{Equation 7.3}$$

$\boldsymbol{U}_{\boldsymbol{wake}}$ is defined here as the velocity induced by the wake vorticity at a point on the duct surface. The selection of that point is discussed later in this section. u_{∞} is used rather than the vector valued $\boldsymbol{U}_{\infty}$ because an axial free stream velocity is assumed throughout this work.

A consequence of the radial component to $\boldsymbol{U}_{\infty,\boldsymbol{eff}}$ is a change in the effective wall angle of the duct α_{eff}, defined as the difference between the wall angle and the angle of the effective free stream velocity in Equation 7.4.

$$\alpha_{eff} = \alpha - \tan^{-1}\left(\frac{v_{\infty,eff}}{u_{\infty,eff}}\right) \qquad \textbf{Equation 7.4}$$

The hypothesis, then, was that these two parameters could be used with results at C_T = 0 to calculate the performance of a ducted turbine at a rotor loading of interest. Since the effective parameters were found using simulation results, the method here cannot be used to reduce the number of simulations needed to characterise duct performance. This study serves only as a test of the aerofoil conceptual model.

Approach

There were two phases in predicting the velocity at a rotor, as part of testing the hypothesis. First, the influence of duct wall chord angle at C_T = 0 was found from the set of NACA 4-digit duct shapes in Section 4.2.4, where wall angle was varied in isolation from the other geometrical parameters. For simplicity, this study used only the ducts with a chord length ratio of 0.1 due to the almost linear variation of velocity with angle seen when angles less than 0 were excluded. One such example can be seen in Figure 7.15, with the parameters of each least squares linear fit shown in Table 7.5.

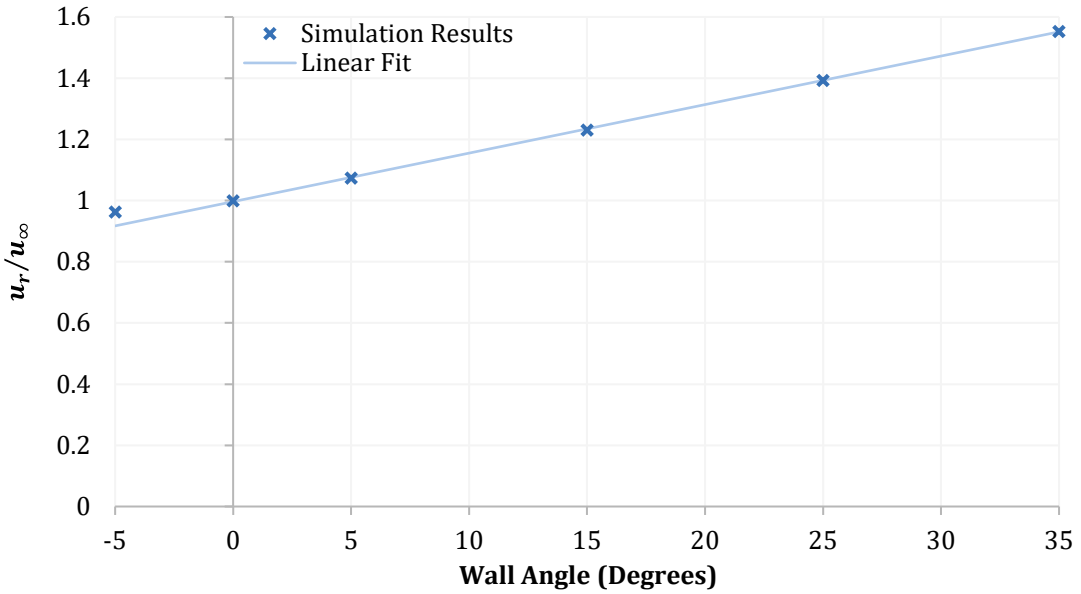

Figure 7.15: Variation of axial velocity at the rotor u_r with wall angle α, for a NACA 4-digit duct shape without camber and with a chord length ratio of 0.1. A linear fit for wall angles from 0° to 35° is also shown.

Table 7.5: Gradient, y-axis intercept, and coefficient of determination R^2 for linear fits of velocity at the rotor u_r to the duct wall chord angle α, for each value of duct camber.

Camber	Gradient	Intercept	R^2
0%	0.1586	0.997	0.9998
5%	0.1548	1.060	0.9991
10%	0.1488	1.131	0.9991
15%	0.1429	1.204	0.9999
20%	0.1389	1.277	0.9999
25%	0.1363	1.347	0.9993

The second phase in predicting the velocity at the rotor was to calculate the effective parameters at the desired rotor loading. These stem from the velocity induced by the combination of wake and free stream, a velocity that is not constant over the duct surface. To calculate which of these velocities was $\boldsymbol{U}_{\infty,eff}$, it was assumed that the tilt of the effective free steam velocity from axial would match the tilt of the duct force from

the radial direction. The effective free stream velocity was therefore found by an optimisation algorithm [161] that varied the location until the difference in tilt angles was at a minimum.

Sufficient information then existed to predict the velocity at the rotor for the chosen C_T. The duct wall angle was added to the free stream velocity tilt angle to give the effective wall angle, from which an initial velocity value could be calculated using the data from wall angles at $C_T = 0$. This velocity was then scaled by the ratio of $\left|\boldsymbol{U}_{\infty,\boldsymbol{eff}}\right|$ to u_∞: as the throat velocity ratio is unaffected by changes in u_∞, a change in the free stream velocity seen by the duct has a linear effect on u_r. This process is shown in Equation 7.5, where for this equation only m is the gradient of the linear fit and c the y-axis intercept.

$$\frac{u_r}{u_\infty} = \left(m\alpha_{eff} + c\right)\frac{\left|\boldsymbol{U}_{\infty,\boldsymbol{eff}}\right|}{u_\infty} \qquad \textbf{Equation 7.5}$$

To test the accuracy of this approach, results were taken from the NACA 4-digit duct shapes at $C_T > 0$. Discretisation convergence was checked using four duct shapes at the limits of the geometrical parameters described in Section 4.2 with the chord length ratio fixed at 0.1. Simulations with a low value for the coefficient of total duct force per radian C_F suffered from low accuracy, so results with $C_F \leq 0.05$ were excluded. Discretisation convergence was otherwise good at $C_T \leq 8/9$, as shown in Table 7.6, with changes rising above 1% only at $C_T = 0.95$.

Table 7.6: Worst and median magnitude change in result when discretisation was changed for the discretisation checking duct shapes. Last duct panel length began at $0.00125\boldsymbol{D}$ and expanding wake length at $8\boldsymbol{D}$.

		% Difference with			
		Halved Panel Length		Doubled Wake Length	
Loading	**Result**	**Worst**	**Median**	**Worst**	**Median**
$C_T = 0.15$	α_{eff}	0.07	0.01	0.00	0.00
	$\left\|U_{\infty,eff}\right\|$	0.00	0.00	0.00	0.00
	u_r/u_∞	0.37	0.13	0.00	0.00
$C_T = 8/9$	α_{eff}	0.84	0.73	0.04	0.04
	$\left\|U_{\infty,eff}\right\|$	0.06	0.06	0.01	0.01
	u_r/u_∞	0.42	0.33	0.02	0.01
$C_T = 0.95$	α_{eff}	2.33	2.18	0.34	0.29
	$\left\|U_{\infty,eff}\right\|$	0.16	0.13	0.05	0.02
	u_r/u_∞	0.83	0.63	0.09	0.07

Results

The combination of 36 duct shapes with simulations at a range of rotor loading values above zero gave a set of 496 results. After excluding those with $C_F \leq 0.05$ and those where α_{eff} fell below the wall angle fit limit of 0°, a validation set of 191 results remained. These are compared to predictions from the effective parameters in Figure 7.16. Visually good agreement can be seen for the majority of the results, although there is a noticeable divergence as the velocity ratio falls below 1.

At worst, the error magnitude reached 16.4%. As can be seen in Figure 7.17, however, large errors were associated with high C_T and low C_F, suggesting that they may simply be a consequence of reduced simulation accuracy. The majority of predictions were reasonably accurate in any case, with only 6 results reaching error magnitudes over 7%. Even in the less accurate region below u_r/u_∞ = 1 the median error magnitude was 3.9%, and the overall median was just 1.49%.

The overall high accuracy of the predictions made using $\left|\boldsymbol{U}_{\infty,\boldsymbol{eff}}\right|$ and α_{eff} supports the hypothesis that they can be used to represent the influence of the wake on the duct. It also supports the assumption made in equating the tilt angles of $\boldsymbol{U}_{\infty,\boldsymbol{eff}}$ and C_F, which could perhaps lead to a satisfying circulation based explanation for the perfect relationship between duct drag and augmentation seen in Sections 3.1.6 and 6.2.1. Although the circulation dispersion ratio is important for understanding the circulation explanation of augmentation, these results also show that it need not always be directly considered.

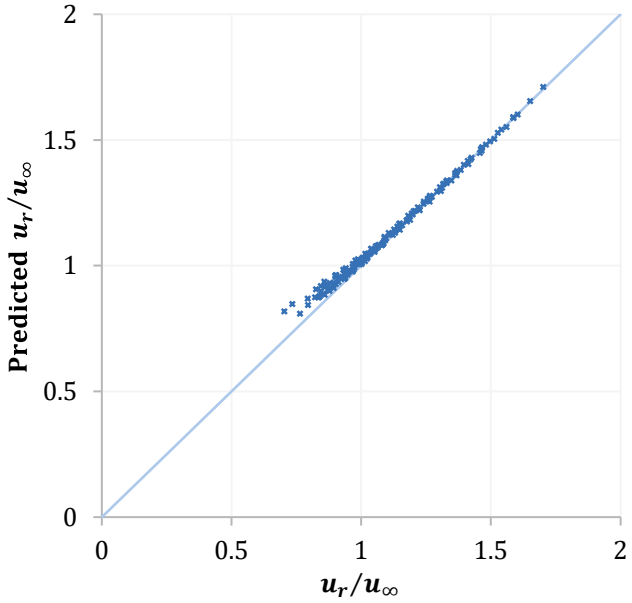

Figure 7.16: Comparison of predicted and actual axial velocity at the rotor u_r, with the line of perfect agreement shown, where predictions were made using effective free stream velocity $U_{\infty,eff}$ and wall angle α_{eff}.

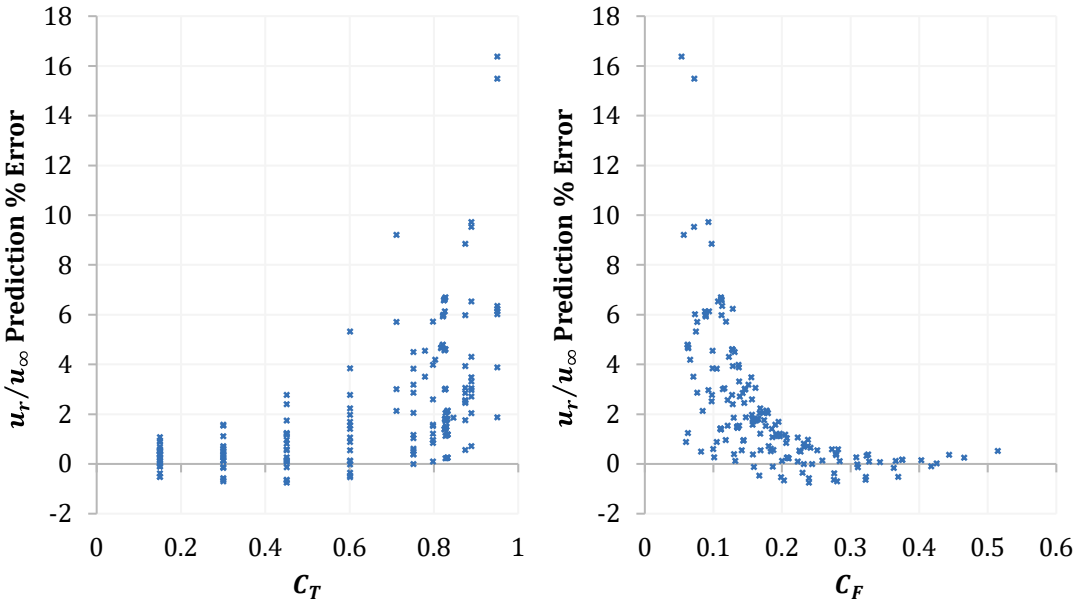

Figure 7.17: Variation of axial velocity u_r prediction error with rotor loading coefficient C_T (left) and the coefficient of total duct force per radian C_F (right).

7.2.4 Circulation: A Validated Theory

An explanation for the augmentation provided by ducted turbines in inviscid flow has now been provided by the combination of circulation and circulation dispersion, resolving an earlier inconsistency in the aerofoil conceptual model. Despite the underlying difference between a planar aerofoil and an axisymmetric duct, accurate quantitative predictions can still be made from effective free stream parameters. While the prediction approach requires simulation results to already exist at the desired C_T, limiting the practical usefulness, it lends credence to the conceptual model in a general sense and provides a tool for the analysis of optimum rotor loading.

7.3 Optimum Rotor Loading: Applying the Theory

Every numerical investigation in this work found optimum rotor loading coefficients less than 8/9, including the large scale searches in Section 7.1. Being numerical investigations, however, they cannot show that C_{Topt} must always be reduced. Another type of evidence will be added here: an explanation for reduced C_{Topt} due to an increasingly negative influence on duct performance from the wake as C_T increases.

7.3.1 Analytical Approach

An analytical solution for the strength of a wake vortex ring could not be found in Section 2.2.2 for the general case. Simplifying by attributing the velocity at a wake panel only to the free stream velocity, however, led to Equation 2.31 for a cylindrical wake. This relationship is repeated here as Equation 7.6.

$$\Gamma = -\frac{\Delta p \Delta s}{\rho u_\infty} \qquad \textbf{Equation 7.6}$$

For any positive free stream velocity, wake panel length Δs, and rotor pressure drop Δp, the simplified wake panel strength is negative. Combining the velocity induced by such a panel with a free stream velocity leads to the velocity field in Figure 7.18 upstream of the vortex ring. A velocity component in the outward radial direction is induced, along with a reduction in the velocity magnitude for radial positions less than the ring radius. One small exception exists for the latter point: close to the axial position of the ring, and where the radial velocity approaches its largest value, the velocity magnitude is increased.

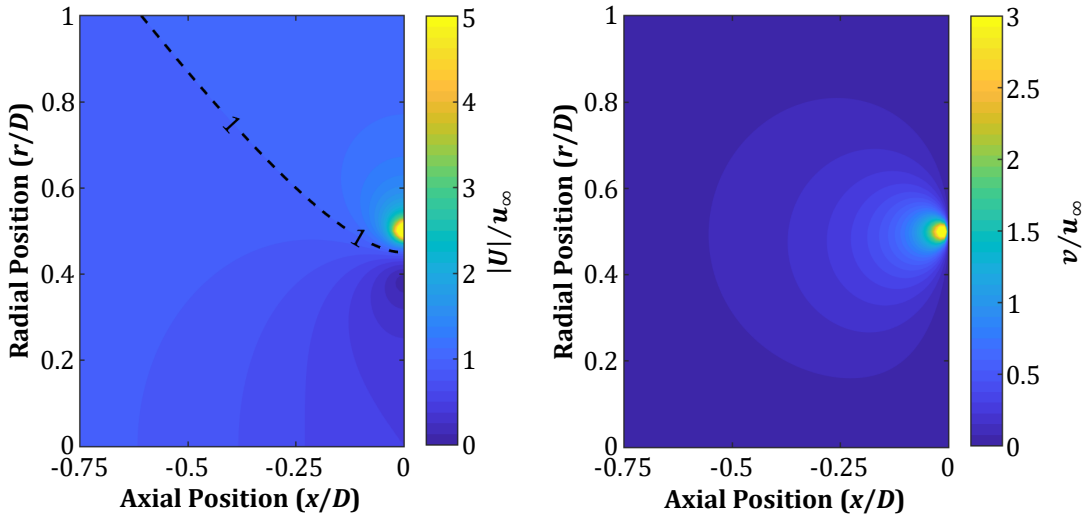

Figure 7.18: Velocity magnitude (left) and radial velocity (right) upstream of a single vortex ring of negative strength. Position is given in terms of the ring diameter D, with velocity magnitude $|U|$ and radial velocity v given as a proportion of the free stream velocity. Velocity values are capped approaching the vortex ring's singularity.

Extrapolating to an entire wake by summing individual contributions, radial velocities upstream of the wake will increase compared to the single ring, and velocity magnitudes will decrease at radii less than the wake upstream end. For a duct of smaller radius than the wake, as would be expected for an expanding duct, the effective free stream velocity and wall angle will both therefore be reduced as rotor loading increases. If the exception of increased velocity magnitude near the ring still exists, it will coincide with a significantly reduced effective wall angle.

7.3.2 Numerical Approach

Moving beyond the simplified analytical approach required a set of numerical results. Effective free stream velocities and wall angles were therefore found for the set of 200 NACA 4-digit duct shapes randomly generated in Section 4.2.3. As discussed in Section 7.2.3, results with a low total duct force suffered from accuracy problems and so

simulations with $C_F \leq 0.05$ were again excluded. An additional problem was found with the wider range of shapes used here, as the optimisation algorithm could not always match the velocity and force angles in the search for the effective free stream velocity. These cases are visible with a large α_{eff} error in Figure 7.19.

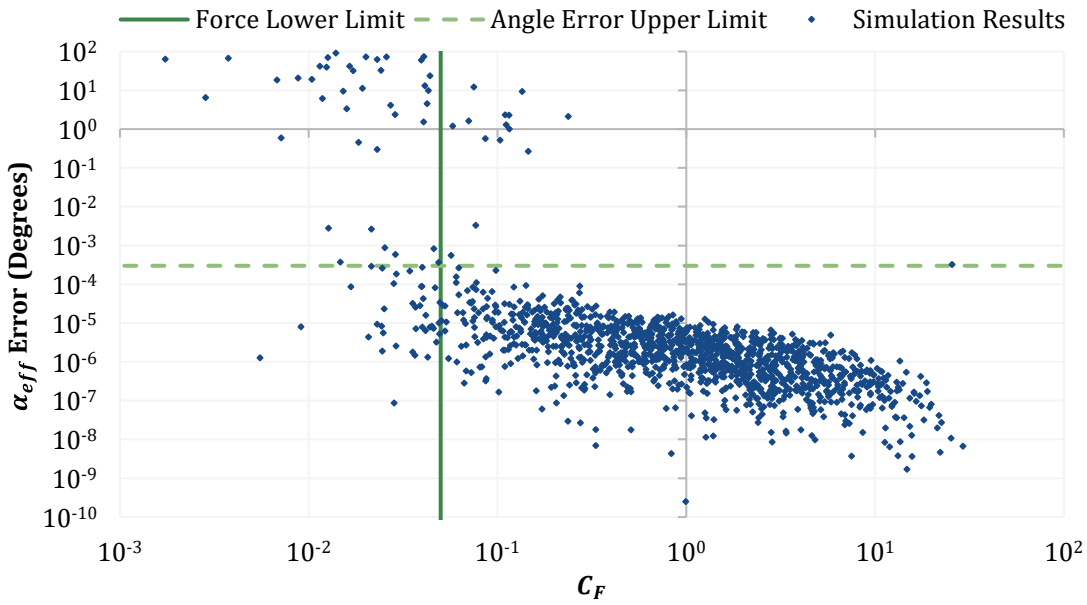

Figure 7.19: Variation of effective wall angle α_{eff} error, as calculated from velocity, with the coefficient of total duct force per radian C_F. Force and angle error exclusion criteria are also marked.

The majority of the problematic simulations fell below $C_F = 0.05$ and were excluded anyway, but a number did not. Large α_{eff} errors were associated with lower total force and were more common at higher rotor loadings, suggesting numerical error as a likely cause. A second exclusion criterion was therefore set to remove the suspect simulations with an α_{eff} error greater than 0.0003°. The particularly tight threshold was chosen to exclude the result away from the main group at $C_F \approx 25$.

Discretisation convergence was acceptable at $C_T \leq 8/9$ with the exclusions applied, as shown in Table 7.7, although the worst difference was elevated for the circulation dispersion ratio at $C_T = 8/9$. Excluding a small value of Λ_Γ reduced the worst difference to 1.48%. $C_T = 0.95$ also saw a small value of Λ_Γ, but even excluding that the worst difference was 4.28%. Other changes reached 3.4%, so some caution is warranted at the highest rotor loading.

Table 7.7: Worst and median magnitude change in result when discretisation was changed for the discretisation checking duct shapes. Last duct panel length began at $0.00125D$ and expanding wake length at $8D$.

		% Difference with			
		Halved Panel Length		Doubled Wake Length	
Loading	**Result**	**Worst**	**Median**	**Worst**	**Median**
C_T = 0.15	α_{eff}	0.07	0.01	0.00	0.00
	$\lvert U_{\infty,eff} \rvert$	0.00	0.00	0.00	0.00
	u_r	0.37	0.10	0.00	0.00
	Λ_Γ	0.21	0.08	0.00	0.00
C_T = 8/9	α_{eff}	0.84	0.43	0.09	0.04
	$\lvert U_{\infty,eff} \rvert$	0.09	0.05	0.21	0.01
	u_r	1.08	0.33	0.39	0.02
	Λ_Γ	2.80	0.14	0.07	0.02
C_T = 0.95	α_{eff}	2.33	0.78	0.47	0.31
	$\lvert U_{\infty,eff} \rvert$	0.18	0.11	0.64	0.05
	u_r	3.41	0.54	1.20	0.09
	Λ_Γ	7.95	0.20	0.56	0.14

Gradients were calculated to assess the changes of α_{eff} and $\lvert \boldsymbol{U}_{\infty,\boldsymbol{eff}} \rvert$ with C_T. Accuracy was only required insofar as testing if the gradients were above or below zero, therefore they were calculated using a backwards difference between somewhat widely spaced C_T values. Where n indicates results for the nth C_T value in an increasing sequence and φ the result of interest, the gradient was therefore calculated using Equation 7.7.

$$\left(\frac{\Delta\varphi}{\Delta C_T}\right)_n = \frac{\varphi_n - \varphi_{n-1}}{C_{T,n} - C_{T,n-1}} \qquad \textbf{Equation 7.7}$$

Increasingly strong wake vorticity was found to reduce α_{eff} in all but 6 out of 1292 cases and $\lvert \boldsymbol{U}_{\infty,\boldsymbol{eff}} \rvert$ in all cases, as shown in Figure 7.20. The 6 positive α_{eff} gradients can likely be dismissed on the basis that they were associated with both high rotor loading and low total duct force, conditions that have previously led to reduced accuracy. Extending the analysis to include Λ_Γ and u_r in Figure 7.21 found that increasing C_T led to less dispersed circulation and decreased velocity, even though more concentrated circulation implies greater u_r at a given value of circulation.

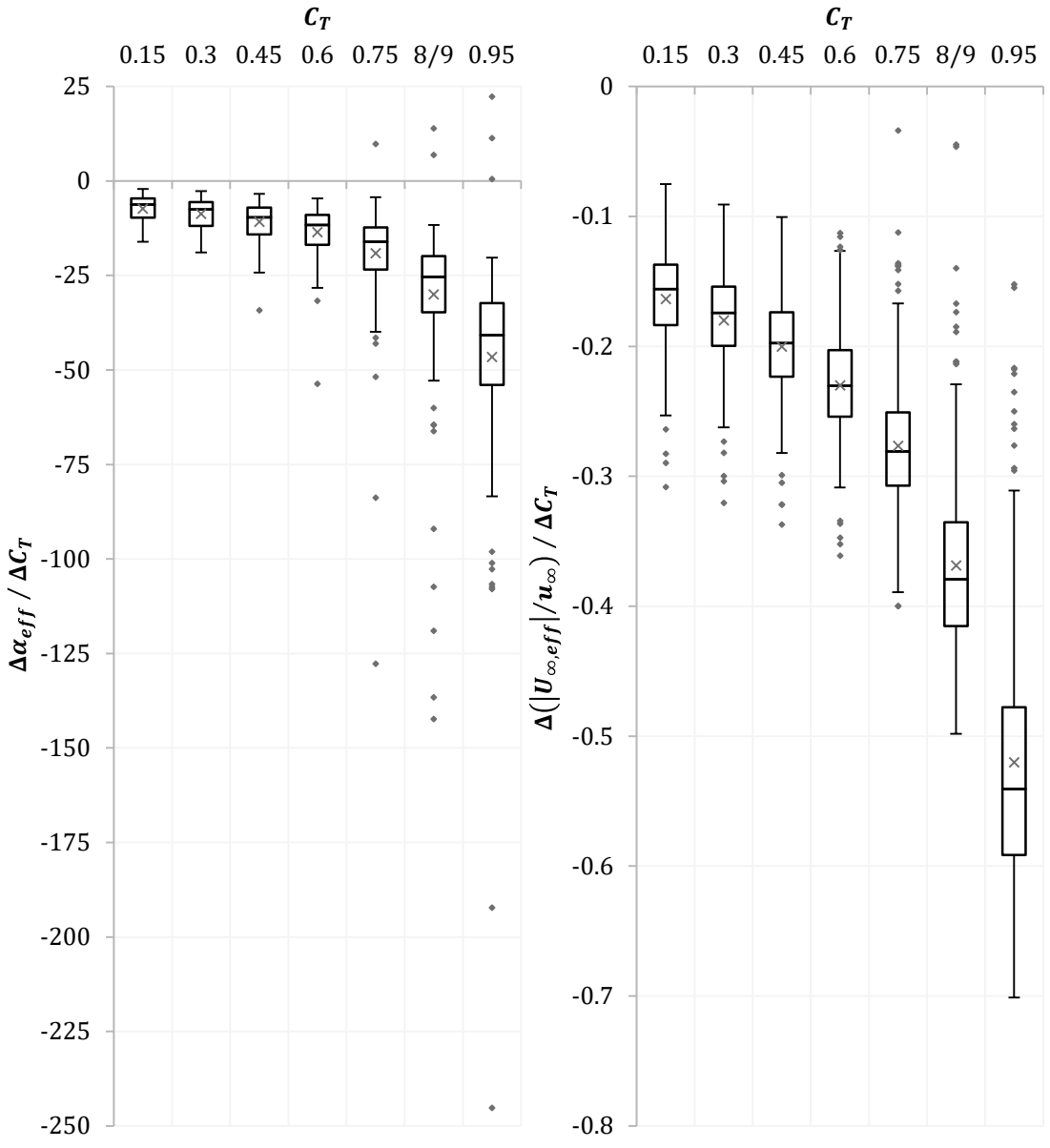

Figure 7.20: Tukey box and whisker plots showing the gradient of effective wall angle α_{eff} (left) and effective free stream velocity magnitude ratio $U_{\infty,eff}/u_\infty$ (right) with rotor loading. Gradients calculated using a backwards difference between the rotor loadings shown.

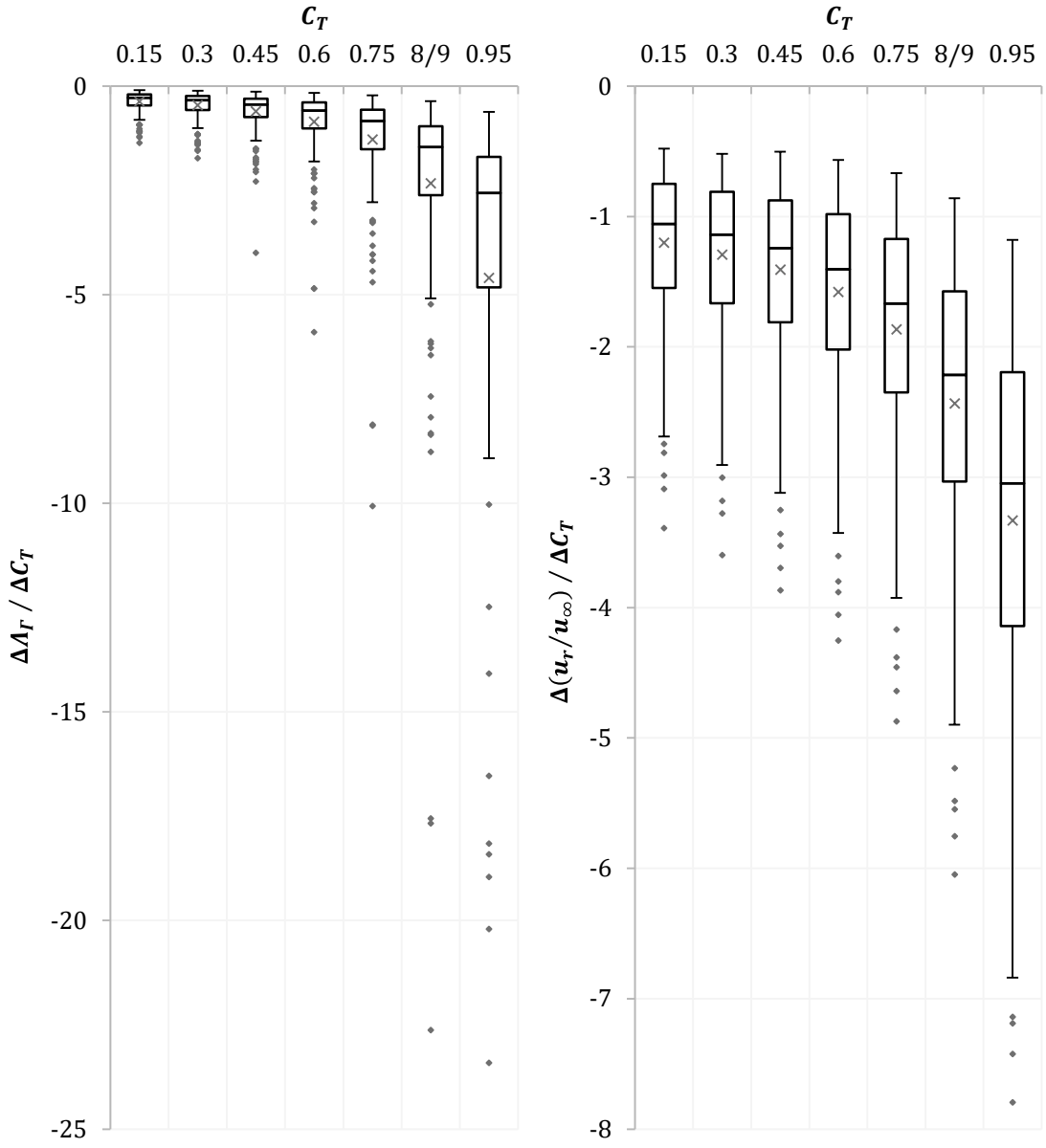

Figure 7.21: Tukey box and whisker plots showing the gradient of the circulation dispersion ratio Λ_r (left) and velocity ratio at the rotor u_r/u_∞ (right) with rotor loading. Gradients calculated using a backwards difference between the rotor loadings shown. The left plot excludes three outliers at -42.4, -42.9, and -57.5 for C_T = 0.95.

7.3.3 The Negative Influence on Optimum Rotor Loading

Both the simplified analytical approach and the numerical results suggest that the influence of the wake increasingly reduces $|\boldsymbol{U}_{\infty,\boldsymbol{eff}}|$ and α_{eff} as C_T increases. Reductions in the effective free stream velocity can be expected to always reduce the axial velocity at the rotor: a velocity ratio u/u_∞ is not affected by changes in u_∞ for incompressible inviscid flow, demonstrating the linear relationship between u and u_∞. Numerical tests illustrated this point with a perfect linear relationship between u_∞ and duct circulation, consistent with thin aerofoil theory [69], and no change in the circulation dispersion ratio with u_∞.

Changing α_{eff} has a less certain influence on performance. Reduced effective wall angle would always lead to reduced performance in the aerofoil model, but that model is imperfect due to the influence of circulation dispersion. Indeed, Figure 7.21 shows a decrease in Λ_Γ with rotor loading and therefore a greater u_r at a given C_Γ for the duct shapes examined here. The velocity at the rotor nevertheless always decreased with rotor loading, as seen on the right of Figure 7.21, but it is not certain from this evidence that decreases in circulation would always outweigh decreases in the dispersion ratio.

These results nevertheless provide an explanation for reduced C_{Topt}: the combined changes in α_{eff} and $|\boldsymbol{U}_{\infty,\boldsymbol{eff}}|$ lead to reduced duct performance as rotor loading increases. Decreased mass flow then outweighs the increased fraction of energy extracted at higher rotor loadings, favouring a lower value of C_{Topt}. The optimum rotor loading for a particular turbine therefore depends on the rate at which duct performance reduces with C_T.

Alone, the numerical results in Section 7.1 could not prove that C_{Topt} must always be reduced. Together with the reasoning here, however, there is a credible argument: every duct shape examined numerically had $C_{Topt} < 8/9$, and there is an explanation that could plausibly apply to all duct shapes generally. Absent any counterexamples, there is strong support for the conclusion that the optimum rotor loading is reduced for ducted turbines in inviscid flow.

7.4 The Aerofoil Explanation for Ducted Turbine Performance

A number of conclusions can be drawn concerning the behaviour of ducted turbines from the investigations in this chapter, going beyond the main conclusion that the optimum rotor loading is reduced in inviscid flow. In combination with results from earlier chapters, it is now possible to explore the duct circulation, force, and augmentation relationships. The variation in these parameters with rotor loading is examined in this section from an aerofoil point of view to give a more complete picture of the inviscid component of ducted turbine performance.

At Zero Rotor Loading

Beginning at C_T = 0, a ducted turbine will induce a circulation around the duct wall that acts to increase the axial velocity at the rotor position u_r. Associated with this augmentation is a radially inwards force on the duct, with zero drag in inviscid flow at this rotor loading. Despite both being considered by other authors as causes of the increased velocity, neither circulation nor radial force were found to be perfectly correlated with velocity in Section 7.2.1.

The imperfection for circulation is caused by the dependence of u_r on both the total value of circulation and how the contributions to that total are distributed along the duct's surface, as shown in Section 7.2.2. Where positive contributions are concentrated near the rotor, the axial velocity is higher than when the positive contributions are dispersed away from the rotor. This effect can be quantified by the circulation dispersion ratio Λ_Γ, which is large for dispersed contributions, or the circulation effectiveness ratio η_Γ, which is small for dispersed contributions.

Above Zero Rotor Loading

When the rotor begins operating, and C_T increases to some moderate value, there are consequent changes in duct performance. Section 7.2.3 demonstrates that this influence can be thought of as a change in the effective free stream velocity seen by the duct; the rotor reduces this velocity and tilts the velocity vector so that the effective wall angle of the duct is reduced. A decrease in augmentation therefore follows, which can be explained using the aerofoil conceptual model through a decrease in duct circulation.

Examining the changes directly, Section 7.3.2 confirms a decrease in circulation with rotor loading. It also shows a decrease in the circulation dispersion ratio, although the positive effect on u_r is never sufficient to overcome the reduction caused by the drop in circulation. To explain the reduction in Λ_Γ, it is necessary to consider the vorticity that is shed by the rotor and forms the wake surface: a radially outward velocity is induced on the duct surface by this vorticity, and this velocity contribution increases in magnitude towards the duct trailing edge.

To balance the outward velocity induced by the wake vorticity, and maintain zero flow through the duct wall, the duct's vorticity must induce an inward velocity of equal magnitude at each point on the duct surface. The strength of the duct's vorticity therefore decreases near the trailing edge, where the largest velocity magnitude is required. By reducing the positive contributions to the overall circulation away from the rotor, the contributions that remain are concentrated closer to the rotor and Λ_Γ decreases.

Changes in the effective free stream velocity do not only affect augmentation, with Section 7.2.3 demonstrating an impact on the duct force: as the velocity vector tilts away from the axial direction, there is an equal tilt in the total inviscid force vector away from the radial direction. This connection is important, firstly, because the influence of the rotor on velocity varies over the surface of the duct. Finding the location where the velocity tilt angle matches the force tilt angle allows the correct effective free stream velocity to be selected.

The tilt angle connection also explains the existence of a drag force in inviscid flow. Since the total force vector remains perpendicular to the effective free stream velocity vector, an axial force component must be introduced as the velocity vector tilts away from the axial direction. This force is conceptually similar to the induced drag on a finite wing, which is caused by a change in the effective free stream velocity due to the vorticity shed by the wing itself [69].

At High Rotor Loadings

As the rotor loading increases further, the effective free stream velocity continues to tilt and reduce in magnitude, the duct circulation and circulation dispersion ratio continue to decrease, and the augmentation of the flow through the rotor drops further. The duct may eventually begin to curtail the flow rather than augment it, depending on the duct design, reducing power extraction below that from a bare rotor at the same rotor loading.

If the duct does begin to curtail the flow, the inviscid drag becomes negative and there is an upstream force on the duct. This change is discussed in terms of the momentum drop caused by the rotor in Section 6.2.1, but it can also be thought of in terms of the aerofoil conceptual model and the effective free stream velocity. Although there is not a perfect correlation between force and augmentation, Section 6.2.1 suggests that the radial component is inwards for augmentation and outwards for curtailment. For the force vector to remain perpendicular to the effective free stream velocity, the axial component must therefore be downstream for augmentation and upstream for curtailment.

The Optimum Rotor Loading

In addition to the direct influence of the duct on power extraction at each value of C_T, there is an indirect influence through a reduction in the rotor loading for maximum power. Section 7.3.3 explains the change in C_{Topt} through the change in the effective free stream velocity: as the rotor loading increases, the velocity tilts and decreases in magnitude, reducing the duct circulation and augmentation. The mass flow is therefore decreasing at a faster rate than for a bare rotor, outweighing the increased fraction of energy extraction at higher rotor loadings, and leading to a lower value of C_{Topt}.

An explanation can also be provided in somewhat different terms by considering the combination of rotor and duct as a net resistance to the flow. This net resistance is negative for a ducted turbine, at least at lower rotor loadings, since the influence of the duct overcomes the resistance of the rotor to accelerate the flow. As C_T increases, the increased resistance from the rotor causes an expansion of the flow, a change in the velocity local to the duct, and a consequent decrease in the duct's augmentation.

Decreased augmentation is equivalent to increased resistance, so the net resistance to the flow is therefore increasing at a faster rate with C_T than for a bare rotor alone. There must then be a more rapid drop in mass flow through the rotor, which is equivalent to a more rapid drop in the energy available for the rotor to extract. Since ducted turbines do not affect the fraction of energy extracted from the flow at a given rotor loading, lower C_T values become advantageous and C_{Topt} is reduced.

Underlying these explanations are the investigations of the effective free stream velocity in Sections 7.3.1 and 7.3.2. These investigations took simplified analytical and numerical approaches respectively, so there cannot be the certainty that exact analytical expressions would bring. A numerical optimisation seeking to maximise C_{Topt} in Section 7.1.1 and an examination of 1776 duct shapes in Section 7.1.2, however, found a maximum C_{Topt} of 0.84. Combining a plausible explanation with the absence of a single duct reaching $C_{Topt} = 8/9$ strongly supports the conclusion that the optimum rotor loading is always reduced for ducted turbines in inviscid flow.

7.5 Summary

Earlier chapters have confirmed that the optimum rotor loading for ducted turbines can be less than 8/9, both through numerical results and an analysis of the theory. Here, the aim was to discover if C_{Topt} must always be less than 8/9 in inviscid flow. Numerical results support this hypothesis: an optimisation seeking maximum C_{Topt} with 30 starting duct shapes found no more than C_{Topt} = 0.81, while an examination of 1776 other duct shapes reached 0.84 by allowing shorter ducts. Direct searches of this type, however, leave open the possibility that duct shapes with larger optimum rotor loadings exist but were simply not found.

An accurate understanding of why ducts augment the flow through a rotor could make the C_{Topt} conclusion more general, but even the most promising lead of circulation and the aerofoil model has not been perfect. Tests using the radial or total force on the duct similarly suffered from an imperfect association with augmentation. This problem was solved by using circulation in conjunction with a circulation dispersion parameter that measures the distribution of circulation along a duct's surface.

The circulation dispersion ratio introduces a significant difference between ducted turbines and an aerofoil-based model of their performance. Nevertheless, that model can still be the basis of accurate predictions using the effective free stream velocity and duct wall angle caused by the combination of u_∞ and the velocity induced by the wake. Calculating the mass flow through the duct with changes in C_T using that approach gave a median magnitude error of just 1.49% in 191 test cases, although note that the method is useful only for improving understanding and not for real world predictions.

Both a simplified analytical approach and a numerical approach with 200 duct shapes found a reduction in these effective parameters with increasing rotor loading. This result adds a plausible explanation to the search for C_{Topt} = 8/9: the performance of the duct reduces with rotor loading, shifting the balance between mass flow and the fraction of energy extracted, and reducing the optimum rotor loading.

8 Chapter

Conclusions

A wide range of investigations were carried out for this work, all working towards the overall aim of building a better understanding of fundamental aspects of ducted turbine performance. These investigations are split here into the four objectives chosen in Section 1.6: exploring the inviscid behaviour of ducted turbines, evaluating the competing conceptual models, examining the validity of theory, and deepening understanding of the influences on optimum rotor loading. This chapter describes the main conclusions, limitations, and future work for each of the objectives.

8.1 The Inviscid Behaviour of Ducted Turbines

8.1.1 The Influence of Duct Geometry on Performance

Influence of Diffuser Parameters

An assessment of how duct shape affects power extraction formed part of the inviscid exploration objective, for geometrical parameters based on diffuser and aerofoil points of view separately. The full set of diffuser parameters was used in Section 4.1, showing increased C_{Pmax} with increased exit area ratio and exit angle, and both positive and negative changes with increased length. Substantial uncertainty was introduced by the need to use a regression analysis to isolate the interrelated parameters, however, so it is unclear how far the results can be trusted. Future work could quantify how changes in the shape generation approach affect the results, and repeat the process if a way to isolate the parameters without regression is found.

Certain specific questions raised relating to diffuser parameters could be answered, however, without needing to rely on a regression analysis. Inlet design and duct length were expected to be immaterial in inviscid flow from a review of the literature, but Sections 3.3.3 and 3.2.2 found otherwise. Although a change in C_{Pmax} of up to 4% when adding inlet sections up to 0.2 rotor diameters long may still be minor, a 30% increase when lengthening a duct by 0.5 rotor diameters is not. Another important question was whether area ratio has significantly more impact than other aspects of duct shape. It can be concluded that the answer is no, from results in Section 3.1.2 showing C_{Pmax} more than doubling with changes in shape at a fixed area ratio.

Influence of Aerofoil Parameters

No regression was necessary for the aerofoil parameters, and increases in C_{Pmax} were found with wall angle and camber in Section 4.2. A larger chord length ratio generally

acted to magnify the existing augmentation or diminution of C_{Pmax}, but not in every case. Although only a single aerofoil family was examined at fixed thickness and point of maximum camber, these results constitute an investigation that is significantly wider ranging and more systematic than any known to have been conducted previously.

A more limited investigation was conducted into duct wall thickness in Sections 3.3.1 and 3.3.2. While the variation in rotor area with thickness complicates matters, changes in mass flow of less than 6% going from a 0% to 6% thick duct suggest that a zero thickness duct wall can reasonably approximate a moderately thick one. It appears that the zero thickness representation should be the camber line, rather than the inside or outside surface, although agreement may sometimes be improved by translating it radially to match the rotor area. Confirmation with additional duct shapes is required, ideally using the same simulation code for the thick and thin ducts.

8.1.2 Applicability to Viscous Flows

Care must be taken when applying the simulation results in this work to real flows, as they lack any contribution from viscous mechanisms of augmentation and the limiting effect of flow separation on performance. The large values of power coefficient sometimes seen cannot be expected of a real turbine, and the optimised duct shapes are not design recommendations. Rotor induced rotation of the flow, however, may suppress separation [79, 88] and allow performance closer to the inviscid case than expected.

The inviscid results may even be directly applicable to real flows where separation is avoided: Section 3.3.4 found agreement within 10% for viscous and inviscid power coefficients with attached flow, for a single duct shape at four wall angles. Either way, the results can be combined with an intuitive understanding of viscous effects to consider how geometry affects the performance in a real flow, and they allow future studies to quantify the influence of geometry on the viscous component of performance.

8.1.3 Power Extraction, Flow Rate, and Rotor Loading

Two important power relationships were investigated. Further confirmation was found of a linear relationship between power extraction and flow velocity, from numerical results in Section 3.1.3 and theoretical derivations in Section 6.2.2, hopefully helping to dispel the velocity cubed misconception. Numerical results also showed that augmentation decreases with rotor loading in Section 3.1.5, rather than staying constant, with the error in assuming otherwise reaching above 30% at maximum power. Further studies discussed later in Section 8.4.2 suggest that the presence of a rotor must always decrease augmentation in inviscid flow.

8.1.4 Inapplicability of the Betz Limit

An assessment of the Betz limit in Section 3.1.8 provides what is perhaps the first irrefutable evidence that it does not apply at all to ducted turbines, whether on the basis of rotor or exit area. Results even exceeded C_{Pmax} = 1 with exit area, far above the Betz limit of 0.593. With an analysis showing that the power coefficient loses its expected physical meaning when applied to a ducted turbine, however, the absence of a theoretical limit is not concerning and large values of C_{Pmax} simply reflect an abundance of available power.

With a power coefficient that is no longer a measure of actual to available power, debate over whether it is more correct to use the rotor or duct exit area in the definition of C_P is rendered somewhat redundant. The decision need not be arbitrary, however, as the more convenient option can be chosen. Overall, it appears that rotor area gives more linear changes in C_P with changes in the aerofoil parameters for duct shape, as discussed in Section 4.2.1, although only a single aerofoil family was tested. As it is also consistent with the bare rotor definition, rotor area appears to be the better choice.

In place of a theoretical limit, Section 3.2.2 uses right angled shapes to suggest upper limits for a given size of duct. Although the result of an inviscid shape optimisation process, this approach provides only an estimate. More extreme shapes that may increase performance were prevented by the optimisation bounds, and it was assumed that viscous mechanisms of augmentation cannot overcome viscous limitations to exceed inviscid performance. Nevertheless, it would be interesting to carry out an economic analysis with these results: if ducted turbines are not viable in this idealised case, what future can they have?

8.2 A Comparison of Conceptual Models

Ducted turbines are customarily thought of as diffusers reducing pressure to draw more flow through the rotor. Augmentation has alternatively been explained through an aerofoil mechanism, but practical applications of this approach have been rare. Both of these conceptual models were evaluated for their usefulness in this work's second objective, in terms of the ability to explain augmentation and to provide the better set of parameters for duct geometry.

8.2.1 Explanations for Augmentation

Diffuser Explanation

A reduction in exit pressure was the viewpoint selected to represent the diffuser conceptual model in Section 1.2.2, but Section 3.1.6 shows the association with augmentation to be an imperfect one. Support for the diffuser explanation was found,

however, in an equation derived from a momentum balance in Section 6.3.2: inequalities of less than 0.2% when tested with simulation results suggest an exact relationship. The introduction of a correction factor for radial variations in the exit plane explains the improvement, with Section 3.1.7 showing that the variations change with rotor loading and duct shape, but a method of predicting the radial variation from the diffuser model was not apparent.

Aerofoil Explanation

Radial force and circulation are alternative viewpoints for the aerofoil explanation, but neither showed a perfect relationship with augmentation in Sections 7.2.1 and 3.1.6. A reason for the radial force imperfections has been put forward in the form of changes in leading edge stagnation point location [74], although it could perhaps be argued that the location changes as a result of the changes in augmentation rather than vice versa. That reason was not tested here, but results in Section 6.2.1 are consistent with an inwards radial force for augmentation and an outwards radial force for curtailment; further work may show scatter in the results near zero augmentation to be numerical error.

To achieve a perfect relationship with circulation, Section 7.2.2 shows that the distribution of circulation along the duct's surface must be considered. A circulation dispersion ratio was defined to represent this distribution, resolving discrepancies in the circulation explanation. This parameter increased at C_{Topt} with wall angle and camber, and also with chord length ratio for the better performing ducts. Logical next steps would be to examine the influence of thickness and point of maximum camber, and test with different aerofoil shape families and rotor loadings.

The aerofoil model can be extended to view the influence of the rotor as a change in the flow seen by the duct. Accurate predictions for flow velocity at a chosen rotor loading were made on this basis in Section 7.2.3, using results at C_T = 0 and the effective free stream velocity and wall angle, with a median error across 496 results of just 1.49%. While the approach required simulation results at the desired C_T and therefore has no practical use, it provides further support for the circulation explanation and suggests an intuitive way of thinking about the influence of the rotor.

Although the circulation dispersion changes with wall angle, and so would be expected to change with the effective wall angle, it was not necessary to directly consider it when making predictions. This apparent exclusion is surprising given the link it provides between circulation and augmentation, and would make an interesting topic in future investigations. It would also be useful to test the accuracy of predictions with additional duct shapes, particularly longer ones without a linear relationship between velocity and wall angle, while a method to determine the effective free stream flow without simulations would be invaluable.

Explanations Compared

Exact relationships between augmentation and both exit pressure and circulation were found, albeit both requiring the inclusion of a further parameter, supporting their use in explaining augmentation. An exact relationship in itself doesn't prove that they actually cause augmentation – no one would consider duct drag a cause of augmentation despite its exact relationship – but addressing this point is perhaps of philosophical rather than practical value. Of much more importance is whether the explanations are helpful for understanding how ducted turbines behave.

Expectations from an aerofoil inducing circulation better matched the simulation results in Sections 3.4 and 4.3, compared to a diffuser reducing pressure. A conceptual model that more often gives the correct intuition would certainly be more helpful in practice. An application of the aerofoil model may also help explain the rather counterintuitive increases in drag with augmentation discussed in Section 6.2.1: Phillips [4] speculated that some kind of relationship between the axial and radial duct forces may be the cause, a relationship found by equating the angles of effective velocity and total force in Section 7.2.3.

With the circulation explanation best for standard ducts, it is worth considering whether it can be applied to those with a flange. Inviscid power coefficients for right angled shapes in Section 3.2.2 were around 1/3rd greater than those for flanged ducts [44] of the same overall size in viscous flow, so separation on a flanged duct could well be a limitation on performance rather than a cause. One avenue to consider this possibility would be to check if an increase in the strength of the vortices caused by the flange is always associated with an increase in performance when compared to inviscid results.

8.2.2 Parameters for Duct Geometry

Aerofoil parameters were found to be significantly more useful than diffuser parameters in Chapter 4. Even choosing a duct shape was more difficult with the diffuser approach, as the parameters used to create the shape were not the set of diffuser parameters measuring it. A regression analysis was also needed to isolate the influence of each diffuser parameter, with prediction intervals up to 50% of the prediction values. A clearer link to performance therefore exists in the aerofoil case, as each parameter had an independent effect and there was no ambiguity introduced by the regression.

It is not certain whether the shortcomings found for the diffuser parameters here are inherent or simply a consequence of the methodology used. Only a single approach to shape generation was tested, and it is unclear whether a better approach using the

diffuser parameters themselves is possible. Some of the uncertainty introduced by the regression could have been caused by the use of an automated process without manual fine tuning, although validation of the fits was reasonable.

Further investigations could possibly lead to a method for directly generating duct shapes from the set of diffuser parameters, or if not then perhaps a way to vary the diffuser parameters in isolation. But why exert that effort rather than using the aerofoil parameters, which are now known to work well? Not only are they straightforward to use, but there already exists a vast array of aerofoil families that could be adapted to ducted turbines. It is worth considering, however, whether or not the aerofoil parameters should change to match the geometrical parameters of whichever aerofoil family is used in a study.

Future work to determine the applicability of existing aerofoil data to ducted turbines would be worthwhile, particularly if a way could be found to account for the influence of the rotor. It may be sensible to examine analytical solutions for particular aerofoil shapes to test the possibility of reformulation for ducted turbines. The analysis undertaken here could also be improved by comparing expectations from a ring wing formulation of thin aerofoil theory to the simulation results in Section 4.2.5 rather than the standard 2D theory that was used.

8.2.3 The Benefits of an Aerofoil Model

Both parts of this analysis led to the same conclusion: an aerofoil conceptual model outperforms a diffuser one. The former is easier to work with, leads to intuition that better matches how ducted turbines actually perform, and has a range of existing data that may be applicable to ducted turbines. It is recommended that the aerofoil model now be used as standard rather than the previously customary diffuser approach.

8.3 Tests and Extensions of Theory

8.3.1 The Validity of Existing Theories

Three existing theories were examined for their validity as part of the third objective in Chapter 5. While there was a base of valid equations on the level of actuator disc theory, errors of up to 94% after invalid simplifying assumptions leave the requirement of empirical testing in force. It is therefore recommended that these assumptions are avoided: that the duct axial force coefficient is constant with rotor loading, that C_{Topt} = 8/9, that the exit pressure coefficient does not vary with mass flow rate near C_{Topt}, and that the ratio of duct drag to rotor thrust does not vary with mass flow rate or far wake velocity near C_{Topt}.

Jamieson [137] introduced the ideal diffuser in another derivation, a theoretical concept designed to improve understanding by considering a duct of infinitely variable shape to account for the changing interaction between the duct and a variably loaded rotor. Tests in Section 5.7 showed that 7 of Jamieson's equations apply to real ducts, and clarified the definition of ideal diffuser. It appears that it is one without drag, or with a variation of shape that allows a fixed empirical parameter, or both.

Two limitations exist for the approach taken to validation. Simulation results, firstly, cannot be completely accurate, so disagreement could have been caused by errors in the simulations rather than in the theories. Secondly, assessing whether a particular theory was valid required subjective judgement. Generally, however, invalid equations had disagreements far larger than the expected simulation error and could not reasonably be argued as valid. The use of multiple simulation results minimised the chance of an invalid equation appearing valid by coincidence.

A logical extension of this work would be to increase the complexity of the simulations above axisymmetric inviscid flow, and determine the impact of factors such as viscosity and radially varying rotor loading on the validity of theory. While previous validation work has taken place on a viscous level, no investigation was encountered testing on an equation by equation basis. Further theories could also be examined. Bontempo and Manna's [193] is attractive as it uses a semi-analytical approach, and ducted propeller theories could be surveyed for any useful differences to ducted turbine theories.

8.3.2 A Correction Factor for Radially Varying Flows

The quasi-one dimensional theories were found to apply to the radially varying flow of the simulation results when using an area weighted average value instead of a radially constant one. An exception exists for derivations from Bernoulli's equation, however, where a correction factor is required due to the velocity squared term. Neglecting this factor led to error increases of up to 950 percentage points in Phillips' theory, with a peak factor value of 2.

Accurate results could not be achieved with the factor typically specified in fluid dynamics textbooks, however, so the one derived in Section 5.3.1 must be used instead. Further tests of the influence of radial variations would be useful in viscous flow, particularly to examine diffuser efficiency. The definition of that parameter neglects radial variations, and it would be interesting to see if there is a stronger or weaker correlation with augmentation once corrected for.

8.3.3 The Missing Derivation for Inviscid Drag

A numerical examination in Section 6.1.3 found the missing link in the detailed derivation of a power equation involving duct drag: the forces acting on the streamtube

control volume are equal and opposite to the total inviscid duct drag. Confidence in the accuracy and generality of this conclusion would be improved with an analytical proof, but the numerical approach did use a number of simulations and found errors of 1.2% or less. It would also be interesting to carry out a detailed derivation similar to that performed here, but with the aim of reaching a set of validated equations for viscous flow.

8.3.4 Suitability of Empirical Parameters

An equation for power coefficient formulated using velocity at the rotor and rotor loading is recommended in Section 6.4 over exit pressure and inviscid duct drag, with the former parameters viewed as the direct causes of augmentation and the latter as abstracted and potentially distracting. Further opinions on the selection of empirical parameters and formulation of equations would be valuable, as reaching a consensus approach would ease comparisons between theories, simulations, and experiments. It is also suggested that equations involving exit area ratio be avoided because of the undue emphasis over other geometrical parameters.

8.4 The Optimum Rotor Loading

8.4.1 Studies of Theory and Geometry

The final objective of this work was to improve understanding of the optimum rotor loading for ducted turbines. An investigation based on theory in Section 6.2.3 could not determine whether a duct must affect C_{Topt}, but did suggest that it is the form of the relationship between C_T and augmentation that governs any increase or decrease that does occur. Initial numerical results for a small number of duct shapes in Section 3.1.4 demonstrated a reduction in C_{Topt} to values as low as 0.71

The study in Section 4.2.4 found asymptotically increasing C_{Topt} with duct wall angle and camber, starting from a base of $C_{Topt} < 8/9$, and asymptotically decreasing C_{Topt} with chord length ratio. A variation in the underlying inviscid values with duct shape is likely part of the reason for the range of C_{Topt} values found in the literature. Improved understanding could be reached by extending this study to other aerofoil families, by examining the influence of thickness and point of maximum camber, and by repeating the analysis for viscous flow to determine the viscous contribution by comparison to these results.

8.4.2 An Inherent Reduction in Inviscid Flow

Further numerical studies suggest that a duct always acts to reduce C_{Topt} in inviscid flow. An optimisation of duct shape with two movable nodes and fixed end points

reached only C_{Topt} = 0.81 in Section 7.1.1, while an examination of 1776 duct shapes in Section 7.1.2 achieved the higher value of 0.84 as the ducts were allowed to be shorter. Although $C_{Topt} > 8/9$ was found in one previous study [46] for inviscid flow, the evidence here suggests that numerical error in the previous study, which caused impossible results of $C_T > 1$, led to the increased C_{Topt}.

A direct search cannot prove that C_{Topt} must be reduced, as there will always be other optimisation approaches to try or duct shapes left unexamined, but the reductions can be explained with the aerofoil conceptual model. An analytical approach with a simplified wake suggests in Section 7.3.1 that the presence of a rotor has a negative influence on the effective free stream flow in the vicinity of the duct, which would reduce the duct's circulation and performance. Given the connection between augmentation and C_{Topt} discussed above, a reduction in C_{Topt} would be expected.

A numerical approach without the simplifications of the analytical study in Section 7.3.2 also generally found a negative influence on the effective free stream flow. Six outliers out of 1292 cases were found which showed a positive influence, but these appear to be due to numerical error. More problematic were decreases in the circulation dispersion ratio, equivalent to increases in the circulation effectiveness ratio. Although these did not overcome the negative changes in the effective free stream to give an increased C_{Topt}, the evidence presented is not sufficient to show that they never could.

By investigating changes in the circulation dispersion ratio with duct shape, future work could assess whether changes in the effective free stream are ever likely to be overcome. Another potential direction would be to examine other aerofoil families in the numerical approach to increase the quantity of evidence. Higher resolution simulations could be used to determine if the small number of positive changes in the effective free stream were truly due to numerical error. Finally, an improved analytical approach would increase confidence in the conclusions.

Despite the imperfections of the analytical and numerical approaches, they introduce a plausible explanation for values of C_{Topt} less than 8/9. With increased rotor loading comes a reduction in the effective duct wall angle and velocity magnitude in the vicinity of the duct, reducing power extraction due to decreased circulation and thereby favouring a lower C_{Topt}. Together with the absence of a single reliable counterexample, this explanation is suggestive of an inherently reduced C_{Topt} in inviscid flow.

8.4.3 Increases in Viscous Flow

Combined with the evidence presented in this work, the best fitting explanation for the range of C_{Topt} values seen in the literature is a lowering of the inviscid base C_{Topt} that can then be brought back up above 8/9 when certain viscous effects are significant

enough. Wake mixing has been recognised as one possible mechanism of increased C_{Topt}, as discussed in Section 1.5.6, but a change in effective wall angle and rotor induced swirl may also contribute.

Section 7.3.2 demonstrated that the effective wall angle decreases with C_T, supporting those authors discussed in in Section 1.5.3 who have recognised that the presence of a rotor can change the effective duct wall angle and reduce separation. Any separation present without the rotor will therefore progressively decrease with C_T, potentially increasing C_{Topt} through increased augmentation at higher loadings.

Swirl in the flow induced by the spinning rotor increases with rotor loading at fixed tip speed ratio [175] and has been suggested to reduce separation [79, 88]. C_{Topt} could therefore be increased where separation is reduced at higher rotor loadings. Phillips [4] argued that turbulence induced by the rotor explained reduced separation instead of swirl, and it would be interesting to test that belief and whether it could also increase C_{Topt}. Investigations into the suggestion that the flow experiences less expansion per unit duct length due to its tangential velocity may also be fruitful.

Viscous effects appear able to increase C_{Topt} compared to bare rotors, whatever the exact cause, with Phillips [4] suggesting that a 5% increase is possible. The inviscid conclusion here casts those findings in a new light, changing a 5% increase above C_{Topt} = 8/9 into a larger increase from a lower inviscid base. For example, the increase would be 11% above the maximum C_{Topt} found in Section 7.1.2 or 17% above the median. With viscous effects playing a greater role in determining C_{Topt} than would otherwise appear, there is a greater impetus to determine their relative impact and to maximise the potential benefit.

8.5 A Better Understanding of the Fundamentals

Much is left to be done to achieve an economically viable ducted turbine, but the studies here help solidify the base of knowledge needed to efficiently reach that goal. The intuition of future researchers will be improved by an awareness of the inviscid behaviour and a change to the aerofoil conceptual model, and ambition need not be constrained by the Betz limit any longer. Effort can be based on equations known to be trustworthy and clear, and augmentation could be increased by exploiting the influences on optimum rotor loading. A better understanding of fundamental aspects of ducted turbine performance will now hopefully lead to improved aerodynamic and economic performance.

8.6 Summary of Conclusions

An exploration of the inviscid behaviour of ducted turbines has led to useful insights, not least concerning the influence of duct shape on the flow. It is now clear that area ratio cannot be considered the primary geometrical factor, and that duct length and inlet design are relevant to more than just viscous effects. A systematic examination of geometrical parameters was performed, and may even directly apply to viscous flows when separation is avoided.

Highly accurate simulations led to strong evidence that the Betz limit does not apply at all to ducted turbines, whether on the basis of rotor or exit area, as augmentation deprives the power coefficient of its expected physical meaning. Neither the rotor or exit area is any more correct in the definition of C_P, therefore, but the former is more practically useful. Other studies gave further confirmation of a linear relationship between power and flow velocity, and demonstrated a decrease in augmentation with rotor loading.

An aerofoil conceptual model for a ducted turbine outperformed a diffuser one in tests of their augmentation explanations and a comparison of their parameters for duct geometry. The former leads to intuition that better matches how ducted turbines actually perform and parameters that are easier to work with. It is recommended that the aerofoil model now be used as standard rather than the previously customary diffuser approach.

Attractive simplifications in ducted turbine theories were unfortunately found to be invalid, leaving the requirement for empirical parameters intact. Velocity at the rotor may be more suited to that role than exit pressure or inviscid duct drag, as the latter are abstracted and potentially distracting. Other investigations of theory led to a previously missing detailed derivation for the relationship between inviscid drag and augmentation, and demonstrated the applicability of quasi-one dimensional theories to radially varying flows once a correction factor was derived and introduced where appropriate.

Theoretical considerations show that it is the form of the relationship between rotor loading and augmentation that governs any increase or decrease in the optimum rotor loading. It appears, however, that the presence of a duct inherently reduces the optimum in inviscid flow: with increased rotor loading comes a reduction in the effective duct wall angle and velocity magnitude in the vicinity of the duct, reducing power extraction due to decreased circulation. Certain viscous effects may then increase the optimum, and play a larger role than otherwise appears due to the reduced inviscid base.

Applying inviscid results to real flows requires caution, but studies throughout this work show that it is possible to reach practically useful conclusions. As ducted turbines are a difficult problem, leading to uncertainty and disagreement in the literature, the inviscid approach has a real advantage in reducing the complexity. With a consequentially better understanding of the fundamentals, future investigations are now hopefully able to improve the aerodynamic and economic performance of ducted turbines.

8.7 Summary of Future Work

Further exploration of the inviscid behaviour of ducted turbines could confirm the influence of duct thickness with additional duct shapes, ideally using the same simulation code for the thick and thin ducts. It would also be interesting to carry out a best case economic analysis with the inviscid right angle duct results. If diffuser parameters are ever used to specify duct shape, the impact of the shape generation approach on the relationships between geometrical parameters and performance could be quantified. The ability to isolate the diffuser parameters from each other without regression would also be useful.

Logical next steps for the aerofoil conceptual model would include further examinations of the circulation dispersion ratio with additional geometrical parameters and rotor loadings. Increased trust in the model would be provided by understanding why it was unnecessary to account for circulation dispersion when making predictions from effective free stream conditions, as well as further predictions with additional duct shapes. A method of calculating the effective conditions without simulations would give practical value to the predictive approach.

The investigation of aerofoil parameters could be extended by considering whether or not the parameters should change to match those used for the aerofoil family defining the duct shape, and the analysis improved by utilising a ring wing formulation of thin aerofoil theory to assess performance expectations. Testing the applicability of existing aerofoil data, adapting analytical solutions for particular aerofoil shapes, and considering whether the circulation explanation applies to flanged ducts would all aid in application of the aerofoil model to design problems.

Existing theories could be further tested by increasing the complexity of simulations above axisymmetric inviscid flow, while the investigation could be widened to include other theories and a survey of ducted propeller theories for any useful differences. Quantifying the influence of radial variations in viscous flow would also be useful. Confidence in the theory derived here would be improved with a completely analytical proof, and it would be interesting to carry out a similar derivation for viscous flow.

Further opinions on the selection of empirical parameters for theoretical descriptions would be helpful in reaching a consensus approach.

Additional evidence for assessing the inherent reduction of optimum rotor loading in inviscid flow could be found in a number of ways. Examining the influence of duct geometry with other aerofoil families would increase the quantity of data, while higher resolution simulations could exclude numerical error as a factor. Assessing whether decreases in circulation dispersion are ever likely to overcome negative changes in the effective free stream conditions would be valuable, as would an analytical approach that makes less simplifications.

Further examining the relationship between duct geometry and optimum rotor loading with more geometrical parameters and other aerofoil families would provide a useful base of knowledge for design work. There is also a strong incentive to investigate any beneficial viscous effects: with a reduced inviscid base for the optimum rotor loading, any viscous increases play a larger role than otherwise appears, have greater scope for maximising the potential benefit, and could potentially lead to a reduced cost of energy for ducted turbines.

References

[1] Y. Ohya, T. Karasudani, T. Nagai, and K. Watanabe, "Wind lens technology and its application to wind and water turbine and beyond," *Renew. Energy Environ. Sustain.*, vol. 2, p. 2, Jan. 2017.

[2] S. Hjort and H. Larsen, "A Multi-Element Diffuser Augmented Wind Turbine," *Energies*, vol. 7, no. 5, pp. 3256–3281, May 2014.

[3] R. A. Oman and K. M. Foreman, "Advantages of the Diffuser-Augmented Wind Turbine," in *Wind Energy Convers. Syst. Work. Proc.*, 1973, pp. 103–106.

[4] D. G. Phillips, "An Investigation on Diffuser Augmented Wind Turbine Design," The University of Auckland, 2003.

[5] T. Burton, D. Sharpe, N. Jenkins, and E. Bossanyi, *Wind Energy Handbook*. Chichester: John Wiley & Sons, 2001.

[6] V. L. Okulov and G. A. M. van Kuik, "The Betz-Joukowsky limit: on the contribution to rotor aerodynamics by the British, German and Russian scientific schools," *Wind Energy*, vol. 15, no. 2, pp. 335–344, Mar. 2012.

[7] "Vortec Energy collapses -- economics questionable," *Wind Power Monthly*, Aug-2001.

[8] CITA Wind, "Archive Version of CITA Wind Website from 13/10/2002," 2002. [Online]. Available: https://web.archive.org/web/20021013144820/http://cita-wind.com/English/FR/faqJDC.htm. [Accessed: 31-Jan-2019].

[9] Ever Kinetiq, "Archive Version of Ever Kinetiq Website from 17/5/2011," 2011. [Online]. Available: https://web.archive.org/web/20110517065237/http://www.everkinetiq.nl/. [Accessed: 31-Jan-2019].

[10] Y. Schilp, H. Terlouw, and J. Cace, "Urban wind turbines in The Netherlands," in *Comm. Forum Urban Wind Turbines*, 2010.

[11] M. J. Blanch, "Wind Energy Technologies for use in the Built Environment," *Wind Eng.*, vol. 26, no. 3, pp. 125–143, 2002.

[12] Marquiss Wind Power, "Archive Version of Marquiss Wind Power Website from 19/1/2009," 2009. [Online]. Available: https://web.archive.org/web/20090119141039/http://www.marquisswindpower.com/. [Accessed: 31-Jan-2019].

[13] S. Marquiss, "Variable Aperture Velocity Augmented Ducted Fan Wind Turbine," US 7,256,512 B1, 2007.

[14] S. Kirsner, "What went wrong with that weird wind turbine on Deer Island?," *The Boston Globe*, Boston, 05-May-2017.

[15] Ogin, "Archive Version of Ogin Website from 14/8/2017," 2017. [Online]. Available: https://web.archive.org/web/20170814074043/http://www.oginenergy.com/. [Accessed: 31-Jan-2019].

[16] Lunar Energy, "Archive Version of Lunar Energy Website from 24/12/2017," 2017. [Online]. Available: https://web.archive.org/web/20171224170425/http://www.lunarenergy.co.uk/index.htm. [Accessed: 31-Jan-2019].

[17] Z. Zhou, F. Scuiller, J. F. Charpentier, M. Benbouzid, and T. Tang, "An up-to-date review of large marine tidal current turbine technologies," in *Proc. 2014 IEEE PEAC*, 2014, pp. 448–484.

[18] SIMEC Atlantis Energy, "Archive Version of Technology History." [Online]. Available: https://web.archive.org/web/20191118125314/https://simecatlantis.com/services/turbines/history/. [Accessed: 31-Jan-2019].

[19] SIMEC Atlantis Energy, “Archive Version of Ocean Trials Prove Solon™ the Most Efficient Tidal Current Turbine Ever Tested,” 2008. [Online]. Available: https://web.archive.org/web/20191118125434/https://simecatlantis.com/2008/09/29/press-1/. [Accessed: 31-Jan-2019].

[20] Y. Ohya, “Multi-Rotor Systems Using Five Ducted Wind Turbines for Power Output Increase (Multi Lens Turbine),” in *AIAA Scitech 2019 Forum*, American Institute of Aeronautics and Astronautics, 2019.

[21] Halo Energy, “Archive Version of Halo Energy Acquires Shrouded Wind-Turbine Technology From Ogin Inc.,” *Cision PR Newswire*, 2017. [Online]. Available: https://web.archive.org/web/20180104200833/https://www.prnewswire.com/news-releases/halo-energy-acquires-shrouded-wind-turbine-technology-from-ogin-inc-300572813.html. [Accessed: 31-Jan-2019].

[22] B. Kirke, “Developments in ducted water current turbines,” 2005.

[23] A. A. Jadallah, S. R. Farag, and J. D. Hamdi, “Performance enhancement of a darrius 3-bladed wind turbine using convergent-divergent ducting system,” *J. Eng. Sci. Technol.*, vol. 13, no. 7, pp. 1891–1904, 2018.

[24] C. Vermillion and L. Fagiano, “Electricity in the Air: Tethered Wind Energy Systems,” *Mech. Eng.*, vol. 135, no. 09, pp. S13–S21, Sep. 2013.

[25] A. Saleem and M.-H. Kim, “Aerodynamic analysis of an airborne wind turbine with three different aerofoil-based buoyant shells using steady RANS simulations,” *Energy Convers. Manag.*, vol. 177, pp. 233–248, Dec. 2018.

[26] A. Grant and N. Kelly, “The Development of a Ducted Wind Turbine Simulation Model,” in *Eighth Int. IBPSA Conferece*, 2003, pp. 407–414.

[27] A. Grant, C. Johnstone, and N. Kelly, “Urban wind energy conversion: The potential of ducted turbines,” *Renew. Energy*, vol. 33, no. 6, pp. 1157–1163, Jun. 2008.

[28] A. Dilimulati, T. Stathopoulos, and M. Paraschivoiu, “Wind turbine designs for urban applications: A case study of shrouded diffuser casing for turbines,” *J. Wind Eng. Ind. Aerodyn.*, vol. 175, pp. 179–192, Apr. 2018.

[29] S. J. Watson, D. G. Infield, J. P. Barton, and S. J. Wylie, “Modelling of the performance of a building-mounted ducted wind turbine,” *J. Phys. Conf. Ser.*, vol. 75, no. 1, 2007.

[30] S.-Y. Hu and J.-H. Cheng, “Innovatory designs for ducted wind turbines,” *Renew. Energy*, vol. 33, no. 7, pp. 1491–1498, Jul. 2008.

[31] D. Petković, S. Shamshirband, Ž. Ćojbašić, V. Nikolić, N. B. Anuar, A. Q. M. Sabri, and S. Akib, “Adaptive neuro-fuzzy estimation of building augmentation of wind turbine power,” *Comput. Fluids*, vol. 97, pp. 188–194, 2014.

[32] D. P. Georgiou and N. G. Theodoropoulos, “Grounding and the influence of the total pressure losses in ducted wind turbines,” *Wind Energy*, vol. 13, no. 6, pp. 517–527, Sep. 2010.

[33] S.-H. Chang, Q.-H. Lim, and K.-H. Lin, “Design of a wind energy capturing device for a vehicle,” in *Fifth Int. Conf. Intell. Syst. Model. Simul.*, 2014, pp. 435–440.

[34] T. Y. Chen, Y. T. Liao, and C. C. Cheng, “Development of small wind turbines for moving vehicles: Effects of flanged diffusers on rotor performance,” *Exp. Therm. Fluid Sci.*, vol. 42, pp. 136–142, 2012.

[35] S.-H. Chang, Q.-H. Lim, and K.-H. Lin, “A novel hybrid car design using a wind energy capturing device,” *Int. J. Simul. Syst. Sci. Technol.*, vol. 15, no. 3, pp. 21–29, 2014.

[36] C. S. K. Belloni and R. H. J. Willden, “Flow Field and Performance Analysis of Bidirectional and Open-centre Ducted Tidal Turbines,” in *Proc. 9th Eur. Wave Tidal Energy Conf.*, 2011.

[37] T. Setoguchi, N. Shiomi, and K. Kaneko, “Development of two-way diffuser for fluid energy conversion system,” *Renew. Energy*, vol. 29, no. 10, pp. 1757–1771, Aug. 2004.

[38] C. Shonhiwa and G. Makaka, “Concentrator Augmented Wind Turbines: A review,” *Renew. Sustain. Energy Rev.*, vol. 59, pp. 1415–1418, 2016.

[39] O. Igra, “Research and development for shrouded wind turbines,” *Energy Conversion and Management*, vol. 21, no. 1. pp. 13–48, 1981.

[40] K. M. Foreman and B. L. Gilbert, “A Free Jet Wind Tunnel Investigation of DAWT Models,” Bethpage, New York, RE-668, SERI/TR 01311-1, 1983.

[41] D. G. Phillips, R. G. J. Flay, and T. A. Nash, “Aerodynamic analysis and monitoring of the Vortec 7 diffuser-augmented wind turbine,” *IPENZ Trans.*, vol. 26, no. 1/EMCh, pp. 13–19, 1999.

[42] D. P. Coiro, G. Troise, F. Scherillo, A. De Marco, G. Calise, and N. Bizzarrini, “Development, deployment and experimental test on the novel tethered system GEM for tidal current energy exploitation,” *Renew. Energy*, vol. 114, pp. 323–336, 2017.

[43] E. Daniele, E. Ferrauto, and D. P. Coiro, “Horizontal Axis Hydroturbine Shroud Airfoil Optimization,” in *Advances in Evolutionary and Deterministic Methods for Design, Optimization and Control in Engineering and Sciences*, D. Greiner, B. Galván, J. Périaux, N. Gauger, K. Giannakoglou, and G. Winter, Eds. Cham: Springer, 2015.

[44] N. Oka, M. Furukawa, K. Yamada, A. Oka, and Y. Kurokawa, “Aerodynamic Performances and Flow Fields of Pareto Optimal Solutions in an Aerodynamic Design of a Wind-Lens Turbine,” in *Proc. ASME Turbo Expo 2015 Turbine Tech. Conf. Expo.*, 2015.

[45] R. A. Oman, K. M. Foreman, and B. L. Gilbert, “Investigation of Diffuser-Augmented Wind Turbines: Part II - Technical Report,” Bethpage, New York, RE-534, 1977.

[46] A. L. Loeffler, “Flow Field Analysis and Performance of Wind Turbines Employing Slotted Diffusers,” *J. Sol. Energy Eng.*, vol. 103, no. 1, pp. 17–22, 1981.

[47] M. T. S. Badawy and M. E. Aly, “Gas dynamic analysis of the performance of diffuser augmented wind turbine,” *Sadhana*, vol. 25, no. 5, pp. 453–461, 2000.

[48] B. Buehrle, R. Kishore, and S. Priya, “Computational modeling of ducted wind turbines for residential applications,” in *ASME 2013 Int. Mech. Eng. Congr. Expo.*, 2013, vol. 6A, p. V06AT07A095.

[49] C. A. J. Fletcher, “Computational analysis of diffuser-augmented wind turbines,” *Energy Convers. Manag.*, vol. 21, no. 3, pp. 175–183, 1981.

[50] K. M. Foreman, B. Gilbert, and R. A. Oman, “Diffuser augmentation of wind turbines,” *Sol. Energy*, vol. 20, no. 4, pp. 305–311, 1978.

[51] S. A. H. Jafari and B. Kosasih, “Flow analysis of shrouded small wind turbine with a simple frustum diffuser with computational fluid dynamics simulations,” *J. Wind Eng. Ind. Aerodyn.*, vol. 125, pp. 102–110, 2014.

[52] M. Kardous, R. Chaker, F. Aloui, and S. Ben Nasrallah, “On the dependence of an empty flanged diffuser performance on flange height: Numerical simulations and PIV visualizations,” *Renew. Energy*, vol. 56, pp. 123–128, Aug. 2013.

[53] W. D. Lubitz and A. Shomer, “Wind Loads and Efficiency of a Diffuser Augmented Wind Turbine (DAWT),” in *Proc. Can. Soc. Mech. Eng. Int. Congr. 2014*, 2014.

[54] C. Cardona-Mancilla, J. S.-D. Rio, D. Hincapié-Zuluaga, and E. Chica, “A numerical simulation of horizontal axis hydrokinetic turbine with and without augmented diffuser,” *Int. J. Renew. Energy Res.*, vol. 8, no. 4, pp. 1833–1839, 2018.

[55] M. O. L. Hansen, N. N. Sørensen, and R. G. J. Flay, “Effect of Placing a Diffuser around a Wind Turbine,” *Wind Energy*, vol. 3, no. 4, pp. 207–213, Oct. 2000.

[56] C. J. Lawn, “Optimization of the power output from ducted turbines,” *Proc. Inst. Mech. Eng. Part A J. Power Energy*, vol. 217, no. 1, pp. 107–117, Feb. 2003.

[57] M. Shives and C. Crawford, “Developing an empirical model for ducted tidal turbine performance using numerical simulation results,” *Proc. Inst. Mech. Eng. Part A J. Power Energy* , vol. 226, no. 1, pp. 112–125, Feb. 2012.

[58] G. J. W. van Bussel, “An Assessment of the Performance of Diffuser Augmented Wind Turbines,” in *3rd ASME/JSME Jt. Fluids Eng. Conf.*, 1999.

[59] K. Abe, M. Nishida, A. Sakurai, Y. Ohya, H. Kihara, E. Wada, and K. Sato, “Experimental and numerical investigations of flow fields behind a small wind turbine with a flanged diffuser,” *J. Wind Eng. Ind. Aerodyn.*, vol. 93, no. 12, pp. 951–970, Dec. 2005.

[60] C. I. Coşoiu, A. M. Georgescu, M. Degeratu, L. Haşegan, and D. Hlevca, “Device for passive flow control around vertical axis marine turbine,” *IOP Conf. Ser. Earth Environ. Sci.*, vol. 15, p. 062031, 2012.

[61] O. Igra, “The shrouded aerogenerator,” *Energy*, vol. 2, no. 4, pp. 429–439, Dec. 1977.

[62] R. G. J. Flay, D. G. Phillips, and P. J. Richards, “Development of Diffuser Augmented Wind Turbine Designs in New Zealand,” in *Eur. Wind Energy Conf.*, 1999, pp. 349–352.

[63] K. M. Foreman and B. L. Gilbert, “Technical Development of the Diffuser Augmented Wind Turbine (DAWT) Concept,” in *Wind Energy Innov. Syst. Conf. Proc.*, 1979, pp. 121–135.

[64] D. G. Phillips, P. J. Richards, G. D. Mallinson, and R. G. J. Flay, “Computational Modelling of Diffuser Designs for a Diffuser Augmented Wind Turbine,” in *13th Australas. Fluid Mech. Conf.*, 1998, pp. 207–210.

[65] R. F. Ghajar and E. A. Badr, “An Experimental Study of a Collector and Diffuser System on a Small Demonstration Wind Turbine,” *Int. J. Mech. Eng. Educ.*, vol. 36, no. 1, pp. 58–68, Jan. 2008.

[66] G. J. W. van Bussel, “The science of making more torque from wind: Diffuser experiments and theory revisited.,” *J. Phys. Conf. Ser.*, vol. 75, no. 1, p. 12010, 2007.

[67] H. Grassmann, F. Bet, G. Cabras, M. Ceschia, D. Cobai, and C. DelPapa, “A partially static turbine-first experimental results,” *Renew. Energy*, vol. 28, no. 11, pp. 1779–1785, 2003.

[68] O. Igra, “Design and performance of a turbine suitable for an aerogenerator,” *Energy Convers.*, vol. 15, no. 3–4, pp. 143–151, 1976.

[69] J. D. Anderson Jr, *Fundamentals of Aerodynamics*, 5th ed. New York: McGraw-Hill, 2011.

[70] B. Franković and I. Vrsalović, “New high profitable wind turbines,” *Renew. Energy*, vol. 24, no. 3–4, pp. 491–499, Nov. 2001.

[71] I. Vrsalović, “Senj wind power plant,” *Sol. Wind Technol.*, vol. 7, no. 2/3, pp. 169–175, 1990.

[72] R. Venters, B. T. Helenbrook, and K. D. Visser, “Ducted Wind Turbine Optimization,” *J. Sol. Energy Eng.*, vol. 140, no. 1, p. 011005, Nov. 2017.

[73] V. V. Dighe, G. de Oliveira, F. Avallone, and G. J. W. van Bussel, “On the effects of the shape of the duct for ducted wind turbines,” in *2018 Wind Energy Symp.*, 2018.

[74] A. C. Aranake, V. K. Lakshminarayan, and K. Duraisamy, “Computational analysis of shrouded wind turbine configurations using a 3-dimensional RANS solver,” *Renew. Energy*, vol. 75, pp. 818–832, 2015.

[75] E. Dick, “Power Limits for Wind Energy Concentrator Systems,” *Wind Eng.*, vol. 10, no. 2, pp. 98–115, 1986.

[76] E. Dick, “Momentum analysis of wind energy concentrator systems,” *Energy Convers. Manag.*, vol. 24, no. 1, pp. 19–25, 1984.

[77] M. O. L. Hansen, “Shrouded Rotors,” in *Aerodynamics of Wind Turbines*, 3rd ed., Oxford: Routledge, 2017, pp. 12–15.

[78] C. I. Coşoiu, A. M. Georgescu, M. Degeratu, and D. Hlevca, “Numerical predictions of the flow around a profiled casing equipped with passive flow control devices,” *J. Wind Eng. Ind. Aerodyn.*, vol. 114, pp. 48–61, 2013.

[79] B. L. Gilbert and K. M. Foreman, “Experiments With a Diffuser-Augmented Model Wind Turbine,” *J. Energy Resour. Technol.*, vol. 105, no. 1, pp. 46–53, Mar. 1983.

[80] A. L. Loeffler and D. Vanderbilt, “Inviscid flow through wide-angle diffuser with actuator disk,” *AIAA J.*, vol. 16, no. 10, pp. 1111–1112, Oct. 1978.

[81] J. M. Laurens, M. Ait-Mohammed, and M. Tarfaoui, “Design of bare and ducted axial marine current turbines,” *Renew. Energy*, vol. 89, pp. 181–187, 2016.

[82] M. Nachtane, M. Tarfaoui, D. Saifaoui, A. El Moumen, O. H. Hassoon, and H. Benyahia, “Evaluation of durability of composite materials applied to renewable marine energy: Case of ducted tidal turbine,” *Energy Reports*, vol. 4, pp. 31–40, 2018.

[83] S. Kale and S. N. Sapali, “Development and Field Testing of An Inclined Flanged Compact Diffuser for a Micro Wind Turbine,” in *ASME 2014 Int. Mech. Eng. Congr. Expo.*, 2014, no. 46521, p. V06BT07A070.

[84] K. Mansour and P. Meskinkhoda, “Computational analysis of flow fields around flanged diffusers,” *J. Wind Eng. Ind. Aerodyn.*, vol. 124, pp. 109–120, 2014.

[85] V. Nikolić, D. Petković, S. Shamshirband, and Ž. Ćojbašić, “Adaptive neuro-fuzzy estimation of diffuser effects on wind turbine performance,” *Energy*, vol. 89, pp. 324–333, 2015.

[86] A. M. El-Zahaby, A. E. Kabeel, S. S. Elsayed, and M. F. Obiaa, “CFD analysis of flow fields for shrouded wind turbine’s diffuser model with different flange angles,” *Alexandria Eng. J.*, vol. 56, no. 1, pp. 171–179, 2017.

[87] J.-F. Hu and W.-X. Wang, “Upgrading a shrouded wind turbine with a self-adaptive flanged diffuser,” *Energies*, vol. 8, no. 6, pp. 5319–5337, 2015.

[88] Y. Ohya, T. Karasudani, A. Sakurai, K. Abe, and M. Inoue, “Development of a shrouded wind turbine with a flanged diffuser,” *J. Wind Eng. Ind. Aerodyn.*, vol. 96, no. 5, pp. 524–539, May 2008.

[89] Y. Ohya, T. Karasudani, A. Sakurai, and M. Inoue, “Development of a High-Performance Wind Turbine Equipped with a Brimmed Diffuser Shroud,” *Trans. Jpn. Soc. Aeronaut. Space Sci.*, vol. 49, no. 163, pp. 18–24, 2006.

[90] K. Toshimitsu, K. Nishikawa, W. Haruki, S. Oono, M. Takao, and Y. Ohya, “PIV measurements of flows around the wind turbines with a flanged-diffuser shroud,” *J. Therm. Sci.*, vol. 17, no. 4, pp. 375–380, 2008.

[91] A. Tourlidakis, K. Vafiadis, V. Andrianopoulos, and I. Kalogeropoulos, “Aerodynamic Design and Analysis of a Flanged Diffuser Augmented Wind Turbine,” in *ASME Turbo Expo 2013 Turbine Tech. Conf. Expo.*, 2013, p. V008T44A022.

[92] A. Nasution and D. W. Purwanto, “Optimized curvature interior profile for Diffuser Augmented Wind Turbine (DAWT) to increase its energy-conversion performance,” in *IEEE First Conf. Clean Energy Technol.*, 2011, pp. 315–320.

[93] M. I. Maulana, A. Syuhada, and M. Nawawi, “Analysis of diffuser augmented wind turbine (DAWT) with flange and curved interior using CFD,” in *AIP Conf. Proc.*, 2018, vol. 1984, p. 020025.

[94] A. Agha and H. Nasarullah Chaudhry, “State-of-the-art in development of diffuser augmented wind turbines (DAWT) for sustainable buildings,” *MATEC Web Conf.*, vol. 120, p. 08008, 2017.

[95] R. Bontempo and M. Manna, “Effects of the duct thrust on the performance of ducted wind turbines,” *Energy*, vol. 99, pp. 274–287, 2016.

[96] J. R. P. Vaz and D. H. Wood, “Aerodynamic optimization of the blades of diffuser-augmented wind turbines,” *Energy Convers. Manag.*, vol. 123, pp. 35–45, 2016.

[97] V. V. Dighe, G. de Oliveira, F. Avallone, and G. J. W. van Bussel, “Towards improving the aerodynamic performance of a ducted wind turbine: A numerical study,” *J. Phys. Conf. Ser.*, vol. 1037, p. 022016, Jun. 2018.

[98] W. Shi, D. Wang, M. Atlar, B. Guo, and K. Seo, “Optimal design of a thin-wall diffuser for performance improvement of a tidal energy system for an AUV,” *Ocean Eng.*, vol. 108, pp. 1–9, 2015.

[99] C. F. Fleming, S. C. McIntosh, and R. H. J. Willden, “Design and analysis of a bi-directional ducted tidal turbine,” in *9th Eur. Wave Tidal Energy Conf.*, 2011.

[100] B. Kosasih and H. Saleh Hudin, “Influence of inflow turbulence intensity on the performance of bare and diffuser-augmented micro wind turbine model,” *Renew. Energy*, vol. 87, pp. 154–167, 2016.

[101] N. Bagheri-Sadeghi, B. T. Helenbrook, and K. D. Visser, “Ducted wind turbine optimization and sensitivity to rotor position,” *Wind Energy Sci.*, vol. 3, no. 1, pp. 221–229, Apr. 2018.

[102] H. A. Heikal, O. S. M. Abu-Elyazeed, M. A. A. Nawar, Y. A. Attai, and M. M. S. Mohamed, “On the actual power coefficient by theoretical developing of the diffuser flange of wind-lens turbine,” *Renew. Energy*, vol. 125, pp. 295–305, Sep. 2018.

[103] B. Kanya and K. D. Visser, “Experimental validation of a ducted wind turbine design strategy,” *Wind Energy Sci.*, vol. 3, no. 2, pp. 919–928, Dec. 2018.

[104] J. Tang, F. Avallone, and G. J. W. van Bussel, “Experimental study of flow field of an aerofoil shaped diffuser with a porous screen simulating the rotor,” *Int. J. Comput. Methods Exp. Meas.*, vol. 4, no. 4, pp. 502–512, 2016.

[105] D. A. Tavares Dias do Rio Vaz, A. L. Amarante Mesquita, J. R. Pinheiro Vaz, C. J. Cavalcante Blanco, and J. T. Pinho, “An extension of the Blade Element Momentum method applied to Diffuser Augmented Wind Turbines,” *Energy Convers. Manag.*, vol. 87, pp. 1116–1123, Nov. 2014.

[106] J. R. P. Vaz and D. H. Wood, “Effect of the diffuser efficiency on wind turbine performance,” *Renew. Energy*, vol. 126, pp. 969–977, Oct. 2018.

[107] M. L. Helmy, “Dimensions of the axial flow turbine design for wind power,” *Renew. Energy*, vol. 1, no. 2, pp. 303–307, 1991.

[108] M. J. Werle and W. M. Presz, “Ducted Wind/Water Turbines and Propellers Revisited,” *J. Propuls. Power*, vol. 24, no. 5, pp. 1146–1150, Sep. 2008.

[109] H. Ahmadi Asl, R. Kamali Monfared, and M. Rad, “Experimental investigation of blade number and design effects for a ducted wind turbine,” *Renew. Energy*, vol. 105, pp. 334–343, 2017.

[110] D. P. Dadula and J. C. Maglasang, “Development of a Diffuser-Augmented Multi-Bladed Micro-Scale Wind Turbine with Guide Vanes,” in *6th Int. Conf. Humanoid, Nanotechnology, Inf. Technol. Commun. Control. Environ. Manag.*, 2013.

[111] W.-X. Wang, T. Matsubara, J. Hu, S. Odahara, T. Nagai, T. Karasutani, and Y. Ohya, “Experimental investigation into the influence of the flanged diffuser on the dynamic behavior of CFRP blade of a shrouded wind turbine,” *Renew. Energy*, vol. 78, pp. 386–397, 2015.

[112] R. A. Kishore, T. Coudron, and S. Priya, “Small-scale wind energy portable turbine (SWEPT),” *J. Wind Eng. Ind. Aerodyn.*, vol. 116, pp. 21–31, 2013.

[113] R. Luquet, D. Bellevre, D. Fréchou, P. Perdon, and P. Guinard, “Design and model testing of an optimized ducted marine current turbine,” *Int. J. Mar. Energy*, vol. 2, pp. 61–80, Jun. 2013.

[114] Y. Ohya, T. Uchida, T. Karasudani, M. Hasegawa, and H. Kume, “Numerical Studies of Flow around a Wind Turbine Equipped with a Flanged-Diffuser Shroud using an Actuator-Disk Model,” *Wind Eng.*, vol. 36, no. 4, pp. 455–472, Aug. 2012.

[115] J. Reinecke, T. W. von Backström, and G. Venter, “Effect of a Diffuser on the Performance of an Ocean Current Turbine,” in *Eur. Wave Tidal Energy Conf.*, 2011.

[116] S.-H. Wang and S.-H. Chen, “The Study of Interference Effect for Cascaded Diffuser Augmented Wind Turbines,” in *Seventh Asia-Pacific Conf. Wind Eng.*, 2009.

[117] F. Wang, L. Bai, J. Fletcher, J. Whiteford, and D. Cullen, “The methodology for aerodynamic study on a small domestic wind turbine with scoop,” *J. Wind Eng. Ind. Aerodyn.*, vol. 96, no. 1, pp. 1–24, 2008.

[118] O. Igra, “Compact shrouds for wind turbines,” *Energy Convers.*, vol. 16, no. 4, pp. 149–157, 1977.

[119] T. Matsushima, S. Takagi, and S. Muroyama, “Characteristics of a highly efficient propeller type small wind turbine with a diffuser,” *Renew. Energy*, vol. 31, no. 9, pp. 1343–1354, Jul. 2006.

[120] M. Rashidi, J. R. Kadambi, and A. Ebiana, “Performance of a Rooftop Wind Turbine System Having a Wind Deflecting Structure, Experimental Results,” in *ASME 2015 Int. Mech. Eng. Congr. Expo.*, 2015, p. V07AT09A012.

[121] N. W. Cresswell, G. L. Ingram, and R. G. Dominy, “The impact of diffuser augmentation on a tidal stream turbine,” *Ocean Eng.*, vol. 108, pp. 155–163, Nov. 2015.

[122] D. L. F. Gaden and E. L. Bibeau, “A numerical investigation into the effect of diffusers on the performance of hydro kinetic turbines using a validated momentum source turbine model,” *Renew. Energy*, vol. 35, no. 6, pp. 1152–1158, Jun. 2010.

[123] T. Saravana Kannan, S. A. Mutasher, and Y. H. K. Lau, “Design and flow velocity simulation of diffuser augmented wind turbine using CFD,” *J. Eng. Sci. Technol.*, vol. 8, no. 4, pp. 372–384, 2013.

[124] E. S. Nortrup, “CFD study of the effects on diffuser augmented wind turbine performance,” University of Illinois at Urbana-Champaign, 2010.

[125] S.-H. Wang and S.-H. Chen, “Blade number effect for a ducted wind turbine,” *J. Mech. Sci. Technol.*, vol. 22, no. 10, pp. 1984–1992, 2008.

[126] H. Grassmann, F. Bet, M. Ceschia, and M. L. Ganis, “On the physics of partially static turbines,” *Renew. Energy*, vol. 29, no. 4, pp. 491–499, Apr. 2004.

[127] D. P. Coiro, E. Daniele, and P. Della Vecchia, “Diffuser shape optimization for GEM, a tethered system based on two horizontal axis hydro turbines,” in *2nd Asian Wave Tidal Energy Conf.*, 2014.

[128] T. Foote and R. Agarwal, “Optimization of power generation from shrouded wind turbines,” *Int. J. Energy Environ.*, vol. 4, no. 4, pp. 549–560, 2013.

[129] M. Shives and C. Crawford, “Ducted Turbine Blade Optimization Using Numerical Simulation,” in *Proc. Int. Offshore Polar Eng. Conf.*, 2011, pp. 407–413.

[130] S. N. Leloudas, G. N. Lygidakis, G. A. Strofylas, and I. K. Nikolos, “Aerodynamic Shape Optimization of Diffuser Augmented Wind Turbine Shrouds Using Asynchronous Differential Evolution,” in *ASME 2018 Int. Mech. Eng. Congr. Expo.*, 2018, p. V007T09A085.

[131] R. Chaker, M. Kardous, F. Aloui, and S. Ben Nasrallah, “Relationship between open angle and aerodynamic performances of a DAWT,” in *Fourth Int. Renew. Energy Congr.*, 2012, pp. 93–100.

[132] T. A. Khamlaj and M. Rumpfkeil, “Analysis and Optimization Study of Shrouded Horizontal Axis Wind Turbines,” in *2018 Wind Energy Symp.*, 2018.

[133] T. A. Khamlaj, “Analysis and Optimization of Shrouded Horizontal Axis Wind Turbines,” University of Dayton, 2018.

[134] B. Knight, R. Freda, Y. Young, and K. Maki, “Coupling Numerical Methods and Analytical Models for Ducted Turbines to Evaluate Designs,” *J. Mar. Sci. Eng.*, vol. 6, no. 2, p. 43, Apr. 2018.

[135] A. L. Loeffler and J. S. Steinhoff, “Computation of wind tunnel wall effects in ducted rotor experiments,” *J. Aircr.*, vol. 22, no. 3, pp. 188–192, Mar. 1985.

[136] A. C. Aranake, V. K. Lakshminarayan, and K. Duraisamy, “Assessment of low-order theories for analysis and design of shrouded wind turbines using CFD,” in *J. Phys. Conf. Ser.*, 2014, vol. 524, p. 12077.

[137] P. M. Jamieson, “Beating Betz: Energy Extraction Limits in a Constrained Flow Field,” *J. Sol. Energy Eng.*, vol. 131, no. 3, p. 031008, 2009.

[138] D. L. M. Barbosa, D. A. T. D. R. Vaz, J. R. P. Vaz, S. W. O. Figueiredo, M. O. Da Silva, C. J. C. Blanco, and A. L. A. Mesquita, “A Proposed Mathematical Model for the Velocity Profile Internally to a Conical Diffuser,” *Rev. Eng. Térmica*, vol. 12, no. 2, p. 69, Dec. 2013.

[139] O. Igra, “Shrouds for Aerogenerators,” *AIAA J.*, vol. 14, no. 10, pp. 1481–1483, Oct. 1976.

[140] M. Nasir, I. Bayu Dwianditya, K. Suryopratomo, and Sihana, “The effect of inlet curvature and flange on wind turbine diffuser performance,” *E3S Web Conf.*, vol. 43, p. 01025, Jun. 2018.

[141] J. Tang and G. J. W. van Bussel, “Wind Tunnel Testing Airfoil with Screens at Low Reynolds Number,” in *2018 Wind Energy Symp.*, 2018.

[142] J. Tang, F. Avallone, R. Bontempo, G. J. van Bussel, and M. Manna, “Experimental investigation on the effect of the duct geometrical parameters on the performance of a ducted wind turbine,” *J. Phys. Conf. Ser.*, vol. 1037, p. 022034, Jun. 2018.

[143] M. O. L. Hansen, N. N. Sørensen, and R. G. J. Flay, “Effect of Placing a Diffuser around a Wind Turbine,” in *Eur. Wind Energy Conf.*, 1999, pp. 322–324.

[144] P. V. M. Maia, R. M. J. Santos, J. R. P. Vaz, M. O. Silva, and E. F. Lins, “Experimental Study of Three Different Airfoils Applied to Diffuser-Augmented Wind Turbines,” *J. Urban Environ. Eng.*, vol. 12, no. 1, pp. 147–153, 2018.

[145] H. M. Elbakry, A. A. A. Attia, O. E. Abdelatif, and M. S. Zahran, “Simulation of Diffuser Augmented Wind Turbine Performance,” in *2016 World Congr. Sustain. Technol.*, 2016, pp. 40–48.

[146] F. Qashidi Putra, D. Rifai, K. Suryopratomo, and R. Budiarto, “Multilevel Diffuser Augmented for Horizontal Axis Wind Turbine,” *E3S Web Conf.*, vol. 42, p. 01001, Jun. 2018.

[147] R. L. Mitchell and E. W. Jacobs, “The SERI Advanced and Innovative Wind Energy Concepts Program,” in *Sixth Bienn. Wind Energy Conf. Work.*, 1983, pp. 265–275.

[148] J. Katz and A. Plotkin, *Low-Speed Aerodynamics*, 2nd ed. New York: Cambridge University Press, 2001.

[149] Z. Galias, “The dangers of rounding errors for simulations and analysis of nonlinear circuits and systems - and how to avoid them,” *IEEE Circuits Syst. Mag.*, vol. 13, no. 3, pp. 35–52, 2013.

[150] "MATLAB Release 2014a - 2016a." The MathWorks Inc., Natick, Massachusetts, United States.

[151] S. S. Yoon and S. D. Heister, "Analytical formulas for the velocity field induced by an infinitely thin vortex ring," *Int. J. Numer. Methods Fluids*, vol. 44, no. 6, pp. 665–672, 2004.

[152] B. de Bernardinis, "Unsteady axisymmetric flow by the method of discrete vortices," Imperial College London, 1980.

[153] The MathWorks Inc., "pchip," in *MATLAB Function Reference*, Natick, 2016.

[154] The MathWorks Inc., "mldivide," in *MATLAB Function Reference*, Natick, 2016.

[155] G. van Kuik, *The Fluid Dynamic Basis for Actuator Disc and Rotor Theories*. Amsterdam: IOS Press BV, 2018.

[156] I. S. Gibson, "On the velocity induced by a semi-infinite vortex cylinder: with extension to the short solenoid," *Aeronaut. J.*, vol. 78, no. 762, pp. 262–268, 1974.

[157] The MathWorks Inc., "roots," in *MATLAB Function Reference*, Natick, 2016.

[158] The MathWorks Inc., "fzero," in *MATLAB Function Reference*, Natick, 2016.

[159] W. F. Durand, "Fluid Mechanics, Part I," in *Aerodynamic Theory: A General Review of Progress Under a Grant of the Guggenheim Fund for the Promotion of Aeronautics*, W. F. Durand, Ed. Berlin, Heidelberg: Springer-Verlag, 1934.

[160] R. J. S. Simpson, R. Palacios, and J. Murua, "Induced-Drag Calculations in the Unsteady Vortex Lattice Method," *AIAA J.*, vol. 51, no. 7, pp. 1775–1779, 2013.

[161] The MathWorks Inc., "fminbnd," in *MATLAB Function Reference*, Natick, 2016.

[162] "ANSYS Academic Research 15.0." Ansys Inc.

[163] J. F. Wendt, Ed., *Computational Fluid Dynamics*, 3rd ed. Berlin, Heidelberg: Springer Berlin Heidelberg, 2009.

[164] ANSYS Inc., *ANSYS Fluent User's Guide Release 15.0*. Canonsburg, 2014.

[165] ANSYS Inc., *ANSYS Fluent Theory Guide Release 15.0*. Canonsburg, 2013.

[166] M. Shives and C. Crawford, "Computational Analysis of Ducted Turbine Performance," in *3rd Int. Conf. Ocean Energy*, 2010.

[167] ANSYS Inc., *ANSYS Meshing User's Guide Release 15.0*. Canonsburg, 2013.

[168] ESDU, "ESDU 85020: Characteristics of atmospheric turbulence near the ground: Part II Single point data for strong winds (neutral atmosphere)," 2001.

[169] The Danish Energy Agency's Approval Scheme for Wind Turbines, "Recommendation for Technical Approval of Offshore Wind Turbines," 2001.

[170] K. Røkenes, "Investigation of terrain effects with respect to wind farm siting," Norwegian University of Science and Technology, 2009.

[171] I. B. Celik, U. Ghia, P. J. Roache, C. J. Freitas, H. Coleman, and P. E. Raad, "Procedure for Estimation and Reporting of Uncertainty Due to Discretization in CFD Applications," *J. Fluids Eng.*, vol. 130, no. 7, p. 78001, 2008.

[172] H. K. Versteeg and W. Malalasekera, *An Introduction to Computational Fluid Dynamics: The Finite Volume Method*, 2nd ed. Harlow: Pearson Education Limited, 2007.

[173] P. J. Roache, "Perspective: A Method for Uniform Reporting of Grid Refinement Studies," *J. Fluids Eng.*, vol. 116, no. 3, pp. 405–413, 1994.

[174] K. L. Kreider, “MATLAB code for fixed point algorithm.” The University of Akron, Akron, Available: http://www.math.uakron.edu/~kreider/num1/fixedpoint.pdf. [Accessed: 06-Oct-2015].

[175] P. Jamieson, *Innovation in Wind Turbine Design*. Chichester: John Wiley & Sons, Ltd., 2011.

[176] The MathWorks Inc., “fmincon Interior Point Algorithm,” in *MATLAB Optimization Toolbox User’s Guide*, Natick, 2017.

[177] Y. Ohya and T. Karasudani, “A Shrouded Wind Turbine Generating High Output Power with Wind-Lens Technology,” in *Wind Turbine Technology: Principles and Design*, M. Adaramola, Ed. Oakville: Apple Academic Press, Inc, 2014.

[178] L. Ladson, Charles and C. W. Brooks Jr., “Development of a Computer Program to Obtain Ordinates for NACA 4-Digit, 4-Digit Modified, 5-Digit, and 16-Series Airfoils,” NASA TM X-3284, 1975.

[179] I. H. Abbott and A. E. von Doenhoff, *Theory of Wing Sections: Including a Summary of Airfoil Data*. New York: Dover Publications, 1959.

[180] J. J. Wang, Y. C. Li, and K. S. Choi, “Gurney flap-Lift enhancement, mechanisms and applications,” *Prog. Aerosp. Sci.*, vol. 44, no. 1, pp. 22–47, 2008.

[181] The MathWorks Inc., “stepwiselm,” in *Statistics and Machine Learning Toolbox User’s Guide*, Natick, 2017.

[182] The MathWorks Inc., “fgoalattain,” in *Optimization Toolbox User’s Guide*, Natick, 2017.

[183] C. L. Ladson, C. W. Brooks, A. S. Hill, and D. W. Sproles, “Computer Program To Obtain Ordinates for NACA Airfoils,” NASA TM 4741, 1996.

[184] The MathWorks Inc., “Coefficient of Determination (R-Squared),” in *Statistics and Machine Learning Toolbox User’s Guide*, Natick, 2017.

[185] J. N. Sørensen, *General Momentum Theory for Horizontal Axis Wind Turbines*. Cham: Springer International Publishing AG, 2016.

[186] P. Jamieson, “Generalized limits for energy extraction in a linear constant velocity flow field,” *Wind Energy*, vol. 11, no. 5, pp. 445–457, 2008.

[187] H. Chanson, *The Hydraulics of Open Channel Flow: An Introduction*, 2nd ed. Oxford: Elsevier Butterworth-Heinemann, 2004.

[188] J. A. Liggett, “Critical Depth, Velocity Profiles, and Averaging,” *J. Irrig. Drain. Eng.*, vol. 119, no. 2, pp. 416–422, 1993.

[189] Y. A. Çengel and R. H. Turner, *Fundamentals of Thermal-Fluid Sciences*, 2nd ed. New York: McGraw-Hill, 2005.

[190] J. V. Boussinesq, “Essai sur la Théorie des Eaux Courantes (‘Essay on the Theory of Water Flow’),” *Mémoires présentés par Divers savants à l’Académie des Sci. l’Institut Natl. Fr.*, vol. 23, ser. 3, no. 1, supplément 24, pp. 1–680, 1877.

[191] H. Snel, “Review of Aerodynamic Investigations and Design Work Underlying the Vortec 1 MW Wind Turbine and Suggestions for Further Optimization,” Energieonderzoek Centrum Nederland, ECN-CX—01-070, 2001.

[192] B. W. McCormick Jr, *Aerodynamics of V/STOL Flight*. New York: Academic Press, 1967.

[193] R. Bontempo and M. Manna, “Solution of the flow over a non-uniform heavily loaded ducted actuator disk,” *J. Fluid Mech.*, vol. 728, pp. 163–195, 2013.